UNIVERSITY OF CAPE TOWN

IYUNIVESITHI YASEKAPA • UNIVERSITEIT VAN KAAPSTAD

Improved estimates and understanding of interannual trends of CO_2 fluxes in the Southern Ocean

Luke Gregor

March 2017

A thesis presented for Doctor of Philosophy

Department of Oceanography

University of Cape Town

Supervisor 1: Dr. Pedro M. S. Monteiro (Council for Scientific and Industrial Research)

Supervisor 2: Assoc. Prof. Marcello Vichi (University of Cape Town)

Supervisor 3: Assoc. Prof. Schalk Kok (University of Pretoria)

Acknowledgements

This PhD was funded by the ACCESS program and I would like to thank them for granting me this opportunity.

I would like to thank Dr. Pedro Monteiro for his thoughtful guidance and understanding throughout the PhD. For the invaluable opportunities he has provided over the course of the last seven years by allowing me to travel and attend conferences, student exchanges, research cruises. Similarly I would like to thank Dr. Schalk Kok for his technical advice, rigour and pragmatic insights provided over many long phone calls. I would like to thank Dr. Marcello Vichi for stepping in as a supervisor in the eleventh hour.

I would like to thank Dr. Marina Lévy for hosting me at L'OCEAN during the SOCCLI exchange and allowing me to use the BIOPERIANT05-GAA95b model data. Thanks to Dr. Nicolette Chang for running the BIOSATLANTIC12-CNCRAD07A model configuration (and sustaining us with her stash of sweets).

The continued input, advice and support from my office mates in the SOCCO Rosebank office: Sarah, Marcel, Precious, Sandy, Nicolette, Tommy, Emma, Stuart, Lisl, Marjo, Marie and Christo. And to Warren and Seb, both who have left the SOCCO group, but have made a lasting impression on my view of science-life balance.

A special thanks to my social support group throughout the PhD, particularly over the course of the last two years during the persistence of The Glandge (glandular fever and fatigue). With that I like to thank the De Korte family for feeding, supporting and praying for me, particularly during the last two years. Also to Simone for being a supportive sister who frequently housed and entertained me on my visits to Pretoria. A special thanks to the other two members of the FOLD, Faure and Ollie, who have kept up my spirits and put up with my dining table takeovers.

Last, but not least, my parents, whom I cannot thank enough, for supporting me throughout the PhD and all the years leading to it. For providing me with the best opportunities they could and their continued prayers. I could not have walked this path without them.

L.G.

Abstract

The Southern Ocean plays an important role in mitigating the effects of anthropogenically driven climate change by being a sink for atmospheric carbon, but this is foreseen to change with increasing greenhouse gas emissions. Studies have already shown that Southern Ocean CO_2 is subject to interannual variability. Measuring and understanding this change has been difficult due to sparse observational data that is biased toward summer. Machine learning has been successful in estimating CO_2 in may parts of the ocean by extrapolating existing data with satellite measurements of proxy variables of CO_2. However, in the Southern Ocean machine learning has proven less successful. Large differences between machine learning estimates stem from the paucity of data and complexity of the mechanisms that drive CO_2 in the Southern Ocean. In this study the aim is to reduce the uncertainty of estimates, improve the understanding of the drivers, and optimise sampling of CO_2 in the Southern Ocean.

Improving the estimates of CO_2 was achieved by investigating: the impact of increasing the gridding resolution of input data and proxy variables, and Support vector regression (SVR) and Random Forest Regression (RFR) as alternate machine learning methods. It was found that the improvement gained by increasing gridding resolution was minimal and only RFR was able to improve on existing error estimates. Yet, there was good agreement of the seasonal cycle and interannual trends between RFR, SVR and estimates from the literature.

The ensemble mean of these methods was used to investigate the variability and interannual trends of CO_2 in the Southern Ocean. The analysis showed that wind was the overall driver of dominant decadal interannual trends, being more important during winter due to the increased efficacy of entrainment processes. Moreover, the Indian sector of the Southern Ocean was prominent in driving this interannual variability. Summer interannual variability of CO_2 was driven primarily by Chl-a, which responded to basin scale changes in drivers by the complex interaction with underlying physics and possibly sub-mesoscale processes.

Lastly CO_2 sampling platforms, namely ships, profiling floats and moorings, were tested in an idealised simulated model environment using a machine learning approach. Ships, simulated from existing cruise tracks, failed to adequately resolve CO_2 below the uncertainty threshold that is required to resolve the seasonal cycle of Southern Ocean CO_2. Eight high frequency sampling

moorings narrowly outperformed 200 profiling floats, which were both able to adequately resolve the seasonal cycle. Though, a combination of ships and profiling floats achieved the smallest error.

Acronyms

ACC Antarctic Circumpolar Current

ACW Antarctic Circumpolar Wave

ANN Artificial Neural Network

Chl-*a* Chlorophyll-*a*

CO_2 Carbon dioxide

CSIR Council for Scientific and Industrial Research

ΔpCO_2 Atmospheric pCO_2 – Oceanic pCO_2

DIC Dissolved Inorganic Carbon

ENSO El Niño – Southern Oscillation

FCO_2 Air-sea CO_2 flux

fCO_2 Fugacity of carbon dioxide

FFN Feed Forward Neural Network

MIZ Marginal Ice Zone

MLD Mixed Later Depth

MLR Multi-Linear Regression

MOC Meridional Overturning Circulation

pCO_2 Partial pressure of carbon dioxide

PF Polar Front

PFZ Polar Frontal Zone

RFB Radial Basis Function

RF Random Forest

RFR Random Forest Regression

SAM Southern Annular Mode

SAZ Sub-Antarctic Zone

SOCAT Surface Ocean Carbon Atlas

SOCCO Southern Ocean Carbon and Climate Observatory

SOCCOM Southern Ocean Carbon and Climate Observations and Modelling

SOCOM Surface Ocean CO_2 Mapping project

SST Sea Surface Temperature

SSS Sea Surface Salinity

SVM Support Vector Machine

SVR Support Vector Regression

SVs Support Vectors

TA Total Alkalinity

$x\mathbf{CO_2}$ Mole fraction of CO_2

Contents

List of Figures

List of Tables

Chapter 1

Introduction and literature review

1.1 Defining the problem

Over the last century, burning of fossil fuels has increased atmospheric carbon dioxide concentration (CO_2) from approximately 280 to 400 ppm (Le Quéré et al., 2016). The additional anthropogenic component of CO_2 (CO_2^{ant}) is the primary driver of climate change due to the green house effect (Arrhenius, 1896; Stocker et al., 2013; Le Quéré et al., 2016). The oceans have played a large role in mitigating climate change by taking up nearly half of emitted CO_2^{ant} to date and a large amount of heat (Sabine et al., 2004; Khatiwala et al., 2009; Le Quéré et al., 2016). The Southern Ocean plays a large part in this mitigation role, accounting for 43% of oceanic CO_2^{ant} uptake and storage (42 ± 5 PgC) and 75% of oceanic heat uptake ($23 \pm 9 \times 10^2 2$ J) since the start of the industrial era (Frolicher et al., 2015). The uptake of CO_2^{ant} is over and above the natural outgassing flux of CO_2 (CO_2^{nat}), which is assumed to have been steady in the pre-industrial period (McNeil and Matear, 2013a; Le Quéré et al., 2016). The magnitude of CO_2 fluxes in the Southern Ocean is thus a balance between outgassing of CO_2^{nat} and uptake of CO_2^{ant}.

The current state of CO_2 uptake in the Southern Ocean is not steady, suggesting a shift in the equilibrium between the outgassing of CO_2^{nat} and uptake of CO_2^{ant} (McNeil and Matear, 2013b; Devries et al., 2017). Le Quéré et al. (2007) found that the Southern Ocean CO_2 sink was weakening due to a southerly shift in westerly winds, resulting in increased outgassing of CO_2^{nat} (Devries et al., 2017). Subsequently, Landschützer et al. (2015) reported a reinvigoration of the Southern Ocean CO_2 sink, driven by a change in the zonal nature of atmospheric circulation that

led to a basin specific interaction between marine carbonate chemistry and the thermal response of pCO_2. This illustrates that the response of CO_2 to drivers is complex.

Given the importance of the Southern Ocean in the global carbon cycle it is key that we are able to accurately monitor and predict changes in the uptake of CO_2^{ant} and outgassing of CO_2^{nat}. However, we are not able to accurately monitor year-to-year, let alone intra-seasonal, CO_2 changes in the Southern Ocean due to the paucity of observations exacerbated by the large seasonal signal of CO_2 in the Southern Ocean (Lenton et al., 2006; Monteiro et al., 2010). Moreover, our current understanding of the seasonal drivers of CO_2 in the Southern Ocean are not yet at a point where mechanistic models are able to accurately represent the seasonal cycle of CO_2 – a key component in correctly predicting future changes (Lenton et al., 2013; Mongwe et al., 2016). These goals are important if we, as a community, are to "better understand the global carbon cycle, support the development of climate policies, and project future climate change" (Le Quéré et al., 2016)

The community has responded to this problem in two ways:

1. *Make use of existing data.* Empirical modelling (or CO_2 mapping) has proven an adequate tool for filling data gaps by extrapolating *in-situ* CO_2 measurements with remote sensing data.

2. *Increasing the number of observations.* A concerted effort has been made to increase the number of ship based measurements in the Southern Ocean. Recently, this task has been aided by the progress in autonomous sampling technology that can measure CO_2 with sufficient accuracy.

The remainder of this chapter looks at the literature and how the community has approached the problem of sparse data in the Southern Ocean. The first part of the literature review gives an overview of the marine carbonate cycle and the potential mechanisms that act to change CO_2. This is followed by an introduction of the physical setting of the Southern Ocean. The role of these mechanisms in the Southern Ocean is then investigated in the context of the seasonal cycle and the broader trends of interannual variability. This leads into how the community has been using empirical models to fill the sampling gap. Lastly, I review the literature that has recommended CO_2 sampling strategies, with the aim of closing the sampling gap more efficiently. Questions

and aims of this thesis are laid out with the structure of the thesis.

1.2 Carbon dioxide in the ocean

1.2.1 The marine carbonate system

Marine carbonate chemistry forms the core of our understanding of the drivers of CO_2 in the ocean. The chemical dynamics of CO_2 in the ocean are more complex than inert gasses, such as N_2, as the former interacts with water to form carbonic acid (H_2CO_3). Carbonic acid dissociates to form several species of the marine carbonate system summarised by:

$$\overbrace{\underbrace{H_2O + CO_{2(aq)}}_{pCO_2} \overset{K_0}{\rightleftharpoons} H_2CO_3 \overset{K_1}{\rightleftharpoons} \underbrace{HCO_3^- \overset{K_2}{\rightleftharpoons} CO_3^{2-}}_{TA^*}}^{DIC} \quad \underbrace{\underbrace{H^+}_{}\quad\underbrace{H^+}_{}}_{pH} \tag{1.1}$$

Dissolved inorganic carbon (DIC) encompasses all of the species of carbon in the equation, while total alkalinity (TA*) is the sum of bicarbonate (HCO_3^-) and carbonate (CO_3^{2-}) (Dickson et al., 2007). In the equation TA* is defined as the number of protons that the carbonate system can accept in a titration, where carbonate accepts two protons (TA$\approx[HCO_3-] + 2[CO_3^{2-}]$) (Wolf-Gladrow et al., 2007). Strictly speaking this definition of TA is incomplete and is thus shown as TA*. The full formulation of TA includes several other ions that also accept protons. The concentration of the other contributing ions can be estimated from salinity, phosphate and silicate (Wolf-Gladrow et al., 2007). The respective dissociation of carbonic acid to bicarbonate and carbonate results in free H^+ ions of which the sum is pH ($-\log_{10}[H^+]$). The partial pressure of CO_2 (pCO_2) is the sum of dissolved carbon dioxide ($CO_{2(aq)}$) and carbonic acid. The dissociation constants, which are temperature dependent, are shown by K_0, K_1 and K_2.

An important feature of the marine carbonate system is that only two of its parameters (DIC, TA, pCO_2 or pH) are needed to calculate the full speciation of Equation (1.1). Temperature, pressure, salinity and nutrients (phosphate and silicate) are required alongside the two parameters. This is because the dissociation of the species are sensitive to some of the aforementioned

variables. Importantly, DIC and TA are conservative with regard to temperature and pressure, meaning that they are not affected by mixing and are thus used to represent the marine carbonate system in biogeochemical process models (Wolf-Gladrow et al., 2007). Measuring DIC and TA is typically done by coulometric and potentiometric titration respectively, with both methods being very accurate (Dickson et al., 2007). However, Lee et al. (2006) presented an empirical formulation of surface ocean TA with temperature and salinity as the only input. This formulation is often used to estimate TA when only one of the other carbonate system parameters is known.

1.2.2 Mechanisms affecting pCO_2

The partial pressure of CO_2 is of particular interest in this study as it defines the gradient between atmospheric and oceanic CO_2 and is the parameter from which air-sea CO_2 fluxes (FCO_2) are calculated (Wanninkhof et al., 2009). As shown in Equation (1.1), the reduction of pCO_2 can be achieved by altering either the dynamics of the equation or changing the concentration DIC, meaning any one of the carbon components in Equation (1.1). In the surface ocean, where pressure is constant, temperature alters the dynamics of the equation, in other words a change in the dissociation constants. The pH of seawater is also able to change the dynamics of Equation (1.1), meaning that an increase in DIC will not always result in the same increase in pCO_2 – this effect is described by the Revelle factor and is often referred to as the ocean's buffering capacity (Sabine et al., 2004). Processes that lead to a change in DIC are: air-sea gas exchange, entrainment of deeper waters, and biological uptake or remineralisation. The theory of these processes is described in the sections that follow, thereafter these processes will be described in context of their modes of variability in the Southern Ocean.

The effect of temperature on pCO_2

Unlike DIC and TA, pCO_2 is affected by temperature and pressure, but the latter can be ignored in surface waters. This effect of temperature on the pCO_2 of a parcel of water with constant pressure is well understood and described by:

$$pCO_2^{T2} = pCO_2^{T1} \cdot e^{0.0423 \cdot (T2 - T1)} \tag{1.2}$$

Where $T1$ and $T2$ represent temperatures (in °C) at different periods and pCO_2^{T1} and pCO_2^{T2} are the partial pressures of CO_2 at those temperatures (Takahashi et al., 1993, 2002).

Air-sea gas exchange

Conceptually, this air-sea CO_2 exchange occurs as a function of the CO_2 gradient between the oceanic and atmospheric boundary layers with turbulent mixing playing an important role (Wanninkhof et al., 2009). In practice, the bulk fluxes of CO_2 over the ocean are captured by:

$$FCO_2 = k_w \cdot K_0 \cdot (pCO_2^{sea} - pCO_2^{atm}) \tag{1.3}$$

where k_w is the gas transfer velocity, K_0 represents the solubility of CO_2 in seawater, and pCO_2^{sea} and pCO_2^{atm} represent the oceanic and atmospheric partial pressure of CO_2 respectively – this difference is often represented as ΔpCO_2. While ΔpCO_2 determines the direction of the flux (in or out of the ocean), the magnitude is determined primarily by the gas transfer velocity (with K_0 playing a lesser role). Numerous formulations of k_w have been put forward, nearly always being represented as a quadratic or cubic function of wind speed (Liss and Merlivat, 1986; Wanninkhof, 1992; Wanninkhof and McGillis, 1999; McGillis et al., 2001; Nightingale et al., 2000; Ho et al., 2006; Wanninkhof et al., 2009). The Methods (Chapter 2) will describe the choice of k_w for the rest of this study in greater detail.

Biological reduction of DIC

Often referred to as the biological carbon pump, primary production results in a decrease of DIC in the surface layer of the ocean due to the uptake of CO_2 during photosynthesis. However, primary production (PP) is perhaps the most complex driver of pCO_2 due to the conditions required for phytoplankton to thrive.

Reliance of photosynthesis on light restricts PP to euphotic zone (Sverdrup, 1953). Given the Lagrangian nature of phytoplankton, PP is dependent the mixed layer depth (MLD) – the depth defining the bottom of the homogeneous mixed surface layer. This does not mean that a phytoplankton population cannot grow if the MLD is deeper than the euphotic zone. Sveredrup's critical depth hypothesis describes that if the integrated production of the water column is greater

than the integrated respiration phytoplankton proliferate (Sverdrup, 1953).

An added complexity is that phytoplankton require nutrients to photosynthesise – typically nitrate, phosphate and, in the case of diatoms, silicate[1] (Anderson and Sarmiento, 1994; Sarmiento and Gruber, 2006). These macro-nutrients are typically used up in the mixed layer if the light conditions are favourable, meaning that the mixed layer needs to be shallower than the critical depth. Phytoplankton are then limited by nutrients until the mixed layer is deepened sufficiently to entrain nutrients to sustain the bloom. This presents an interesting dichotomy where a shallower MLD is required to sustain PP, but deepening MLDs are required to replenish the nutrient supply by entrainment (Fauchereau et al., 2011). However, the Southern Ocean is iron limited (Martin, 1990). Iron is a micro-nutrient that plays an integral part in the conversion of sunlight to energy, and is thus required in minute quantities (Boyd et al., 2007; Tagliabue et al., 2014). The iron limitation leaves upwelled macro-nutrients underutilised, making the Southern Ocean a high–nutrient, low–chlorophyll (HNLC) region (Sarmiento et al., 2004; Venables and Moore, 2010). Exceptions to iron limitation are along shallow continental shelf regions, areas with sea ice and islands wakes, where iron is supplied to the surface ocean allowing for increased PP (Blain et al., 2007; Boyd and Ellwood, 2010). The mechanisms of iron supply to the euphotic zone is best described in the context of the seasonal cycle.

Phytoplankton eventually sink out of the mixed layer into the deep ocean, resulting in the export of organic carbon and nutrients (Eppley and Peterson, 1979; Anderson and Sarmiento, 1994). As the particulate organic carbon and organic forms of nutrients slowly sink, they are remineralised to DIC and inorganic forms of nutrients at depth. This effectively results in the transport of carbon against the concentration gradient, resulting in a larger DIC concentration in the deep ocean compared to the surface ocean, with the same applying to nutrients (Sarmiento and Gruber, 2006). This two layered system that typically has low (high) DIC and nutrient concentrations in the surface (deep) ocean sets the scene for the entrainment.

Entrainment of DIC

Consider a scenario where mixed layer pCO_2 is in equilibrium with the atmosphere, thus with no changes in DIC. The bottom layer has a higher DIC concentration, with the assumption that

[1] silicate is required for structural purposes in diatoms rather than photosynthesis

diffusion is too slow to have a noticeable impact on the mixed layer. A mixing event drives the deepening of the mixed layer resulting in the entrainment of deeper high DIC waters. The entrained water is homogeneously mixed resulting in an overall increase in mixed layer DIC.

Deepening or shoaling of the mixed layer is driven by the balance between mixing and stratification Mahadevan et al. (2010). A gain in heat is the primary mechanism that drives the stratification or shoaling of the MLD, resulting in stronger buoyancy of the mixed layer (Mahadevan et al., 2010). Conversely, heat loss, which decreases the buoyancy of the surface layer, allows mixing processes such as wind or eddy driven turbulence to deepen the mixed layer (Mahadevan et al., 2010). The strong seasonal cycle of temperature and persistent winds over the Southern Ocean drives strong gains/losses in buoyancy, making entrainment one of the primary mechanisms by which pCO_2 is altered in the Southern Ocean (Lenton et al., 2013).

Processes that affect TA

For the most part TA can be explained by the regional empirical relationships of TA with SST and salinity as defined by Lee et al. (2006). However, there are a few situations in which TA can be altered that would not be reflected by the empirical derivation of Lee et al. (2006).

The photosynthetic uptake of nitrate results in a minor increase in TA with a stoichiometric ratio tied to the Redfield ratio, where DIC : TA at $-6.6:1$ (Wolf-Gladrow et al., 2007). This small increase results in a nominal decrease in pCO_2. This opposing relationship between TA and pCO_2 may seem counter-intuitive, but is clearer when pCO_2 is defined as (Dickson et al., 2007):

$$pCO_2 = \frac{K_0}{K_1 \cdot K_2} \cdot \frac{[HCO_3^-]^2}{[CO_3^{2-}]} \tag{1.4}$$

where K_0, K_1 and K_2 are the dissociation constants shown in Equation (1.1).

Blooms of shell forming phytoplankton (typically coccolithophores) reduce TA and DIC by precipitating calcium carbonate ($CaCO_3$), thus reducing CO_3^{2-} leading to a DIC : TA ratio of 1 : 2 where the charge of carbonate accounts for two units of TA (Wolf-Gladrow et al., 2007). This decrease in TA results in an increase in pCO_2, but is partially offset by the uptake of DIC by photosynthesis. The formation or melting of sea-ice can lead to $CaCO_3$ precipitation and dissolution leading to the reduction of increase of TA (Fransson et al., 2011; Bates et al., 2014).

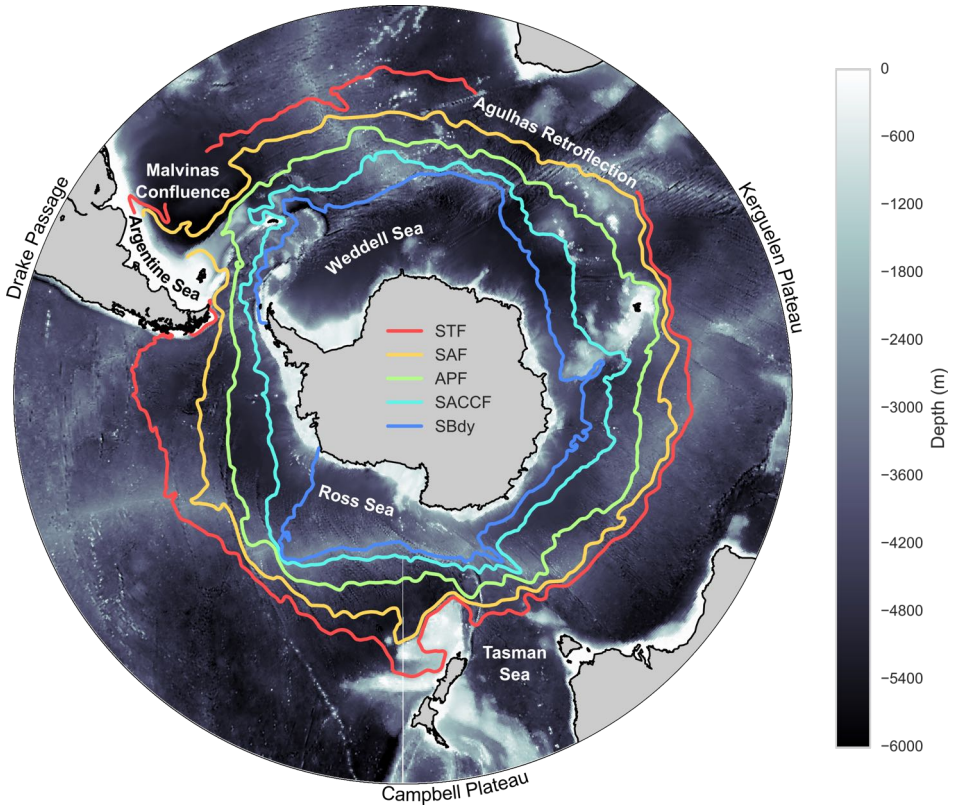

Figure 1.1: Antarctic Circumpolar Current front positions overlaid on ETOPO1 bathymetry (m). The fronts are calculated from criteria stipulated in Swart et al. (2010) using AVISO absolute dynamic topography. Only the primary branches of the fronts are shown: Sub-Tropical Front (STF), Sub-Antarctic Front (SAF), Antarctic Polar Front (APF), Southern ACC Front (SACCF), Southern Boundary of the ACC (SBdy). Note that the STF and the SBdy are occasionally omitted as ACC fronts as their flow is not continuous, but these are often used to define the boundaries of the ACC and Southern Ocean (in the case of the STF).

In the context of this study these effects would be negligible and the physical transport mechanisms of DIC and TA are much more likely to play an important role (Dufour et al., 2013).

1.3 Large scale Southern Ocean circulation

Southern Ocean circulation is dominated by the eastward flowing Antarctic Circumpolar Current (ACC). The ACC is the largest ocean current with a flow of 134 ± 13 Sv measured in the Drake passage (70°E) – a convenient choke-point in the otherwise fragmented flow (Rintoul et al., 2001). The flow of the ACC is characterised by several dynamic eddying fronts, of which the two dominant are the Sub-Antarctic Front (SAF) and the Polar Front (PF) (Rintoul et al., 2001). The three lesser fronts in the Southern Ocean are the Subtropical Front (STF) to the north of the ACC, and to the south the Southern ACC Front (SACCF) and the Southern Boundary (SBdy) as shown

in Figure 1.1. The STF and SBdy are often omitted as ACC fronts as their flow is not meridionally continuous. Topographic steering plays an important role in determining the location of the fronts, with bathymetric features such as the Kerguelen (80°E) and Campbell Plateaus (175°E) forcing the fronts to group together to the north or south of these bathymetric features as shown in Figure 1.1 (Rintoul et al., 2001; Sokolov and Rintoul, 2007; Graham et al., 2012; Marshall and Speer, 2012). Oceanographic properties (density, temperature and salinity) are often used to identify the location of these fronts, which serve as water-mass boundaries Orsi et al. (1995); Sokolov and Rintoul (2002), and more recently satellite measured sea surface height has been used successfully (Sokolov and Rintoul, 2007; Swart et al., 2010; Graham et al., 2012).

The unbounded flow of the ACC (Figure 1.1) mixes waters between the Atlantic, Indian and Pacific Oceans (Rintoul, 2006). This makes the Southern Ocean an important component of Meridional Overturning Circumpolar (MOC) and consequently a key player in global climate (Marshall and Speer, 2012). The slow movement of deep waters allows the MOC to serve as both a transport and storage mechanism for heat, CO_2 and nutrients (Marshall and Speer, 2012). Deep water formation in the North Atlantic drives a slow southward creep of waters that eventually upwell in the Southern Ocean as Circumpolar Deep Water (CDW) (Speer et al., 2000).

An idealised model of Southern Ocean meridional transport is shown in Figure 1.2. Ekman divergence due to strong persistent westerlies over the Southern Ocean drives upwelling of CDW along isopycnals. To the south of the wind stress maximum, water is advected southward forming the lower limb of Southern Ocean meridional transport, which is key in the formation of Antarctic Bottom Water (AABW). To the north of the wind stress maximum, Ekman transport drives water northward along the surface allowing for ventilation and concomitant water-mass transformation to occur. This leads to the formation of Antarctic Intermediate Water (AAIW) and Subantarctic Mode Water (SAMW) in the Polar Frontal Zone (PFZ) and Subantarctic Zone (SAZ) respectively (Iudicone et al., 2008). These waters are subducted by Ekman convergence in the Sub-Antarctic Zone where lighter subtropical waters lie to the north. The subduction of SAMW and, to a lesser extent, AAIW is key to the uptake of CO_2^{ant} and explains the large column inventory of CO_2^{ant} between 30°S and 50°S (Sabine et al., 2004; Mikaloff Fletcher et al., 2006; Khatiwala et al., 2009; Iudicone et al., 2011). While Ekman transport does contribute to the subduction of SAMW, Sallée et al. (2012) showed that the subduction is not zonally uniform due to the contribution of eddies

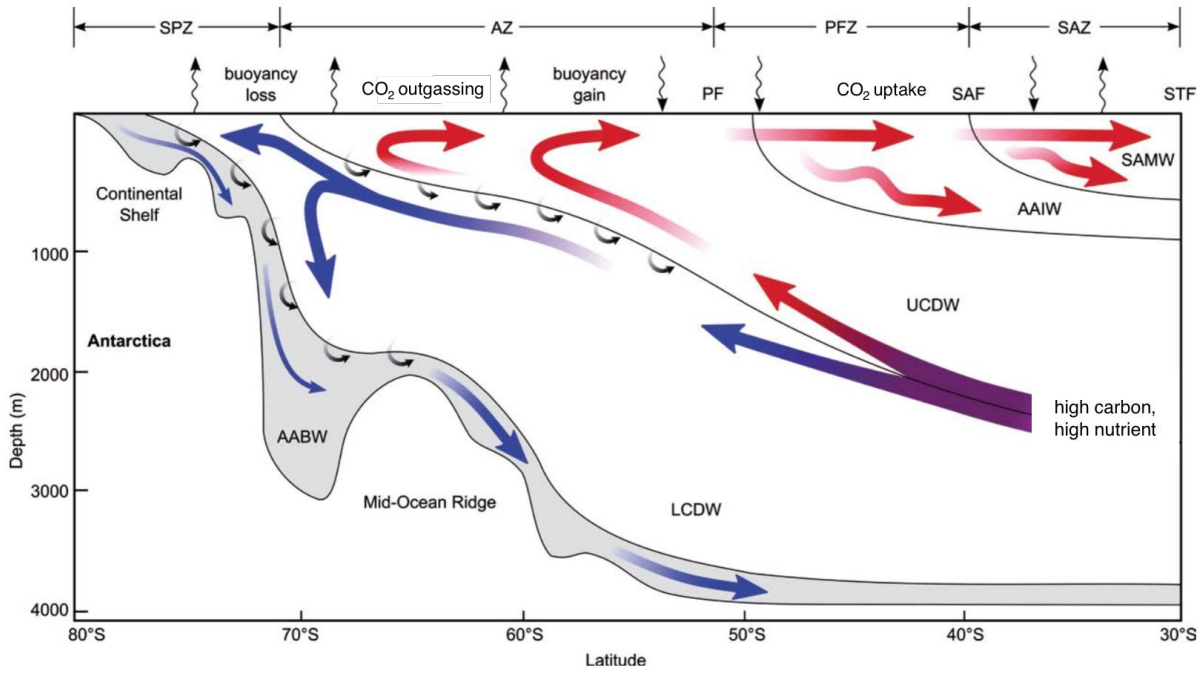

Figure 1.2: A schematic cross section of vertical–meridional Southern Ocean circulation adapted from Post et al. (2014). Diapycnal upwelling south of the Polar Front (PF) occurs along sloping isopycnals and is due to wind driven Ekman pumping over the ACC. There is a clear distinction made between an upper and lower branch of (Circumpolar Deep Water) CDW. LCDW consists primarily of North Atlantic Deep Water (NADW) which will ultimately contribute to the formation of cold and saline Antarctic Bottom Water (AABW). The upper branch is a mix of NADW and Pacific Subarctic Intermediate Water (PSIW). The upwelled water (Antarctic Surface Water) is advected north, where it is subducted in the Polar Frontal and Sub-Antarctic Zones by Ekman convergence. The Sub-Antarctic Zone (SAZ), between the Sub-Antarctic Front (SAF) and the Subtropical Front (STF), is the major role player in the uptake of CO_2 in the Southern Ocean (Sabine et al., 2004).

and mean flow[2].

Key to understanding the dynamics of the Southern Ocean is the role that mesoscale eddies play in both the flow of the ACC and overturning circulation (Marshall and Speer, 2012). The northward Ekman flow of upwelled waters leads to an imbalance and thus an instability in the ACC fronts (Abernathey et al., 2011). These instabilities cause poleward moving eddies, transporting mass and heat, that compensate for the instability. Meredith and Hogg (2006) have shown that this compensating effect of eddies is observable in the ACC by an increase in eddy kinetic energy (EKE) when wind stress over the Southern Ocean increases.

[2]mean flow is the advective transport of water across the mixed layer resulting in subduction or ventilation.

1.4 CO_2 variability Southern Ocean

The aforementioned processes act to change pCO_2 in the surface ocean, but changes to these drivers occur at various modes of temporal and spatial variability. In the sections that follow I introduce the variability of these drivers of pCO_2 and how these modes of variability act on to create complex responses of pCO_2.

1.4.1 Seasonal cycle: the dominant mode

Seasonal cycle is the dominant mode of pCO_2 variability in the Southern Ocean, with outgassing of CO_2 being dominant during winter and biological uptake during summer (Metzl et al., 1999, 2006; Takahashi et al., 2009; Lenton et al., 2013). Strongly intertwined with the larger seasonal variability is sub-mesoscale variability that leads to heterogeneous distribution of pCO_2 in space and time (Lévy et al., 2001; Mahadevan et al., 2004, 2011). These processes that act together are described through the phenology of the Southern Ocean, starting in winter.

Winter in the Southern Ocean is characterised by strong mixing, meaning the MLDs are deep ($\sim$ 300 m) (de Boyer Montégut et al., 2004). Weak buoyancy gradients due to heat loss and seasonal wind stress maxima allows deep MLDs to occur in winter (Luis and Pandey, 2004; Marshall and Speer, 2012). Concomitant with the deep mixing is an increase in DIC and macro-nutrients (nitrate, phosphate and silicate). Unlike the nutricline (which is the strongest subsurface gradient of nutrients), the ferricline is decoupled with the MLD, meaning that it is typically deeper than even the winter mixed layer (Tagliabue et al., 2014). This decoupling results in the HNLC status of the Southern Ocean. However, a small amount of iron is entrained into the mixed layer due to the weak gradient of iron above the ferricline Tagliabue et al. (2014).

South of the Polar Front, CWD is entrained into the mixed layer enhanced by stronger wind stress (Lovenduski, 2007; Lenton and Matear, 2007; Lenton et al., 2013). The DIC associated with CDW is CO_2^{nat}, due to the pre-industrial formation of the source water masses (Lovenduski et al., 2007; Lenton and Matear, 2007; Devries et al., 2017). The increase in surface DIC results in positive ΔpCO_2, which results in strong outgassing due to the winter wind stress maximum (Luis and Pandey, 2004). The pCO_2 is partially muted by colder winter sea surface temperatures, but the pCO_2 signal is still dominated by the entrainment of DIC rich deep waters (Metzl et al., 2006;

Lenton et al., 2013).

Similarly in the SAZ, to the north of the PF, Metzl et al. (1999) found that entrainment of DIC dominates the temperature effect. This raises winter pCO_2 compared to summer, but the pCO_2 in the SAZ is still lower than atmospheric pCO_2, meaning that the region is a perpetual CO_2 sink. Here, cooling plays an important role in water mass transformation, resulting in the formation of dense SAMW, which is subducted and transported northward along isopycnals by Ekman convergence (Rintoul and England, 2002). This makes the SAZ one of the key regions of CO_2^{ant} uptake (Metzl et al., 1999; Khatiwala et al., 2009; Iudicone et al., 2011; Lenton et al., 2013; Devries et al., 2017).

Further south, in the MIZ, sea ice dampens outgassing of $CO_2$from the upwelled DIC rich waters (Hoppema et al., 2000; Bakker et al., 2008; Takahashi et al., 2009). Measurements of air-sea CO_2 flux by eddy flux covariance in sea ice covered regions have found that fluxes are damped proportional to the fraction of sea ice cover (Butterworth and Miller, 2016). Moreover, the formation of sea ice may also be an important drawdown mechanism of DIC by means of brine rejection (Fransson et al., 2011).

Insolation (and light) increases with the onset of spring resulting in increased buoyancy, though MLDs remain deep due to strong mixing. It is during this period, when mixed layers are still deep, that the potential for eddy-driven slumping, a sub-mesoscale process that acts to restratify the water column, is largest (Mahadevan et al., 2012). The process requires two adjacent water masses of different densities to be separated by a vertical front that is held up by along-front wind stress – a scenario that is fairly common in the ACC during spring (Swart et al., 2014). The slumping is initiated by the relaxation of the winds that hold the front up, allowing the lighter of the two water masses to "slump" over the other. This results in rapid shoaling of the mixed layer, which is able to sustain the net growth of phytoplankton (Mahadevan et al., 2010, 2012). The specific conditions required for eddy-driven slumping to occur could contribute to the heterogeneity of phytoplankton blooms in the Southern Ocean, as suggested by Swart et al. (2014).

As heat flux into the ocean increases into summer, stratification of the water column strengthens, thus limiting the entrainment of DIC rich deep waters. This also has the effect of increasing pCO_2 by the thermal effect, but observations have shown that this is offset by NPP (Metzl et al.,

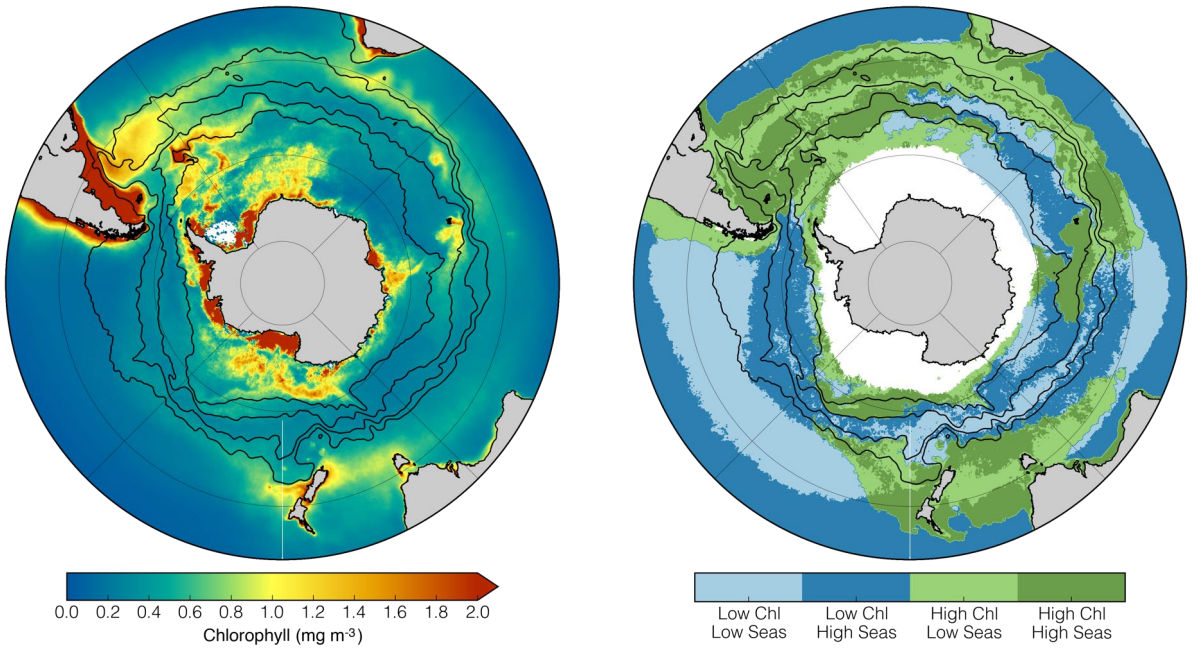

Figure 1.3: (a) Mean chlorophyll-a concentration for the period 2000 – 2009 using IMOS' Johnson et al. (2013) chlorophyll product. The ACC fronts (STF, SAF, APF and SACCF), shown in black, were calculated using updated values from Swart et al. (2010). The figure shows higher PP on continental shelves, island wakes and along some of the ACC's fronts. (b) Regions of chlorophyll biomass and seasonal cycle reproducibility from Thomalla et al. (2011) (using SeaWIFS data). Seasonality is calculated as the correlation between the mean annual seasonal cycle compared to the observed chlorophyll time series. A correlation threshold of 0.4 was applied to each time series to distinguish between regions of high and low seasonality; similarly, a threshold of 0.25 mg m^{-3} was used to distinguish between low or high chlorophyll waters. Black lines showing the fronts are the same as described in figure (a)

1998, 1999; Takahashi et al., 2002; Bakker et al., 2008). Rapid growth of phytoplankton occurs during spring/summer due to the stratification of the water column, thus alleviating light limitation (Arrigo et al., 1998, 2008; Thomalla et al., 2011). However, in the Southern Ocean, this growth quickly becomes stunted by iron limitation resulting in ephemeral blooms during late spring, early summer (Boyd and Ellwood, 2010; Tagliabue et al., 2014).

There are regions in the Southern Ocean where iron is less limited due to supply mechanisms that allow for stronger and more sustained phytoplankton blooms (Boyd and Ellwood, 2010). According to Boyd and Ellwood (2010) these mechanisms include (but are not limited to): island-wake effects, seasonal ice-melt, lateral transport of iron-rich sediments, aeolian dust deposition, and bathymetric interactions with the ACC. The majority of these mechanisms are highly regional (e.g. island-wake effect) or seasonally driven (e.g. sea ice melt), resulting in highly seasonal phytoplankton blooms (Thomalla et al., 2011). For example, Blain et al. (2007) found that the

island-wake effect in the lee of the Kerguelen Plateau sustained a phytoplankton bloom and resulted in twice the carbon uptake rate of HNLC waters. And in the Weddell Sea, Bakker et al. (2008) found that NPP in the Weddell Sea reduced pCO_2 by 100 μatm, from a CO_2 source to a sink, shortly after sea ice melt – indicating that iron was replete in these conditions. However, Arrigo et al. (2008) reported that while NPP in the marginal ice zone is high, it accounts for only 10% of the total production of the Southern Ocean.

Thomalla et al. (2011) reported that there are regions in the Southern Ocean, primarily in the SAZ, where Chl-*a* concentrations are sustained into late summer and the seasonal cycle characterised by large intra-seasonal variability. Boyd and Ellwood (2010) proposed the "ferrous wheel" of microbial iron remineralisation, a process that allows recycling of iron, that could sustain Chl-*a* for extended periods, but this would imply that organic carbon is also remineralised to DIC, thus with little impact on CO_2 sequestration. However, it is unlikely that iron remineralisation is able to sustain high chlorophyll concentrations (> 0.25 mg m^{-1}), thus Thomalla et al. (2011) attributed this variability to intra-seasonal forcing that acts to shoal and deepen the MLD, thus inducing the competition between light and iron limitation/alleviation. Nicholson et al. (2016) used an idealised model to propose storm mixing as a mechanism by which iron is supplied into the euphotic zone to sustain NPP throughout summer. It was found that better representation of storm driven mixing resulted an increase of NPP of up to 60%, with large implications for CO_2 uptake. This process helps close the gap between observations in the Southern Ocean and our understanding of the processes that give rise to the heterogeneous spatio-temporal distribution of summer pCO_2. For example, high frequency (hourly) pCO_2 measurements in the SAZ showed that intra-seasonal pCO_2 variability was the dominant mode of variability (Monteiro et al., 2015). The storm driven deepening of the mixed layer and subsequent eddy-driven slumping could be key mechanisms in explaining the strong intra-seasonal variability observed by Monteiro et al. (2015).

In autumn, as atmospheric temperatures start to cool, heat is lost from the ocean and the surface layer loses buoyancy and becomes less stratified. There is evidence that this cooling may lead to a brief reduction of pCO_2, though it is thought that this would be short-lived as entrainment of DIC would quickly overwhelm the thermal decrease pCO_2 (Hoppema et al., 2000). The seasonal loss of water column buoyancy and increased wind stress erodes the mixed layer

until the ocean state returns to a well mixed scenario where deep DIC rich waters are entrained.

This description of Southern Ocean seasonal dynamics shows that the processes driving pCO_2 are complex. Though there are two clear distinctions that emerge. In winter, the dominant deep mixing process is thought to be a zonally uniform, with entrainment driving an increase in pCO_2 with the region south of the PF being a source and to the north a sink. In summer, the picture is much more heterogeneous with NPP being the primary driver of variability. The competition between light and iron limitation results in heterogeneous distribution of Chl-*a* in both space and time, with similar implications for pCO_2. The interaction between the large scale drivers, wind stress, surface heating and ocean dynamics are the primary cause of this complex picture. The seasonal magnitude of these processes is large, resulting in the seasonal cycle being the dominant mode of variability in the Southern Ocean.

1.4.2 Interannual variability of Southern Ocean CO_2

The last two decades have seen a large increase in the effort and focus on understanding the interannual variability of the drivers CO_2 in the Southern Ocean. Where the priority has been to understand the potential changes in winter outgassing and the change in the summer biological carbonate pump (Lenton and Matear, 2007; Lovenduski et al., 2007; Lovenduski and Ito, 2009; Hauck et al., 2013, 2015; Landschützer et al., 2015). Importantly, it is the subtle regional shift in the magnitude of the dominant seasonal drivers that causes interannual variability of pCO_2, (Lenton et al., 2013).

Once of the most cited drivers of change in the Southern Ocean is the southerly shift of the westerlies (Marshall, 2003; Lenton and Matear, 2007; Visbeck, 2009; Swart and Fyfe, 2012). The shift is attributed to the anthropogenically driven reduction of stratospheric ozone (Arblaster and Meehl, 2006; Lenton et al., 2009b). This is captured by an increasingly positive Southern Annular Mode (SAM), an index based on the sea-level pressure differential between 40 and 65°S (Marshall, 2003). Model studies have shown that the positive SAM trend will drive in increased meridional overturning, thus increasing pCO_2 by enhancing the entrainment of DIC (Lenton et al., 2006; Lovenduski, 2007; Lenton et al., 2009b). Le Quéré et al. (2007) used inverse modelling to show that the Southern Ocean CO_2 sink was in fact weakening in the 1990's into the early 2000's, as later confirmed by other methods shown in Figure 1.4. The authors attributed the "saturation" to

the strengthening of the westerlies that led to increased upwelling of CDW and thus outgassing of CO_2^{nat}.

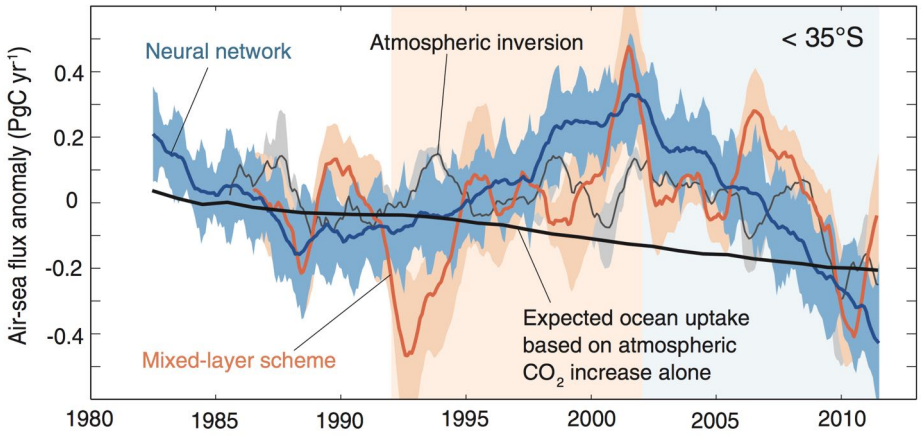

Figure 1.4: The mean air-sea CO_2 fluxes for the Southern Ocean from the study by Landschützer et al. (2015). Flux estimates are shown calculated by three different methods: two-step Neural Network in *blue* (Landschützer et al., 2014); mixed layer scheme in *orange* (Rödenbeck et al., 2014) and an atmospheric inversion in *black* Rödenbeck et al. (2003). The thick black line shows the expected CO_2 uptake based on the increase of atmospheric CO_2 based on model simulations. A decrease in the strength of the sink is shown between 1992 and 2002, after which there is a strong increase in the sink beyond the expected uptake due to increasing atmospheric CO_2 concentrations.

More recent work by Landschützer et al. (2015) has found that the Southern Ocean sink has since strengthened (Figure 1.4) — though not due to the reduction of wind stress/SAM as one would expect. The authors proposed that atmospheric modes of circulation had become zonally asymmetric, resulting in the northward flow of cool air over the Pacific and southward flow of warm air over the Atlantic. This drove anomalous cooling in the Pacific and southward movement and downwelling of warm waters in the Atlantic, resulting in a zonally symmetric strengthening of the sink (Figure 1.5). Importantly, the authors recognised the relative importance between the mechanisms that drive the marine carbonate system, in this case the thermal effect and the addition or removal of DIC/TA. In the Atlantic, an anomalous southward shift of the high pressure system advected and downwelled warmer waters, thus suppressing upwelling of high DIC waters. Conversely, in the Pacific anomalous upwelling of DIC was offset by cooling (Figure 1.5). These basin specific responses to the thermal and DIC/TA driven trends led to the zonally symmetric "reinvigoration" of the Southern Ocean CO_2 sink.

In a subsequent study, Landschützer et al. (2016) showed that the variability of pCO_2 in the Southern Ocean is tied to the decadal oscillation of the SAM. This ties in well with the Antarctic Circumpolar Wave, first described by White and Peterson (1996), who found that

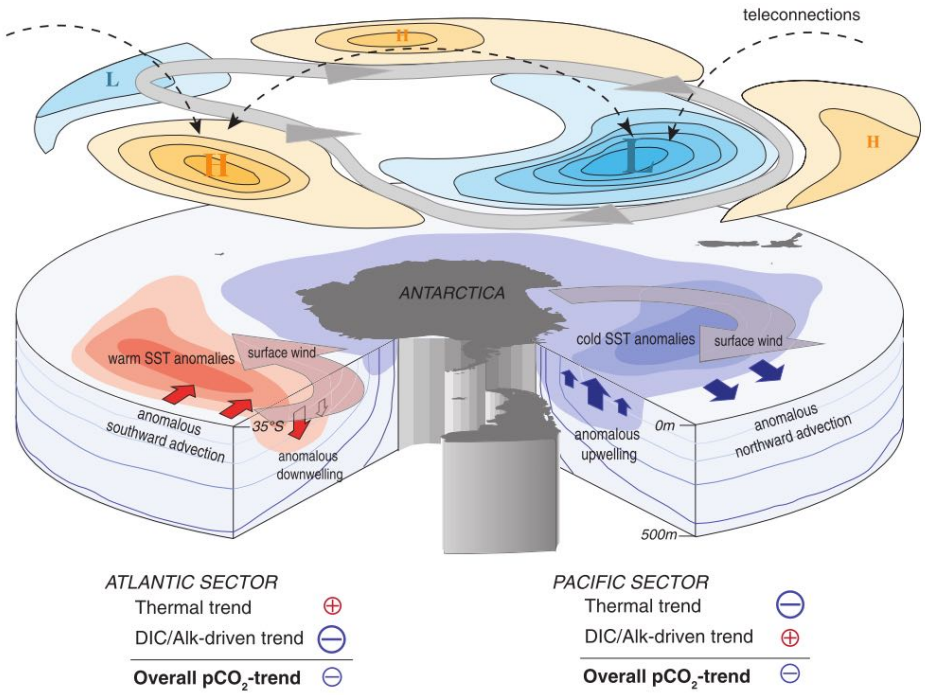

Figure 1.5: The proposed mechanisms for the zonally symmetric reinvigoration of the Southern Ocean CO_2 sink Landschützer et al. (2015). The asymmetric response of the Atlantic and Pacific are key to the symmetric reinvigoration.

sea level pressure, SST and sea ice extent anomalies propagate eastward around the Southern Ocean. The sea level pressure and SST anomalies coincide with the proposed mechanisms by Landschützer et al. (2015). Moreover, White and Peterson (1996) found that these "waves" encircle the pole every eight to ten years. Later studies have shown that these anomalies coincide with the SAM and the El Niño – Southern Oscillation (ENSO) (Verdy et al., 2006; Giarolla and Matano, 2013; Yeo and Kim, 2015). Yeo and Kim (2015) found that the sum of the first or second empirical orthogonal modes of SAM and ENSO were able to represent the propagating SST anomalies. The authors found that a shift from an eastern to central ENSO events around 1998 resulted in a change in the characterisation of the SST anomalies. This shows that the impact of teleconnections in the equatorial Pacific on carbon fluxes in the Southern Ocean could be significant (Verdy et al., 2006; Yeo and Kim, 2015).

While it is generally accepted that intensification of wind stress closer to the poles would lead an increase in meridional overturning circulation, there is evidence that intensification of the westerlies could also lead to changes in the ACC eddy field (Abernathey et al., 2011; Marshall

and Speer, 2012; Hogg et al., 2015; Langlais et al., 2015). Satellite observations of sea surface height first showed that the increase in wind stress over the Southern Ocean may lead to a lagged increase in eddy kinetic energy (EKE) along the ACC (Meredith and Hogg, 2006). Model studies later showed that the intensification of the westerlies increases the baroclinic instability of ACC fronts that manifests in the form of mesoscale eddies that act to balance the instability by moving mass and heat poleward (Abernathey et al., 2011; Marshall and Speer, 2012). Eddy resolving models have shown that the increase in poleward transport largely compensates for the increase in Ekman transport (Abernathey et al., 2011; Marshall and Speer, 2012; Dufour et al., 2012). Dufour et al. (2013) showed that these eddies only partially compensated (one third) for DIC transport associated with increased meridional overturning. Patara et al. (2016) that the increase in EKE to enhanced overturning is regionally dependent and that some areas are intrinsically more sensitive to changes in overturning.

In summary the interannual changes in FCO_2 and its drivers have been shown to be linked with the SAM, with teleconnections to other climate indices, such as ENSO, playing important roles regulating the modality of FCO_2. The primary change is caused by the intensification of the westerlies Lenton and Matear (2007); Lovenduski (2007). Sea surface temperature and sea surface height have also shown to vary in time and space with the SAM and ENSO resulting in the Antarctic Circumpolar Wave (Verdy et al., 2006; Giarolla and Matano, 2013; Yeo and Kim, 2015). The correlation of these drivers to the SAM has resulted in a dominant decadal mode of interannual air-sea CO_2 flux variability (Landschützer et al., 2016).

The next section looks at how the community has been monitoring the seasonal and interannual CO_2 variability in the Southern Ocean, in particular the role that empirical modelling has played in recent years.

1.5 CO_2 estimates in the Southern Ocean

1.5.1 Limits to CO_2 observations

The accuracy of CO_2 estimates in the Southern Ocean (south of 30°S) is limited by the paucity of observations due to remoteness and rough seas that make *in-situ* measurements difficult

(Takahashi et al., 2012; Landschützer et al., 2015). Figure 1.6a shows how sparse the ship based measurements of CO_2 remain for large portions of the Southern Ocean. Moreover, this image does not demonstrate the strong seasonal bias of CO_2 sampling towards summer Bakker et al. (2016). Up until the rise of empirical modelling methods, the best estimates of decadal air-sea CO_2 fluxes were based on these sparse data (Takahashi et al., 1997, 2002, 2009). There was, and still is, much uncertainty around these estimates: this is exemplified in Takahashi et al. (2002) and Takahashi et al. (2009) where an increase in observations resulted in an adjustment of flux estimates south of 50°S (-0.38 and -0.05 PgC y^{-1} respectively). Moreover, the authors estimated that under-sampling contributed 20% to the error of estimates (Takahashi et al., 2009). This large contribution is due to the fact that measurements were spatially extrapolated, in some cases (as in the Pacific) to an extraordinary degree as shown in Figure 1.6b (Takahashi et al., 2012).

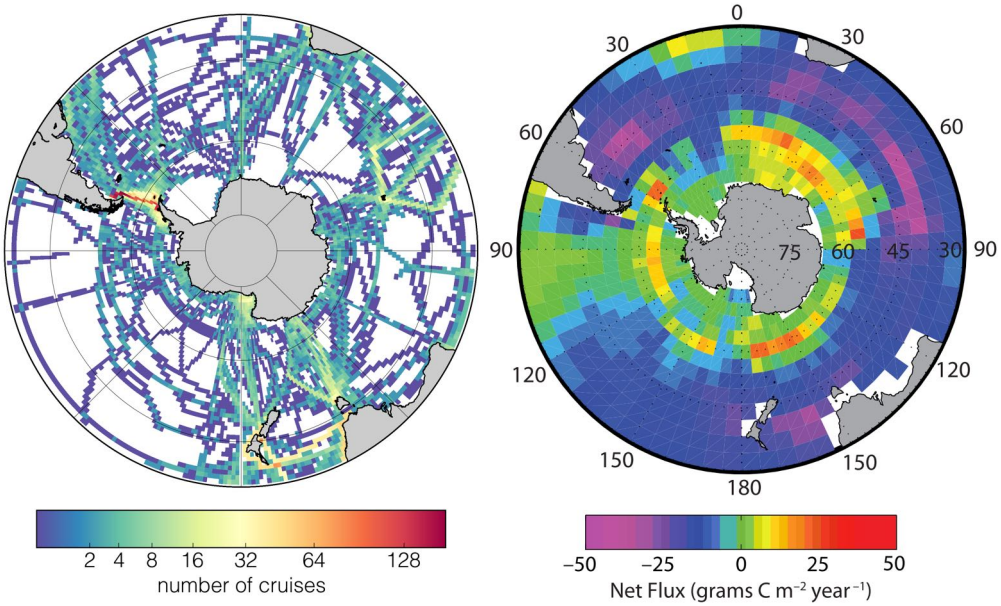

Figure 1.6: (a) The number of SOCAT v3 cruises in the Southern Ocean (Bakker et al., 2014). Data in the Southern Ocean is sparse with the majority of regions only being measured only once. (b) Our current best estimate of decadal air–sea CO_2 fluxes based on the data shown in *a*. Takahashi et al. (2009) found that this missing data was a large contributor to uncertainties (20%).

Biogeochemical process models are a potential solution to the sparse CO_2 data problem in the future. However, our mechanistic understanding of the processes that drive CO_2 is not yet adequate for these models to accurately represent CO_2. Both Lenton et al. (2013) and Mongwe et al. (2016) showed that models are not able to replicate the seasonal cycle of CO_2 in the Southern

Table 1.1: Modified table from Rödenbeck et al. (2015) showing basic information about 14 models that estimate pCO_2 from proxy parameters. The first method column shows the fundamental approach of the method: *SI*=statistical interpolation; *R*=regression; *M*=Model-based. The second method column briefly describes the key method used to estimate pCO_2 from parameters. *MLR*=Multi-linear regression; *SOM*=Self-Organising Map; *FFN*=Feed-forward Neural Network; *NN*=Neural Network

Name	Reference	Method and Details		Start	Space	Time
UEA-SI	Jones et al. (2015)	SI	Splines and spatial interp.	1985	2.5° x 2.5°	mon
OceanFlux-SI	Shutler et al. (2015)	SI	Binned Kriging	1995	1° x 1°	mon
Jena-MLS	Rödenbeck et al. (2014)	SI	Bayesion interpolation	1986	4° x 5°	day
CU-SCSE	Jacobson et al. (2015)	SI	Kalman filter with error est.	1970	1° x 1°	mon
AOML-EMP	Park et al. (2010)	R	SST based linear regression	1985	4° x 5°	mon
UEx-MLR	Schuster et al. (2013)	R	MLR with 20 regions	1990	1° x 1°	mon
JMA-MLR	Iida et al. (2015)	R	MLR with 44 regions	1990	1° x 1°	mon
UNSW-SOMLO	Sasse et al. (2013)	R	Clustering SOM + MLR	1998	1° x 1°	mon
ETH-SOMFFN	Landschützer et al. (2014)	R	Clustering SOM + FFN	1982	1° x 1°	mon
CARBONES-NN	www.carbones.eu/wcmqs/	R	Assimalitive NN	1990	2° x 2°	mon
NIES-SOM	Nakaoka et al. (2013)	R	SOM	1998	1° x 1°	mon
NIES-NN	Zeng et al. (2014)	R	FFN	1990	1° x 1°	mon
PU-MCMC	Majkut et al. (2014)	M	Bayesion inversion	1980	4° x 5°	mon
NIES-OTTM	Valsala and Maksyutov (2010)	M	Data assimilation	1980	1° x 1°	mon

Ocean.

1.5.2 A case for empirical modelling

The ocean CO_2 community has turned to empirical (statistical/machine) learning as an intermediate solution to resolve CO_2 fluxes (Rödenbeck et al., 2015). The basic concept is to estimate pCO_2 from an algorithmically established relationship between satellite observable variables and ship based measurements of pCO_2. Hereafter, CO_2 fluxes can be calculated from satellite wind speeds, sea surface temperature and estimated pCO_2.

Early studies showed that multiple linear regression (MLR) was able to estimate pCO_2 in regions where temperature was the dominant driver (Lefèvre and Taylor, 2002; Ono et al., 2004) – where this relationship is linear as shown in Equation (1.2). When applied to larger, more complex regions, where more non-linear dynamics, such as biological uptake of DIC and entrainment of DIC rich waters, are important drivers of CO_2, the simple linear approach was lacking (Lefèvre et al., 2005). The application of non-linear methods, specifically artificial neural networks (ANN), in the data sparse North Atlantic of the 2000's (much like the contemporary Southern Ocean) showed that these more sophisticated methods outperformed MLR.

An increasing number of publications on empirical estimates of pCO_2 in the late 2000's

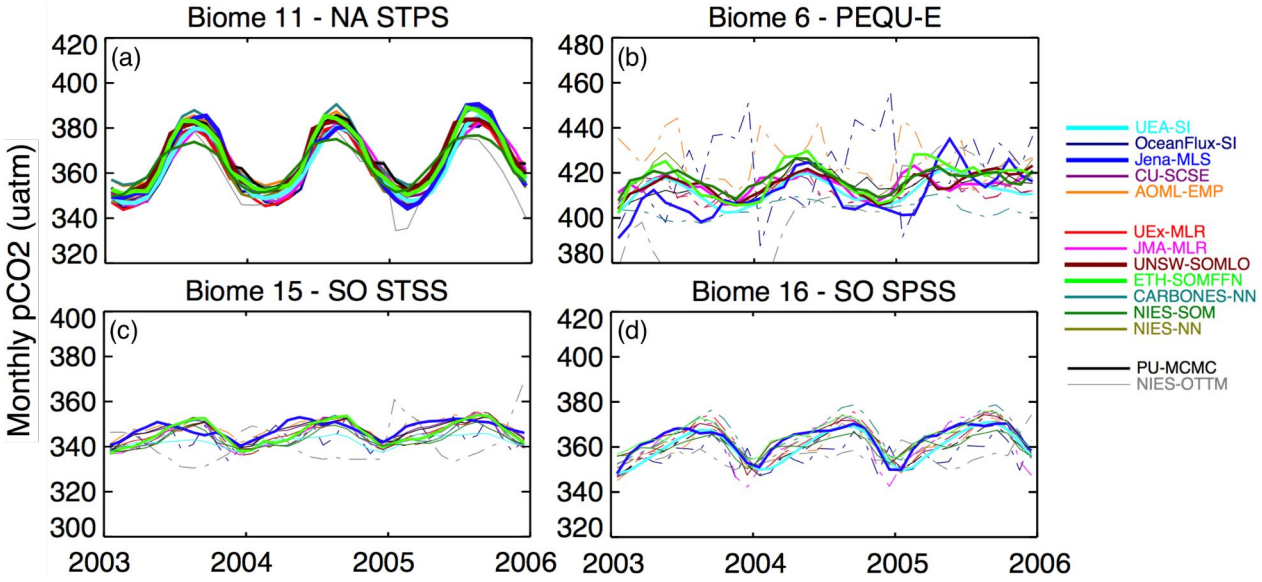

Figure 1.7: Monthly pCO_2 variations for four key biomes from the Rödenbeck et al. (2015) paper. Biomes are defined by Fay and McKinley (2014) and are as follows: (a) North Atlantic Subtropical permanently stratified; (b) East Pacific Equatorial; (c) Southern Ocean Subtropical seasonally stratified; (d) Southern Ocean Sub-Polar seasonally stratified. The key on the left is consistent for all figures and with Table 1.1. The thick lines represent the models that perform well in the given biomes (< 30% R^{month} from given publications). Note that Jena-MLS is the only model to perform well in both Southern Ocean biomes.

shows that the ingredients for the successful implementation of these methods were becoming more accessible (Friedrich and Oschlies, 2009a,b; Telszewski et al., 2009; Schuster et al., 2009; Chierici et al., 2009)[3]. And while algorithms and computer power were improving, access to ship based measurements of pCO_2 was limiting these studies to one or two ocean basins. The public release of the Lamont-Doherty Earth Observatory dataset (LDEO, Takahashi et al., 2002) and the Surface Ocean Carbon Atlas (SOCAT, Pfeil et al., 2013; Bakker et al., 2014, 2016) allowed for global estimates of surface ocean fluxes (Rödenbeck et al., 2013; Landschützer et al., 2014; Rödenbeck et al., 2015). The success and scientific merit of easy access to quality controlled data, such as SOCAT, is exemplified by the SOCOM study (Surface Ocean CO_2 Mapping) where 14 different empirical CO_2 mapping methods were compared (Rödenbeck et al., 2015) – details of these methods are shown in Table 1.1.

[3]Note that nearly all these studies were based in the North Atlantic

Merit of multiple approaches

The primary aim of SOCOM study was to identify the methods with the lowest uncertainty. Figure 1.7 showed that there was agreement between methods in the well sampled sub-tropical North Atlantic (a) and the lack of coherence in other regions, particularly in the equatorial pacific (b). In Southern Ocean (Figure 1.7c,d), there was less agreement amongst compared to regions such as the sub-tropical North Atlantic. Two methods, the Jena mixed layer scheme (MLS) and ETH self-organising map feed-forward neural network (SOMFFN), performed well globally and achieved coherent results in the Southern Ocean. However, there is merit in multiple approaches beyond the ability of a method to fit the data, where some methods provide utility beyond estimates of surface pCO_2.

For example, the CU-SCSE model (presented in the intercomparison) addressed the problem of error in pCO_2 by producing statistical estimates of uncertainty with the Kriging method (also known as Gaussian processes)[4]. The method statistically identifies regions where data is sparse in the interpolation space and produces uncertainty estimates based on these interpolation "distances". This information could pave the way to a more efficient strategy to fill the gaps in our current sampling strategy.

Another example is the continued use of MLR, which Lefèvre et al. (2005) found to be inferior to ANN. These simpler methods offer greater interpretability over the non-linear methods. The MLR methods in the intercomparison (UEx-MLR, JMA-MLR) employed a regional approach with a discrete regression for each area. With this approach the MLR methods performed comparably to the non-linear methods in less complex, well sampled regions. However, these methods were less successful in the Southern Ocean where drivers of CO_2 are complex and data is sparse (Lenton et al., 2013; Rödenbeck et al., 2015; Mongwe et al., 2016).

An important consideration is that the SOCOM intercomparison did not standardise the satellite or proxy data used to interpolate the data. This is important as there is no real consensus on the best combination of proxy variables that describe surface pCO_2. Jamet et al. (2007) found that the inclusion on SST, Chl-*a* and a climatology of MLD as a proxy in the North Atlantic yielded better than without MLD estimates. Similarly, Nakaoka et al. (2013) found that sea surface salinity (SSS), estimated by an assimilative model, accounted for 12% of the variability of pCO_2 in the

[4] this work has not yet been published outside of the intercomparison study of Rödenbeck et al. (2015)

northern Pacific. It is then not surprising that most studies in the intercomparison used SST, SSS, Chl-*a* and MLD as proxies to estimate pCO_2 (Rödenbeck et al., 2015). A few of the methods in the intercomparison included atmospheric CO_2 (xCO_2 or pCO_2) or coordinate variables, meaning latitude, longitude and, in one case time.

The majority of the studies in the intercomparison used monthly × 1° resolution, with several using coarser spatial resolution. Nakaoka et al. (2013), a study not included in the intercomparison, estimated pCO_2 in the northern Pacific at daily × 0.25° resolution. Interestingly, the root mean squared error estimate of pCO_2 estimates in this study were larger than those reported by a low resolution study in the North Atlantic by Landschützer et al. (2013), with RMSEs of 17.6 μatm and 10 μatm. However, the RMSEs of these methods with independent datasets were similar, with errors of 20.1 μatm and 22.83 μatm for the North Pacific and Atlantic respectively. Landschützer et al. (2013) implied that the majority of this error was caused by poor high latitude estimates of pCO_2. This suggests that despite large differences in RMSE estimated from training data, high and low resolution estimates may perform equally.

These points demonstrate the need for continuous experimentation with new methods and improvements of input data.

Empirical estimates of CO_2 in the Southern Ocean

Rödenbeck et al. (2015) concluded their study by stating that the mapping methods "constrain the seasonality of regional pCO_2 *essentially* in all biomes". However, they mention that for two of the three Southern Ocean biomes low data coverage leads to a spread of estimates. Two of the best performing methods from Rödenbeck et al. (2015), ETH-SOMFFN and Jena-MLS, were used to show trends of air-sea CO_2 fluxes in the Southern Ocean.

The findings of this study have been covered in Section 1.4.2, here the methodology of the approach, which is introduced in Landschützer et al. (2013, 2014), is discussed in greater detail. The SOM-FFN is a two step ANN approach that reduces dimensionality by first clustering data into 16 biogeochemical provinces of similar variability using a self-organising map (SOM – a derivative of ANN). These clusters were selected based on SST, SSS, MLD and pCO_2 climatology from Takahashi et al. (2009) and were allowed to vary in time, thus one location could belong to several clusters as shown in Figure 1.8. Feed-forward neural networks (FNN) are then applied

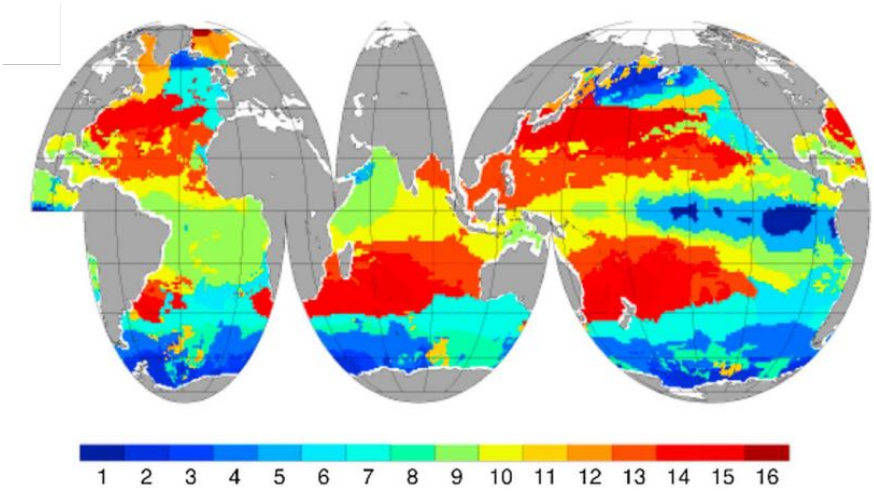

Figure 1.8: A figure from Landschützer et al. (2014) to show the distribution of SOM estimated provinces. More specifically, the province to which a region most frequently belongs, in other words the mode province.

to each "cluster" in the second step, achieving a high degree of non-linearity. Moreover, the clustering approach allows for regions similar in function, not location or period, to train each FFN – an elegant solution to a sparse dataset. The elegance of the approach and the remarkable accuracy that this method achieves has made the SOM-FFN a benchmark of performance in the field.

Chierici et al. (2012) created high resolution (8-day × 9 km) regional MLR estimates of pCO_2 in the Pacific sector of the Southern Ocean for the summer of 2006. The high resolution was required to capture the high frequency variability of pCO_2 in the marginal ice zone. The authors found that adding satellite estimates of biological production (not Chl-*a*) did not improve estimates of pCO_2, nor did MLD, though the authors do state that this is likely due to the fact that MLD is not an important driver of pCO_2 during summer.

One of the important issues raised by Chierici et al. (2012) is the problem of cloud cover for satellite Chl-*a* estimates. To overcome this issue the authors used assimilated model output to of Chl-*a* to fill the cloud gaps, but this study did not have to consider missing Chl-*a* data during winter when satellites are not able to measure Chl-*a* due to insufficient light. The SOM-FFN approach circumvented this by estimating pCO_2 with the remaining variables (SST, SSS and MLD), thus making the assumption that these variables are able to represent pCO_2. Similarly, Nakaoka et al. (2013), who's study was based in the North Pacific, also estimated pCO_2 with SST, SSS and MLD in the absence of Chl-*a*. An interesting approach to this problem was demonstrated

by Friedrich and Oschlies (2009b), where estimating model pCO_2 with an ANN showed that using Chl-*a* climatology improved the RMSE of estimates in the North Atlantic from 21.1 μatm to 19.0 μatm.

It is important to remember that empirical estimates of CO_2 in the Southern Ocean were not in strong agreement in the SOCOM intercomparison. Moreover, the paucity of data in these three biomes makes it difficult to evaluate the estimates, particularly in winter when measurements are sparse Rödenbeck et al. (2015). One of the ways in which the community has approached the problem of sparse data is to increase sampling effort (Bakker et al., 2016). The next section introduces at the literature that has looked at this problem in the Southern Ocean and the approaches that could be taken to resolve pCO_2 adequately to resolve both seasonal and interannual variability through *in-situ* observations.

1.6 Optimisation of CO_2 sampling in the Southern Ocean

Carbon dioxide sampling in the Southern Ocean is made difficult due to inclement weather and remoteness, meaning that the successful VOS (Voluntary Operated Ships) program has not contributed significantly to pCO_2 observations. This is exacerbated by the interaction of complex oceanography and drivers of the seasonal cycle that results in heterogeneous distribution of pCO_2 in both space and time (Thomalla et al., 2011; Jones et al., 2012). Increasing scientific interest in the role of the Southern Ocean in regulating climate change (Marshall and Speer, 2012; Aoki et al., 2013; Khatiwala et al., 2013; Wanninkhof et al., 2013) has encouraged in increasing pCO_2 observations (Bakker et al., 2014). While this is a major improvement, there is a strong bias of these measurements toward the summer months when calmer weather makes the region more accessible to research vessels (Figure 1.6a) (Monteiro et al., 2010).

This has long been recognised as a problem in air-sea CO_2 flux calculations with empirical and deterministic models. At present, deterministic models fail to capture the seasonal cycle of CO_2 in the Southern Ocean and the empirical studies find that uncertainties of CO_2 flux estimates in the Southern Ocean are still high due to lack of measurements (Lenton et al., 2013; Landschützer et al., 2014; Mongwe et al., 2016). A solution to this problem is to use persistent measuring platforms such as moorings, floats and gliders. With these additional platforms an

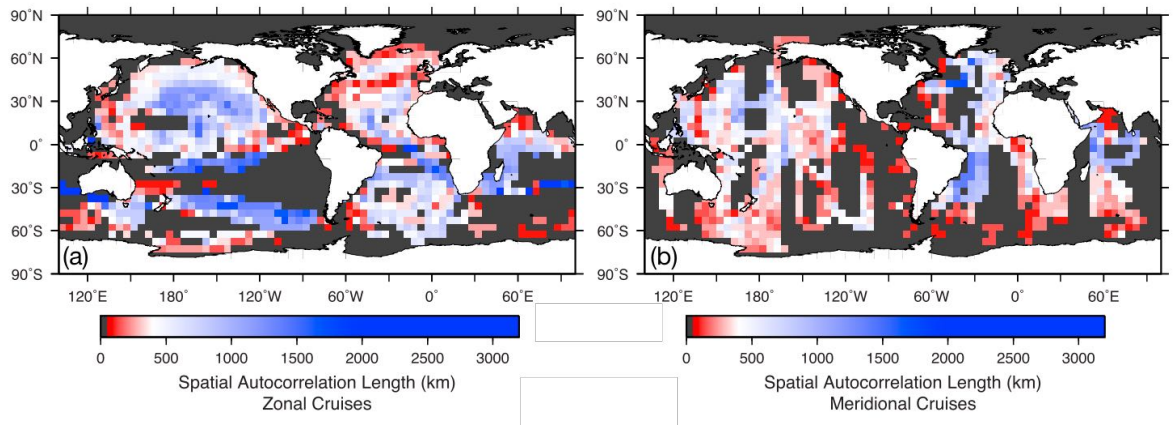

Figure 1.9: The autocorrelation length scales SOCAT pCO_2 as calculated by Jones et al. (2012). (a) shows the autocorrelation length of zonal cruises and (b) of meridional cruises.

integrated sampling strategy needs to be developed in order to create a cost effective strategy that is able to resolve the seasonal cycle of air-sea CO_2 fluxes.

An early attempt to define a sampling strategy for Southern Ocean CO_2 was based on a N – S transect at 170°W (Sweeney et al., 2002). The authors suggested that pCO_2 be sampled every 300 km in summer and 800 km in winter to achieve an uncertainty of < 4.3 μatm. This threshold equates to 10% of Southern Ocean annual CO_2 flux (0.1 PgC yr^{-1}) and is the accuracy required to capture 90% of the seasonal cycle. The problem with the recommendation by Sweeney et al. (2002) is that it is based on only two transects.

In a similar, but more comprehensive approach, Jones et al. (2012) calculated the autocorrelation length scales of pCO_2 in the Southern Ocean. Their data was in agreement with Sweeney et al. (2002). However, they showed that the Pacific transect, on which Sweeney et al. (2002) based their estimates, was in one of the regions of the Southern Ocean with the longest autocorrelation length scales (Figure 1.9). As demonstrated in Figure 1.9, the zonal autocorrelation length scales are typically much longer (> 500 km) than the meridional autocorrelation length (~ 50 km) in the Southern Ocean.

These studies by Sweeney et al. (2002) and Jones et al. (2012) highlight the problem of data paucity in sampling optimisation in the natural environment. And simply increasing the number of observations is expensive due to the high cost of instruments and platforms. It is thus important to have a way of testing sampling strategies to insure that cost is optimised and sampling is able to adequately resolve the system being measured.

1.6.1 Idealised sampling experiments: OSSEs

The use of deterministic biogeochemical ocean models in *Observing System Simulation Experiments* (OSSE) overcomes this problem.

Lenton et al. (2006) was the first to use the OSSE approach to optimise CO_2 sampling in the Southern Ocean. The authors found that the majority of the Southern Ocean CO_2 climatological signal was dominated by interannual variability, meaning that pCO_2 needed to be sampled continually. Their Fourier analyses of FCO_2 variability showed that increasing temporal or spatial sampling frequency to < 20 days and < 5° respectively, did not improve variability of flux estimates. Their analyses showed that a sampling frequency required to meet the same threshold of 0.1 PgC yr^{-1} set by Sweeney et al. (2002) was met by a 3° latitude ×30° longitude ×3 month grid. A result that corresponds with the autocorrelation lengths of pCO_2 estimated by Jones et al. (2012). This result was validated using a simulation of ship tracks in the model. This sampling grid is shown in Figure 1.10, where the red dots show the required spatial sampling scale. The figure also shows the recommended sampling strategy in the North Pacific and Atlantic regions, developed by Lenton et al. (2009a) based on the same principle as the Southern Ocean sampling strategy. However, the required sampling rate for these basins was slightly higher than in the Southern Ocean: 6° latitude × 10° longitude × 3 months.

However, Lenton et al. (2006) only aimed to resolve mean Southern Ocean CO_2 fluxes rather produce an estimate that would improve our understanding of the drivers of CO_2, in other words a spatially interpolated result. And while a useful gauge of the require sampling effort to resolve Southern Ocean CO_2 fluxes, the suggested sampling strategy was still ambitious due to winter measurements of CO_2.

A recent proposal to deploy up to 200 pH capable floats as a part of the SOCCOM project (Southern Ocean Carbon and Climate Observations and Modelling) is a major step towards constraining air-sea CO_2 fluxes in the Southern Ocean (Majkut et al., 2014; Riser et al., 2016). In preparation for the deployment of these floats, Majkut et al. (2014) used an OSSE to try to show that 200 floats would be sufficient to estimate air-sea CO_2 fluxes within the 10% limit. The authors used GFDL-ESM2M monthly output (1995-2000) to test the errors around a random float like sampling scheme for a range of number of floats deployed. They found that 150–200 randomly deployed stationary floats would be sufficient to capture Southern Ocean fluxes to

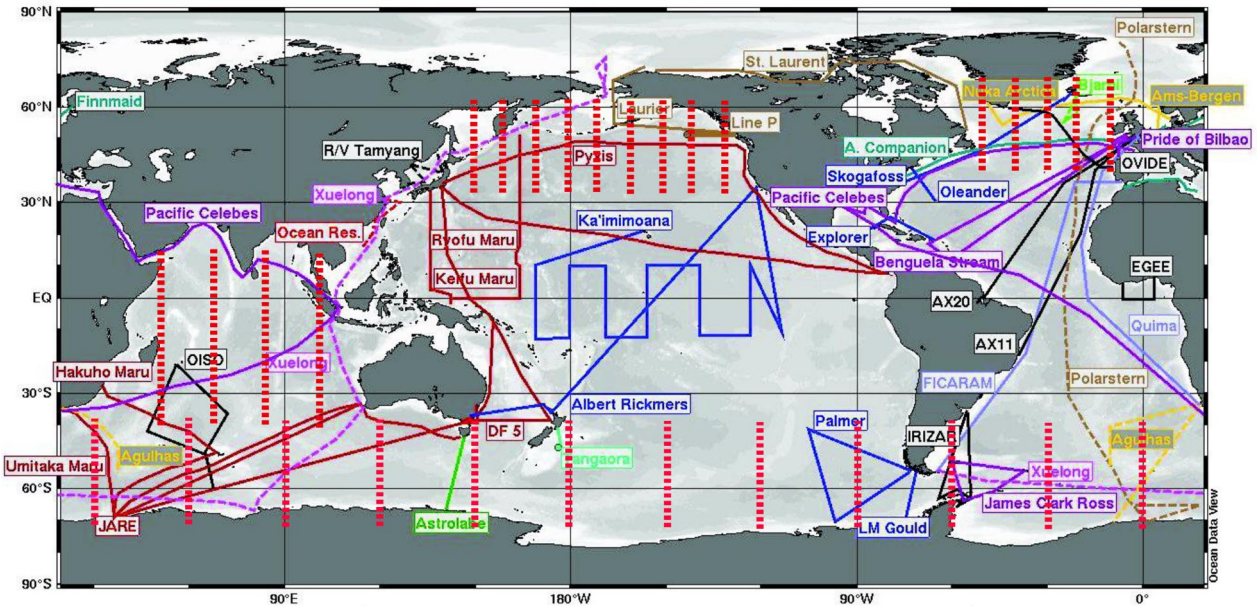

Figure 1.10: An proposed global CO_2 sampling strategy from Monteiro et al. (2010). The Southern Ocean 3° × 30° sampling grid is from Lenton et al. (2006). Repeat ship tracks are shown in different colours as a representation of the nation responsible for that particular cruise.

within 0.1 Pg C yr^{-1}. Majkut et al. (2014) recognised that the low resolution ESM2M model output would not accurately represent mesoscale and synoptic scale variations, thus a random error component of only 3 μatm, derived from Lenton et al. (2006), was added to measurements of pCO_2.

Monteiro et al. (2015) addressed the high frequency variability in the Atlantic SAZ with a time series of hourly pCO_2 data collected with a wave glider over a four month period. By sub-sampling this hourly dataset at increasing intervals, the authors found that intra-seasonal variability was in fact a significant contributor to uncertainty. Sampling at greater than three or four day intervals led to uncertainty in CO_2 flux estimates beyond the targeted 4.3 μatm threshold used in Sweeney et al. (2002). The authors surmised that this has implications for point measurements, such as those made by profiling floats. Similarly Resplandy et al. (2014) used high frequency pCO_2 observations measured with drifting floats to show that sub-mesoscale variability was in fact important. The authors showed that variability was on the order of 5 – 50 μatm over 100 km length scales, but as with Monteiro et al. (2015), these estimates were based in dynamic regions, biased by the floats tendency to aggregate along frontal zones.

Each of the strategies mentioned thus far have looked at sampling strategy in terms of achiev-

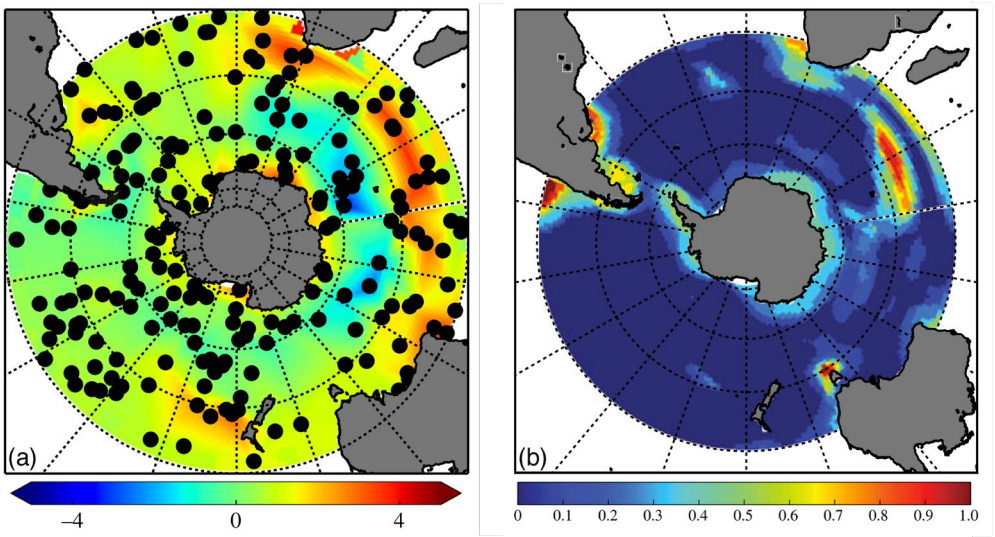

Figure 1.11: (a) Shows an example of one sampling step for 200 randomly placed floats as proposed by Majkut et al. (2014). (b) the fraction of months for which the bootstrapped error estimate is larger than 1 molC m^{-2} yr^{-1} using 200 floats.

ing accuracy of CO_2 estimates from a spatial interpolation paradigm. Though their study was in the North Atlantic, Friedrich and Oschlies (2009b) used an OSSE approach to test the bias of ANN estimates of CO_2 based on available VOS ship tracks. This presents an interesting idea, particularly for an environment for the Southern Ocean when sparse data, particularly in winter, makes the it difficult to evaluate estimates of pCO_2.

1.7 Aims and Outline

In Section 1.1 importance of the Southern Ocean in the global carbon cycle was outlined, but the inability to accurately track changes in this region continues to be a problem. This is exacerbated by the gap in our understanding of the processes that drive interannual changes, which are typically associated with climate change. The community has answered to this problem by: 1) making the most of current data with empirical models; 2) increase CO_2 sampling efforts in the Southern Ocean. Addressing these two aspects of the problem will allow the community to better understand current drivers of CO_2 in the Southern Ocean.

In this thesis I aim to contribute to each of these areas: empirical estimates, understanding of the drivers of CO_2 and sampling optimisation. The key scientific questions that frame each of these topics are laid out below along with an outline of how these questions will be answered.

Empirical estimates of pCO_2 in the Southern Ocean

In Chapter 3, the broad aim is to find out if empirical estimates of Southern Ocean CO_2 can be improved on given the sparse and biased dataset of surface pCO_2. The key questions guiding this chapter are:

- Can non-linear empirical methods, new to this application, improve on uncertainty estimates of the SOM-FFN by Landschützer et al. (2014)?
- Does increasing the gridding resolution lead to improved estimates of ΔpCO_2?

The empirical methods selected to answer the first question are support vector regression (SVR) and random forest regression (RFR) – both well established non-linear regression methods (Vapnik, 1999; Breiman, 2001). These algorithms, SVR and RFR, are introduced in Chapter 2. The concepts of empirical learning and the data to which the methods are applied are also introduced in Chapter 2. In Chapter 3, SVR and RFR are applied to high and low resolution gridded versions of ship based measurements of CO_2 (SOCAT v3) and gridded satellite data. The output of high and low resolution implementations of SVR and RFR are compared with SOM-FFN estimates by Landschützer et al. (2014). Finally, the cause for methodological differences between these five approaches are investigated and discussed.

Improving the understanding of pCO_2 drivers in the Southern Ocean

The ensemble of results from Chapter 3 are used in Chapter 4 to asses the interannual variability of both ΔpCO_2 and FCO_2, where the questions are:

- Are mean trends of FCO_2 driven primarily during winter or summer?
- What are the primary drivers of interannual variability of pCO_2 for summer and winter?
- Does the reinvigoration observed by Landschützer et al. (2015) continue beyond 2010?

It is clear from the questions that there is a strong emphasis on the seasonality of the drivers of pCO_2 in the Southern Ocean, in other words, pCO_2 is driven by different processes in winter and summer. In this chapter I try to identify the dominant drivers and processes that lead to the interannual variability of pCO_2. The additional three years of data, compared to the SOM-FFN

output, are used to investigate if the strengthening of the Southern Ocean CO_2 sink continues.

Improving the CO_2 sampling strategy of the Southern Ocean

Chapter 5 takes a step back and assess current and future CO_2 sampling strategies of the Southern Ocean from an empirical modelling perspective. This is done with sampling simulation experiment, where model data is used as an idealised environment in which sampling strategies are simulated. The key questions in this chapter are:

- Is there a bias in SOCAT estimates of pCO_2 and thus FCO_2 given the summer sampling bias?
- How many moorings are required to estimates pCO_2 adequately with an SVR?
- Would 200 profiling floats, with large sampling error, be adequate to estimate pCO_2 using an SVR approach?
- Do mixed platform observations achieve better FCO_2 estimates that single platform approaches?

These questions are answered by simulating three sampling platforms: ships using the SOCAT database, randomly placed stationary moorings, and 200 Lagrangian profiling floats. Combinations of these platforms are also compared. An integrated CO_2 sampling strategy is suggested based on the findings of the chapter.

Chapter 6 concludes the thesis drawing together the outcomes of the thesis. The implications of these findings on the broader context of climate change are discussed. The thesis is finished off with suggestions and questions raised by this that could lead to future work.

Chapter 2

Data, methods and theory

This chapter describes the data and the methods used throughout this thesis. The multifaceted approaches used in this study meant that model, *in-situ* and remote sensing data were used. The technical details of each of the products are described. The second half of the chapter introduces statistical learning using linear regression to explain some fundamental theories. Support Vector Regression (SVR) and Random Forest Regression (RFR), more sophisticated regression methods, are then introduced.

2.1 Gridded data products

In this chapter the various remote sensing products used throughout this thesis will be introduced. The primary use of the remote sensing data was to estimate pCO_2^{sea} using Support Vector Regression and Random Forest Regression (Chapter 3). In order for this to be done, all data was remapped onto the same 0.25° × 0.25° grid using the bilinear interpolation method provided in Climate Data Operators (CDO, 2015). Additional processing was done with the SciPy stack in Python 2.7. Details of products are summarised in Table 2.1 and maps of the mean values for several of these variables are shown in Figure 2.1 to provide basic overview of the proxies.

ETOPO1 is a 1 arc-minute global relief product (Amante and Eakins, 2009), but was remapped to 0.25°. The ice-surface version of the product was used in this study – this is inconsequential as only ocean bathymetry was used. This file can be downloaded at: http://www.ngdc.noaa.gov/.

Cross Calibrated Multi-Platform winds incorporates several wind sensors into one ocean

Table 2.1: Information about remote sensing products used in this thesis. Note that the products marked with * are not remote sensing products, but gridded reanalysis products. These are used together with the remote sensing data and are thus introduced in this chapter. Note that all data are available in netCDF format.

Group / Product	Variables	Date Range (Years)		Resolution	
		Start	End	Temporal	Spatial
ETOPO1	Bathymetry	-	-	-	1 min
CCMP v2	Winds [u, v]	1987	2015	6 hrs	0.25°
SSALTO / DUACS	ADT, Geostrophic currents [u, v]	1993	2016	1 day	0.25°
GHRSST	SST, Sea ice fraction	1981	2016	1 day	0.25°
Globcolour	Chlorophyll	1997	2016	1 day	0.25°
*ECCO2 (cube92)	Mixed Layer Depth, Salinity	1992	2016	1 day	0.25°

surface wind product (Atlas et al., 2011). Microwave radiometer products provide accurate wind speed estimates and scatterometer products, used to estimate the direction, add rigor to the wind speed estimates. *In-situ* buoy and ship data are used to further improve the wind velocity estimates. The use of multiple products allows for a temporally high resolution product of six hourly estimates. Wanninkhof et al. (2013) recommended this product over NCEP-II as the latter is inconsistent over the ocean. The data was downloaded from: http://www.po.daac.noaa.com.

SSALTO/DUACS is a project that processes satellite altimetry data into an absolute dynamic topography (ADT) product. This product is distributed by AVISO and can be downloaded from: http://www.aviso.altimetry.fr/duacs/. ADT is calculated by summing the mean dynamic topography (MDT) and the sea level anomaly (SLA). Three ADT variables are available for download: h, dynamic height; u and v, where geostrophic velocity components are calculated from the dynamic height.

GRHSST (Group for High Resolution Sea Surface Temperature) is a community that create multi-platform SST products offering continuous data for more than 30 years. The product used in this instance is a daily, 0.25° level 4 blended product that covers gaps by optimal interpolation (Reynolds et al., 2007). Sea ice fraction data are available alongside the SST data. This product can also be downloaded from: http://www.po.daac.noaa.com.

The **Globcolour** satellite chlorophyll (*Chl-a*) product is a global merged product that calibrates a range of ocean colour products from 1997 to present. The project has made 4 km, 0.25° and 1° products available at 1 day, 8 day and monthly intervals. The shortcomings of the product are discussed in Johnson et al. (2013) where the authors found that Globcolour underestimates Chl-a in the Southern Ocean. This should not contribute to uncertainties in of pCO_2 as machine

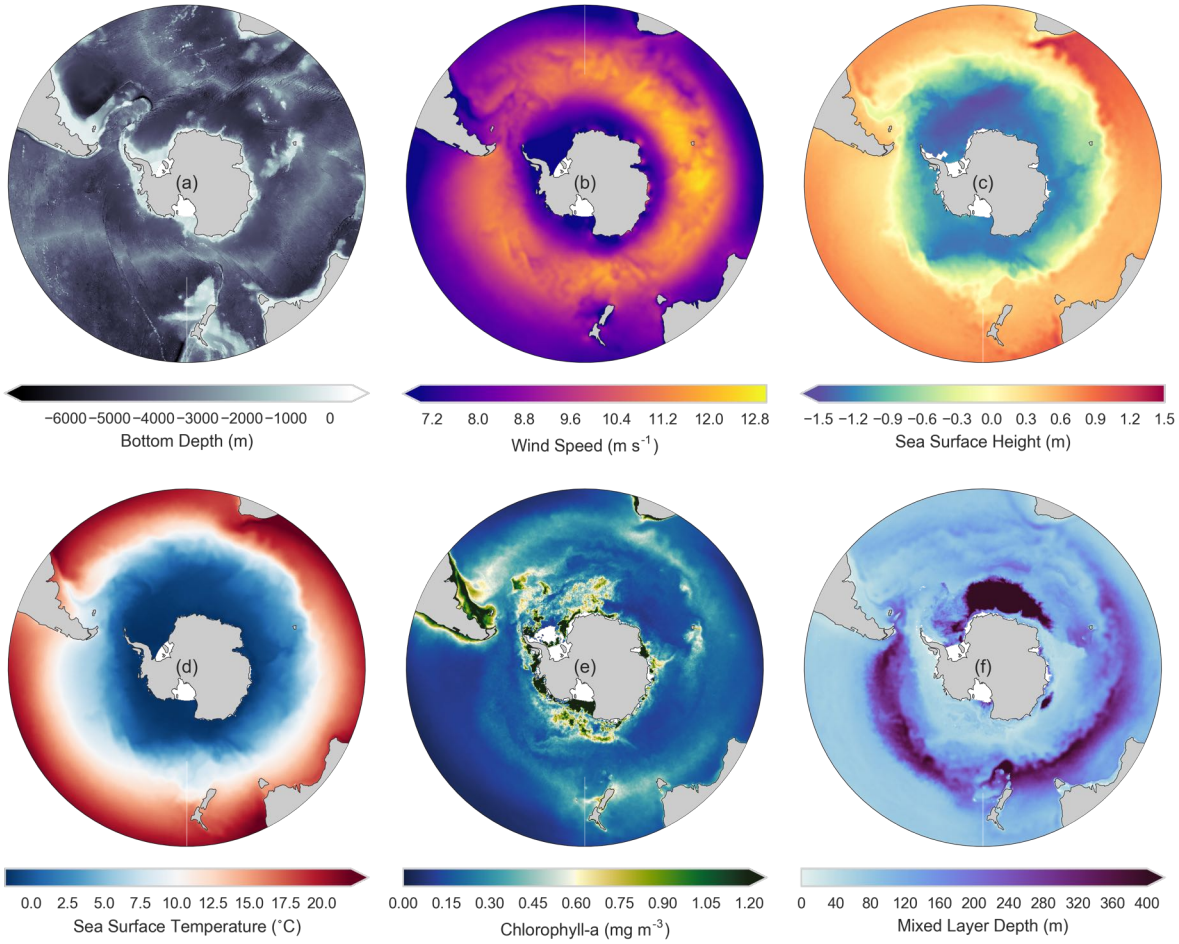

Figure 2.1: Mean values for several of the remote sensing and reanalysis variables shown in Table 2.1. (a) ETOPO1 Bathymetry, (b) CCMP wind speed, (c) AVISO absolute dynamic height (sea surface height), (b) GRHSST sea surface temperature, (d) Globcolour chlorophyll-*a*, (f) ECCO2 mixed layer depth.

learning only considers measurements relative to the training dataset. A consistent dataset is much more important in machine learning applications and a longer time series would offer far greater value – this is what Globcolour offers. More information about this product can be found on the product website: http://www.globcolour.info.

ECCO2 (Estimating the Circulation and Climate of the Ocean, Phase II) is a global assimilative model run with physics driven by MITgcm (Menemenlis et al., 2008). Several iterations of this model have been produced, but in this study we refer to the *cube 92* iteration of the ECCO2. This model output provided sea surface salinity and mixed layer depth as additional proxies of CO_2 for this study (as was done by Landschützer et al. (2014)). Menemenlis et al. (2008) found that the assimilated solution of ECCO2 performed well in the polar oceans and reduced biases found in

non-optimised output. In a comparison of ECCO2 with observational data, Dotto et al. (2014) found that ECCO2 was only able to represent sea surface salinity (SSS) well when observations were assimilated, though variability of the estimates were still not realistic. More information about ECCO2 and data access can be found at: http://ecco2.org.

2.2 *In-situ* Data

2.2.1 SOCAT

The Surface Ocean CO_2 Atlas (SOCAT) is a community initiative to produce a dataset of quality controlled surface ocean pCO_2 (Pfeil et al., 2013; Bakker et al., 2014). The database is currently on its 3^{rd} iteration and can be downloaded from http://www.socat.info. Figure 2.2 shows the improved coverage gained with each iterations.

A persistent problem with the SOCAT observations in the Southern Ocean is that data are biased toward the summer months and this problem persists with new versions. This is due to the inclement weather and rough sea state during the winter months, producing a large gap in the observations. Another problem with the current state of current observations is that the majority of observations in the Southern Ocean are located along repeated cruise tracks in the Drake Passage, south of New Zealand and Tasmania and around the Kerguelen Plateau region (Figure 1.6a). These repeat measurements are invaluable, but it highlights the fact that other regions, such as the South Pacific are under-sampled. The problem of under-sampling will be addressed comprehensively in Chapter 5.

CO_2 calibration and quality control

The majority of observations in the SOCAT database are made with ship based autonomous underway pCO_2 systems for which recommendations can be found in Pierrot et al. (2009). These systems measure the dry mole fraction CO_2 (xCO_2) of equilibrated seawater and air using an infra-red sensor (LICOR analyzer). Seawater xCO_2 is measured every one to two minutes, while atmospheric xCO_2 is measured every four hours (due to larger scales of variability). Importantly, the LICOR sensor is calibrated with four known gas concentrations at the same interval that

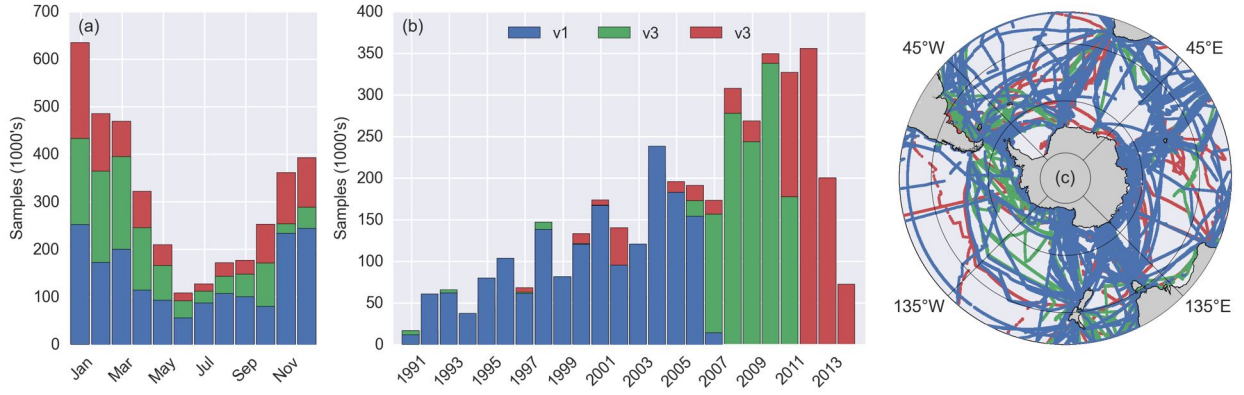

Figure 2.2: A comparison of the improving distributions of CO_2 observations in the Southern Ocean for SOCAT versions 1–3. (a). The seasonal distribution of pCO_2 measurements shows that sampling is biased towards summer even with later releases. (b) The number of observations over time is increasing and (c) the spatial distribution is improving, slightly with each new version of SOCAT. Note that the key is the same for all three figures.

atmospheric xCO_2 is measured at. A linear correction is applied to the measured xCO_2 based on the concentrations of the known gases. Calculating pCO_2 and the fugacity of CO_2 (fCO_2) is done retrospectively in CO_2 data reduction software developed by Pierrot et al. (2009).

Once initial calibration has been done, data are submitted to SOCAT, but is not released publicly until it has undergone secondary community based quality control. In the quality control process each cruise is first graded on various metadata criteria: xCO_2 submitted, precision of instruments (calibration sheets), at least two calibration gases, and various water warming rate criteria (Bakker et al., 2014). Once a cruise has been deemed fit for SOCAT, individual observations receive WOCE flags (2 = good, 3 = questionable, 4 = bad). For more in depth information on the quality control procedure, see Pfeil et al. (2013) and Bakker et al. (2014).

2.3 Model Data

Outputs from a NEMO model were used as idealised testing environments. NEMO (Nucleus for European Modelling of the Ocean) forms the framework in which the models for various spheres of modelling operate (Madec, 2015). The configuration used in this thesis is:

- OPA (Océan Parallélisé) ocean dynamics and thermodynamics model, which is a primitive equation model that forms the base of the NEMO framework with which other models can be interfaced, such as LIM and PISCES (Madec et al., 1998);

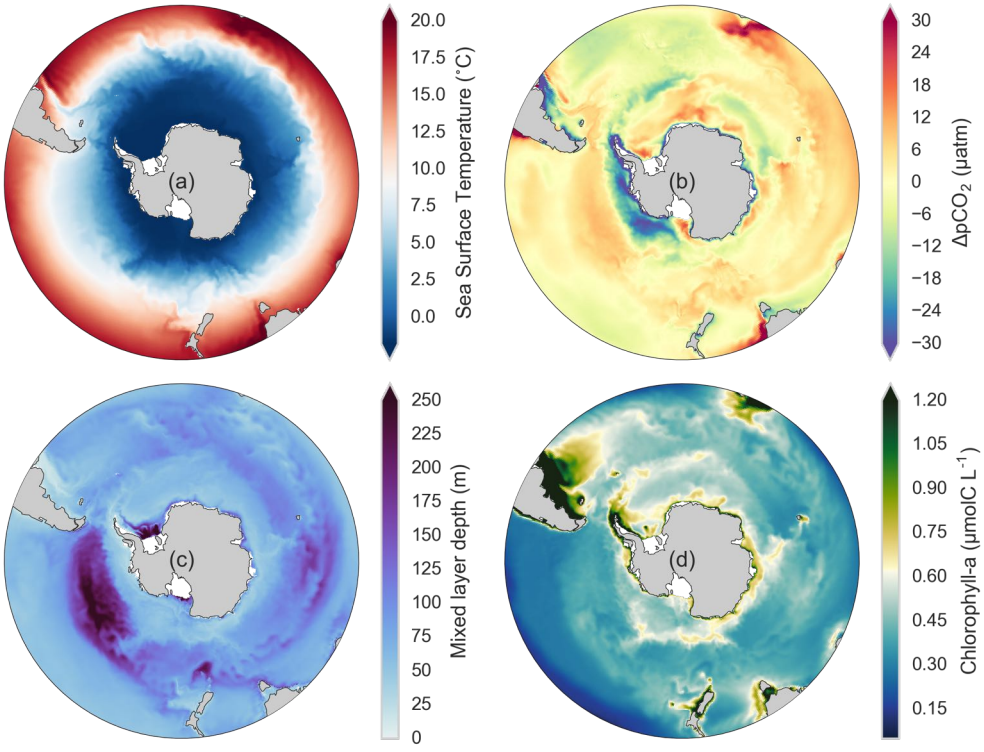

Figure 2.3: The above four figures show temporal mean (2004 – 2008) values of (a) sea surface temperature, (b) ΔpCO_2 (sea-atm), (c) mixed layer depth, and (d) total chlorophyll (diatom + nano phytoplankton).

- LIM (Louvain-la-Neuve sea ice model) sea ice dynamics model, which solves for sea ice thickness, enthalpy, salinity and age distributions. More information on LIM can be found in Vancoppenolle et al. (2012);
- PISCES biogeochemical model that solves for ocean nutrients (phosphate, nitrate, iron, and silicate) and phyto-, microzoo- and mesozooplankton (Aumont et al., 2015).

A full description of the NEMO–PISCES coupled setup can be found in Aumont and Bopp (2006).

2.3.1 BIOPERIANT05

The model configuration, BIOPERIANT05-GAA95b, is an updated version of the model used by Dufour et al. (2012), where BIOPERIANT05-GAA95b includes biogeochemistry with PISCES-v2 and uses NEMO 3.4 instead of NEMO 3.2 used in Dufour et al. (2012). BIOPERIANT05-GAA95b is a regional model with a peri-Antarctic domain (run by A. Albert at Le Laboratoire de Glaciologie et Geophysique de l'Environnement). The open northern boundary of the model (30°S) is forced

Table 2.2: Specifications of the BIOPERIANT05-GAA95b configuration. Table adapted from Mongwe (2014).

Domain	Regional Circumpolar	72.75 – 73.25°E 78.59 – 29.59°S	
Horizontal Grid	Resolution 0.5°	x = 722 y = 202	
Vertical grid	46 vertical levels z-coordinate	upper 200 m below 200 m	16 levels () 19 levels
Initial conditions	Started from rest T and S from Levitus Ice from ORCA05-g70.112		
Run duration	Spin-up (3 years) Run (20 years)	1989 – 1991 1992 – 2009	
Lateral Boundary	Only northern boundary open	5 day ocean dynamics from ORCA05-GAA95b 1 mon tracer climatologies: Alk, DIC, DOC, De, NO_3, O_2, PO_4, Si	
Surface Boundary	Atmospheric forcing	ERA Interim	
		10m u and v swrad, lwrad. tair, thumi (t2, q2) precip, snow	3 hours 24 hours 3 hours 24 hours
	Damping	T and S are damped to climatologies	
	Runoffs	S and T, are included at a frequency of 24 hours. River treatments, mixing over upper 10m	
	Sea surface restoring	Salinity only - using Levitus climatology	
	Penetration of light	2 bands, constant	
Bottom boundary	Non-linear bottom friction		
Model numerics	Advection scheme: TVD Eddy mixing parameterised (Gent and McWilliams scheme) Laplacian lateral diffusion for tracers along isoneutral surfaces Biplacian lateral diffusion of momentum along geopotential surfaces Implicit time stepping vertical diffusion is handled by TKE scheme, with tke source below the ML, langmuir paramererisation, surface mixing length scale is a function of wind stress first vertical derivative of mixing length bounded by 1		

by a global 0.5° model, ORCA05 as presented in Biastoch et al. (2008). The horizontal resolution of the configuration is 0.5° cos(latitude) with 46 vertical levels. Output was saved as five day averages. The simulation was run from 1992 to 2009 with a three year spin-up period from 1989 to 1991 (as shown in Table 2.2). All details of the model are is shown in Table 2.2.

The model data are used to test biases of empirically estimated pCO_2 when trained with data sampled with various platforms. Data usage is thus limited to the surface layer of the model – i.e. satellite observable variables. These include sea surface temperature (SST), salinity, sea surface height, and chlorophyll (the sum of nano-phytoplankton and diatoms). Partial pressure of CO_2 (pCO_2) and air-sea CO_2 flux (FCO_2) are also used (derived by the model from DIC and TA, wind stress and other ancillary data). BIOPERIANT05 wind stress is also used to calculate

FCO_2 in Chapter 5. Maps of the mean values for some of these variables are shown in Figure 2.3 to provide basic overview of the model output. One of the assumptions made, is that the upper layer of the model is representative of what a satellite would observe, e.g. skin temperature of the ocean. I also do not account for Chl-a optical depth as only the surface layer is used. One caveat of the BIOPERIANT05-GAA95b configuration is that pCO_2^{atm} forcing was ~ 10 μatm higher than pCO_2^{atm} observations for corresponding years. This has no foreseeable effect on the results of this study as BIOPERIANT05 data is used in an observation system simulation experiment, meaning that the model's ability to represent pCO_2 variability is far more important.

2.4 Statistical Learning

Statistical learning dates as far back as 1795 when Gauss used the least squares method to track planetary orbits. The paradigm of this field is one of rigour, probability and understanding. However, in recent years a more pragmatic divergence from this philosophy has emerged: *machine learning*. This has been driven primarily by increasingly large datasets and growing computational power. These two factors have allowed practitioners to forgo the rigorous mindset that is needed for smaller sample sizes and instead focus only on exactitude of the result.

The current state of empirical modelling in the surface ocean CO_2 community (with exceptions) lends itself towards the machine learning realm, where complex methods are often used to good effect, but are difficult to interpret (Rödenbeck et al., 2015). The downside of this approach is that there is very little systematic understanding of the drivers of CO_2. In this thesis we estimate CO_2 using SVR, traditionally a more statistical approach, and RFR. Before these more complex statistical regression methods are introduced, simple least squares linear regression will be explained and used as a means to explain the theory of learning.

All machine learning in this thesis was done using the *scikit-learn* package for Python 2.7 (Pedregosa et al., 2011). There are several alternatives, but *scikit-learn* is the most active open-source package and integrates well with other Python packages (*pandas, numpy*).

2.4.1 Linear Regression by least squares

Linear regression is a widely used statistical learning tool that is simple and easy to understand. In the formulation of a statistical learning problem we are given a training dataset $\mathbf{x} = \{(x_1, y_1), ..., (x_n, y_n)\} \in \mathbf{X}$, where n is the number of target observations (or rows), $\mathbf{X}$ denotes the entire population, domain or space of the input variables Hastie et al. (2009). We make the assumption that the relationship between x_i and y_i can be represented by:

$$f(\mathbf{x}) = \beta\mathbf{x} + \epsilon \tag{2.1}$$

where β represents a vector of estimated coefficients, and ϵ is undefined noise or error that cannot be estimated by $\beta\mathbf{x}$. The most popular and well known form of linear regression is ordinary least squares (OLS), which is described by:

$$\hat{y} = \hat{\beta}_0 + \sum_{j=1}^{p} x_j \hat{\beta}_j \qquad \text{OR} \qquad \hat{y} = \mathbf{x}^T \hat{\beta} \tag{2.2}$$

In both cases $\hat{y}$ is the estimated or predicted output, $\mathbf{x}$ is a column matrix of the input parameters and $\hat{\beta}$ is a vector of estimated coefficients. The formal estimation of these coefficients is achieved by minimizing the *residual sum of squares* (RSS):

$$RSS(\beta) = \sum_{i=1}^{N} (y_i - x_i^T \beta)^2 \qquad \text{OR} \qquad RSS(\beta) = (y - \mathbf{x}\beta)^T (y - \mathbf{x}\beta) \tag{2.3}$$

This solution can be found by stochastic gradient descent or by linear algebra where the differential form (with respect to β) simplifies to the normal equation:

$$\hat{\beta} = (\mathbf{x}^T \mathbf{x})^{-1} (\mathbf{x}^T y) \tag{2.4}$$

This is the most basic form of the normal equation. There are adjustments to this equation to avoid the computational complexity of calculating the inverse of $\mathbf{x}^T\mathbf{x}$, the most common being QR decomposition (proof outside of the scope of this Ph.D). It is important to be aware that the majority of linear solvers will implement some optimization technique. For more details on this method read page 54 of *The Elements of Statistical Learning* (Hastie et al., 2009).

When multiple input variables are available, the input $\mathbf{x}$ can be represented as an $m \times n$

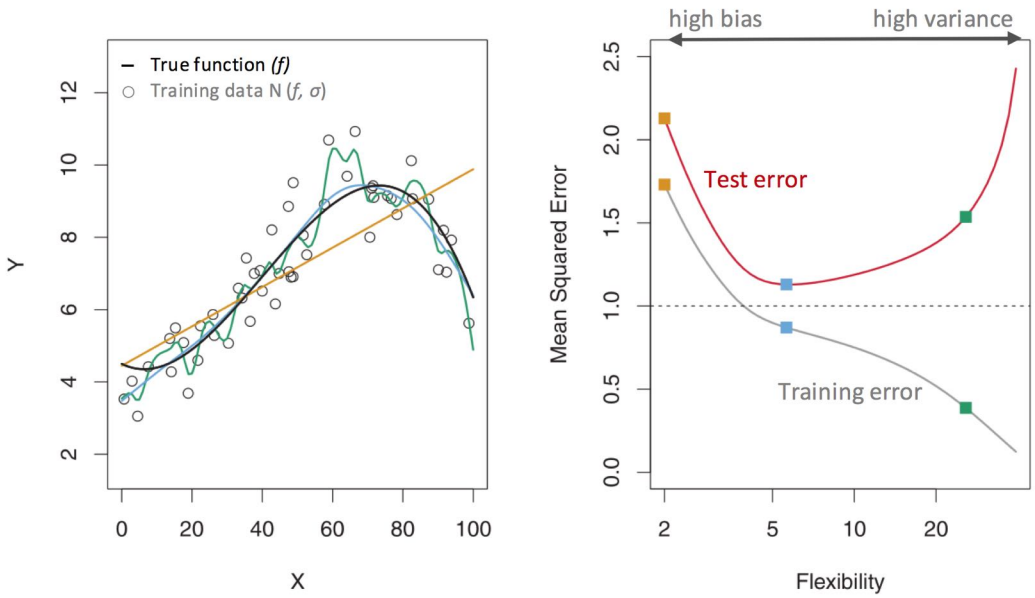

Figure 2.4: An example of underfitting and overfitting with simulated data from James et al. (2013). The black line in the left-hand figure is the true function with the training points normally distributed around this function. The orange, blue and green lines are examples of fits to the data with increasing levels of flexibility. Here the orange line is representative of underfitting and the green line overfitting. The performance of these is shown in the right figure. The grey line is the error based on the training dataset (points) and the maroon line is the out-of-sample error (black line) based on the true function.

dimensional matrix, where m is the number of cases and n the number of variables. The number of coefficients for a linear regression model is $n+1$ for the case where a non-zero intercept is included. Using multiple variables in linear regression is referred to as multiple linear regression (MLR).

2.4.2 Underfitting and Overfitting

Given a regression problem, such as predicting pCO_2 from proxy variables, we are given a limited number of inputs: SST, Chl, ADT and MLD. Using these variables as inputs to a multi-linear regression, after Lefèvre et al. (2005), shows that these variables alone do not perform well as predictors of pCO_2, with low prediction scores (r^2). The simple MLR method used in Lefèvre et al. (2005) is an example of model underfitting — also known as *bias*.

To avoid bias by underfitting data one can increase the dimensionality of the problem by introducing more terms or variables allowing for a better fit. Creating Q^{th} degree polynomials from the existing inputs is a good way of increasing the dimensionality of a linear regression

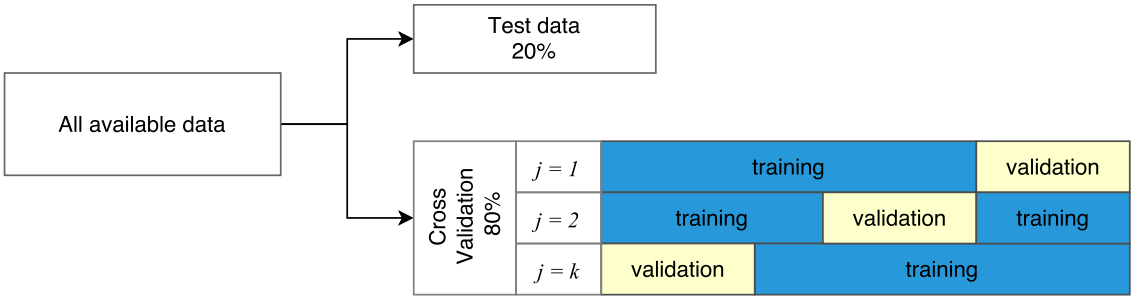

Figure 2.5: Schematic showing the procedure by which data should be split for testing, and cross-validation

problem, e.g.

$$\mathbf{X} = \begin{bmatrix} \vdots & \vdots & \vdots & \vdots & \vdots & \vdots & \vdots & \vdots \\ SST^2 & Chl^2 & MLD^2 & ADT^2 & SST & Chl & MLD & ADT \\ \vdots & \vdots & \vdots & \vdots & \vdots & \vdots & \vdots & \vdots \end{bmatrix}$$

Given enough inputs MLR should theoretically be able to fit a dataset very well. However, the given training dataset (a subset of true dataset) may not be representative of the out-of-sample data – there may be variability in the training subset that does not occur outside of the training sub-sample. If an MLR is made to fit the variability of the subset it can lead to *overfitting*, also called *variance* error. These concepts of bias and variance are illustrated graphically in Figure 2.4.

To reduce the variance errors, variations of linear regression have been developed. Ridge regression, one such method, introduces a shrinking penalty to the cost function (RSS). The modified cost function is:

$$RSS + \lambda \sum_{j=1}^{p} \beta_j^2 \tag{2.5}$$

where λ is the *tuning parameter*. Setting λ to 0 results in no penalty at all and equates to an ordinary least squares regression, but as λ is increased the penalty drives β_j towards 0. To estimate the tuning parameter, one needs to iterate through various options to find the lowest out-of-sample error. This is typically done by *cross-validation* (Hastie et al., 2009).

2.4.3 Training, testing, cross-validation and tuning

To tune hyper-parameters (λ or other hyper-parameters) and estimate performance, data are split into three separate portions: testing, training and validation datasets. There is no fixed rule

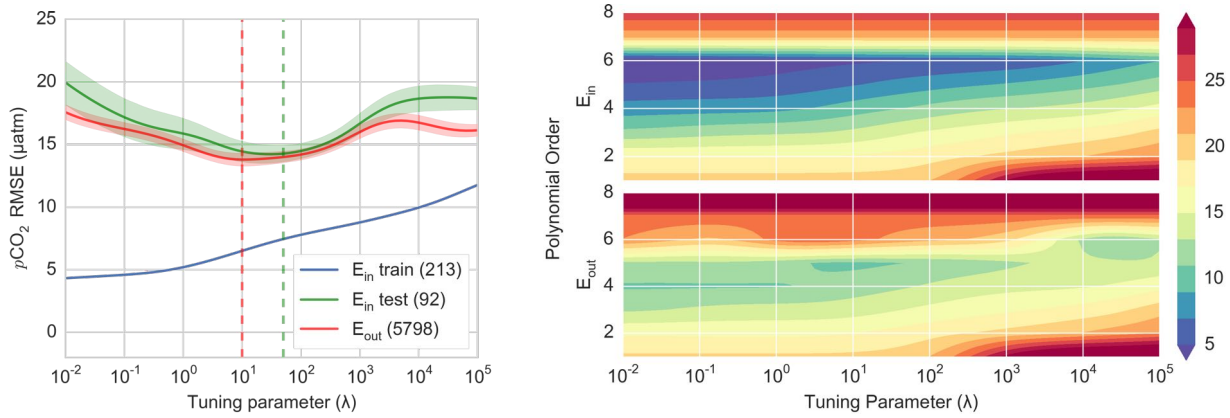

Figure 2.6: Root mean squared errors of pCO_2 estimates from a single transect in the Southern Ocean. (a) regularisation demonstrated with a fifth order polynomial. The out-of-sample error (E_{out}) would typically not be available in a learning problem. Here it demonstrates that, with cross-validation, a subset of the training sample can be used to estimate the tuning parameter. (b) Polynomial order demonstrates the effect of dimensionality. A higher order polynomial achieves low errors in the training sample without cross-validation (*i.e.* 5 and 6). The out-of-sample error shows that higher dimensions may be overfitting the data.

about the proportions by which the data should be split, but the ratios shown in Figure 2.5 are common.

The *testing* dataset is kept separate from the datasets used in cross-validation (see Figure 2.5). This is used to determine an error estimate independent of the cross-validation process. Several cross-validation process exist, but k-fold validation is the most widely used. Data is split into k groups where the training and the validation dataset are chosen for each k and iterated through. It is generally recommended to use 5 – 10 folds in k-fold cross-validation (Hastie et al., 2009). It is important to mention that the final training (once hyper-parameters have been selected), is done using the entire training set (no k subsets).

Figure 2.6a demonstrates the effect of regularisation (achieved here by using Ridge regression) with pCO_2 estimated for a single cruise in the Southern Ocean. A 5^{th} order polynomial was created from four input variables. Cross validation was applied to find the appropriate value of the tuning parameter. As λ tends to ∞ the bias error increases due to a large penalty value and conversely as λ approaches 0 the variance error increases. Figure 2.6b shows the coupled effect of regularisation with increasing dimensionality. Importantly, the in sample error does not match the out-of-sample error due to overfitting.

2.4.4 Support Vector Regression

Support vector machines are firmly rooted in a statistical framework having been developed out of statistical learning theory by Vladimir Vapnik and co-workers in the 1990's (Vapnik, 1999). In short, the theory of the method is that it selects only the important points in a dataset and extracts a relationship from those points. Moreover, kernelisation allows the method to address one dimensional to theoretically infinite dimensional problems. A comprehensive description of SVM can be found in Smola and Olkopf (2004) or Muller et al. (2001) – the equations that follow are taken primarily from these publications.

Basic formulation of SVM

The basic formulation of support vector machines is:

$$f(x) = \langle w, \mathbf{x} \rangle + b \qquad \text{with} \quad b \in \mathbb{R} \tag{2.6}$$

with close resemblance to the basic formulation of linear regression (Equation (2.2)). b is an intercept, $\langle \cdot, \cdot \rangle$ denotes the dot product of the weights (w) and $\mathbf{x}$ (notation defined at the beginning of Section 2.4.1). The weights and intercept are found by solving the optimization problem:

$$\text{minimise} \quad \frac{1}{2}||w||^2 \text{ subject to} \qquad \begin{cases} y_i - \langle w, x_i \rangle - b & \leq \epsilon \\ \langle w, x_i \rangle + b - y_i & \leq \epsilon \end{cases} \tag{2.7}$$

In this form, w is minimised to a precision of ϵ – *i.e.* there is no room for error greater than ϵ. However, with the majority of problems, meeting these constraints is not possible if data are noisy or ϵ is set small. The inclusion of *slack variables* (ξ_i, ξ_i^*) relaxes the constraints and the optimization problem is now formulated as:

$$\text{minimise} \quad \frac{1}{2}||w||^2 + C\sum_{i=1}^{n}(\xi_i + \xi_i^*) \qquad \text{subject to} \quad \begin{cases} y_i - \langle w, x_i \rangle - b & \leq \epsilon + \xi_i \\ \langle w, x_i \rangle + b - y_i & \leq \epsilon + \xi_i^* \\ \xi_i, \xi_i^* & \geq 0 \end{cases} \tag{2.8}$$

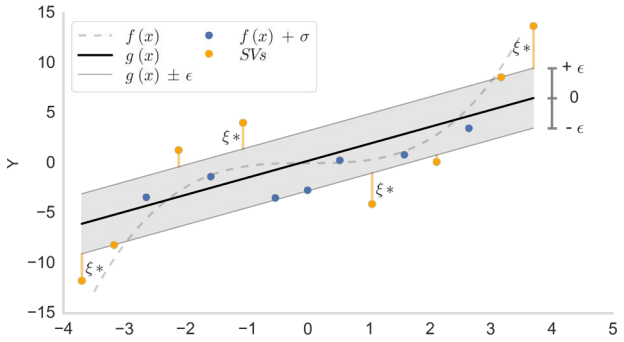

Figure 2.7: A linear SVR trained on simulated data: a cubic polynomial, $f(x)$, with noise added to training points (σ). The SVR estimates a regression line $g(x)$ and the margins are $g(x) \pm \epsilon$. Any training points outside of the margins are considered support vectors (SVs). The slack variable, ξ_i^*, is the distance between the margin and the SV and only these contribute to the minimisation problem in Equation (2.8).

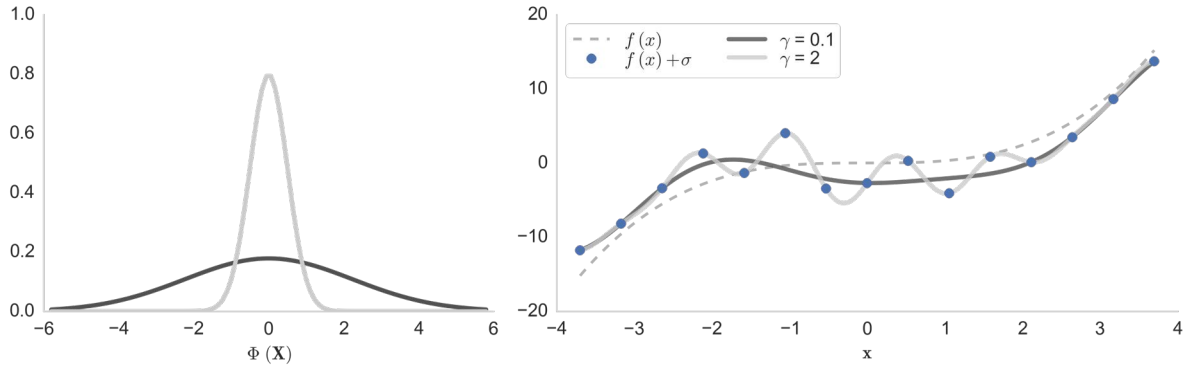

Figure 2.8: The effect of changing the width of the *RBF* kernel with the tuning parameter γ. (a) shows the width of the kernel for two different values of γ. Φ represents the mapping function that transforms $\mathbf{X}$ to F. (b) The predicted SVR curves with *RBF* kernels. All other tuning parameters are kept constant: $C = 10,000$, $\epsilon = 0$. The data from Figure 2.7 was used.

Here C is a parameter that adjusts for the amount of error that the minimisation allows. The slack variable $|\xi|$ is only counted towards the cost if the point lies outside the margin ($|\xi| \geq \epsilon$). The points on or outside the margins are called support vectors, hence the name support vector machine. This is visually shown in Figure 2.7 where a linear SVR is fitted to noisy data produced from a cubic spline. The optimisation problem shown in Equation (2.8) is solved in its dual formulation (see Hastie et al. (2009) for the full description). The optimisation of the dual formulation is beyond the scope of this thesis and is often dealt with by existing quadratic optimisation packages. Importantly, solving the dual formulation allows for kernelisation of SVM.

The kernel trick and Radial Basis Functions

The example shown in Figure 2.7 is linear and would not work on all problems. One of the features of SVM, is that one can easily add non-linearity by switching the linear dot product, $\langle w, \mathbf{x} \rangle$, for a non-linear kernel. A kernel function maps the input data, $\mathbf{x}$, to a new, higher dimensional feature space, F, where the mapping function is denoted by Φ. The beauty of an SVM is that $\Phi(\mathbf{x})$ is never explicitly calculated, thus reducing effort and otherwise large computational costs.

The radial basis function (RBF) or Gaussian kernel is the most widely used kernel for non-linear problems due to its success for a wide range of problems. The formulation of the RBF kernel is:

$$K\langle x, x' \rangle = \exp\big(-\gamma ||x - x'||^2 \big) \tag{2.9}$$

where $||x - x'||^2$ is the squared Euclidean distance and γ is a tuning parameter that determines the width of the Gaussian function. The effect of tuning the width of the Gaussian is shown in Figure 2.8 where it is shown that as γ increases, the flexibility of the curve increases.

2.4.5 Random Forest Regression

Random Forest Regression is a versatile method made up of a bagged ensemble of random decision trees. The method has been used with success in remote sensing where it has been used to estimate biomass of wetlands (Mutanga et al., 2012) and estimation of rainfall (Islam et al., 2015) for example. Random forests are also often used as classifiers and have proven efficient in remote sensing (Pal, 2005). Pal (2005) found that the method performs comparably to support vector machines, but the data preparation for the RF is far less than for the SVM.

Basic formulation of RFR

Random forest regression returns the average result of a group of cleverly implemented decision trees. I will thus first introduce the concept of decision trees – often referred to as Classification and Regression Trees (CART).

The basic idea of CART is to iteratively partition data into boxes using simple rules that

minimize the error at each split – these boxes would become hypercubes in higher dimensional problems. This process is described by the basic formulation as described in Loh (2011):

1. *Start at the root node*
2. *For each X, find the set S that minimizes the sum of the node impurities in the two child nodes and choose the split $X \in S$ that gives the minimum overall X and S.*
3. *If a stopping criterion is reached, exit. Otherwise, apply step 2 to each child node in turn.*

The mathematical equivalent of this formulation is shown in Hastie et al. (2009). This process is shown by the middle diagram in Figure 2.9b. Figure 2.9c shows that CART does not result in a

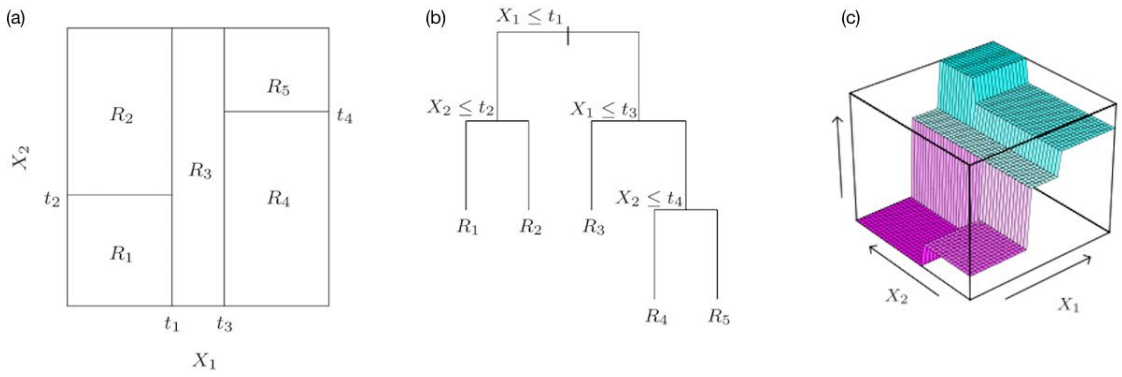

Figure 2.9: (a) shows the partitioned boxes (R) of a two dimensional problem with each of the iterative splits (t also called nodes). (b) shows the tree that matches the splits shown in (a). Here the rules that minimize the error for each split are shown – these are also known as nodes. (c) shows a three dimensional representation of the prediction surface of the model. These figures were taken directly from Hastie et al. (2009).

continuous result, but rather discrete estimates even if the true function is smooth. The range of predictions are also limited to the training sample as each of the prediction surfaces is an average of estimates at the end of a tree. Another negative property of CART is that they have high variance, where a small change in the dataset could result in very different split locations, potentially changing the result significantly.

Bagging and random feature selection

Random forest regression overcomes many of these problems by taking the ensemble mean of multiple CARTs trained by sub-sampling the training dataset known as *bagging* (bootstrap aggregating) (Breiman, 2001). The bagging process reduces the high variability associated with

decision trees, but maintains their low bias. This is achieved by sampling the dataset with replacement where the probability of being sampled is $1-(\frac{N-1}{N})^N \sim 0.63$ where N is the size of the training dataset. Increasing the size of the forest thus reduces variability, but increases computational cost and memory requirements. Figure 2.10 shows an example of RFR bagging where the mean of each regression tree produces the final estimate.

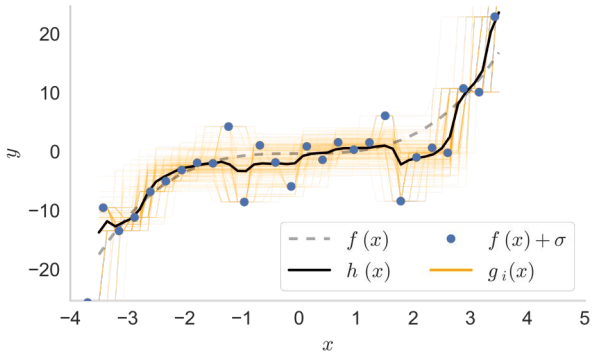

Figure 2.10: A simulated one dimensional example showing the estimate of each decision tree ($g_i(x)$) and the final hypothesised estimate ($h(x)$) as the mean of all the decision tree estimates.

Another defining characteristic of random forests is the use random feature selection in high dimensional problems, which results in improved generalisation (Breiman, 2001). This is achieved by limiting the number of features by which the data is split at each node. For example, at each node only two of eight features (proxy variables) could be used to split the data, where these are a random subset of the eight features.

Hyper-parameter estimation with out-of-bag-error

These properties put together make RFR relatively robust to overfitting to the training dataset even if trees are allowed to grow fully (where each terminal branch contains one observation *a.k.a.* leaf). However, there are some situations where random forests can overfit the training data resulting in poor generalisation, particularly when the data are sparse. The depth of the tree or the minimum number of leaves per terminal branch can thus be limited to reduce overfitting (adjusting these produces similar results, thus only one of these needs to be tuned).

There are thus three hyper-parameters that need to be optimised using cross validation: size of the forest, the number of random features passed to each node and minimum number of leaves per terminal branch. This is where the *out-of-bag-error*, an added advantage of bagging,

is used. The out-of-bag-error is calculated for the samples not used in training due to bagging. This means that roughly 37% of the dataset is intrinsically used as a "cross-validation dataset" without the need for cross-validation methods such as K-fold cross validation used in SVM. The out-of-bag-error and random feature selection also allows the method to determine a ranking of the importance of each variable or feature – details are discussed in Louppe (2014).

Without the need to run expensive cross validation methods the computational efficiency of RFR is much better than SVM. Moreover, the parallelisability of training multiple individual decision trees makes the RFR very efficient with access to a multi-core workstation or high performance computing platform.

2.5 Comparison framework

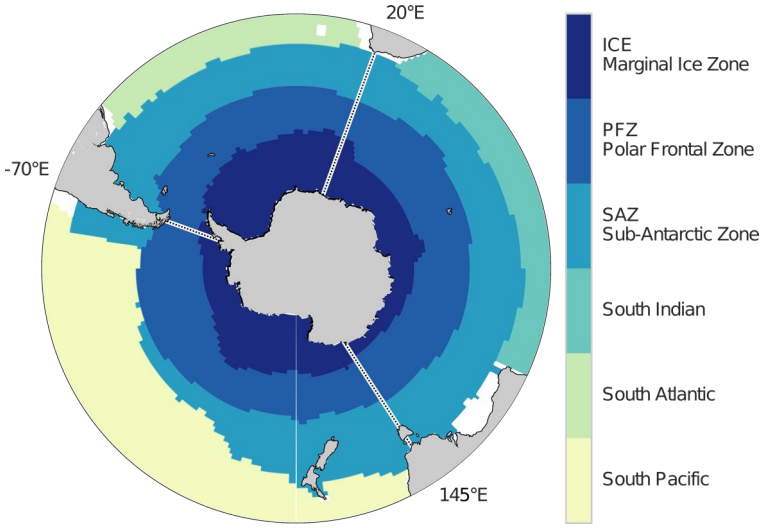

Figure 2.11: Biomes of Southern Ocean CO_2 as specified by Fay and McKinley (2014). These biomes formed the comparison framework used in Rödenbeck et al. (2015) and are also used in this study to compare SVR with Landschützer et al. (2014)'s SOM-FFN. The abbreviations used in the text and figures are listed above the long name for the region, but note that the common names for these regions are used rather than the names given in the publication (Fay et al., 2014). The three dashed white lines show the oceanic boundaries for the Atlantic, Indian and Pacific oceans.

In the study by Rödenbeck et al. (2015), the authors use the open-ocean biomes created by Fay and McKinley (2014) as a regional comparison framework. Fay and McKinley (2014) defined 17 biomes based on SST, Chl-a, MLD and sea ice fraction, allowing the zones to be dynamic in time and space. The region of interest in this study, the Southern Ocean south of 30°S, contains only

six of these zones (shown in Figure 2.11). The authors state that the three Southern Ocean biomes are comparable to the SAZ, PFZ and Antarctic Zone (AZ). Similarly to Rödenbeck et al. (2014), these zones will be used as a regional comparison framework for pCO_2 and air-sea CO_2 fluxes. For a better understanding of the drivers the Southern Ocean is further split into basinswhere the boundaries are defined by lines of longitude (70°W : Atlantic : 20°E : Indian : 145°E : Pacific : 70°W).

2.6 Derived variables

Throughout this study several derived variables are used. Below we define the methods by which air-sea CO_2 fluxes and wind stress are calculated from observable parameters.

Fluxes

Air-sea CO_2 fluxes (FCO_2) are calculated with:

$$FCO_2 = K_0 \cdot k_w \cdot \Delta pCO_2 \cdot (1 - [\text{ice}]) \tag{2.10}$$

where K_0 is the solubility of CO_2 in seawater, k_w is the gas transfer velocity, ΔpCO_2 is the difference between atmospheric and marine partial pressure of pCO_2 and [ice] is sea ice cover as a fraction. K_0 was calculated using coefficients from Weiss and Price (1980) for solubility of CO_2 and the partial pressure of H_2O at the air-sea interface. The inverse linear relationship between sea ice cover and air-sea CO_2 flux is based on a study by Butterworth and Miller (2016) where it was found that flux decreased in proportion to sea ice cover – the same assumption was made in Landschützer et al. (2014). To maintain consistency with Landschützer et al. (2014), the same k_w approximation was used in this study. However, it is recognised that the gas transfer velocity approximation by Nightingale et al. (2000) may offer a better representation of the high latitude conditions of the Southern Ocean. The k_w by Wanninkhof (1992) with the updated constant from Sweeney et al. (2007) was used:

$$k_w = 0.27\, U_{10}^2 \times \sqrt{\frac{660}{Sc}} \tag{2.11}$$

where U_{10} is the wind speed at 10 metres above sea surface and Sc is the non-dimensional Schmidt number, normalised for seawater with 660 (Wanninkhof et al., 2009). Wind vectors (u_{10}, v_{10}) from the cross-calibrated multiplatform wind product (CCMP) were used to calculate wind speed U_{10} (more details on CCMP by Atlas et al. 2011 in Section 2.1).

Wind stress

Wind stress (also shear stress, τ) partially determines mixing (along with stratification) and is thus an indirect driver of surface ΔpCO_2. Wind stress is calculated using:

$$\tau = \rho_{air}\, C_D\, U_{10}^2 \tag{2.12}$$

where ρ_{air} is the density of air (1.23 kg m^{-3}), U_{10}^2 is squared wind speed at 10 m above the surface (CCMP winds as described in Section 2.1), and C_D is the wind-drag coefficient. In this case C_D was determined by the formulation of Large and Pond (1981):

$$10^3\, C_D = \begin{cases} 1.2 & 4 \le U_{10} < 11 \text{ m s}^{-1} \\ 0.49 + 0.065\, U_{10} & 11 \le U_{10} \le 25 \text{ m s}^{-1} \end{cases} \tag{2.13}$$

This may be an old formulation of C_D, but was shown to be a good approximation of wind stress by Donelan et al. (2004).

Chapter 3

Empirical estimates of pCO_2 in the Southern Ocean

3.1 Introduction

Empirical modelling has successfully been used to estimate surface pCO_2 in many regions of the ocean (Rödenbeck et al., 2015). However, in the Southern Ocean, these estimates fail to cohere. This is driven primarily by the sparse, heavily biased distribution of CO_2 observations in the Southern Ocean Rödenbeck et al. (2015). There is thus a need to explore different empirical modelling approaches to see if consensus can be reached on the variability and trends of ΔpCO_2 in the Southern Ocean.

Methodologically there are two ways in which empirical estimates of Southern Ocean pCO_2 can be improved: 1) the use of methods that are able to deal with the sparse and biased observations; 2) to improve the available input data. Both these points are addressed in this chapter. Two methods, support vector regression (SVR) and random forest regression (RFR), both which are new to this application, are used to estimate pCO_2 (as described in Section 2.4). Secondly, the impact of data gridding resolution on the ability of these methods to estimate pCO_2 is tested.

3.1.1 Empirical methods

The current benchmark of CO_2 estimates in the Southern Ocean is the SOM-FFN approach by Landschützer et al. (2014). This is a two step artificial neural network approach that implements first a clustering self-organising map (SOM) approach. Hereafter, individual regressions are applied to each cluster using a feed forward neural network (FFN). Other empirical learning methods that have proven to work well are regional implementations of multiple linear regression (MLR).

The technical details and theory of the algorithm used in this study, SVR and RFR, are presented in Section 2.4. In short, SVR reduces the training dataset to only the points required to minimise the error, called the support vectors – these points are used to create the regression model. Support vector machines (classification) and SVR (regression) have been used widely in remote sensing (Mountrakis et al., 2011). Li and Cassar (2016) used SVR to estimate global net community production (NCP) from ship measured O_2/Ar–NCP and satellite observations. And Kim et al. (2014) used an SVR to estimate coastal water quality from available satellite data.

The second approach, RFR, is an ensemble method that builds a forest of decision trees using a variation of bootstrapping on training data to create an ensemble estimates that is robust, but not immune, to overfitting. RFR is one of the "go to" methods in machine learning due to its easy implementation (Louppe, 2014). RFR has also been used in remote sensing applications, though it does not seem to be as widely used in earth systems sciences despite proving to be a powerful learning algorithm (Caruana and Niculescu-Mizil, 2006; Hastie et al., 2008). Remote sensing applications include vegetation biomass and rainfall estimation (Mutanga et al., 2012; Islam et al., 2015).

3.1.2 The importance of scale

The hypothesis behind increasing the resolution of input data is that the Southern Ocean has been shown to be highly spatially and temporally variable, particularly in summer (Thomalla et al., 2011). Proxies of CO_2, both sea surface temperature (SST) and chlorophyll-a (Chl-*a*), have been shown to vary strongly across short gradients in the Southern Ocean, with concomitant changes in pCO_2 (Resplandy et al., 2014; Monteiro et al., 2015). Using monthly × 1° resolution,

which has become widely used in the field, may average these short space and time scale effects out, potentially leading to aliasing effects (Chierici et al., 2012). Increasing the resolution could reduce this chance of aliasing.

3.1.3 Aims and Questions

In this chapter pCO_2 is estimated from gridded data (as described in Section 2.2) using the SOCAT version 3 dataset, with the aim to create high and low resolution estimates of pCO_2 at 16-day × 0.25° and monthly × 1° respectively. Below are questions that will guide this chapter based on the aims stated above:

- Can SVR and RFR methods improve on the uncertainty estimates of SOM-FFN by Landschützer et al. (2014)?
- Does increasing the resolution of gridded and SOCAT data from 1° × monthly (low resolution) to 0.25° × 16-day (high resolution) improve uncertainties and estimates?

3.2 Methodology

The methodology is introduced in three parts: data preparation, implementation of SVR and of RFR. Many of the details about the data sources and the theory of learning methods have already been introduced in Chapter 2. These methods were applied to both high (0.25° × 16-day) and low (1° × monthly) resolution datasets in the same way. These datasets will be defined as either *HR* or *LR* respectively and any differences in processing are explained if necessary.

3.2.1 Data selection, cleaning and transformation

Data in the supervised statistical learning work-flow can be split into two categories: training and prediction data. The size of the training data is determined by the target variable with length n, in this case pCO_2 from the SOCAT database. Gridded proxy variables, that correspond with SOCAT data in time and space, form part of the training dataset ($x_{n\times m}$) with n being the number of matching cases/rows to the SOCAT dataset and m the number of proxies/columns. Note that

proxy variables also form the prediction dataset ($X_{N\times m}$) so that the training dataset is a subset of the prediction dataset ($x \subset X$), where N is the total number of gridded observations.

Proxy variable selection

The existing gridded monthly × 1° SOCAT v3 product is used for the low resolution data. A high resolution option is not available. Thus, the SOCAT version 3 cruise track dataset (for which no gridding has been performed) is gridded to 16-day × 0.25° by using unweighted averaging with the *pandas* Python package. The 16-day sampling period is chosen as a compromise between temporal resolution, the number of training observations and computational requirement. A shorter sampling period would result in a decrease in the number of matched pCO_2 and observed Chl-*a* training cases (due to cloud cover) as shown by the percentage losses in training data relative to the number of gridded SOCAT observations: 8-day = 23.9%; 16-day = 13.6%; and monthly = 8.3% (with a spatial resolution of 0.25°). Gridding the Southern Ocean SOCAT cruise tracks (3.7 million observations) to a 16-day × 0.25° grid results in ~88 thousand (n = 88368) usable measurements. The gridded locations of pCO_2 are used to co-locate data from gridded proxy variables.

The details for the proxy variables are shown in Table 2.1. The proxies are chosen based on satellite observable variables that might influence pCO_2 directly or indirectly (Jamet et al., 2007; Landschützer et al., 2014; Rödenbeck et al., 2014). A study based in the North Atlantic found that sea surface temperature (SST), chlorophyll-*a* (Chl-*a*) and mixed layer depth (MLD) climatology were the most influential proxy variables of pCO_2 (Jamet et al., 2007). Sea surface salinity (SSS) is included as a proxy as it is an important indicator of overturning and thus CO_2 transport in the Southern Ocean (Dong et al., 2008). Absolute dynamic topography (ADT) is often used to calculate the locations of the ACC fronts and is thus a useful proxy as an indicator of water masses (Swart et al., 2010; Graham et al., 2012). Sea ice is considered in air-sea CO_2 flux calculations, but is not included as a proxy of pCO_2.

Transformation and cleaning

Spatial coordinates are transformed to a three coordinate n-vector system (after Sasse et al. 2013), which, unlike latitude and longitude, preserve area near the poles (Gade, 2010). Tapering lines of

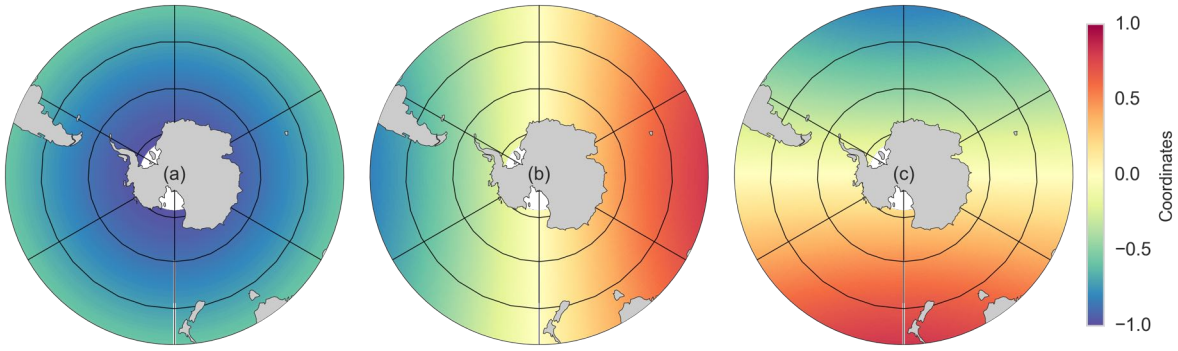

Figure 3.1: Latitude and longitude transformed to the three coordinate n-vector system. These are simply referred to as A, B and C and correspond with the figure numbers. The lines of latitude shown are the 50, 60 and 70°S.

longitude toward the poles result in a reduction of the area of a grid cells from the equator to the poles. The transformation of latitude (λ) and longitude (μ) are calculated with:

$$A, B, C = \begin{pmatrix} \sin(\lambda) \\ \sin(\mu) \cdot \cos(\lambda) \\ -\cos(\mu) \cdot \cos(\lambda) \end{pmatrix} \tag{3.1}$$

The result of these transformations is shown in Figure 3.1.

Similarly a transformation of the day of the year (j) is taken to preserve the seasonality of the data:

$$t = \begin{pmatrix} \cos(j \cdot \frac{2\pi}{365}) \\ \sin(j \cdot \frac{2\pi}{365}) \end{pmatrix} \tag{3.2}$$

In this converted time space December $31^s t$ and January 1^{st} are adjacent. This requires a sin and a cos transformation to preserve autumn/spring and summer/winter.

As previously mentioned (Section 1.5.2), Chl-a coverage is reduced by cloud coverage and the lack of light during the winter months. This means that there are a large number of ΔpCO_2 observations that do not have a matching Chl-a observation. To overcome this, Chl-a cloud gaps are filled using the climatological mean of Chl-a, but this does not resolve the missing chlorophyll in low light winter months. It is assumed that the productivity was low during this winter and missing data is filled with a low concentration of 0.1 ± 0.03 mg m^{-3} (uniform noise), where 0.1 mg m^{-3} is the 10^{th} percentile of winter Chl-a observations.

The untransformed distributions of MLD and Chl-a are log-normal distributions, with the

majority of observations having low values (<100 m and 1 mg m^{-3} respectively). The log (base 10) transformation of these results in a distribution that is much closer to a normal distribution as shown Figure 3.A.1. This means that lower values (of untransformed data) will be given greater weighting in the training process.

Once all variables have been transformed, data are scaled according to the mean (μ) and standard deviation (σ) of each column in x ($\frac{x_m-\mu}{\sigma}$) only for SVR. The scaling is later applied to columns of the prediction dataset using the same μ and σ values (again for only SVR). The final scaled distributions of the training dataset is shown in Figure 3.2 with the majority of distributions not being normally distributed.

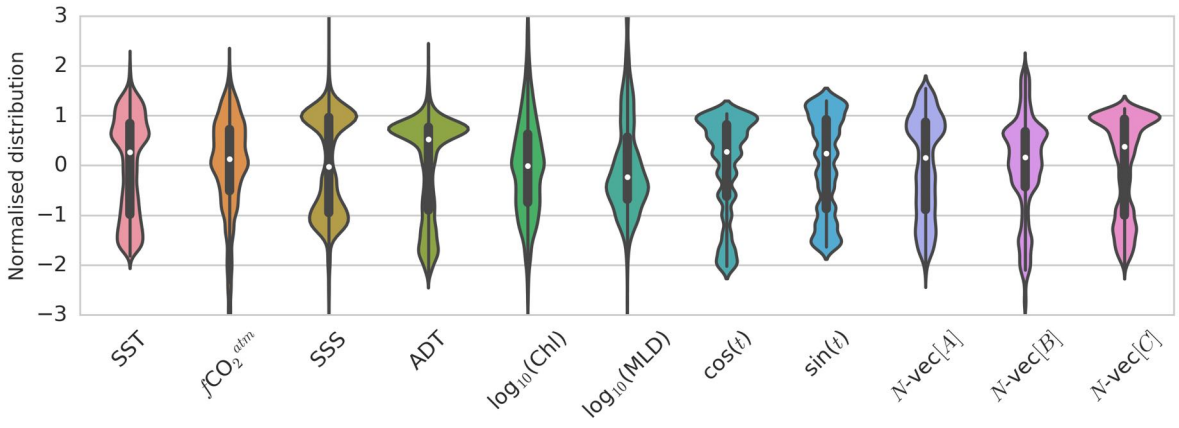

Figure 3.2: Violin plot of the proxy variables standardized to the mean and standard deviation of each variable. This is a representation of the distribution of the training data (x) that is passed to the SVR. The distribution is determined by kernel density estimation (KDE). The small black box inside each KDE is a standard quartile box-plot with the white dot showing the median.

3.2.2 Support vector regression implementation

One of the major challenges of a flexible model, such as an SVR with a Gaussian kernel, is training the hyper-parameters to avoid overfitting as the flexibility of the algorithm allows the model to be too specific to the training subset of the data. This makes the correct implementation important — the theory is discussed in Section 2.4.3 and the specific methodology followed in this study is summarised in Figure 3.3. All steps in this process were done using the *Scikit-learn* package in Python (Pedregosa et al., 2011).

Data was randomly split in 75% : 25% subsets $(x_r,\ y_r) : (x_e,\ y_e)$ respectively where subscripts

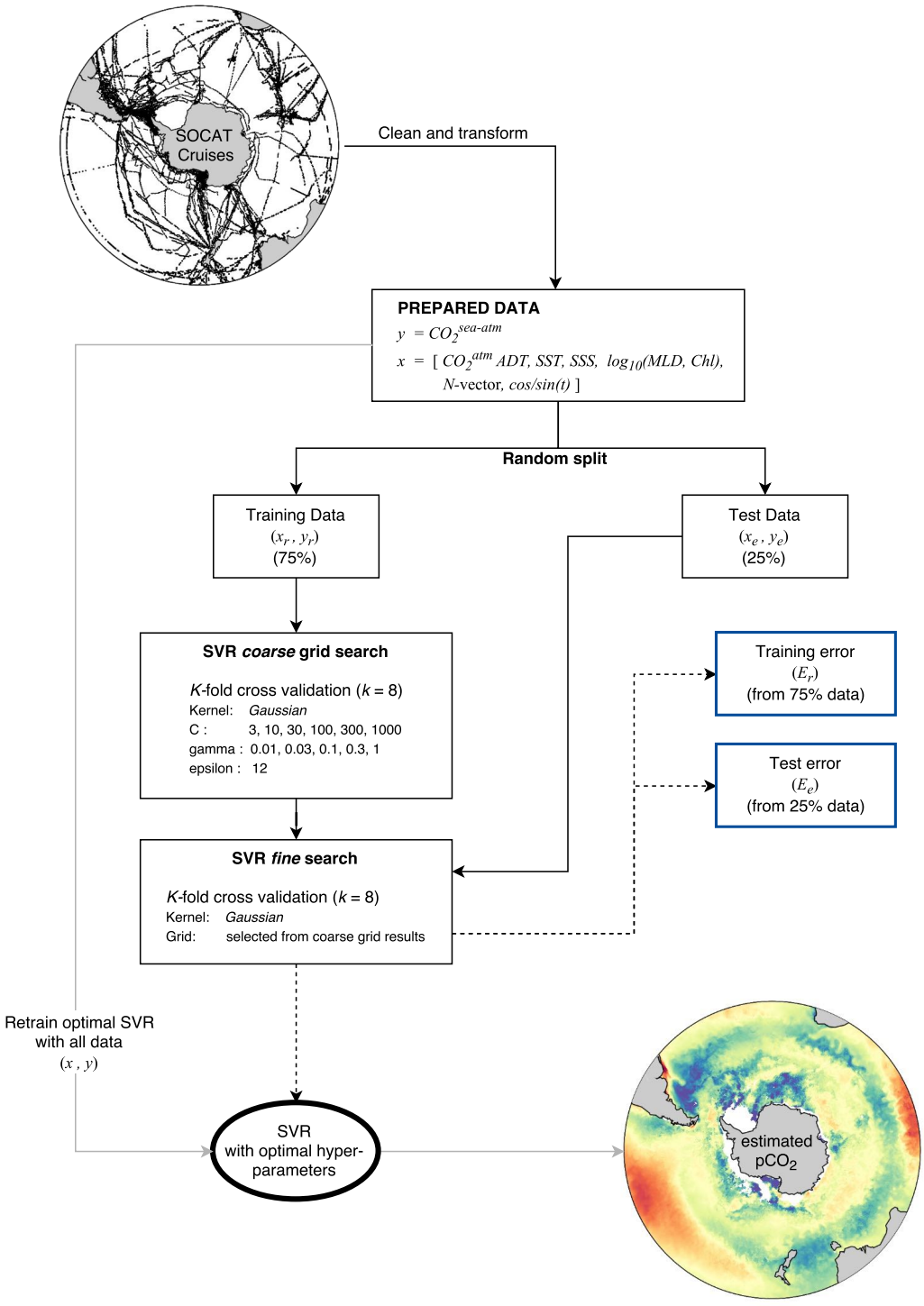

Figure 3.3: Flow diagram showing the training procedure of the support vector regression. y is the target variable pCO_2 and x is the matrix of input proxies. Both x and y are split into training and testing data denoted by r and e respectively. The cross-validation process is done to arrive at the optimal hyper-parameters (C, γ, ϵ) for SVR models where Chl-a observations are available (f_w) and those where they are not (f_s). X represents the full compliment of prediction data (gridded satellite and reanalysis data). See text for more details.

r and e represent training and testing subsets. Hastie et al. (2008) explain that there is no fixed rule on the size of the training and testing subsets and is dependent on the noise to signal ratio of the data. The test data is set aside to estimate the independent error of the validated SVR whereas training data is used to construct the SVR by cross-validation. Hyper-parameter estimation for C (slack parameter) and γ (Gaussian radius) is done with a coarse grid search followed by a finer search informed by the coarse grid outputs (Equations (2.8) and (2.9)). Where these parameters are dimensionless as the data have been normalised. Epsilon (ϵ – allowable error margin) is tuned manually as an exhaustive grid search including this parameter would be very computationally expensive. The values for the coarse grid-search are:

$$\begin{aligned} \gamma &= [0.01,\ 0.03,\ 0.1,\ 0.3,\ 1.0] \\ C &= [3,\ 10,\ 30,\ 100,\ 300,\ 1000] \\ \epsilon &= [12]^{*} \end{aligned} \tag{3.3}$$

where γ is the radius of the Gaussian, ϵ is the allowable error margin and C is the slack parameter that determines the number of points allowed outside the error margins. Epsilon is marked with an asterisk to indicate that the value was manually set to 12 μatm. K-fold cross validation (CV) is used with eight randomised folds (as explained in Section 2.4). The number of SVRs that need to be trained in cross validation is determined by the product of the grid size and K ($5 \times 6 \times 8 = 240$), an expensive exercise if not performed in parallel. Access to the Centre for High Performance Computing (CHPC) allows for a drastic reduction in computational time by using up to 24 CPUs (visit `http://www.chpc.ac.za/index.php/resources/lengau-cluster` for more information). The results from the coarse grid are interpolated onto a finer grid from which the 30 best combinations of hyper-parameters are again tested in parallel. Figure 3.4 shows the graphical output of this process, where the optimal parameters are localised to a relatively wide trough with RMSE > 0.6. From this trough, the best estimates are selected with a fine grid (shown by black dots in Figure 3.4) where the best hyper-parameters are: $C = 63.82$, $\gamma = 0.07$ and $\epsilon = 12$ μatm.

The entire training dataset $(x_r,\ y_r)$ is then used to retrain the SVR with the optimal hyper-parameters. This SVR is used to estimate the training error ($E_r = y_r - f(x_r)$) and the test error ($E_e = y_e - f(x_e)$). Finally the SVR is retrained using both the training and test data $(x_{r|e},\ y_{r|e})$; the

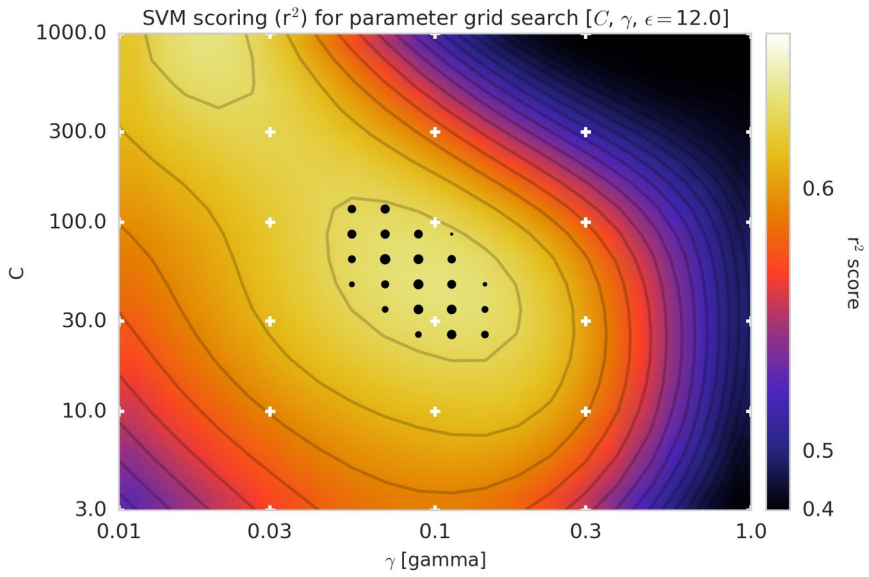

Figure 3.4: The output from the two step search protocol for optimal hyper-parameters with ϵ constant at 12.0 μatm. The white crosses show the sampling locations of the coarse grid. The contours and colour overlay is an interpolation of r^2 scores of the coarse grid output. The black dots show the 30 best hyper-parameters that are chosen in the fine search. The size of the dots shows the relative performance of the fine search results.

independent test error is used as a measure of the goodness of fit and serves as an indicator for how well the SVR generalises.

3.2.3 Random Forest Regression Implementation

While RFR is said to be robust to overfitting (Breiman, 2001), there is still a risk that the model may not generalise well beyond the training dataset if that model is not tuned correctly (Hastie et al., 2008). Tuning the hyper-parameters with RFR follows a different procedure than with SVR as the method offers validation data in the form of the out-of-bag-error (OOB – see the theoretical details in Section 2.4.5). This makes hyper-parameter selection for RFR much more efficient than SVR.

An independent testing dataset is still set apart from a training dataset at a 75% : 25% ratio respectively $(x_r, y_r) : (x_t, y_t)$ (as done for the SVR). The training dataset is then used to estimate three hyper-parameters: number of trees in the forest (t), number of observations at each terminal node (l), and the number of features to be passed to a node when splitting the data (m).

An iterative approach is used to determine t, m and l for which the results are shown in Figure 3.5. As a rule of thumb, RFR is more robust the larger the forest (t). The number of trees

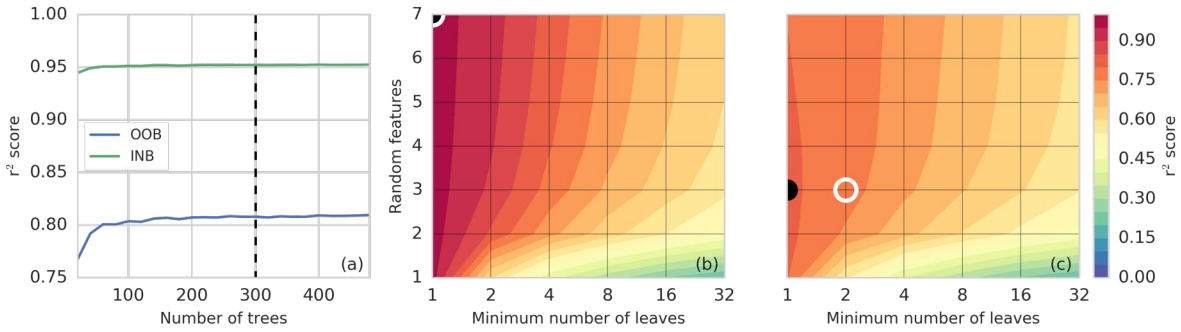

Figure 3.5: The selection of the correct (a) number of trees in the high resolution RFR, (b) number of random features passed to each node (m), and (c) the number of leaves/observations allowed at each terminal node (l). The out of bag errors (OOB) are shown by the blue line and the in bag errors (INB) are shown by the green line. Note that l was manually adjusted to 2 leaves per branch to ovoid overfitting to sparse dataset of the Southern Ocean.

was manually set to 300 based on the results in Figure 3.5a where it is shown that too few trees result in overfitting and high variance. This means that the remaining optimisation problem is 2D rather than 3D – the results of this problem are shown in Figure 3.5a,b. The number of leaves (observations) per terminal branch (l) was estimated at 1 for the SOCAT dataset. However, it is known that the SOCAT dataset is sparse in the Southern Ocean, particularly in winter (Rödenbeck et al., 2015). A more generalised model (more than the data would suggest) is less likely to over-fit to the observations. This is achieved by increasing l to 2 as shown by the white circle in Figure 3.5.

3.3 Results

3.3.1 Performance of empirical methods

Table 3.1 shows the performance metrics of each of the methods used in this study. Both the mapping (that is the method RMSE) and total errors are represented in this table, where the total error is defined by Landschützer et al. (2014) as:

$$\sigma(pCO_2)^2 = \sigma(\text{meas})^2 + \sigma(\text{grid})^2 + \sigma(\text{map})^2 \tag{3.4}$$

A fixed measurement error of 5 μatm is assumed as this is the limit for acceptable errors in the SOCAT database (Bakker et al., 2016). The mapping RMSE are those given by the mapping methods as shown in the SO column in Table 3.1 (SVR, RFR, SOM-FFN). The gridding error is

Table 3.1: A summary of the performances of the various models run with high (HR) and low (LR) resolutions. pCO_2 RMSE is defined for the Southern Ocean and then all biomes as defined by Fay and McKinley (2014). Note that estimates within 150 km of continental landmasses were excluded. The best results for each column are shown in bold. The training time shows the duration of training the method once the correct hyper parameters have been found. Note that the wall times are for 24 cores. The bottom half of the table shows the gridding errors (mean standard deviation of grid cells) for the Southern Ocean (south of 30°S) and each respective biome. Total error estimates are calculated as shown in Equation (3.4) where we assume a sampling error of 5 μatm (Pfeil et al., 2013) and gridding errors for the relevant resolution are used.

Methods	r^2	Bias	Root mean squared error (μatm)				Total	Wall time
		μatm	SO	SAZ	PFZ	MIZ	μatm	secs
RFR-HR	**0.82**	0.41	**11.14**	10.93	**10.11**	**15.13**	**12.61**	468
SVR-HR	0.71	0.70	13.80	12.05	12.62	20.96	15.01	1992
RFR-LR	0.78	**0.24**	11.48	9.92	10.45	17.50	14.10	38.4
SVR-LR	0.70	0.60	13.41	11.22	12.06	21.27	15.71	158.4
SOM-FFN	0.77	2.28	11.65	**9.52**	10.66	17.47	14.24	-
Gridding error HR			3.16	2.82	2.59	4.67		
Gridding error LR			6.48	6.25	4.94	9.46		

defined as the average of the standard deviation of observations (for SOCAT data) in a grid cell during the gridding process. These are calculated for the SOCAT v3 data and show that the high resolution gridding error is less than half than that of the low resolution error (Table 3.1). This is an intrinsic benefit of using high resolution data when calculating the total errors as demonstrated by the RFR-HR, which outperforms the SOM-FFN by a large margin when considering the total score (with estimates of 12.61 and 14.24 μatm respectively).

Looking now in more detail at the mapping errors, RFR performs better than the SVR and SOM-FFN methods, with the HR implementation achieving lower root mean squared errors (RMSE) than the LR implementation (with the exception of the SAZ). Conversely, SVR errors do not improve under a HR implementation (with the exception of the MIZ). A slightly lower r^2 score combined with larger RMSEs indicates that the HR data is more variable as expected. We postulate that the RFR-HR performs better than the RFR-LR due to reduced aliasing in the gridding process, in other words the matching between pCO_2 and proxy variables improves. Support vector regression is not able to achieve such a reduction in error as the method is less non-linear than RFR.

The SOM-FFN bias is larger than those of the SVR and RFR approaches. This is likely due to the regional domain used in this study compared to the global domain of the SOM-FFN.

Figure 3.6 shows the regional and annual breakdown of bias and RMSE for all open water

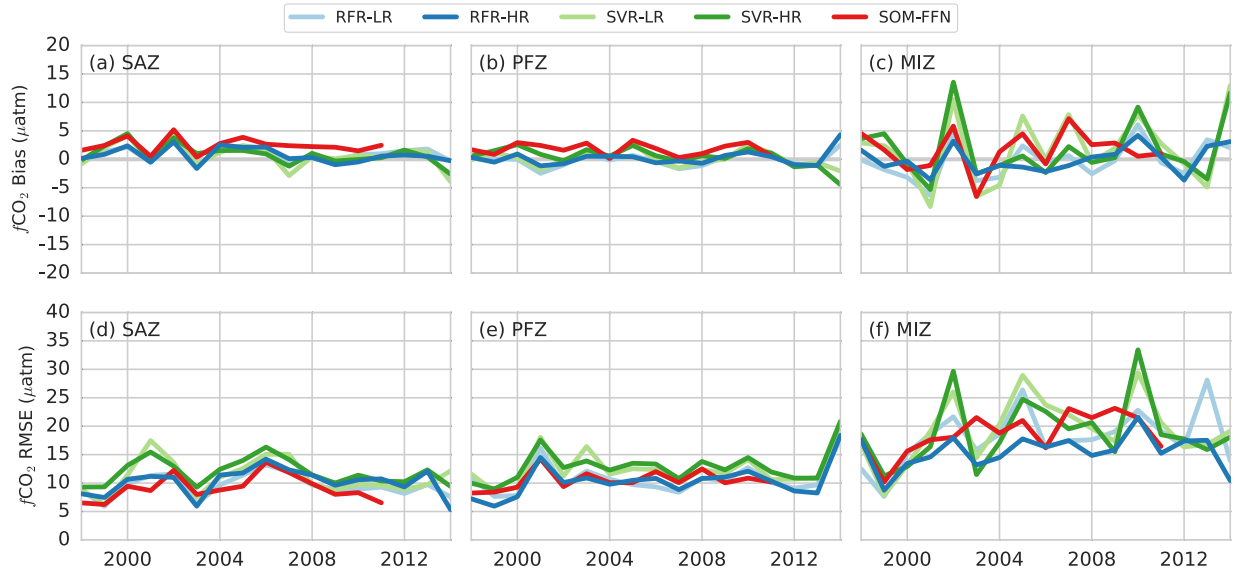

Figure 3.6: (a–c) Bias of each of the Southern Ocean biomes as defined by Fay et al. (2014) – (a) Sub-Antarctic Zone, (b) Polar Frontal Zone and (c) Marginal Ice Zone as shown by the key. Similarly (d-f) show the root mean squared error (RMSE) for each of the methods with the biomes being the same. As in Table 3.1, estimates within 150 km of continental landmasses were excluded.

estimates of pCO_2 (excluding values within 150 km of the coast). It was found that including or excluding high variability coastal waters results in improvements of SVR and RFR RMSE, but does not have as large an impact on the SOM-FFN scores. This is due to an increase in the number of high variability coastal observations, particularly the Argentine Sea, in SOCAT v3 compared to SOCAT v2 as shown in Figure 3.A.2.

The overall lower RMSE scores in the PFZ are likely due to a greater proportion of open ocean to coastal regions. Here island wake regions (South Georgia, Kerguelen Plateau) have large errors compared to open ocean regions due to larger variability driven by increased net primary production (Graham et al., 2015). However, the potential effect of these errors on the total fluxes may be minimal as these areas represent a small fraction of the area of the Southern Ocean. Once again RFR was the best performer in the PFZ with the SVR again being the weakest of the methods. The last year in the time-series (2014) shows a sharp increase in the RMSE (Figure 3.6e), likely due to the fact that SOCAT v3 observations end in March 2014. With summer being a high variability period, an increase in the uncertainty is expected with limited observations.

The MIZ is by far the largest contributor to error for all methods, with RFR (HR and LR) best capturing the high variability of the seasonally covered ice regions (as shown in Figure 3.6f and

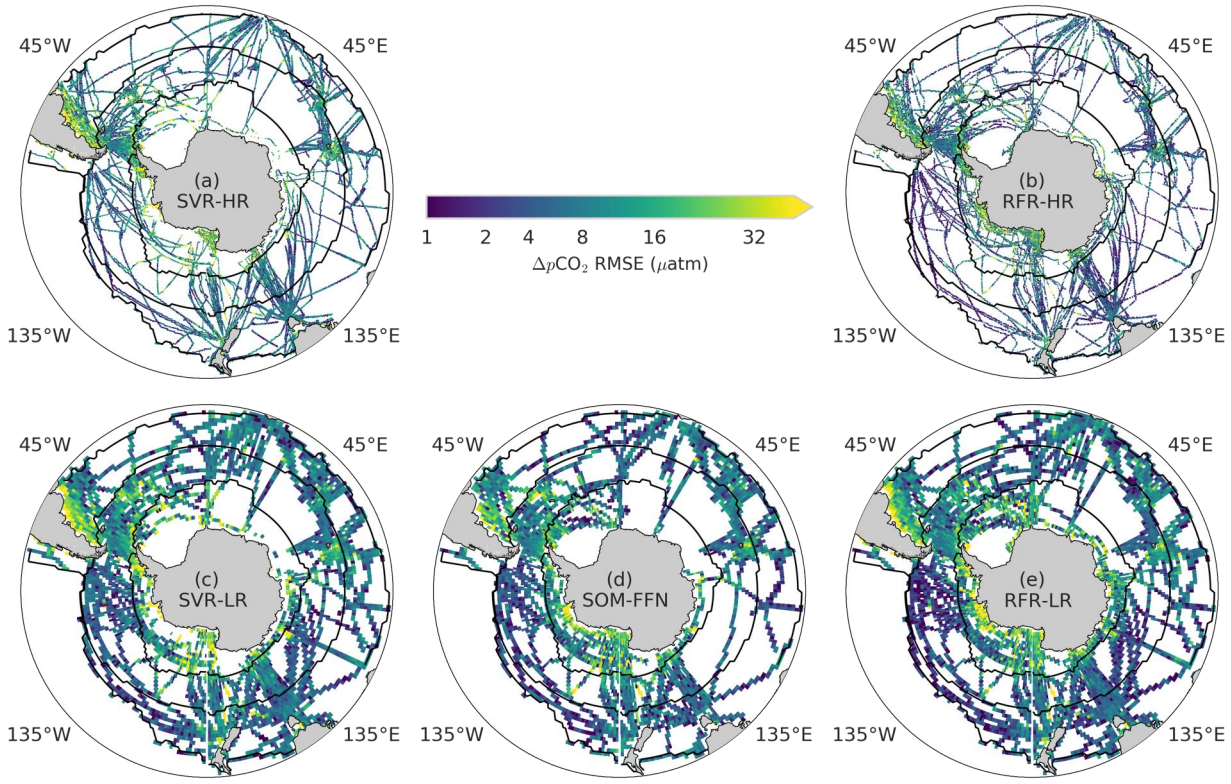

Figure 3.7: Root mean squared error (RMSE) averaged over time for each of the five approaches. Note that the colour bar is not scaled linearly. The black lines show the three Southern Ocean biomes as defined by Fay and McKinley (2014). The SOM-FFN RMSE (d) is trained using SOCAT version 2 while the other approaches were trained with version 3.

Figure 3.7). Larger errors in the MIZ relative to SAZ and PFZ may be due to a combination of two factors: 1) the variability of pCO_2 is largest in this region with short spatial (and temporal) decorrelation length-scales; 2) the available proxies do not adequately represent the processes that result in pCO_2 changes.

3.3.2 Trend differences driven by methodology

As a first comparison the distributions of estimates by each of the approaches serves as a useful indicator for the strengths or weaknesses of each method. The distributions of the estimates for all methods are weakly bimodal with a strong mode at 0 μatm and a weaker mode at $\sim -40\mu$atm. Given the similarity between the distributions, it may difficult to identify differences between methods, but note that the SOCAT v3 distribution in each of the sub-plots is the same, thus serves as a useful comparative metric. There is a large difference between the approaches

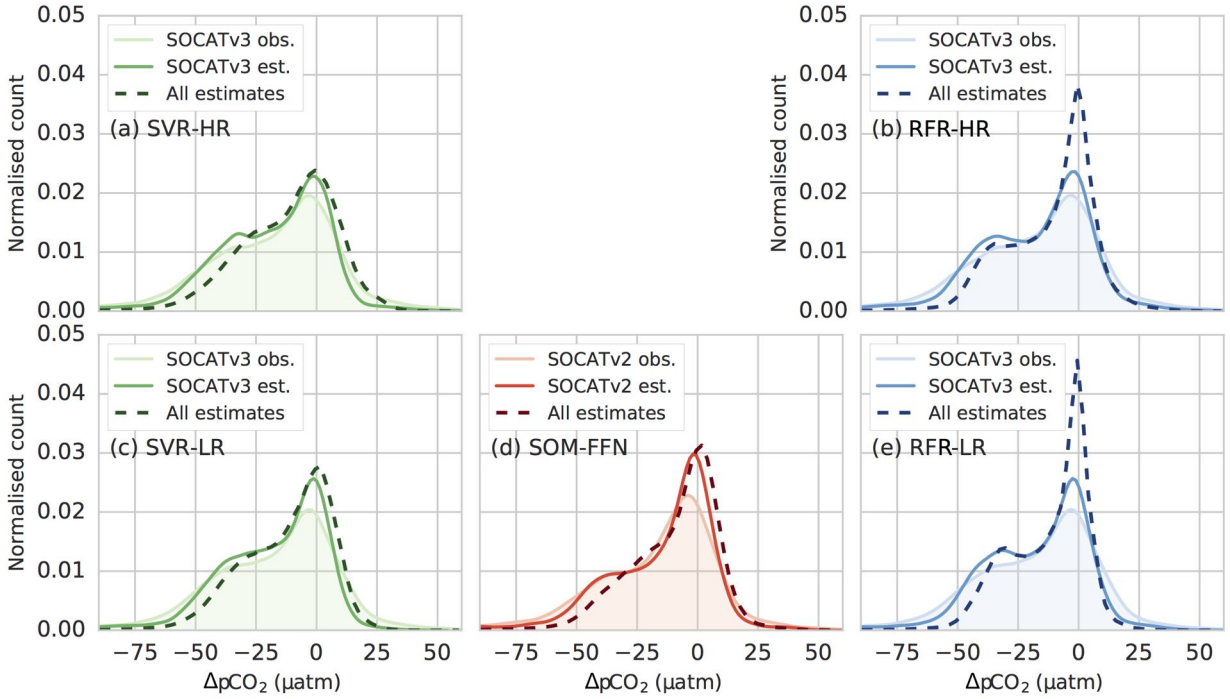

Figure 3.8: Histograms show the distributions of SOCAT (shaded), the distribution of estimated of SOCAT (solid unshaded line), and the distribution of predictions for the entire gridded field or domain (dashed dark line). Here (a) is for the SVR-HR, (b) for RFR-HR, (c) for SVR-LR and (d) is for the SOM-FFN by Landschützer et al. (2014) and (e) for RFR-LR. Note that this data includes only the Southern Ocean biomes as defined by Fay et al. (2014).

around the 0 μatm mode where the RFR has the most pronounced peak. This may be due to the narrower distributions of the RFR approaches, particularly evident in the upper quartile of the distributions. This could translate to weaker outgassing in winter for the RFR relative to the SVR and SOM-FFN methods. The weaker mode (~ -40 μatm) is again most pronounced for RFR (for both test estimates and predictions). The SVR-HR estimates have a much wider distribution (Figure 3.8a dashed line > 0 μatm) compared to the other methods – stronger outgassing could thus be expected relative to the other methods. High resolution estimates capture more seasonal variability, with the distributions being marginally wider than the respective low resolution models especially in the upper quartile of the distributions. Though, the impacts of resolution on the distribution are in general than the impact of the empirical method. The differences in the distributions highlighted above are good precursors for the relative biases that each method may present as the time-series and spatial distributions of pCO_2 are considered.

A regional time-series comparison of ΔpCO_2 is shown in Figure 3.9 and the mean seasonal estimates shows the spatial distribution in Figures 3.10 and 3.11. In general there is good agreement

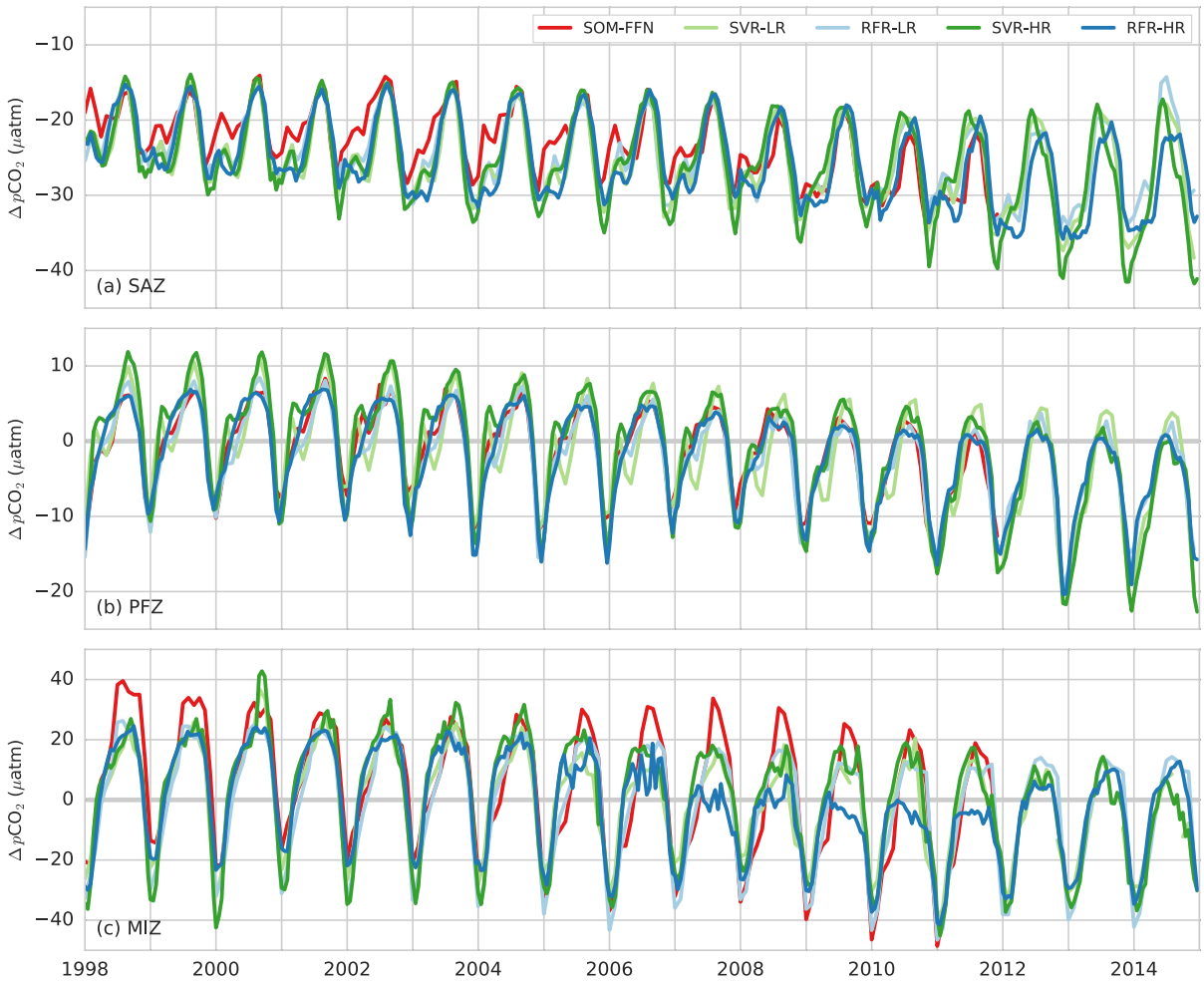

Figure 3.9: The average ΔpCO_2 for each method in each biome: (a) Sub-Antarctic Zone; (b) Polar Frontal Zone; (c) Marginal Ice Zone. The colours show the different method as indicated by the key in (a), with the lighter shades representing the low resolution estimates. Note that ice-covered regions are masked in the calculation of the mean.

between the overall interannual trends, seasonal variability particularly in the PFZ (Figure 3.9b) where interannual variability is large. Similarly the spatial distribution of summer estimates are coherent (Figure 3.11), where the SAZ is a sink with strong uptake in the Malvinas Confluence, Agulhas Retroflection and Tasman Sea. Similarly in the PFZ, the Atlantic is a CO_2 sink during summer, while the rest of the PFZ is a weak sink or source. In winter (Figure 3.10) the SAZ is a weak sink (< -10 μatm), while the PFZ becomes a source of CO_2 (between 5 and 15 μatm).

While there is agreement between methods, differences are also present. The aim here is to explain the methodological reasons for these differences rather than explain the interannual and seasonal trends of the estimates. The wider distribution of the SVR-HR estimates (in Figure 3.8a)

is reflected by the larger comparative seasonal amplitudes (Figure 3.9). It is also apparent that the RFR is the more conservative of the three approaches, with a weaker seasonal amplitude in both the SAZ and PFZ. Though there are periods during summer in the PFZ where RFR-HR estimates are the lowest. Less obvious in the time-series and maps of ΔpCO_2 is the influence of empirical method vs. high and low resolution. These differences appear to be seasonal, periodic and specific to a biome.

The most apparent methodological difference between estimates occurs from 1998 to 2008 in the SAZ during summer, when the SOM-FFN is a weaker sink relative to other methods. A potential cause for this difference could be that the SVR and RFR approaches are implemented with SOCAT v3 data while the SOM-FFN was trained SOCAT v2 data. To investigate this consideration, SVR-LR and RFR-LR were implemented with both SOCAT v2 and v3 data. The results show that the relatively overestimated summer SOM-FFN could not be driven by differences in the dataset as the empirical model plays a more important role than the dataset (Figure 3.A.5). The mean summer maps of ΔpCO_2 for the SOM-FFN (Figure 3.11b) show that the central Atlantic sector (10°W – 20°E) of the SAZ is a weaker sink of CO_2 compared to the RFR and SVR. This could be due to the fact that the SOM-FFN was trained with a global dataset rather than a regional dataset limited to the Southern Ocean, where the latter applied to SVR and RFR. The SOM-FFN could thus be influenced by measurements of CO_2 from any other region that has the same classification (or cluster). An increase in the number of samples in the region from 2008 onward (Figure 3.A.4) suggests that this may be the reason for the converging estimates.

From 2011 through 2014 the method and resolution driven differences are exacerbated between SVR and RFR (there is no SOM-FFN data beyond 2011). The SVR and RFR-LR estimates become more seasonally extreme while RFR-HR maintains a constant seasonality. This is likely due to the relative decrease in sampling effort in the Atlantic sector of the SAZ as shown in Figure 3.A.3. The apparent sampling effort remains high due to continued sampling in the Tasman Sea. This demonstrates the sensitivity of the SVR to a decrease in sampling effort – likely due to the inclusion of coordinate proxies. In this case, samples measured in the Tasman Sea could be used to estimate ΔpCO_2 in the Argentine Sea if proxies are similar.

Methodological differences in the PFZ are also strongest from 1998 to 2008, but occur in winter rather than in summer. This is strongly indicative that the paucity of data may be a driver

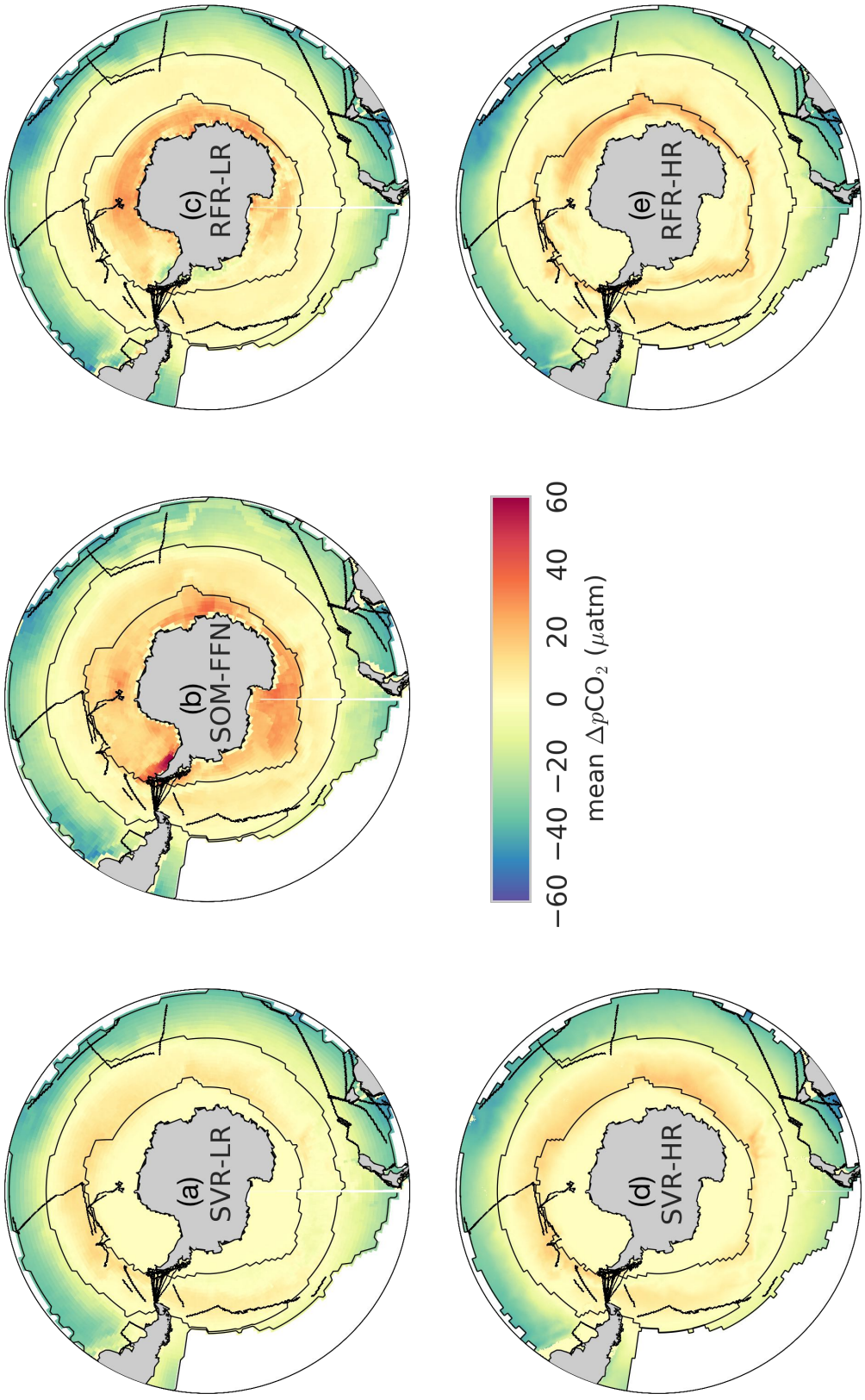

Figure 3.10: The temporal average pCO_2 for each method for winter (JJA). The method associated with each sub-plot are indicated on the figure. The black markers represent pCO_2 measurements in the entire SOCAT v3 database. The thin black lines show the boundaries of the three biomes in the Southern Ocean as defined by Fay et al. (2014). Note that ice cover was not taken into account.

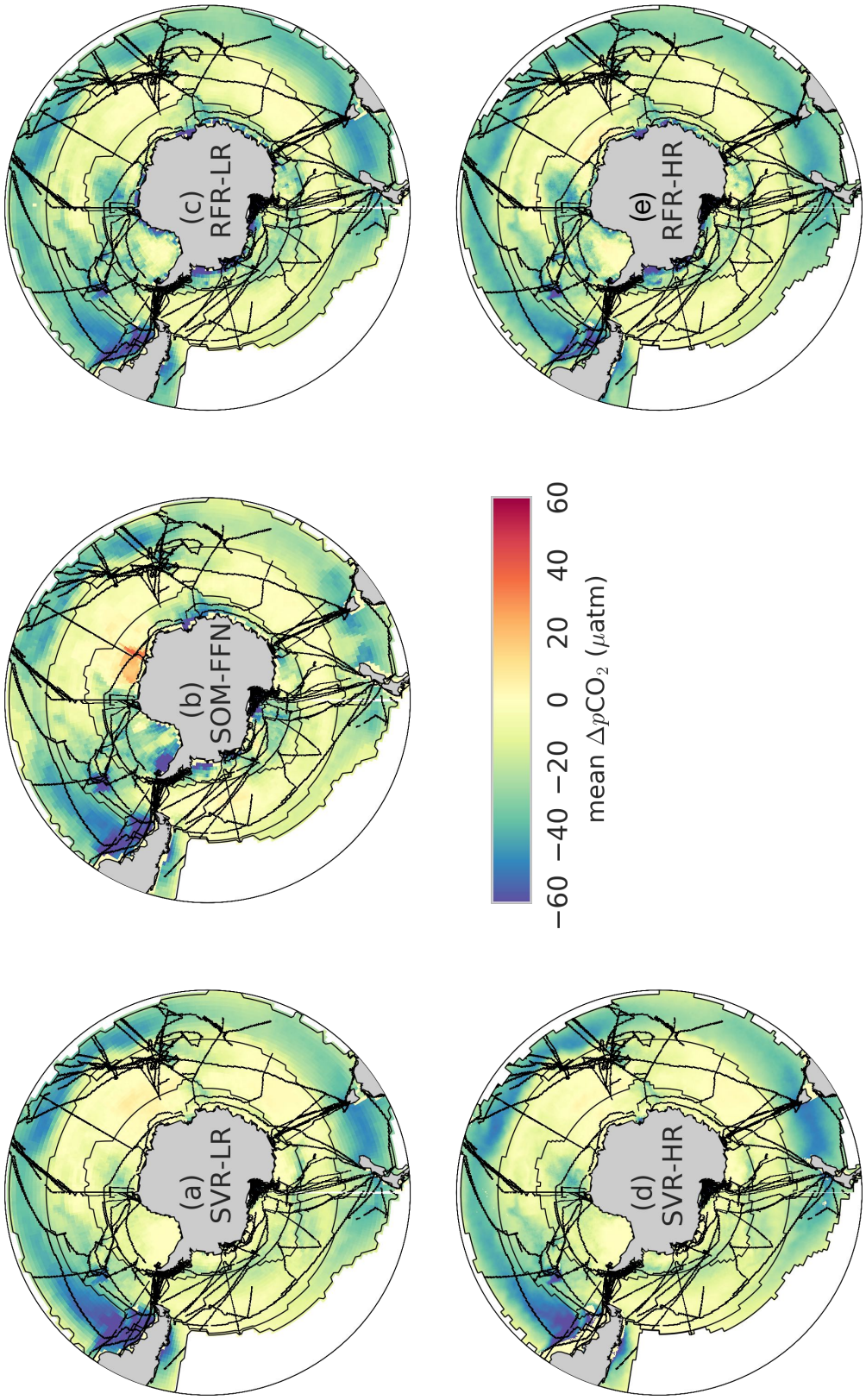

Figure 3.11: The temporal average pCO_2 for each method for summer (DJF). The method associated with each sub-plot are indicated on the figure. The black markers represent pCO_2 measurements in the entire SOCAT v3 database. The thin black lines show the boundaries of the three biomes in the Southern Ocean as defined by Fay et al. (2014). Note that ice cover was not taken into account.

of the observed differences, more specifically that each method deals with sparse data differently. The wider distributions of SVR ΔpCO_2 estimates (Figure 3.8) is apparent in the higher winter ΔpCO_2 estimates. This alludes to the fact that SVRs are sensitive to outliers (Zhang and Wang, 2008). The SVRs may treat winter data as outliers due to the sparse, but large positive ΔpCO_2 compared to the more frequently sampled large negative summer ΔpCO_2. Conversely the lower RFR estimates highlight the method's robustness to outliers (Louppe, 2014). It may be that the RFRs conservative estimates are less correct than the SVRs larger estimates, but the lack of data makes this difficult to test.

A sawtooth pattern in PFZ autumn estimates is another example of methodological differences between methods. Once again the effects manifest strongest in the SVR approaches. But resolution also plays an important role here where the RFR-LR estimates show a stronger sawtooth pattern than the RFR-HR. In fact, this occurs relatively often, where RFR-LR is more akin to the SVR approaches than RFR-HR, as shown in the SAZ in late summer from 2002 to 2008.

Estimates of pCO_2 in the MIZ (Figure 3.9c) are the least coherent of the three regions. RFR-HR pCO_2 estimates are lower in winter between 2006 and 2011, while the SOM-FFN estimates are larger for the same period. However, the impact of these large pCO_2 differences are not very big due to the small surface area of the region that is not covered by ice during winter. In the case of pCO_2 in the MIZ, estimates should be treated sceptically due to large uncertainties, lack of data (particularly in winter) and large differences between methods.

3.3.3 Modes of variability

In Figure 3.12a-c the seasonal cycle reproducibility (SCR) of ΔpCO_2 is shown. This metric is calculated by correlating the seasonal climatology with the estimated ΔpCO_2 minus the annual averages (trend). Removing the annual averages means that the metric is concerned purely with the seasonal cycle. The complication in the Southern Ocean is that we do not know how strong the seasonal cycle (or different modes of variability) should be, but we can make a few important insights with these figures. The SOM-FFN has the weakest SCR, which may be a result of, in part, the non-linearity created by the clustering step of the method. Conversely, SVR-HR has the strongest SCR, likely due to the inclusion of spatial and temporal features (cos(time), sin(time) and N-vectors) in training and predicting leading to a "memory effect". In other words,

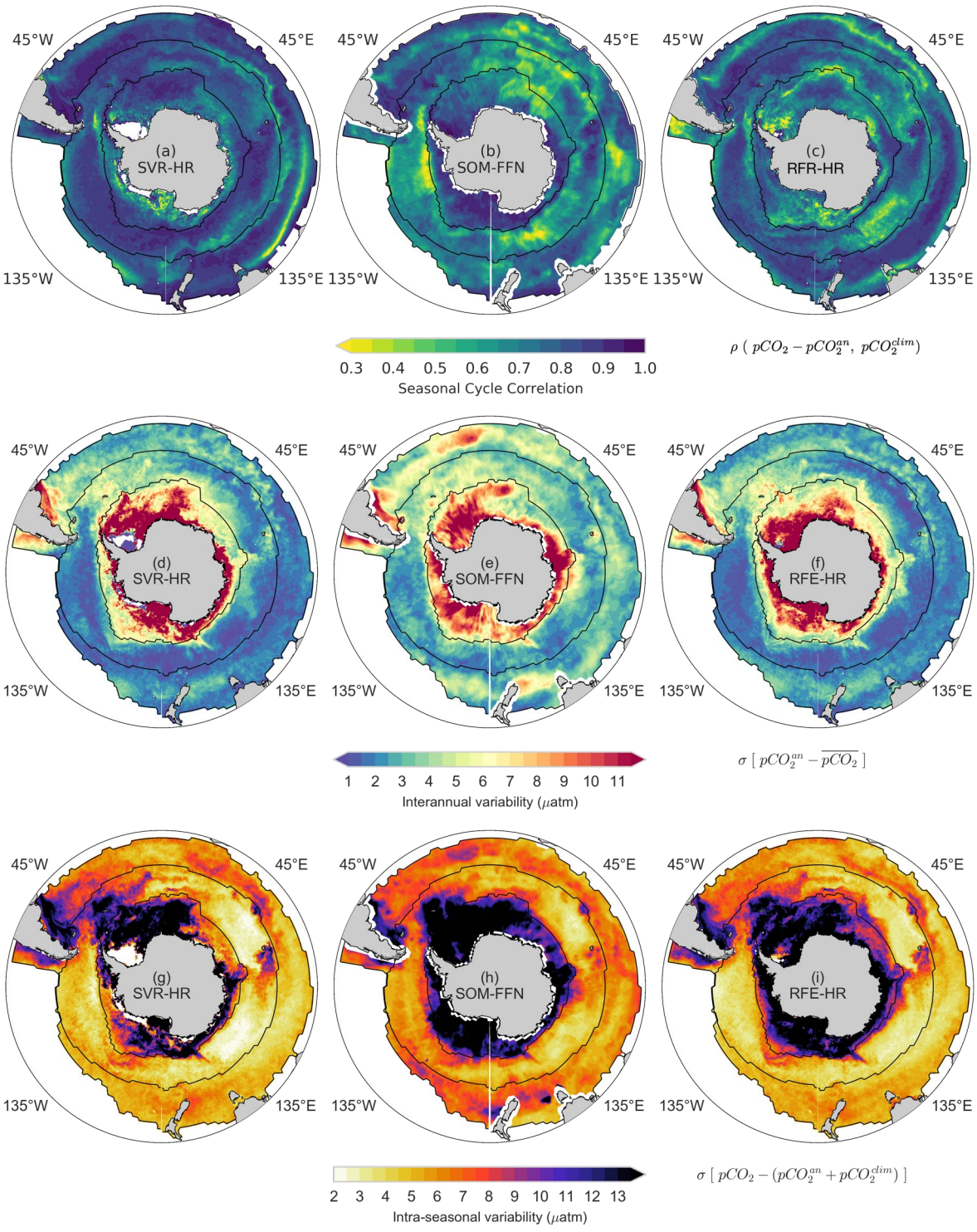

Figure 3.12: Seasonal cycle reproducibility (SCR) of estimated ΔpCO_2 for the (a) SVR-HR,(b) SOM-FFN and (c) RFR-HR models. The methodology used is the same as that presented in Thomalla et al. (2011) where a correlation of the climatology and observed data is taken (with the equations shown to the right of the colour bar). Figures (d–f) show the interannual variability of ΔpCO_2, which is calculated by taking the standard deviation of the mean ΔpCO_2 subtracted from the annual averages. Figures (g–i) show the intra-seasonal variability of ΔpCO_2, which is calculated by taking the standard deviation of estimates after annual averages and climatology have been removed.

the SVR-HR associates a time of year and location with a measurement of ΔpCO_2, which, if the data is sparse in time, would be projected forward to the following year. The absence of spatial and temporal features in RFR may be the reason for the slightly larger reproducibility compared to the SVR-HR, while lack of clustering results in lower seasonal cycle reproducibility than the SOM-FFN.

The interannual variability (Figure 3.12d-f) is calculating by subtracting the mean ΔpCO_2 from the annual averages of ΔpCO_2. Using the annual averages removes the variability that the seasonal cycle contributes to ΔpCO_2. There is a similarity in the spatial distribution of interannual variability between methods, but the magnitude of the SOM-FFN's interannual variability is larger than for the SVR-HR and RFR-HR. In general, the MIZ has the largest interannual variability, with the Atlantic being the basin with the variability ΔpCO_2. The Indian and Pacific sector of the SAZ have low interannual variability. There are two regions in the SAZ where the magnitude of the SOM-FFN differs significantly from the other two methods: ~ 20°W – 5°E in the Atlantic and the Tasman Sea. The first of these is coincides with the region responsible for the divergence of the SOM-FFN and the other two methods in ΔpCO_2 from 1998 – 2008 in the SAZ as shown in Figures 3.A.4 and 3.9.

The intra-seasonal variability of the estimates (Figure 3.12g-i) is calculated by taking the standard deviation of the observations minus the seasonal climatology and annual mean of the estimates. Subtracting the annual mean and climatology from the estimates can be likened to applying a high pass filter. It could be expected that the regions of low SCR would correlate with the regions of high intra-seasonal variability, but this is not the case when comparing the figures. This is because SCR is a dimensionless metric, while the intra-seasonal variability is scaled by the magnitude of the variability. Thus regions with low SCR, such as the east Indian sector of the PFZ, can also have low intra-seasonal variability. This also explains why regions with high intra-seasonal variability, such as the MIZ, have high SCR, where high magnitude variability is superimposed over a strong seasonal amplitude. Importantly, regions of high dynamic variability correspond with the distribution of intra-seasonal variability in the SVR-HR and RFR-HR (Meredith and Hogg, 2006; Frenger et al., 2015; Hogg et al., 2015). However, it should also be noted that these maps could partially represent estimated noise (errors), supported by the fact that the spatial distribution of intra-seasonal variability resembles the RMSE (Figure 3.7).

3.4 Discussion

3.4.1 Strengths, weaknesses and impacts of methods

One of the key hypotheses for this chapter is that using data gridded at a higher resolution would reduce the total error by improving both the gridding and mapping errors. The total error of empirically estimated pCO_2 is defined Equation (3.4). The implications of reducing the gridding and mapping errors (measurement error is fixed at 5 μatm by SOCAT data quality) are discussed in this section.

The reduction of gridding error is straight forward: reducing the size of the grid cell (higher resolution) decreases the standard deviation of the measurements in that cell if the spatial correlation length scale is short. The effect of this is clear in Table 3.1 where the gridding error is reduced by nearly half when gridding to a higher resolution. Note, that in this case, the reduction of gridding error is influenced primarily on the spatial scale as there are very few repeat sub-monthly measurements in the dataset. This would suggest that the impact of gridding to a higher temporal resolution may have a larger impact than is shown by the data.

The proposed reason for a reduction of the mapping error is more nuanced and the hypothesis is as follows: the use of high resolution gridding preserves the time and space information of pCO_2 and the proxy variables more than low resolution gridding. This is especially true for variables with high temporal variability — *e.g.* chlorophyll (Thomalla et al., 2011). For example, Bakker et al. (2008) found that seasonally ice covered regions (specifically the Weddell Gyre region) undergo a rapid transition from being an ice covered source of CO_2 in winter (with the ice damping fluxes) to a strong biologically driven sink in summer. Using monthly gridded chlorophyll would average out sub-seasonal variability or lead to a bias in pCO_2 estimates. This point was also made by Chierici et al. (2012), who found that Chl-*a* even at 8-day × 9 km was not able to "resolve the localized areas of high Chl-*a* associated with fronts and the ice edge". This may also be true for dynamic regions in the SAZ, where Monteiro et al. (2015) showed that high frequency intra-annual variability may, in some cases, lead to sampling biases. This creates a compelling arguement for high resolution gridding, but Table 3.1 shows that only RFR achieved a lower mapping error, while the mapping error for SVR increased.

The non-linearity of RFR allows the method to capture the additional variability of high

resolution data, otherwise lost in the gridding process. The high degree of non-linearity stems from the discrete decision boundaries associated with the nodes of decision trees, the building blocks of RFR. Such non-linearity could result in overfitting to the training dataset, but this is avoided by using a large number of trees in a random forest, which, combined with bagging, results in good generalisation (Louppe, 2014). In contrast to RFR, the non-linearity of SVR is limited by the selection of a constant width of a Gaussian kernel for the entire domain, thus applying the assumption of constant variability to the domain (both temporally and spatially). This can be overcome by clustering regions of similar variability, as was done in the two-step SOM-FFN approach by Landschützer et al. (2014). In fact the similarity between feed forward neural networks (FFN) and SVR (Vapnik, 1999), could lead to similar results if a clustering technique was applied to the latter. However, this introduces the additional complexity of dealing with discontinuities in pCO_2 estimates. The effect of the discontinuities caused by clustering is apparent in the seasonal cycle reproducibility of the SOM-FFN method (Figure 3.12b), where seasonal reproducibility occurs in relatively discrete patches compared to the other two methods.

The non-linearity of RFR also allows the method to perform well without the addition of coordinate features (N-vectors and time transformations), which the SVR required to perform well. The inclusion of these coordinates in the RFR implementation narrows the distribution of the estimated pCO_2 with the training subset becoming more sparse with additional dimensions (Figure 3.A.6). This may be a negative realisation of the often cited robustness of RFs to outliers (Hastie et al., 2008; Louppe, 2014), where in this case, the sparse winter observations are treated as outliers by the algorithm when N-vectors are included and dimensionality increased. Conversely, SVR is sensitive to "outliers" (winter data), which may explain why the method performs better when coordinate features are included. The respective robustness and sensitivity of RFR and SVR to outliers is seen in Figure 3.9b and Figure 3.10 by the relatively low RFR estimates of winter pCO_2 and conversely high estimates for SVR for the same period. Summer estimates do not suffer from this effect as data are not sparse at this time of year.

3.4.2 High resolution hurdles

The argument for using high resolution gridded data in the empirical estimation of pCO_2 is significant when the reduction of the in-sample error of RFR-HR is considered. However, the

majority of studies in the literature use low resolution data (monthly × 1° or coarser) as shown in Table 1.1. This choice to use low resolution over high resolution gridded data may be driven by several reasons: 1) using low resolution data is computationally inexpensive, while higher resolution data increases computational demand; 2) some methods do not scale well as the amount of data is increased; 3) using higher resolution data may lead to a loss of training data (*i.e.* Chl-*a*) in cloudy regions, such as the Southern Ocean. These points will be expounded below.

The increase in the number of training points from a low to high resolution is more than fourfold (with LR there are 19 563 points, while with HR there are 88 368 points) and the increase in the number of gridded proxy variables more than 30 times (with LR there are $12 \times 50 \times 360$ proxy variables while for HR this becomes $23 \times 200 \times 440$). This demands an increase in the computational power, memory usage and storage capacity. This is especially true when implementing cross-validation, which uses an iterative approach to find the optimal hyper-parameters. Cross validation can be sped up significantly by running the process in parallel (easily done with the Scikit-Learn package in Python).

Of the two methods tested in this study, the SVR is less scalable. Pedregosa et al. (2011) recommends that training datasets should be less than 100 000 points for a Gaussian kernel SVR to be feasible. The HR dataset for the Southern Ocean is at the limit that SVR can handle, particularly if strict constraints are set in grid search cross-validation. Using a larger domain may require a clustered or subset approach to make SVR feasible. Alternate implementations of SVR, such as LASVM and Core Vector Regression could be explored as more efficient alternatives in future work.

Random forest regression scales better and benefits from parallel computing and increased memory (via Scikit-Learn). As mentioned in Section 2.4.5, the method becomes more robust when the number of trees in the forest is large (> 100). With a large dataset, each of the trees has to be stored in memory, potentially using a large amount of memory (when the number of trees in the forest is > 100). However, the method is quicker to train and validate than SVR with less than a quarter of the training time required.

Lastly, increasing the resolution results in fewer matches between pCO_2 and observed Chl-*a* due to relatively persistent cloud cover in the Southern Ocean. The sampling period for the empirical modelling is thus a balanced compromise between data loss and aliasing. Using a

simulation experiment, Friedrich and Oschlies (2009b) found that missing Chl-*a* (due to cloud cover) in the North Atlantic reduced the accuracy of neural network estimate of pCO_2 from 19.0 μatm to 21.1 μatm. It is then not surprising that Chl-*a* was found to be the most important variable in the RFR-HR analysis[1] as shown in Figure 3.13. However, these importances would be heavily weighted toward summer observations, when Chl-*a* is high and does in fact play an important role, while the role of MLD or salinity, which are important proxies in winter, may be under represented by Figure 3.13. A potential solution to the problem of missing Chl-*a* is to fill the gaps with assimilated model Chl-*a*, as done by Chierici et al. (2012) who aimed to estimate pCO_2 in the Pacific sector of the Southern Ocean with an MLR. This solution is similar to use of ECCO2 MLD and SSS in this study.

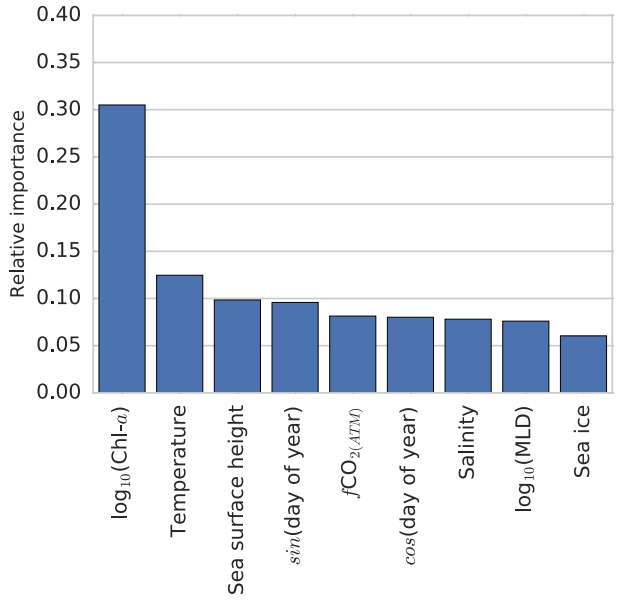

Figure 3.13: The relative importance of variables as determined by the RFR-HR. The sum of the relative importance of all the variables is equal to one. The relative importances are calculated by the *Scikit-learn* implementation of RFR.

3.4.3 Should we use high resolution?

The difference between the high and low resolution estimates of pCO_2 are marked, though the effect varies according to method, regions and period. In the PFZ, for instance (Figure 3.9), the

[1] Some Random Forest software packages, such as *Scikit-learn*, produce an estimate of relative importance of the input features by passing random features to each node.

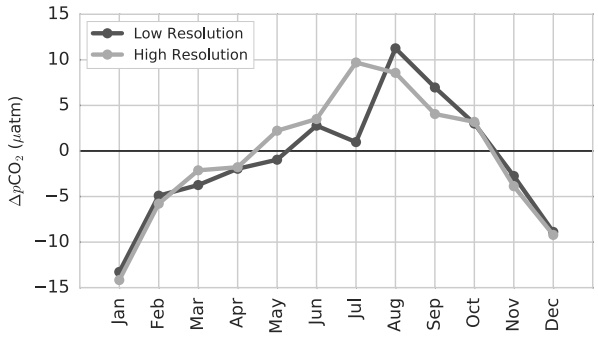

Figure 3.14: The monthly climatologies of high and low resolution in the PFZ compared.

more pronounced sawtooth pattern results in a shift of the mean seasonal peak as shown in Figure 3.14, with the maximum occurring later in the season for the low resolution. However, the difference between estimates by various methods (of the same resolution) is larger than the difference between HR and LR estimates of the same method. This makes the case for multiple approaches stronger than the need for high resolution, but we should not overlook the gains in high resolution estimates. High resolution estimates are more likely to capture mesoscale variability (10 – 100 km) of pCO_2 in the Southern Ocean. This is particularly important given that the southerly shift of the westerlies could increase EKE with implications for air-sea CO_2 fluxes (Dufour et al., 2013; Hogg et al., 2015). A measure of this is perhaps shown by the intra-seasonal variability, where RFR-HR and SVR-HR show larger "noise" in regions associated with high dynamism and chlorophyll (Thomalla et al., 2011). Higher temporal resolution would also increase the likelihood of observing changes to seasonal shifts of pCO_2. These shifts may act as early indicators of change in driving mechanisms (van der Laan et al., 2016).

Methods that scale well or implementations that reduce the computational load need be considered when setting up an implementation with HR gridded data. For example, in this study we showed that SVR is only just able to estimate pCO_2 for the Southern Ocean biome. However, there are alternative methods, such as Core Vector Regression (Tsang et al., 2005) and Approximate Extreme Points Support Vector Machine (Nandan et al., 2014), that are optimised for larger datasets. Alternatives to RFR, that are more likely to weight sparse winter observations strongly, should be explored (including extra trees regression and boosted trees).

3.5 Conclusions

In this chapter we attempt to reduce the uncertainties of satellite estimated pCO_2 by investigating the feasibility of new mapping methods and by improving the input data with higher resolution datasets. Two key questions based on this aim: 1) Can SVR and RFR methods improve on the uncertainty estimates of SOM-FFN by Landschützer et al. (2014)? 2) Does increasing the resolution of gridded and SOCAT data from 1° × monthly (low resolution) to 0.25° × 16-day (high resolution) improve uncertainties and estimates?

Findings show that SVR and RFR approaches perform adequately. Random Forest Regression is able to improve on in-sample uncertainties (RMSE scores) compared to SOM-FFN, where SVR is not able to do so. However, closer inspection of the estimated values suggests that RFR may be "overfitting" to the data. This may be a negative realisation of the method's robustness against outliers results in the treatment of sparse winter data as outliers, with the effect of underestimated winter pCO_2 – though this effect is not severe enough to discard the method. Conversely the SVR may be overestimating winter maxima (characterised by larger outgassing) due to sensitivity to outliers – again, the effect is not severe enough to abandon the method. This these results show that there are methodological differences between approaches, but these differences are small relative to the amplitude of the seasonal cycle and the dominant interannual ΔpCO_2 trends. This makes a compelling case for the use an ensemble approach to investigate trends of ΔpCO_2, as done in Chapter 4. Moreover, the relative under- and overestimation of winter ΔpCO_2 by RFR and SVR respectively presents a good example of how an ensemble approach acts to even out methodological biases.

The use of high resolution data does improve the in-sample uncertainties, but only for the RFR. Conversely, increased data resolution resulted in larger SVR in-sample errors. The RFR's ability to improve these error estimates is attributed to a higher degree of non-linearity than SVR. The SVR's decreased performance with higher resolution is an assumption of constant variability throughout the domain, suggesting that clustering regions of similar variability (as done in Landschützer et al. 2015), would improve in-sample uncertainties of the SVR.

While the results from this chapter show that estimates can improve on in-sample scores, it is important to note that the paucity of data in the Southern Ocean means that it is not possible to

know the methods' out-of-sample/independent scores (Rödenbeck et al., 2015). This emphasises the importance of improving coverage of pCO_2 measurements in the Southern Ocean.

3.A Additional figures

The distribution of the proxy variables used throughout Chapter 3 is shown in Figure 3.A.1. The distributions of the untransformed data are used to inform the preparation of the data, in other words, variables with a log-normal distribution can be identified.

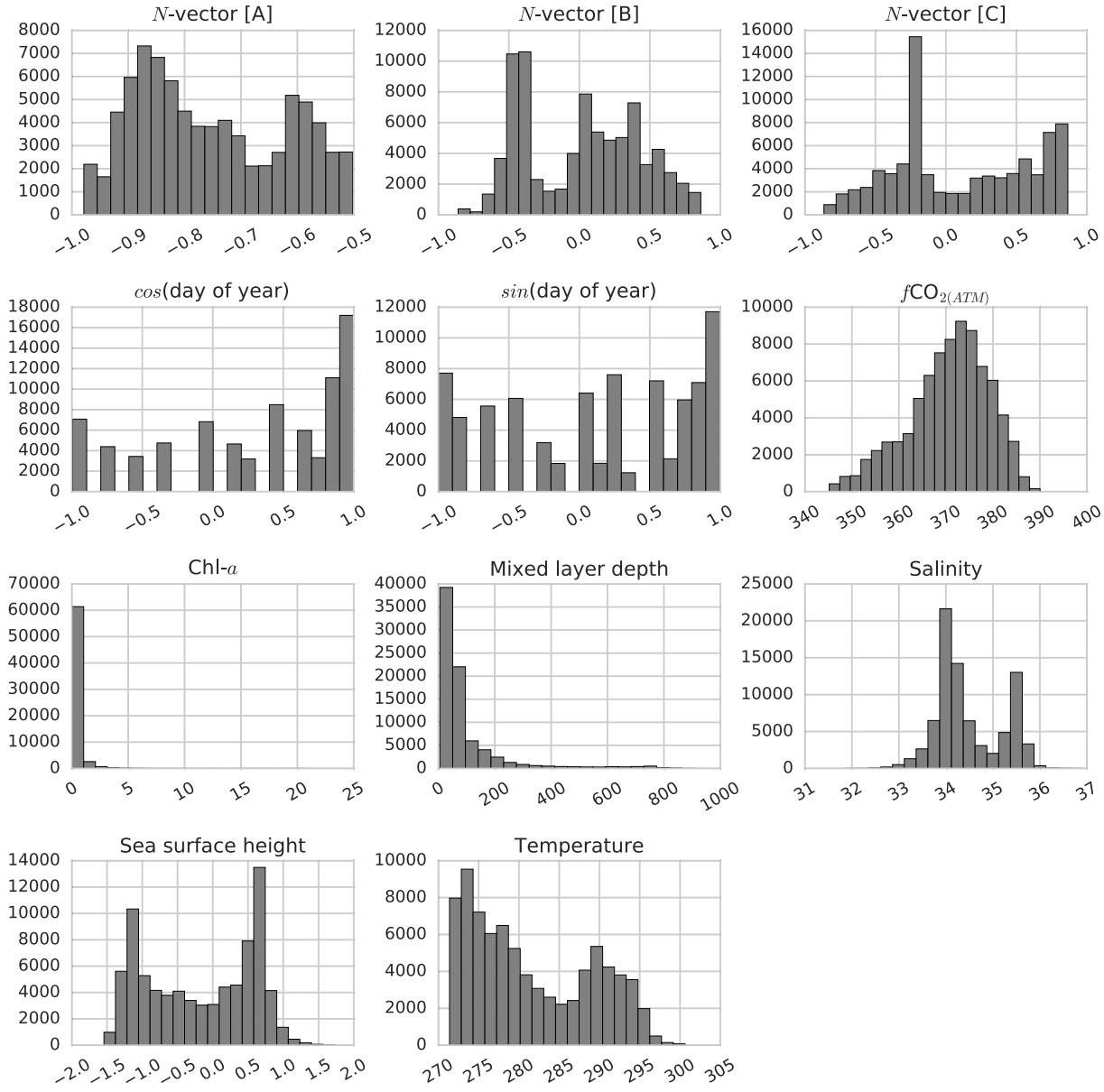

Figure 3.A.1: Histograms of input variables for the SVR in Chapter 3. Note that the variables have been not been transformed or scaled.

Figure 3.A.2 shows the increase in the number of cruises from SOCAT v2 to v3. The increased sampling effort in the Argentine and Tasman Seas leads to increased variability of pCO_2 data, which in turn increases the reported errors for the methods trained with the SOCAT v3 data.]

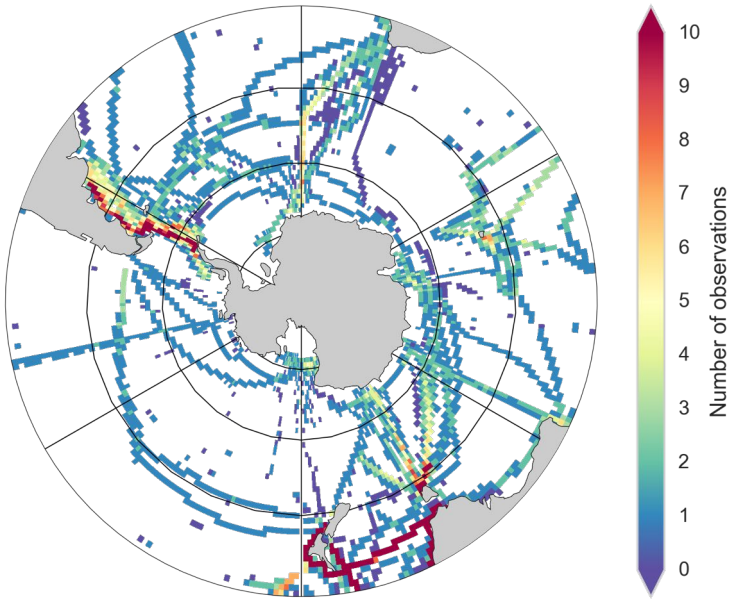

Figure 3.A.2: Map showing the number of additional cruises in SOCAT v3 compared to SOCAT v2 for each grid cell. This is important when considering the errors of products created with the different SOCAT versions. For example, an increase in the number of observations in the coastal SAZ leads to higher reported root mean squared errors for the SOCAT v3 products (as shown in Table 3.1).

Figure 3.A.3 compares the last four years of the SOCAT with the preceding four years. A decrease in sampling effort during the summer months in the SAZ is observed. A longitudinal count of pCO_2 observations reveals that the loss of effort is primarily in the Atlantic sector of the SAZ – specifically the Argentine Sea (70°W to 20°E), where variability of pCO_2 is large.

Figure 3.A.4 shows the number of observations annually in the central Atlantic sector of the SAZ. This figure aims to describe the reason for the difference between the summer SOM-FFN and SVR/RFR estimates in the SAZ from 1998 to 2008. The SOM-FFN, which is trained with a global domain, may be estimating higher ΔpCO_2 due to additional available data.

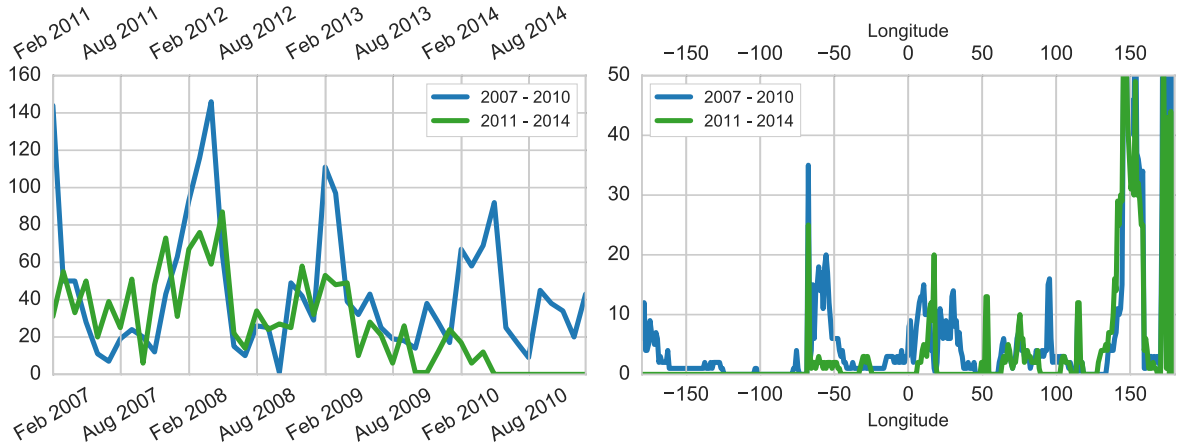

Figure 3.A.3: A figure comparing the last four years (2011 – 2014) of SOCAT v3 to the previous four years (2007 – 2012). (a) shows the number of samples per month and (b) the number of samples per degree of longitude.

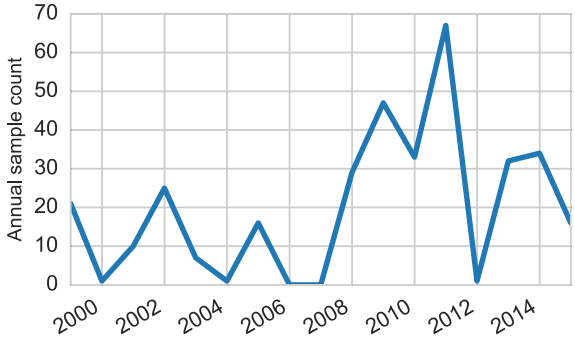

Figure 3.A.4: The number of SOCAT v3 observations in the central Atlantic sector of the SAZ (10°W – 20°E).

Figure 3.A.5 compares the sensitivity of the low resolution methods used in this study (RFR-LR and SVR-LR) to the training dataset: SOCAT v2 and v3. This is done to eliminate the training dataset as a potential source of difference between the methods presented in this chapter and the SOM-FFN, which was trained with SOCAT v2. The results show that both low resolution implementations of the RFR and SVR are relatively insensitive to the differences between SOCAT v2 and v3 (concerning the annual trends).

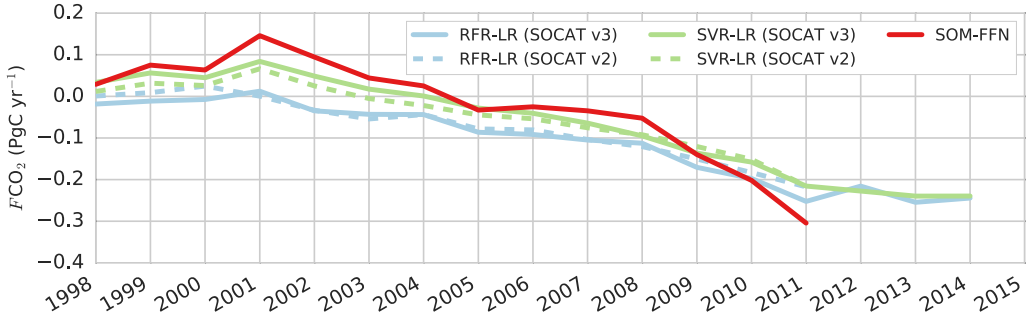

Figure 3.A.5: A comparison of pCO_2 estimates using SOCAT v2 (dashed) and v3 (solid) data for SVR-LR and RFR-HR. SOMFFN results are also shown for comparison. This figure suggests that sensitivity to the version of SOCAT is less than the sensitivity of different methods.

Figure 3.A.6 shows the results of a test that investigated the sensitivity of RFR-HR to the inclusion of the n-vector coordinates. RFR is said to be robust against outliers. Sparse data in winter are consequently treated as outliers, thus narrowing the distribution.

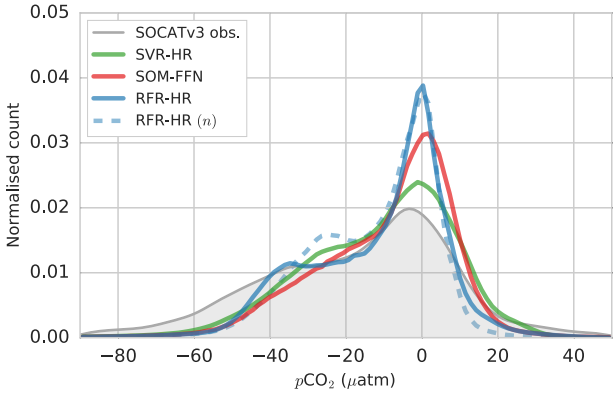

Figure 3.A.6: Histogram showing the comparison of SOMFFN, SVR-HR, RFR-HR without coordinates (solid) and RFR-HR with N-vector coordinates (dashed). The distribution of pCO_2 estimates for the RFR-HR with the N-vector coordinates is narrower than the RFR with the coordinates.

Chapter 4

Drivers of pCO_2 in the Southern Ocean based on an ensemble of estimates

4.1 Introduction

The Southern Ocean plays a key role in the uptake of anthropogenic CO_2 (Khatiwala et al., 2013; Devries et al., 2017). Moreover, it has been shown that the Southern Ocean is sensitive to anthropogenically influenced climate variability, such as the intensification of the westerlies (Le Quéré et al., 2007; Lenton et al., 2009a; Swart and Fyfe, 2012; Devries et al., 2017). Until recently, the community has not been able to measure the changes of CO_2 in the contemporary Southern Ocean due to a paucity of observations (Landschützer et al., 2015).

Landschützer et al. (2015) used empirically estimated CO_2 to identify the drivers of interannual variability, more specifically the reinvigoration of the Southern Ocean CO_2 sink. The authors found that the strengthening sink was not due to a relaxation in wind stress, as previous studies would have suggested (Lenton and Matear, 2007; Lovenduski, 2007; Lovenduski et al., 2007; Lenton et al., 2009b). Rather, the authors suggested that atmospheric circulation has become more zonally asymmetric since the mid 2000's. This has led to anomalous oceanic circulation and cooling/warming leading to the zonally symmetric uptake of CO_2.

4.1.1 Aims and Questions

In this chapter an ensemble of empirical estimates of CO_2 are used to investigate the drivers of CO_2 variability. The ensemble consists of the outputs of the methods used in Chapter 3. A seasonal and regional framework is applied to the ensemble to understand the balance between sea surface temperature (SST), wind stress, mixed layer depth (MLD) and chlorophyll-a (Chl-*a*). The key questions in this chapter are:

- Is mean of trend FCO_2 driven primarily during winter or summer?
- What are the primary drivers of pCO_2 for summer and winter?
- Do we continue to see a reinvigoration of the Southern Ocean CO_2 sink beyond 2010 (the end of the time-series by Landschützer et al. 2015)?

4.2 Methods

4.2.1 Ensemble pCO_2

The estimates of pCO_2 from Chapter 3 are used in this chapter. The ensemble mean of all the empirical approaches is used for analyses for the rest of this chapter. The advantage of an ensemble over a single method approach is that a degree of robustness is added to the estimate, assuming that ensembles have unique biases. This is demonstrated well by the comparison of RFR and SVR estimates, where the former method has conservative estimates relative to the more exaggerated SVR estimates of pCO_2. The ensemble consists of: high and low resolution implementations of Random Forest Regression (RFR-HR, RFR-LR), high and low resolution implementations of Support Vector Regression (SVR-HR, SVR-LR), and the Self-Organising Map – Feed-Forward Neural network by Landschützer et al. (2014). The high and low resolution implementations mentioned above are 16-day × 0.25° and monthly × 1.0° respectively. Results from Chapter 3 show that there are differences in pCO_2 between methods, but there is, in general, good coherence between methods. The ensemble approach also makes the assumption that the majority of methods examined in the previous chapter are correct, thus less weight will be given

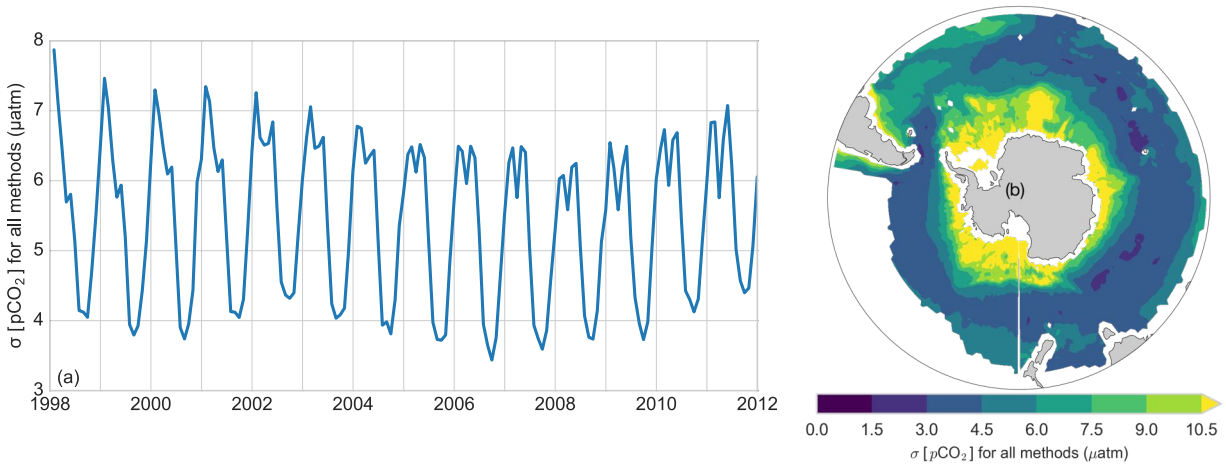

Figure 4.1: The mean of the standard deviation of the five approaches (SVR-LR, SVR-HR, RFR-LR, RFR-HR and SOM-FFN). Standard deviation was calculated for each of the five pCO_2 estimates for each grid cell and time step. The mean of these were taken (a) over space to show the temporal coherence, and (b) over time to show the spatial agreement.

to the SOM-FFN method relative to RFR and SVR. The high resolution output was resampled to match the low resolution data (monthly × 1°).

The air-sea CO_2 fluxes were calculated from the ensemble pCO_2 using Equation (2.10) and the wind stress was calculated using the method defined in Section 2.6.

Figure 4.1b shows that there is good spatial coherence in the majority of regions, where the marginal ice zone (MIZ) is the primary contributor to spatial uncertainty. This is likely due to the inability of the methods to accurately capture the larger intra-seasonal variability in the MIZ where the rapid reduction of pCO_2, due to melting sea ice leads to patchy pCO_2 distributions (Bakker et al., 2008; Chierici et al., 2012). However, the impact of pCO_2 uncertainties on air-sea CO_2 fluxes in the MIZ is lowered by ice cover for much of the year (Figure 4.1). The Atlantic sector is another region where methods show increased standard deviation (5 μatm < $\sigma(pCO_2)$ < 10 μatm), suggesting larger variability of pCO_2. Figure 4.1a shows that the majority of disagreement occurs from summer to autumn, when variability is large. From winter to spring the average standard deviation is far lower. There is also notable interannual variability of the standard deviation (Figure 4.1a), but the magnitude of this variability is small (< 2 μatm). It is shown that uncertainty at the beginning of the time-series is largest (particularly in summer) due to methodologically driven differences. These differences are exacerbated by fewer data in SOCAT, particularly in the SAZ (as explained in Section 3.3.2). This decreases from 2002 through 2008

as the number of observations increase. After this period there is once again an increase in variability suggesting one of two scenarios: 1) the SOCAT dataset is becoming less representative of Southern Ocean pCO_2 or; 2) pCO_2 becomes more variable during these periods. But because these variations are small there is confidence in the ensemble mean.

4.3 Results

4.3.1 Mean seasonal state: spatial characterisation

The spatial distribution of ensemble seasonal averages is shown in Figure 4.1. The average values in each period are coherent with the expected seasonal processes described in Section 1.4.1. In summer ΔpCO_2 values in the SAZ, MIZ and parts of the PFZ are negative, indicating CO_2 uptake. Zonally, the Atlantic sector of the SAZ is a strong sink during summer. From autumn through winter uptake decreases in all regions. The SAZ remains a sink, while the PFZ and MIZ become sources of CO_2 (with positive ΔpCO_2). The Indian sectors of the PFZ and MIZ are the dominant outgassing regions during autumn and winter. In spring ΔpCO_2 in the SAZ decreases, indicating increasing uptake of CO_2. ΔpCO_2 in the PFZ and MIZ are still positive (thus a CO_2 source) during spring, particularly in the Pacific, but less so than during winter.

4.3.2 Seasonal and interannual variability of pCO_2: zonal and basin contrasts

In Figure 4.2 ΔpCO_2 and FCO_2 are separated regionally by biome and basin, where FCO_2 is calculated according to Section 2.6. The open ocean biomes defined by Fay and McKinley (2014) are used to distinguish the SAZ, PFZ and MIZ (ΔpCO_2 for each biome, without basin separation, can be seen in Figure 3.9).

The mean annual ΔpCO_2 is shown by black lines in Figure 4.2 with the dominant difference being between the SAZ and the PFZ/MIZ. The SAZ is a strong continuous sink with a mean ΔpCO_2 of -25.31μatm. The PFZ and MIZ, south of the Polar Front, have low ΔpCO_2 estimates due to the opposing winter and summer estimates (-1.73 and 0.86 μatm for the PFZ and MIZ respectively).

In Figure 4.2 the mean amplitude of the seasonal cycle is shown by the distance between

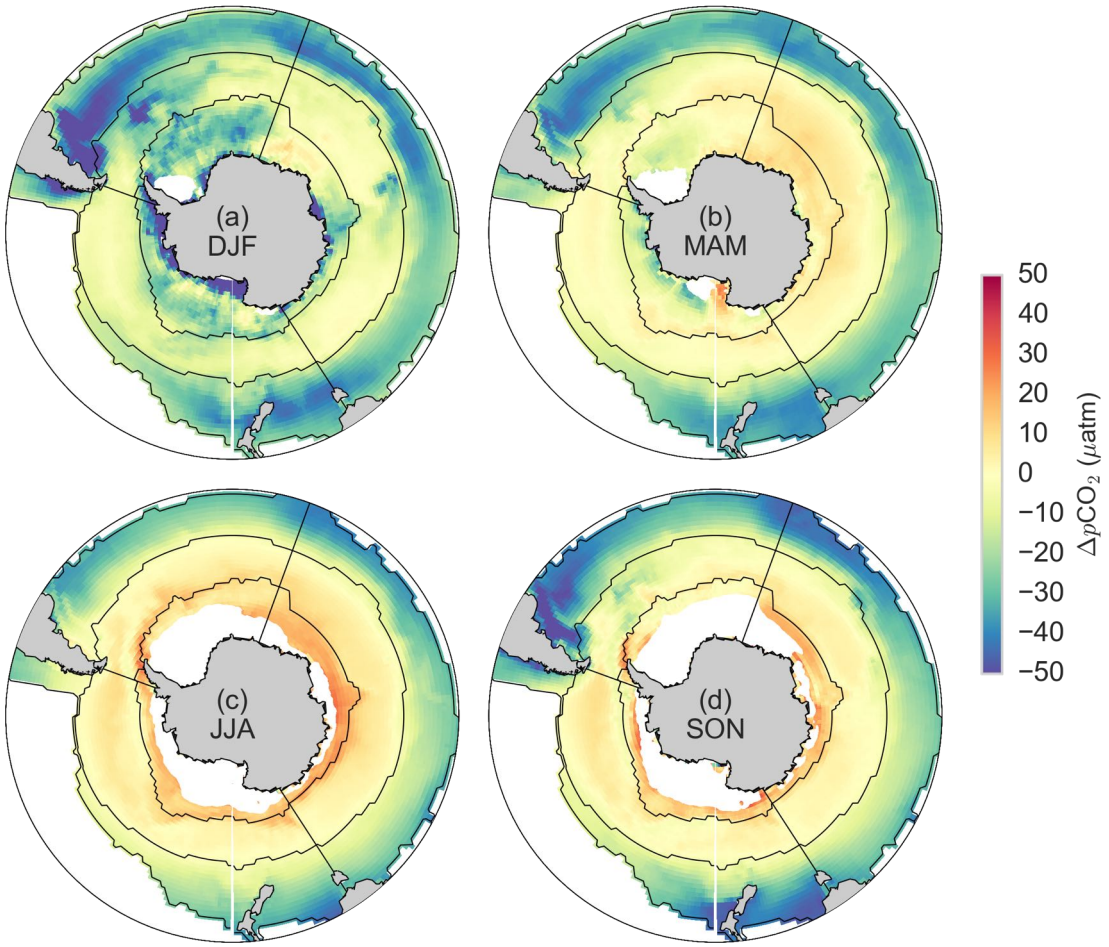

Figure 4.1: Seasonal averages of pCO_2 for the ensemble of ΔpCO_2. These are shown for (a) summer, (b) autumn, (c) winter and (d) spring. The lines show the regional boundaries used throughout the rest of the chapter with the zonal boundaries defined by Fay et al. (2014).

the solid and dashed lines and is calculated by taking the mean of the difference between the annual maxima and minima of ΔpCO_2. The magnitude of the seasonal cycle amplitude shows greater variability zonally than meridionally, in other words, a seasonal cycle amplitude varies by basin rather than by biome. For example, the Atlantic sector of the Southern Ocean has the largest mean seasonal amplitudes of 19.45 and 26.29 μatm for the SAZ and PFZ respectively. The Pacific sector of the SAZ has a similar mean amplitude to the Atlantic (16.92 μatm), but the PFZ amplitude is 18.14 μatm – closer to that of the Indian sector (15.73 μatm). The Indian sector of the SAZ has lowest average amplitude (9.23 μatm).

The dashed red line in Figure 4.2 shows the predicted summer ΔpCO_2 values based on the difference between the winter maxima and mean seasonal amplitude. The deviations of summer

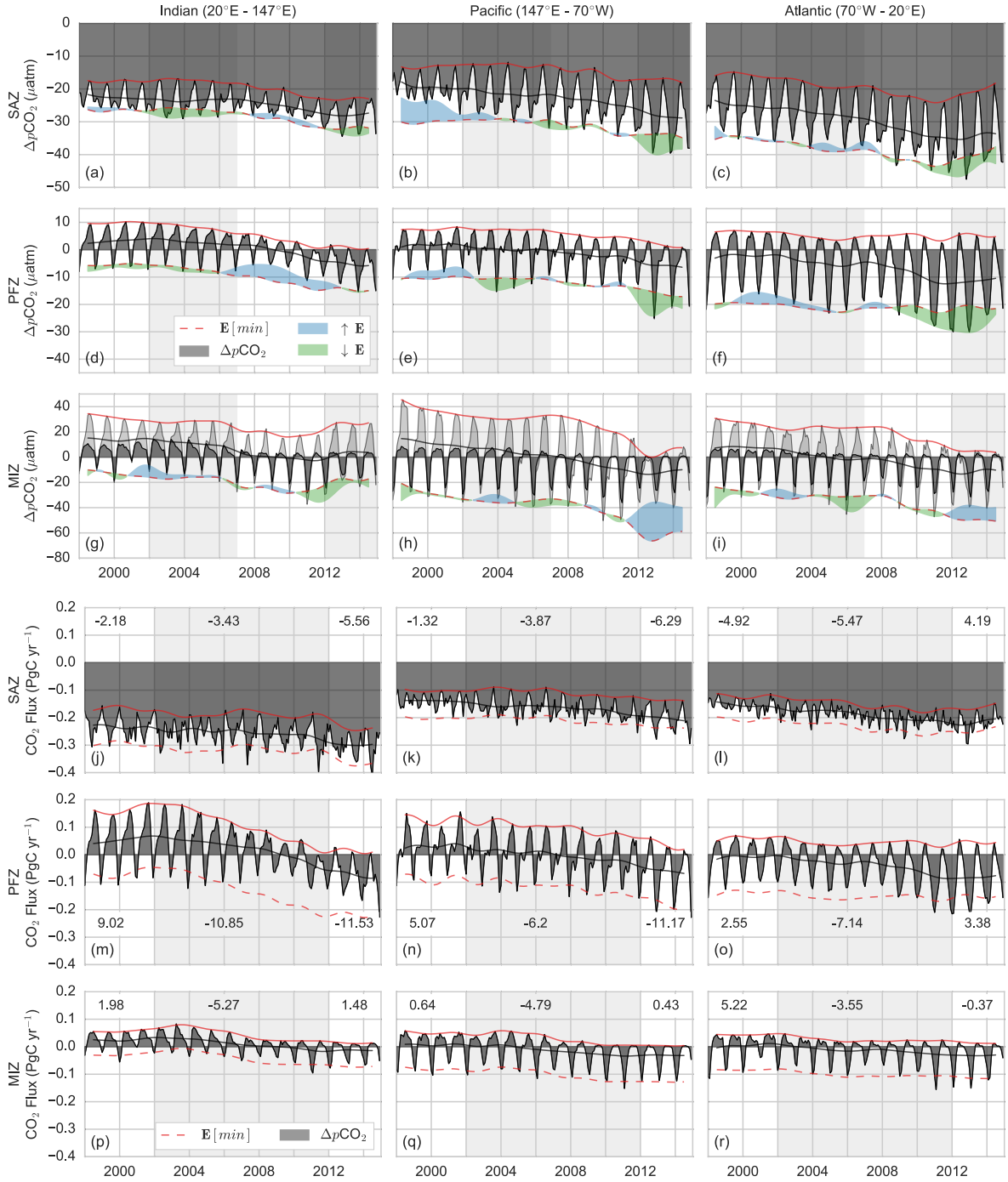

Figure 4.2: Figures (a-i) show ΔpCO_2 (dark grey) and (j-r) show FCO_2 (dark grey) plotted by biome (rows) and basin (columns). Biomes are defined by Fay and McKinley (2014) as shown in figure 2.11. The solid red line shows the maximum for each year (winter outgassing) and the dashed line shows the same line less the average difference between the minimum and maximum – this is the expected amplitude. The shaded blue (green) area shows when the annual minimum is less (greater) than the expected amplitude. ΔpCO_2 for plots (g–i) was normalised to sea ice cover, but under ice ΔpCO_2 estimates were still used to find the expected amplitude. Light grey shading in (a-i) shows the proposed periods used in Figure 4.3 and Figure 4.4 Light grey shading in (j-r) shows the "saturation" period (1998 to 2001) and the "reinvigoration" period (2002 to 2011).

ΔpCO_2 from the predicted summer ΔpCO_2 are shown by the blue and green fill to highlight the decoupling of summer and winter trends. These patches show that winter and summer drivers of ΔpCO_2 may operate on different modes of variability, with winter changes occurring roughly at a decadal scale compared to the four to six year mode of summer variability (Figure 4.2). This is demonstrated well in the Indian sector of the PFZ where a decrease in winter ΔpCO_2 from 2002 to 2011 is offset by weakening of the summer sink from 2006 to 2010. Similarly in the Atlantic and Pacific sectors of the SAZ and PFZ strong decoupling occurs from ~2011 to the end of 2014 with a rapid increase in the strength of the summer sink.

The periods of strong ΔpCO_2 decoupling are partially realised in the time-series of FCO_2, with the effect of wind stress in the calculation of FCO_2 and surface area of each region explaining differences. Most prominent is the amplification of the trends in the Indian sector of the Southern Ocean due to the largest surface area and strongest wind stress (Figure 4.A.1).

The Indian sector of the SAZ thus dominates the uptake of CO_2 with an annual mean flux of -0.25 PgC yr^{-1} compared to -0.19 and -0.17 PgC yr^{-1} for the Atlantic and Pacific sectors respectively (where the latter are significantly different with $p \ll 0.01$). Interestingly, the seasonality of wind stress results in a damped seasonal cycle of FCO_2 in the SAZ (compared to ΔpCO_2), with stronger winter winds compensating for a weaker ΔpCO_2 gradient.

The opposition of summer uptake and winter outgassing of CO_2 is amplified by stronger wind stress in the PFZ compared to the damping of the seasonal cycle amplitude in the SAZ where uptake of CO_2 occurs in both summer and winter (Figure 4.2m-o). Interannual variability is also enhanced, particularly during winter in the Indian sector of the PFZ, where a reduction in outgassing of 0.18 PgC yr^{-1} is observed. The decoupling between summer and winter FCO_2 also becomes more pronounced in this region (Figure 4.2m), resulting in a lag in the decreasing trend. In other words, the trend of FCO_2 for the reinvigoration (2002 through 2011: -10.85 PgC yr^{-1}) would have been stronger if the decoupling had not occurred. Similarly, the seasonal decoupling in the Pacific sector of the SAZ and PFZ results in a stronger growing sink from 2012 to 2014. In the Atlantic sector of the SAZ and PFZ the earlier onset of the seasonal decoupling also means that re-coupling occurs sooner, resulting in a positive trend (Figure 4.2o).

Lastly, FCO_2 in the MIZ is damped during winter due to ice cover and the transition to a sink in summer is rapid and short-lived (Ishii et al., 1998; Bakker et al., 2008).

4.3.3 Decoupling seasonal drivers

To fully investigate the drivers of pCO_2, data is split into seasons (winter, JJA and summer, DJF) and distinct interannual periods. Landschützer et al. (2015) recognised two periods in their study: the saturation period from the 1990's to 2001 as originally found by Le Quéré et al. (2007), and the reinvigoration from 2002 through 2011 (shown by light grey fills in Figure 4.2j-r). These periods are consistent with the annual averages of ΔpCO_2, but fail to capture the decoupled seasonal responses of ΔpCO_2 in summer and winter. To capture these changes, the reinvigoration period is split around the start of 2007 into an early and late, resulting in four periods including additional years 2012 to 2014. The periods are thus: P1 (the saturation period, 1998 – 2001), P2 (start of the reinvigoration, 2002 – 2006), P3 (end of the reinvigoration, 2007 – 2011) and P4 (additional years, 2012 – 2014). These four periods are too short for trend analyses (Fay et al., 2014), but the intention here is to identify the drivers that would otherwise be averaged out over longer periods. Moreover, the periods here are selected to perform an anomaly analysis between each period rather than a trend analysis (for which inflections of ΔpCO_2 would be a more suitable delimiter).

4.3.4 Seasonal anomalies of pCO_2 and drivers in the Southern Ocean

Here I examine the spatial characteristics of the anomalies for each period (P1 to P4). The relative anomalies are the differences between two adjacent periods (*e.g.* P2 – P1). As a result four periods (P1 – P4) give rise to three transitions (A, B and C) showing the relative change for the later of the two periods. Note that only summer and winter are discussed, but it is recognised that autumn and spring could be equally mechanistically important. Anomalies of winter ΔpCO_2, wind stress, SST and MLD are shown in Figure 4.3. The calculation of wind stress is defined in Section 2.6. Summer anomalies of ΔpCO_2, wind stress, SST and Chl-*a* are shown in Figure 4.4 where MLD, in winter, is replaced with Chl-*a* for summer as it is potentially a more important driver than the generally shallow MLD in summer.

The nomenclature of transitions in the sections that follow can be confusing if not adequately defined. Anomalies will always be discussed in terms of absolute values, where a positive anomaly is an increase, stronger, warming or deepening and a negative anomaly is a reduction/decrease, weaker, cooling or shoaling with reference to ΔpCO_2, wind stress, and MLD. Periods where there

is no to little change may be referred to as stagnant. With reference to ΔpCO_2, these anomalies cannot be defined in terms of a sink or a source as this depends on the state of P1, P2, P3 or P4, which are not shown for brevity.

Changes in winter drivers (Figure 4.3)

The relative anomalies of winter ΔpCO_2 and its drivers reveals two dominant features: 1) there is a zonally asymmetric dipole between the Pacific and Indian sectors of the Southern Ocean that dominates the interannual contrast of the drivers, being particularly strong for wind stress during anomalies A and B; 2) ΔpCO_2, SST and MLD seem to respond to the spatial variability of wind stress, mirroring the dipole variability to some extent. These points are explained in more detail in a chronological assessment of the anomalies.

Transition A (the transition from P1, the saturation period, to P2, the start of the reinvigoration) shows a relative increase of ΔpCO_2 in the east Indian and Pacific sectors of the SAZ – suggesting a delay in the onset of the reinvigoration for these regions Landschützer et al. (2015). This increase corresponds with stronger winds and deeper MLDs in the Tasman Sea and surrounds (Figure 4.3d,j). Conversely, in the central Pacific and Atlantic, weaker wind stress corresponds with relative warming and shoaling or stagnation of MLDs.

In transition B (corresponds to changes from P2 to P3 – the two reinvigoration periods) a reduction of ΔpCO_2 in all basins is particularly strong in the Indian basin (Figure 4.3b). This is concomitant with weaker wind stress, shoaling MLDs and warmer surface waters in the Indian sector, with all these changes being coherent to the dipole between the Indian and Pacific basins that was previously highlighted. The opposing response in the Pacific basin is stronger wind stress, deeper MLDs, and cooler surface waters, which leads to a moderate reduction of ΔpCO_2 compared to the Indian sector (Figure 4.3b,e,h,k). Warmer waters and shallower MLDs in the Atlantic are also associated with a moderate decrease in ΔpCO_2 in the Atlantic sector.

In transition C (P4 – P3), ΔpCO_2 further decreases in the Indian and Pacific basins, albeit more spatially heterogeneous. The dipole between the Pacific and Indian basins is not apparent, suggesting that transition A and B capture distinctly different phases in variability, while transition C may be capturing a transition into the following phase (towards resembling transition A). Mixed-layer depth shoals strongly in the Indian and Pacific sectors of the SAZ, which in the west

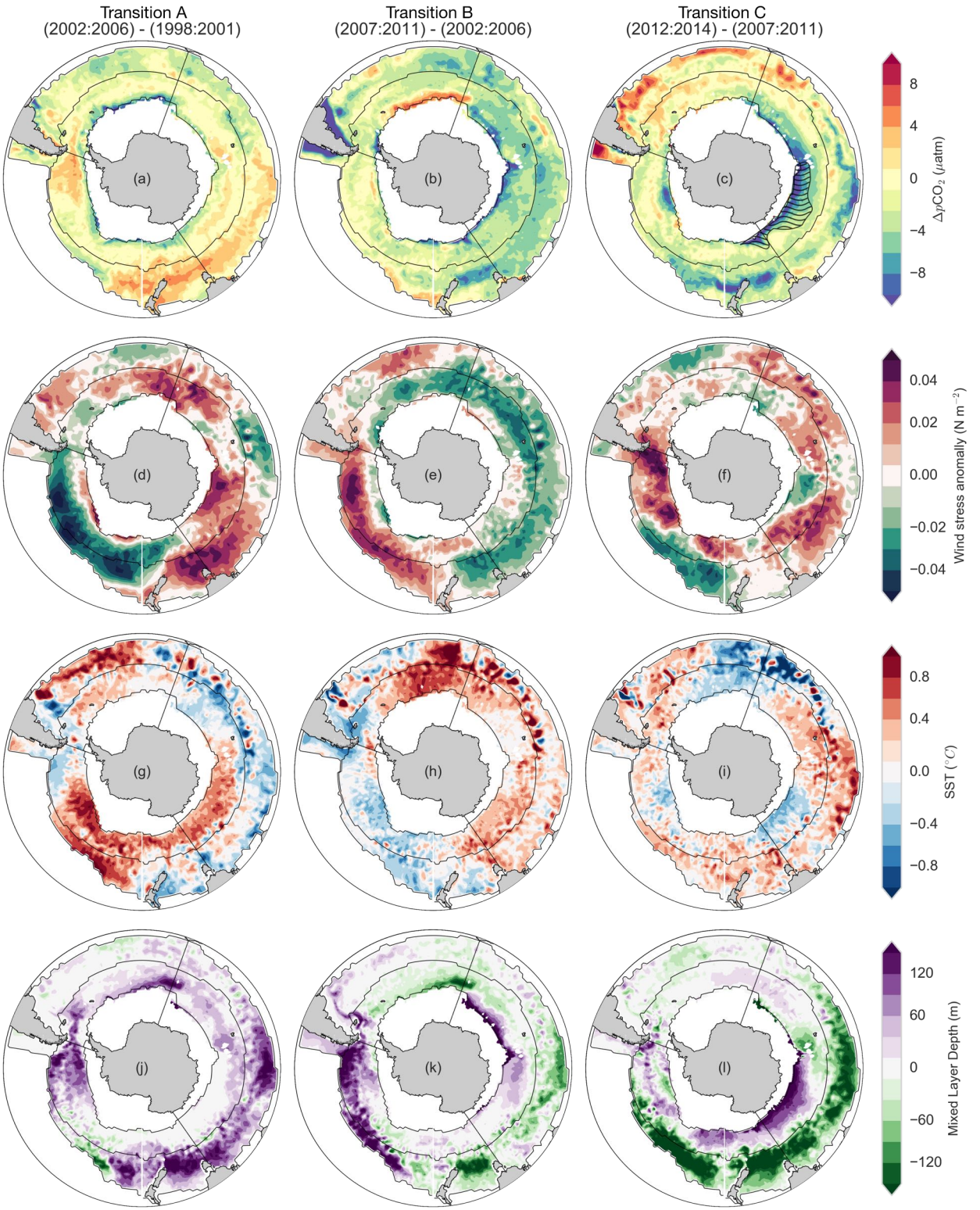

Figure 4.3: Transitions (relative anomalies) of winter ΔpCO_2 (a-c), wind stress (d-e), sea surface temperature (f-h) and mixed layer depth (i-k) for four periods (as shown above each column). The thin black lines show the boundaries for each of the nine regions described by the biomes (Fay et al., 2014) and basin boundaries. The black wavy hatching in (c) shows the region where MLD deepens and MLD counter-intuitively decreases.

Pacific SAZ corresponds with decreasing wind stress and in the east Indian with warmer surface waters. Lastly, deepening of the MLD in the Indian sector of the PFZ results in a counter-intuitive reduction of ΔpCO_2.

Changes in summer drivers (Figure 4.4)

In comparison to winter, summer contrasts of ΔpCO_2 and SST are stronger, but wind stress contrasts are weaker (Figure 4.4). For example, the relative reduction of ΔpCO_2 in the Indian basin during winter for transition B (Figure 4.3b) is in the order of 5 μatm compared to strong summer reductions, which often exceed 8 μatm. A dipole of wind stress anomalies also exists in summer, but is zonally symmetric compared to winter with a meridional shift between the SAZ and PFZ. The coupling between wind stress and SST is not as strong as in winter, where SST displays a strong zonally asymmetric dipole between the Atlantic and Pacific. Lastly, the link between Chl-*a* and ΔpCO_2 is strong, particularly in the Atlantic. These points are again explained in more detail in chronological order.

Focussing in on transition A (P2 – P1, the early reinvigoration minus the saturation period), there is a reduction of ΔpCO_2 in the Tasman Sea, Drake Passage and Argentine Sea corresponding with strong increases of Chl-*a*. A decrease of ΔpCO_2 in the east Pacific sector of the PFZ is concomitant with a reduction of wind stress and warming (> 1.0°C). This inverse relationship in the contrasts between wind stress and SST is consistent throughout the Southern Ocean, where an increase in wind stress over SAZ region corresponds with cooler SSTs. But weaker winds do not always lead to a reduction of ΔpCO_2, as demonstrated in the east Indian sector of the PFZ where ΔpCO_2 is stagnant despite weaker winds – the stagnant ΔpCO_2 caused by a counteracting reduction of Chl-*a*.

In transition B, a strong decrease of ΔpCO_2 is observed in much of the Atlantic, with the exception of the north western part of the SAZ where ΔpCO_2 increases . Once again this reduction links well with Chl-*a*. The increased Chl-*a* is concomitant with strong warming (excluding the north western part of the SAZ) – the same phenomenon observed by Landschützer et al. (2015). Note however, that the relationship between warmer SST and increased Chl-*a* does not extend into the Indian Ocean where warming also occurs. The anomalous cooling in the eastern Pacific reported by Landschützer et al. (2015) is also observed in transition B and corresponds with an

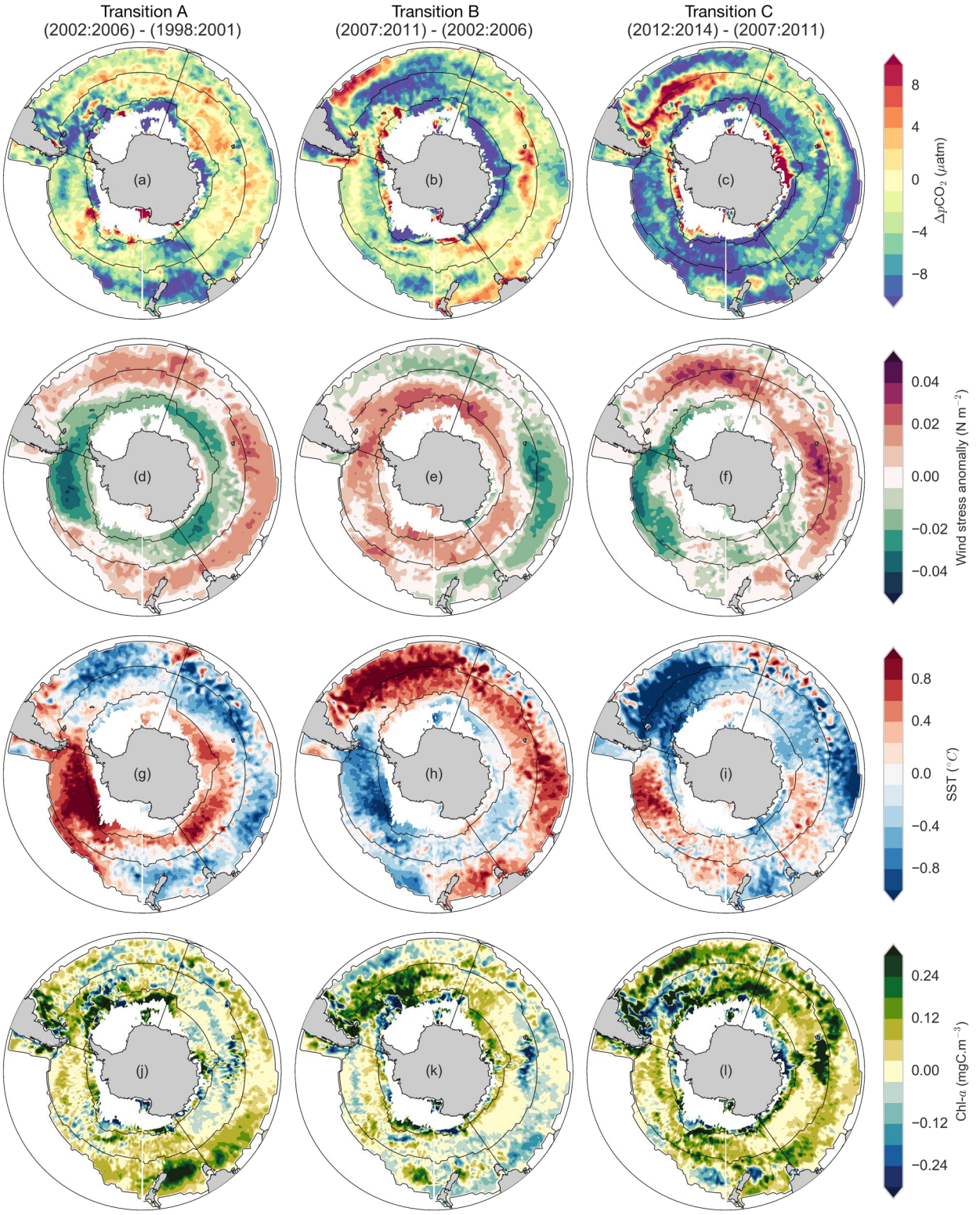

Figure 4.4: Relative anomalies of summer ΔpCO_2 (a-c), wind stress (d-e), sea surface temperature (f-h) and mixed layer depth (i-k) for four periods (as shown above each column). The thin black lines show the boundaries for each of the nine regions described by the biomes (Fay et al., 2014) and basin boundaries.

increase in wind stress over the region.

The reduction of ΔpCO_2 in transition C is widespread and consistent in nearly all basins, with the exception of the Atlantic. In the Atlantic ΔpCO_2 increases over what appears to be the ACC, where Chl-*a* decreases correspond. True to the dipole behaviour of SST contrasts (noted previously), there is strong cooling in the Atlantic as well as increased wind stress. The strong decrease of ΔpCO_2 throughout the rest of the Southern Ocean correspond weakly with increased Chl-*a*. The dipole behaviours of wind stress and SST reinforce the notion that the drivers of pCO_2 shift between two dominant modes of variability.

4.4 Discussion

Southern Ocean ΔpCO_2 has a strong seasonal amplitude due to the opposing influences of the dominant winter and summer drivers, partially damped by the seasonal cycle of temperature (Takahashi et al., 2002; Thomalla et al., 2011; Lenton et al., 2013). Mixing and entrainment in winter results in increased surface pCO_2 and thus outgassing (Takahashi et al., 2009; Lenton et al., 2013; Rodgers et al., 2014). In summer, stratification typically limits entrainment, but this does not exclude the occurrence of entrainment during periods of intense mixing driven by storms. Stratification also allows for increased biological production and the consequent uptake of CO_2, thus reducing the entrained winter DIC (Bakker et al., 2008; Thomalla et al., 2011). The discussion below interprets the results shown in Figures 4.2 to 4.4 based on the balance between these drivers and the impact this has on the seasonal and interannual variability of pCO_2 (and hence FCO_2).

4.4.1 Wind dominated winter

Based on the evidence in Section 4.3, I posit that interannual variability of seasonal wind stress may be the dominant driver of the saturation and reinvigoration (Figures 4.2 and 4.3). This seems to hold true in the Indian sector of the Southern Ocean (Figure 4.2m), which experiences the largest interannual variability of winter FCO_2.

The mechanism by which wind stress impacts on ΔpCO_2 (and thus FCO_2) is proposed to be that increased wind stress drives turbulent mixing and a loss of surface water buoyancy as

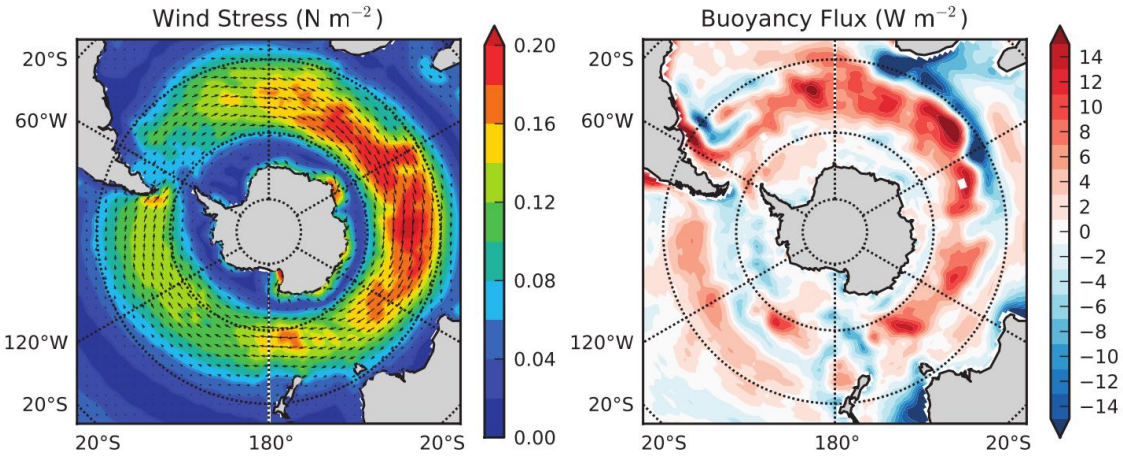

Figure 4.1: Figure is taken from Abernathey et al. (2011) to show (a) wind stress (N m^{-2}) and (b) buoyancy flux (W m^{-2}) which influence mixed layer depth. The data is an average of CORE2 (Coordinated Ocean Research Experiments) data over the period 1949–2006 (Large and Yeager, 2009). The buoyancy flux includes long-wave and short-wave radiative fluxes; latent and sensible heat fluxes; and the buoyancy fluxes due to evaporation, precipitation, and run-off.

heat leaves the ocean, as shown in Figure 4.1 (Abernathey et al., 2011). Weaker stratification deepens the MLD, thus entraining DIC rich deep waters (Abernathey et al., 2011; Lenton et al., 2013). Conversely, decreased wind stress and mixing (on seasonal or interannual time scales) allows for increased warming and buoyancy of the water column. Stronger stratification and shallower MLD limits entrainment of DIC.

The idea that variability of wind stress is the dominant driver of ΔpCO_2 in winter differs from Landschützer et al. (2015), who suggested that wind stress is a lower order driver. There are several reasons that explain why we arrived at a different conclusion.

First and foremost, the seasonal cycle analysis is key in establishing wind stress as a dominant driver. An annually integrated approach, as used by Landschützer et al. (2015), would not be able to represent the decoupling of winter and summer drivers. This could result in under-representation of winter signals due to the large anomalies of ΔpCO_2 and SST in particular (Figure 4.3 *v.s.* Figure 4.4). Conversely winter wind stress and MLD would dominate the annually integrated signals. This would potentially bias the interpretation of the drivers toward summer as SST and ΔpCO_2 are most likely to be in phase due to their summer dominance.

Second, the use of the SAM index as a proxy for wind strength is perhaps too simple as it is a zonally integrating metric (Marshall, 2003). In reality the SAM, as the first empirical mode of atmospheric variability, is zonally asymmetric Fogt et al. (2012). Zonal asymmetry of the SAM is

strongest in winter, particularly over the Pacific sector of the Southern Ocean during a positive phase, thus agreeing well with the zonally asymmetric dipole of wind stress anomaly observed in winter (Barnes and Hartmann, 2010; Fogt et al., 2012). Fogt et al. (2012) noted that the SAM has become more zonally symmetric in summer since the 1980's, matching the wind stress anomalies seen in Figures 4.3 and 4.4.

These asymmetries of the SAM may be important in our understanding of and ability to predict changes in pCO_2, especially with the evidence of an increasingly positive SAM (Marshall, 2003; Visbeck, 2009). Model studies have suggested that greater wind stress over the ACC would increase meridional transport due to enhanced northward Ekman transport (Lenton and Matear, 2007; Lovenduski et al., 2007). However, observations and eddy permitting simulations have found that increased wind stress is concomitant with enhanced eddy kinetic energy (EKE) which acts to offset the northward Ekman transport (Meredith and Hogg, 2006; Hogg et al., 2015; Dufour et al., 2012; Marshall and Speer, 2012; Meredith et al., 2012). This has consequences for the Southern Ocean carbon sink as model studies have shown that eddies compensate for upwelled DIC by one third by entraining total alkalinity to the surface (which reduces pCO_2) (Dufour et al., 2013). This effect may be further complicated by the zonally asymmetric EKE response in the ACC as found by Patara et al. (2016). It was shown that EKE in the Pacific and Indian sectors of the ACC are sensitive to wind stress increases while the Drake passage region and western Atlantic are insensitive to wind stress changes, with a dominant intrinsic EKE variability.

This high intrinsic dynamic variability may explain the apparent insensitivity of the eastern Pacific MLD (Drake Passage region) to increasing or decreasing wind stress. The dynamic variability acts to deepen the MLD, thus entraining DIC rich deep waters despite lower wind speeds (Mahadevan et al., 2012). This suggests that there are regions where ΔpCO_2 may be insensitive to wind stress during winter. However, the principle that MLD deepening results in increased ΔpCO_2 remains true here.

There are regions where this relationship between ΔpCO_2, wind stress and MLD is less consistent, particularly along the ice edge in the Indian and Atlantic sectors (shown by the black hatching in Figure 4.3l). The most likely reason for the decoupling between increasing ΔpCO_2 deepening MLD is that MLD is not correctly represented by the ECCO2 model. This is shown to be true with ECCO2 MLD deepening (shoaling) unrealistically in the Indian (Atlantic) sector of

the MIZ as shown in Figure 4.A.2. This effect may "bleed" into the PFZ for both these areas, thus creating spurious relationships between MLD and ΔpCO_2. This effect may also be exacerbated by the fact that winter measurements of pCO_2 are sparse, thus the true influence of MLD on pCO_2 is not adequately captured (exemplified by the low relative importance of MLD in the RFR methods in Figure 3.13). This peculiar response of ΔpCO_2 to deepening MLD highlights the fact that empirical methods do not impart a mechanistic understanding on estimates. A healthy scepticism should thus be applied to interpretation of empirical data – particularly when data is sparse or, as in this case, derived.

4.4.2 Chlorophyll dominated summer

Results presented in this study suggest that: 1) Chl-*a* is the dominant driver of interannual variability of CO_2, with strong changes in ΔpCO_2 associated with Chl-*a* change (Figure 4.4). 2) In regions of low Chl-*a*, such as the eastern Pacific, entrainment/stratification processes, as described in Section 4.4.1, seem to be more important. 3) Thermally driven changes of ΔpCO_2 is a low order driver of interannual variability, with few regions exhibiting probable temperature driven changes of ΔpCO_2 and even then, only weakly. These points will be discussed in more detail in the rest of this section.

High chlorophyll regions

The fact that Chl-*a* is the dominant driver of interannual ΔpCO_2 variability should not be surprising given that both models and observations support the finding (Hoppema et al., 1999; Bakker et al., 2008; Wang and Moore, 2012; Hauck et al., 2013, 2015; Shetye et al., 2016). As alluded to, the dominance of interannual Chl-*a* variability over ΔpCO_2 is limited to regions where Chl-*a* is high (as shown in Figure 4.2a). The distribution of high Chl-*a* regions in the Southern Ocean is complex and is a function primarily of light and iron limitation (Arrigo et al., 2008; Boyd and Ellwood, 2010; Thomalla et al., 2011; Tagliabue et al., 2014, 2017). The mechanisms of iron supply to the mixed layer are summarised in Figure 4.2b – a figure from Boyd and Ellwood (2010). In their study, Thomalla et al. (2011) related these limiting factors, iron and light, to the spatio-temporal distribution of Chl-*a* in terms of high/low concentrations and high/low seasonal cycle repro-

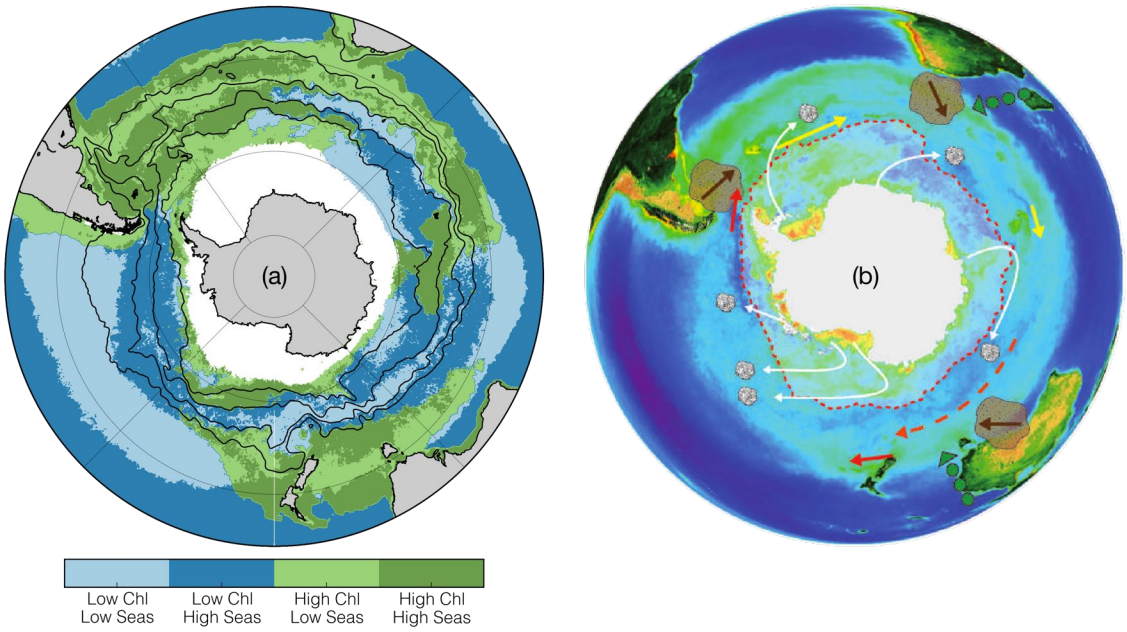

Figure 4.2: (a) Regions of chlorophyll biomass and seasonal cycle reproducibility from Thomalla et al. (2011) (using SeaWIFS data). Seasonality is calculated as the correlation between the mean annual seasonal cycle compared to the observed chlorophyll time series. A correlation threshold of 0.4 was applied to each time series to distinguish between regions of high and low seasonality; similarly, a threshold of 0.25 mg m^{-3} was used to distinguish between low or high chlorophyll waters. Black lines showing the fronts are the same as described in figure. (b) A schematic showing the proposed mechanisms of iron supply in the Southern Ocean from Boyd and Ellwood (2010). Important processes are: dust deposition (brown arrows and patches), island-wake effect (yellow arrows), seasonal ice-melt (inside the red dashed line), iceberg transport (white arrows), sediment transport (red arrows), and eddy transport of iron rich sediment (green arrows). These processes explain the distribution of chlorophyll.

ducibility[1] (SCR) as shown in Figure 4.2a. Here, where the interest is the interannual variability of ΔpCO_2, the low Chl-*a* regions will not be discussed in terms of Chl-*a* variability.

While regions of SCR (Figure 4.2a) do not correspond with the interannual variability of Chl-*a* (Figure 4.4j-k), the study by Thomalla et al. (2011) does present a paradigm through which variability of Chl-*a* and its drivers can be viewed. This is, that the variability of Chl-*a* in a region is a complex interaction between the underlying physics and the interannual drivers that modulate light and iron limitation (MLD, SST and wind stress). The effects of this are exemplified by strong warming in the Atlantic during transition B, which results in both an increase and decrease in Chl-*a*, with inverse consequences for ΔpCO_2. The effect is even stronger transition C, where strong cooling in the Atlantic results in both a decrease and increase of Chl-*a* (Figure 4.4i,l). In both transition A and B the respective increase and decrease of Chl-*a* occur roughly over the

[1] regions of low SCR are characterised by either high interannual variability and/or high intra-seasonal variability.

ACC (between the STF and SACCF as shown in Figure 1.1), while the opposing effects during transitions A and B occur roughly to the north and south of the ACC region. These temperature changes may impact the stratification of the region[2], but complex interaction with the underlying physics results in variable changes in Chl-*a*.

Mesoscale and sub-mesoscale processes may have a part to play in these dynamic responses of Chl-*a* to changes in SST and wind stress (amongst other drivers). For example, eddy-driven slumping is a sub-mesoscale process that acts to rapidly shoal the mixed layer (Mahadevan et al., 2012). The process occurs in spring and early summer when MLDs are still deep and relaxation of down-front winds allows lighter waters to slump over denser waters, thus shoaling the MLD (Lévy et al., 2012; Mahadevan et al., 2012). This allows phytoplankton to remain within the euphotic zone and thus grow (while iron is not limiting). Similarly, Whitt et al. (2017) demonstrated that a combination of high and low frequency oscillation of down-front winds are able to enhance nutrient entrainment (including iron) into the mixed layer on the less dense side of a front. This has important implications for Southern Ocean fronts, where Chl-*a* may benefit from this entrainment mechanism combined with eddy-driven slumping that could subsequently rapidly shoal the mixed layer. Storm driven, intra-seasonal mixing is another sub-mesoscale process that could alleviate iron limitation (Nicholson et al., 2016). Nicholson et al. (2016) showed that storms induce sheer driven mixing along the base of the mixed layer. This entrains small amounts of iron from the mixing transition layer – the portion of the water column between the homogeneous surface mixed layer and the homogeneous deep ocean. Importantly, both storm driven entrainment and the oscillatory enhancement of entrainment, rely on a mixing transition layer that has sufficient iron that is able to sustain growth – weak dissolved iron gradients in the Pacific and east Indian sectors of the Southern Ocean would explain the lack of phytoplankton in these regions Tagliabue et al. (2014); Nicholson et al. (2016).

These sub-mesoscale processes may explain potential changes in intra-seasonal variability of Chl-*a*, but the authors did not investigate the potential of these processes of interannual variability of Chl-*a*. Though it may be that basin-scale interannual variability of the drivers that enable these sub-mesoscale processes, stratification (driven by SST) or wind stress, could result in interannual variability of Chl-*a*. To further understand the effect of these processes on

[2]Summer SST changes in the Atlantic during transitions B and C do not reflect in the modelled MLD Figure 4.A.3

interannual variability of Chl-*a* further sensitivity studies would have to be done.

Low chlorophyll regions

In their study, Landschützer et al. (2015) explained ΔpCO_2 interannual variability as an interaction between entrainment/stratification and thermal forcing of ΔpCO_2. In this study, data show that, in summer, these two mechanisms are only dominant in regions of low Chl-*a*.

Entrainment and stratification can explain much of the variability in the eastern Pacific and Indian sector of the PFZ (with the exception of the wake of the Kerguelen Plateau). For example, in the eastern Pacific in transition A (Figure 4.4a,d,g), strong warming and weaker winds have little impact on Chl-*a*, but a decrease in ΔpCO_2 is observed. Conversely, cooling in the west Indian sector of the PFZ results in a weak increase in ΔpCO_2 during the same transition. In both these cases, the effect of cooling or warming on ΔpCO_2 is negligible relative to the impact of entrainment or stratification respectively. The effect is reversed in the eastern Pacific during transition B where strong cooling results in a weak reduction of ΔpCO_2 rather than the increase that would be expected from entrainment. This is the exact mechanism that Landschützer et al. (2015) describe in the Pacific, where enhanced entrainment of DIC and TA is compensated for by cooling. This emphasises that the balance between SST (as a driver of stratification) and wind stress is far more important than in winter.

Perhaps an important consideration here is that the transition anomalies of wind stress and SST are weakly correlated. This is less obvious than in winter due to the comparatively zonally symmetric dipole in the wind stress transitions during summer, which contrasts the strongly zonally asymmetric SST changes. For example, in the eastern Pacific during transition A, weaker winds correspond with warmer SST and conversely stronger winds during transition B are concomitant with cooler surface temperatures (Figure 4.4d,e,g,k). The same relationship holds for much of the Southern Ocean, though there are exceptions.

This correlation between wind stress and SST is likely linked to the occurrence of Antarctic Circumpolar Waves (ACW), which were first described by White and Peterson (1996). White and Peterson (1996) and later Giarolla and Matano (2013) showed that these anomalies propagate eastward along the ACC with a period of 4 – 5 years and circle the Antarctic continent every 8 – 10 years. Though it must be emphasised that there is still a strong stationary component in the

variability of SST and wind stress (Giarolla and Matano, 2013). These ACWs may also explain the SST dipole observed between transition A and B, particularly in the eastern Pacific and western Atlantic. The resemblance in SST and wind stress between transition A and C (Figure 4.4g,i) is thus in phase with the 10 period of ACW. Moreover, these anomalies have also been linked to the complex interaction between climate modes, SAM and ENSO (Verdy et al., 2006; Yeo and Kim, 2015).

In summary, regions with high biomass, Chl-*a* integrates the complex interactions between SST, wind stress, MLD and sub-mesoscale variability resulting in large interannual pCO_2 variability compared to low biomass regions. In low Chl-*a* regions, entrainment/stratification are in general dominant over thermally driven changes of ΔpCO_2. Stratification due to weaker winds and warmer temperatures often limits entrainment of high DIC and TA waters, thus resulting in a decrease of ΔpCO_2. Thermally driven changes of ΔpCO_2 can occasionally be more dominant than the entrainment/stratification processes.

4.4.3 Annually integrated trends of FCO_2

The trends of regionally integrated fluxes (Figure 4.3) present a good overview of the state of the Southern Ocean sink.

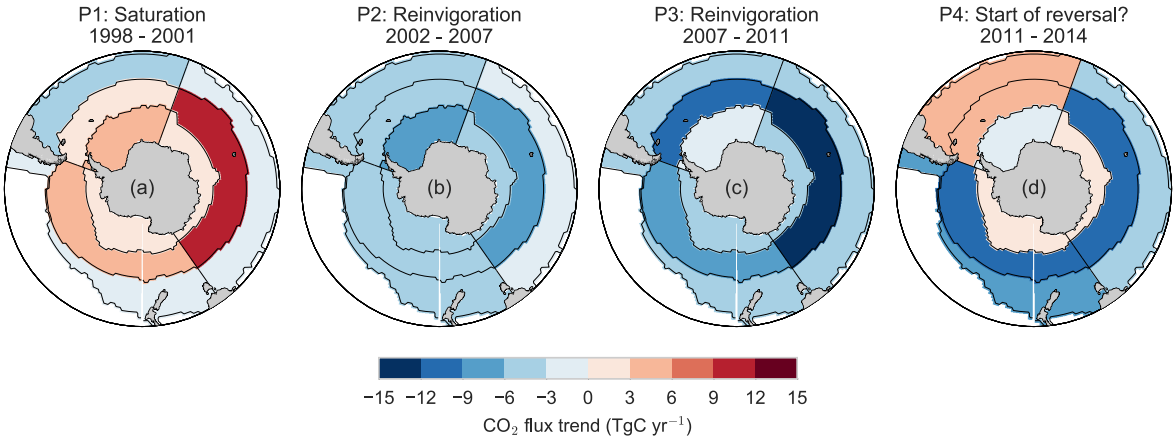

Figure 4.3: A summary of the regionally integrated FCO_2 trends for the four periods shown in Figure 4.2(a-i) where regions are defined by Fay and McKinley (2014). The trends are broken into four periods: (a) the saturation period (1998 – 2001), (b) the first half of the reinvigoration period (2002 – 2006); (c) the second half of the reinvigoration period (2007 – 2011) ; and (d) the start of the reversal (2012 – 2014). Note that the FCO_2 trends for saturation and reversal periods are the same as those in Figure 4.2(j-r).

The dominant role of the PFZ in the interannual variability of FCO_2 is clear in this figure,

where the region south of the polar front was a weakening CO_2 sink during the saturation period (1998 – 2002). A reversal of the trend is observed from the start of the reinvigoration onwards, but trends are weaker during P2 due to decoupled summer and winter fluxes – particularly evident in the Indian sector of the PFZ. During P2, weakening winter outgassing was opposed by a weakening summer sink, but in P3 the summer sink increased resulting in strong increase in the mean trend. This pattern is observed to a lesser extent in both the Atlantic and the Pacific.

The SAZ remained a weakly growing sink throughout the saturation and reinvigoration periods, strengthening weakly during both periods of the reinvigoration. Decoupling of the seasonal fluxes does occur in the SAZ, but strong winds during winter compensate for a weaker sink, therefore resulting in a muted seasonal flux signal and weaker seasonal decoupling.

In the last period there is a reversal of the trend in the Atlantic, going from a growing to a diminishing sink. This reversal is driven by thereduction of biological uptake of CO_2 that drove strong uptake during the reinvigoration. This may signal the start of the reversal of the sink.

4.4.4 End of the reinvigoration?

The points discussed in Section 4.4.1 and Section 4.4.2 imply that all major variability of pCO_2 in the Southern Ocean is linked to the variability of the SAM. Winter ΔpCO_2 is strongly driven by wind stress changes affected by a zonally asymmetric SAM. In summer ΔpCO_2 is strongly influenced by Chl-a (in non-iron limited regions), which in turn, is partially determined by eastward propagating SST anomalies. Both wind stress and SST in the Southern Ocean are said to have ten year modes of interannual variability (White and Peterson, 1996; Giarolla and Matano, 2013). This is in agreement with Landschützer et al. (2016) who found that FCO_2 has a decadal mode of variability in the Southern Ocean. The saturation of the Southern Ocean CO_2 sink in the 1990's as reported by Le Quéré et al. (2007) and the consequent reinvigoration in the 2000's are explained by the SAM's decadal oscillation Giarolla and Matano (2013); Landschützer et al. (2016). In support of the SAM as the dominant driver of CO_2 variability, Devries et al. (2017) reported that the strengthening of the ocean CO_2 sink is a response to weaker overturning circulation.

Based on this dominant decadal mode of SAM variability and the state of proxy variables shown in transition C, a shift in the phase of ΔpCO_2 could be imminent. Early signs of positive ΔpCO_2 anomalies in the Atlantic (Figure 4.3c and Figure 4.4c) may signal the start of this reversal.

The Atlantic sector of the SAZ shows a weakening of the sink during winter, but weakening in the PFZ is driven primarily by a decrease in summer uptake of CO_2. This same decrease may occur in the Pacific sectors of the SAZ and PFZ, where a strong decoupling between winter and summer also occurs (Figure 4.2b,e). However, the weakening may be short-lived as it is, in each of these cases, a reversal of summer variability, which operates on a shorter mode of variability (Figure 4.2).

As in the case of the reinvigoration period, long term interannual variability (on the order of >10 years) is dominated by decreased or increased outgassing south of the Polar Front. The last three years of winter ΔpCO_2 in the Atlantic and Indian sectors of the PFZ remain stagnant (Figure 4.2d,f,m,o). It is difficult to determine whether this period will be followed by weakening or strengthening of the sink and ultimately these trends will only be confirmed with longer time-series and more robust estimates of air-sea CO_2 fluxes.

4.5 Conclusions

In this chapter, an ensemble of empirically ΔpCO_2 estimates was used to investigate the trends of estimated fluxes in the Southern Ocean. The questions asked of this data in Section 4.1.1 are answered below.

Is the mean of trend FCO_2 driven primarily during winter or summer?
Using a seasonal cycle framework it was shown that interannual variability of FCO_2 is in fact dominated by winter fluxes, specifically in the Indian sector of the PFZ. Interannual FCO_2 variability in summer is important on shorter time scales with biology typically acting to offset the DIC upwelled during winter, in other words, winter sets the baseline for summer.

What are the primary drivers of pCO_2 for summer and winter?
Using the seasonal framework it was shown that winter pCO_2 is in fact dominated by wind stress changes. The reinvigoration of the Southern Ocean CO_2 sink during the 2000's was driven largely by a reduction of ΔpCO_2 due to a reduction in wind stress over the Indian ocean. The reduction in wind stress is in phase with the decadal variability of the Southern Annular Mode (Giarolla and Matano, 2013; Landschützer et al., 2016). However, detecting these changes is subtle due to interannual variability and the zonal asymmetry in wind stress changes (and the SAM) (Fogt et al.,

2012). This process is responsible primarily in, but not limited to, winter. Controls of ΔpCO_2 in summer are more complex than winter drivers due to stronger temperature anomalies and the influence of phytoplankton on the uptake of ΔpCO_2. It was found that Chl-*a* was the strongest determinant of ΔpCO_2, where an increase in net primary production would lead to increased uptake. Where Chl-*a* is a function of light and iron limitation controlled by complex interactions of buoyancy control and sub-mesoscale variability. In regions of low Chl-*a* concentration the balance between SST and wind stress were more important, but understanding the interaction of these drivers is perhaps to understand the intrinsic sensitivities to each of these processes respectively.

Do we continue to see a reinvigoration of the Southern Ocean CO_2 sink beyond 2010 (the end of the time-series by Landschützer et al. 2015)?

The modality of proxy anomalies (SST and wind stress) were consistent with the propagation of an SST wave with a decadal period and decadal variability of wind stress linked to the SAM (Lovenduski et al., 2008; Giarolla and Matano, 2013). Given these decadal variability of these drivers, a reversal of the trend of Southern Ocean air-sea CO_2 flux should be imminent. However, evidence for this is weak with weakening of the sink occurring only in the Atlantic basin. Moreover, winter ΔpCO_2 did not signal reversal, but was stagnant in the Indian sector of the PFZ, which dominates interannual variability, for the last three years.

Lastly, I want to emphasise that interpretation of data based on empirical output should be done in the context of a good understanding of the strengths and limitations of empirical approaches. Empirical methods impart no mechanistic knowledge on calculating output. This means that sparse data or poor proxies are used in training, the output will reflect this, as may be the case in the Indian sector of the PFZ where the relationship between MLD and ΔpCO_2 is spurious. This is exacerbated by the fact that training data in winter is very sparse. This emphasises the importance of adequate pCO_2 coverage, particularly in winter. In the next chapter I address the problem of data coverage and sampling strategy in the Southern Ocean by assessing the strengths and biases of various existing sampling platforms.

4.A Additional figures

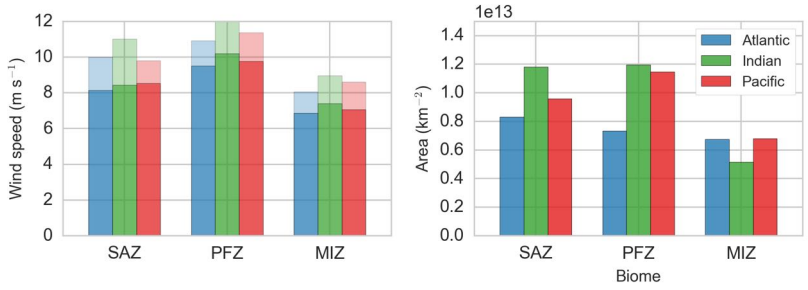

Figure 4.A.1: (a) Wind speed shown for each region in winter (behind) and summer (in front). Cross-calibrated Multiplatform (CCMP) wind product was used to calculate the average wind speeds. (b) Surface area for each region: Atlantic 70°W – 20°E; Indian 20°E – 147°E; Pacific 147°E – 70°W .

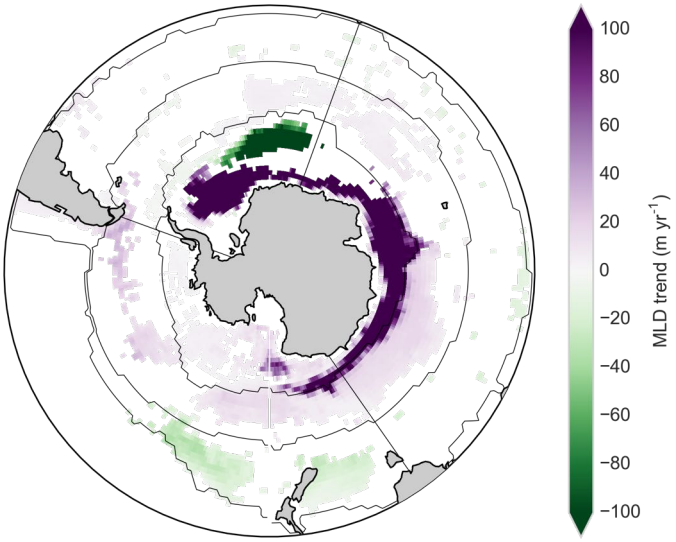

Figure 4.A.2: Trends of ECCO2 MLD for the period 2007 through 2014 (Menemenlis et al., 2008). Only significant trends are shown ($p < 0.05$). Strong deepening trends in the Atlantic and Indian MIZ, and shoaling in the Atlantic MIZ are likely model artefacts rather than representation of reality. These may create spurious correlations between ΔpCO_2 and MLD.

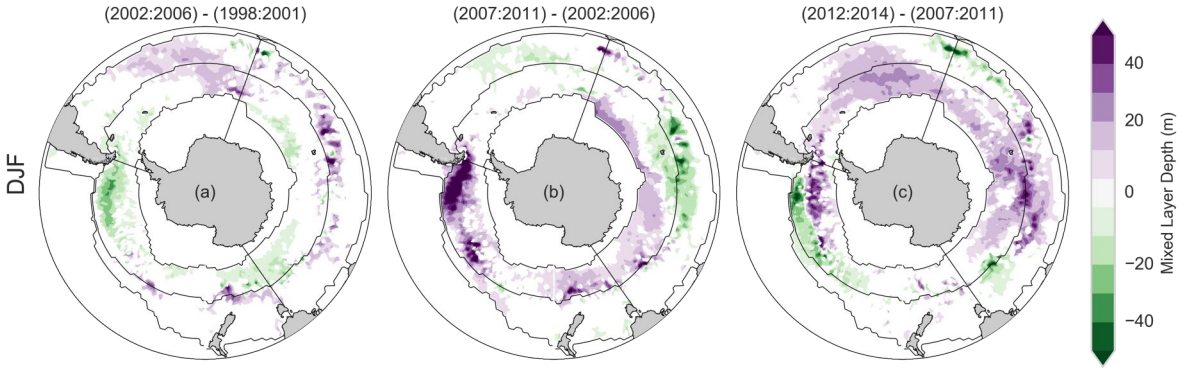

Figure 4.A.3: Relative summer ECCO2 MLD anomalies for three periods as shown above the figures. The scale is adjusted for the shallower summer MLDs (compared to Figure 4.3)

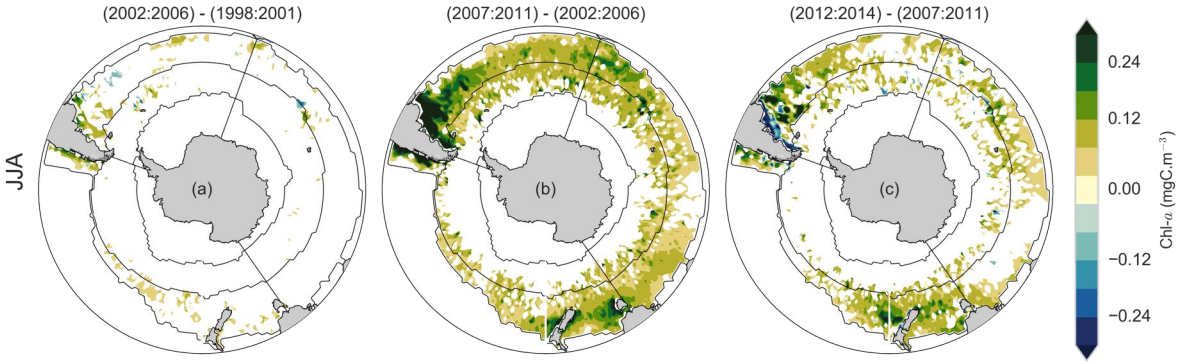

Figure 4.A.4: Relative winter Globcolour chlorophyll-a anomalies for three periods as shown above the figures. The black lines show the boundaries of the regions as shown in Figure 4.2. Figure (b) shows an increase in Chl-*a* for nearly the entire Southern Ocean. This more likely an artefact of the Globcolour product as shown in Figure 4.A.5. Note that ice-covered regions have been masked.

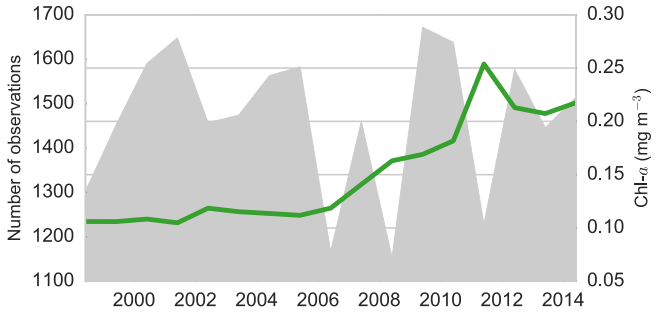

Figure 4.A.5: Mean winter chlorophyll-a concentration for the PFZ and MIZ (green line) with the number of total satellite chlorophyll observations (grey fill). The increase observed over time in winter is more likely an artefact than a true increase in the uptake of Chl-*a*, given how spatially uniform the increase is in Figure 4.A.4b. Note that ice-covered regions have been masked.

Chapter 5

Optimising CO_2 sampling strategies in the Southern Ocean

5.1 Introduction

In Chapter 3 two new interpolation schemes were introduced for the estimation of pCO_2 from satellite based proxy-variables. The accuracy of these models is dependent on how well the training datasets represent the entire domain. The SOCAT v3 dataset was used as the training dataset in Chapter 3 (Bakker et al., 2016). It is recognised that Southern Ocean pCO_2 measurements are biased toward summer as inclement weather limits sampling during winter (Figure 2.2). In this chapter an Observing System Simulation Experiments (OSSE) approach is used to test what the effect of the summer bias in the SOCAT v3 dataset is on Southern Ocean pCO_2 and FCO_2. Autonomous sampling platforms, which are able to sample throughout the year, are explored as alternate and adjunct approaches to ship-based measurements.

Recent developments of autonomous sampling platforms have expanded the potential for perennial sampling of pCO_2 in the Southern Ocean, thus beginning to fill the winter sampling gap. Notably, profiling floats are now able to accurately measure pH, from which pCO_2 can be derived with a relatively low margin of error (Johnson et al., 2016). More than 80 of these floats have already been deployed in the Southern Ocean, with the goal of 200 deployments as part of the SOCCOM project (Russell et al., 2014). Wave gliders, a relatively new surface ocean autonomous sampling platform, are able to directly measure pCO_2 at high frequency and with great accuracy

(Monteiro et al., 2015; Sutton et al., 2014). Moreover, this platform has been successfully proven to function as a pseudo stationary mooring in the Southern Ocean (Monteiro et al., 2015).

Majkut et al. (2014) investigated the viability of stationary floats (moorings) to resolve fCO_2 using an OSSE approach. The measured fCO_2 was spatially interpolated using inverse distance weighted interpolation. The authors found that between 150 and 200 randomly placed moorings would be sufficient to resolve 90% of the seasonal cycle of air-sea CO_2 fluxes.

5.1.1 Aims and questions

In this study an OSSE approach is implemented using BIOPERIANT05 model output (Section 2.3.1) to simulate and test these three sampling platforms: ships, moorings and floats. This approach is used to test the sampling biases of empirical pCO_2 and fCO_2 estimates in the Southern Ocean. The questions framing this study are:

- Is there a bias in SOCAT estimates of the mean annual pCO_2 and fCO_2 given the strong bias towards summer sampling?
- Would 200 profiling floats, with large sampling error, be adequate to estimate pCO_2?
- How many moorings are needed to estimate pCO_2 adequately?
- Do mixed platform observations achieve better fCO_2 estimates than single platform approaches?

5.2 Methods

For the OSSE approach we used the NEMO–PISCES model configuration BIOPERIANT05 as described in Section 2.3.1. The original model resolution (5-day × 0.5°) was used.

Support vector regressions are run with various simulated training datasets to test sampling platforms for potential biases. It is thus important that the model represents the variability of pCO_2, both spatially and seasonally. The ensemble mean of empirically estimated ΔpCO_2 from Chapters 3 and 4 is used for comparison of variability. A time series of standard deviation for BIOPERIANT05 and the ensemble mean is shown in Figure 5.1a, where the domain was

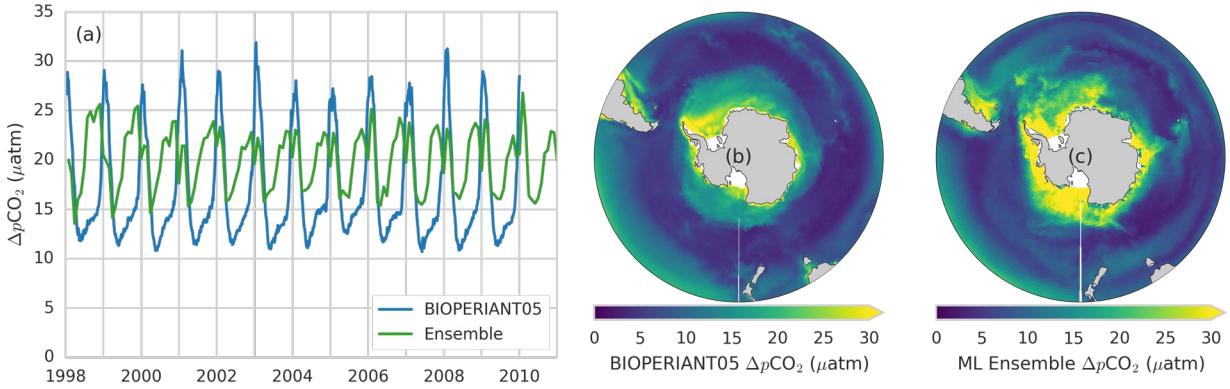

Figure 5.1: (a) A time-series of ΔpCO_2 standard deviation for machine learning estimates (used in Chapter 4) and BIOPERIANT05 model output. The spatial representations of the standard deviations for (b) BIOPERIANT05 and (c) machine learning estimates are also shown.

calculated for the region south of 34°S, as shown in the maps of variability (Figure 5.1b,c). The model captures the increased variability of ΔpCO_2 in summer relative to the ensemble mean as shown in figure Figure 5.1a. However, winter standard deviation of ΔpCO_2 for BIOPERIANT05 is lower than that of the empirical ensemble mean. The seasonal amplitude of standard deviation is thus larger for the model than for the ensemble mean (Figure 5.1a). This may be due to the fact that models do not yet accurately capture the seasonal cycle of pCO_2 in the Southern Ocean (Lenton et al., 2013; Mongwe et al., 2016), thus the relationship between pCO_2 and proxy variables may differ from observations. This may be compounded by the fact that BIOPERIANT05, with a resolution of 0.5°, has smooth topography and is not be able to account for sub-mesoscale variability. Despite this, the spatial distribution of the variability compares well with pCO_2 estimated from satellite proxies (from Chapter 3), with high variability in the MIZ and Malvinas Confluence, but there are regions where the higher variability is under-represented, such as the wake of the Kerguelen Plateau. These discrepancies between the standard deviation of the model and the estimated ensemble are not peculiarities unique to BIOPERIANT05, but rather a reflection of the state-of-the-knowledge in current modelling capabilities.

5.2.1 Support Vector Regression approach

The decision was made to use SVR in this chapter as estimates from Chapter 3 suggest that SVR is more robust to sparse data.

Simulated training datasets are used to train individual SVRs, where the optimal hyper-

parameters are estimated using the nested grid-search described in Section 3.2.2. Epsilon (error margin) is manually set to 5 μatm unless otherwise stated. The proxy variables used in the simulated SVR are: sea surface temperature (SST), chlorophyll-a (Chl-a),sea surface salinity (SSS), mixed-layer depth, N-vector coordinates (after Gade 2010), and the cosine and sine transformations of the day of the year. No noise was simulated for the model variables, thus perfect knowledge is assumed. Similarly, no cloud cover is included implying perfect knowledge of Chl-a. Without the issue of cloud cover, the SVR was trained at the model output resolution (5-day $\times$ 0.5°), which is a much higher temporal resolution than used for observations (16-day and monthly for high and low resolutions respectively).

The partial pressure of CO_2 is then estimated with the trained SVRs. Air-sea CO_2 fluxes are calculated using Section 2.6 with estimated ΔpCO_2 and model winds (Figure 5.A.1), SST, SSS and sea ice cover (as a fraction).

Three different sampling platforms are tested: the SOCAT dataset replicated in the model to represent ship based sampling; randomly placed moorings; and profiling floats that are simulated in BIOPERIANT05. These are now explained in full detail.

5.2.2 Ship based sampling

The SOCAT v3 dataset (Bakker et al., 2016) is used to simulate ship based sampling – this dataset is described in detail in Section 2.2.1. The distribution of measurements in BIOPERIANT05 is shown in Figure 5.2. The diagnostic training plots are in the appendix (Figure 5.A.3), which shows that SVR achieves better scores ($r^2 = 0.83$) in the idealised model environment compared to SVR run with observations ($r^2 = 0.63$ shown in Figure 3.4). This is likely due to the fact that BIOPERIANT05 ΔpCO_2 is strictly defined by model equations, which use some of the chosen proxies to estimate ΔpCO_2.

5.2.3 Mooring locations

Moorings by definition are stationary sampling platforms, which traditionally means that they are anchored to the sea floor – making deployments costly, dangerous and laborious. The development of wave gliders, wave powered remotely operated sampling platforms, has changed

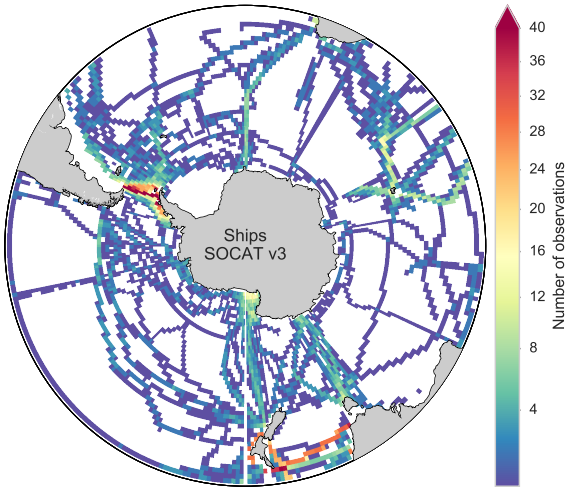

Figure 5.2: Map showing the spatial distribution of the number of samples for ship based sampling on the BIOPERI-ANT05 grid.

how we view surface moorings (see `https://www.liquid-robotics.com` for more information). Monteiro et al. (2015) deployed a high precision pCO_2 enabled wave glider in pseudo mooring mode, where the wave glider maintained an octagon sampling pattern (with a 20 km diameter). Wave gliders are reusable platforms, but typically have to be deployed and retrieved by ship. This makes the notion of a large number of moorings in the Southern Ocean far more economically and logistically feasible than the traditional concept of a mooring.

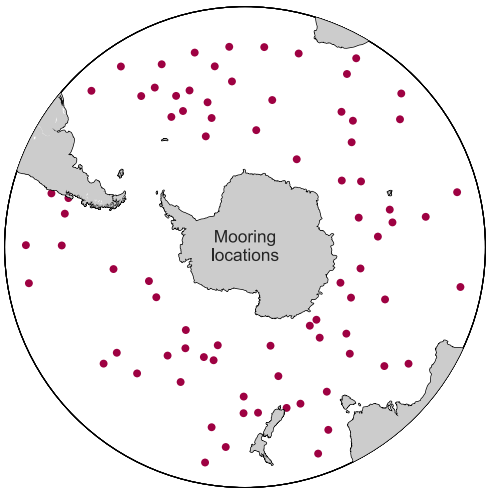

Figure 5.3: Map showing the location of 80 randomly placed moorings.

Majkut et al. (2014) simulated a random mooring sampling strategy and found that 200 moorings[1] were required to adequately (to within 1 molC m^2 yr^{-1}) constrain air-sea CO_2 fluxes if data is interpolated spatially (inverse distance weighted interpolation). Here a similar approach is taken. The sensitivity of errors to the number of randomly placed moorings is tested in the context of estimating pCO_2 from satellite proxies with an SVR. The random placements are uniformly distributed in perennially open waters, meaning that the MIZ is not sampled. It is assumed that the moorings sample at a high temporal frequency, which for the model is at the 5-day average time step. The performance of 20, 40, 60, 80, 100 and 125 moorings is tested on a subset of training data (2003 through 2008). To gain a more robust estimate of uncertainties, five iterations of randomly placed moorings are run. An optimal hyper-parameter grid search is performed independently for each iteration of random moorings. Ideally more than five iterations should be run, but the computational cost of predicting with 5-day × 0.5° data is high and time consuming. In future work the number of iterations will be increased to improve the robustness of the uncertainties. Once the ideal number of moorings is established, a single iteration of randomly placed moorings will be used for the intercomparison of sampling platforms.

5.2.4 Float simulations

Profiling floats are a Lagrangian sampling platform that profile the water column once every ten days using pneumatic oil for buoyancy control (Feder, 2000). This sampling approach has become synonymous with the Argo float program – a global array of > 3800 floats. A typical sampling cycle of an Argo float is as follows: 1) a float sinks down to 1000 m where it remains for the majority of the cycle; 2) on automated command the float descends to 2000 m and then rises to the surface; 3) when the float reaches the surface, the measured data is sent to a server via satellite link and the process begins again.

These floats typically measure pressure, temperature and salinity (fulfilling the function of a CTD). However, in recent years there has been a drive towards equipping these floats with biogeochemical sensors: oxygen, chlorophyll, nitrate and more recently pH (Johnson et al., 2009, 2016; Biogeochemical-Argo Planning Group, 2016). The Southern Ocean Carbon and Climate Observations and Modelling (SOCCOM) project is a six year initiative that aims to deploy ~ 200

[1] The authors refer to their simulated sampling platforms as stationary floats

floats in the Southern Ocean, amongst other goals (Russell et al., 2014). Figure 5.4a shows the current distribution of the 81 floats deployed to date.

Measuring pH with the SOCCOM floats is possible due to an improvement in the accuracy of solid state pH sensors in the last decade. Early studies using mooring based pH sensors found that the instrument had relatively good precision (±0.002), but suffered from considerable drift (Cullison Gray et al., 2011). In their study, Cullison Gray et al. (2011) calculated pCO_2 from pH and total alkalinity, where the latter was derived with the empirical relationship of total alkalinity with salinity and temperature after Lee et al. (2006). This calculation contributes additional uncertainty to pCO_2 estimates. Cullison Gray et al. (2011) found that the sampling error of pCO_2 was ±13 μatm including the conversion from pH – this value is also used by Majkut et al. (2014), the same assumption is made in this study. Additionally, to account for sub-mesoscale variability of pCO_2 in surface water 7.5 μatm of variability is added, thus increasing the amount of simulated noise to 20.5 μatm. The estimate of 7.5 μatm is based on the 10-day rolling standard deviation of hourly pCO_2 measurements made with a wave glider at 43°S, 8°E from October 2013 to February 2014 (Section 5.B). Normally distributed noise is thus added to pCO_2 for the float locations ($\mu = 0$; $\sigma = 20.5$ μatm). Note that with the added noise, the error margins of the SVR were increased to 20.5 μatm to avoid overfitting to the noise. Lastly, it is assumed that there is no drift – a recent study showed success in correcting for float based pH drift by using deep waters as a reference (Johnson et al., 2016).

In their study Majkut et al. (2014) use stationary floats (moorings) instead of Lagrangian moorings based on the assumption that no spatial sampling bias is added due to the Lagrangian nature of the floats (Kamenkovich et al., 2011). However, the dominant role of the ACC in the Southern Ocean could induce a sampling bias as shown by Resplandy et al. (2014) found that surface floats were biased to dynamic regions. To account for this potential bias, 200 float trajectories are simulated (as the SOCCOM project aims). Simulated deployment locations are based on the CLIVAR/GO-SHIP repeat hydrography cruises (Hood et al., 2010). Deployments occur every 5° along cruise tracks and timing coincides with past cruises (as shown in Figure 5.4b). These data were obtained from `http://cdiac.ornl.gov/oceans/RepeatSections`.

Float trajectories are calculated from surface and 1000 m depth current velocities in the model, where it is assumed that floats spend 10% of the time at the surface, and 90% of the time at 1000

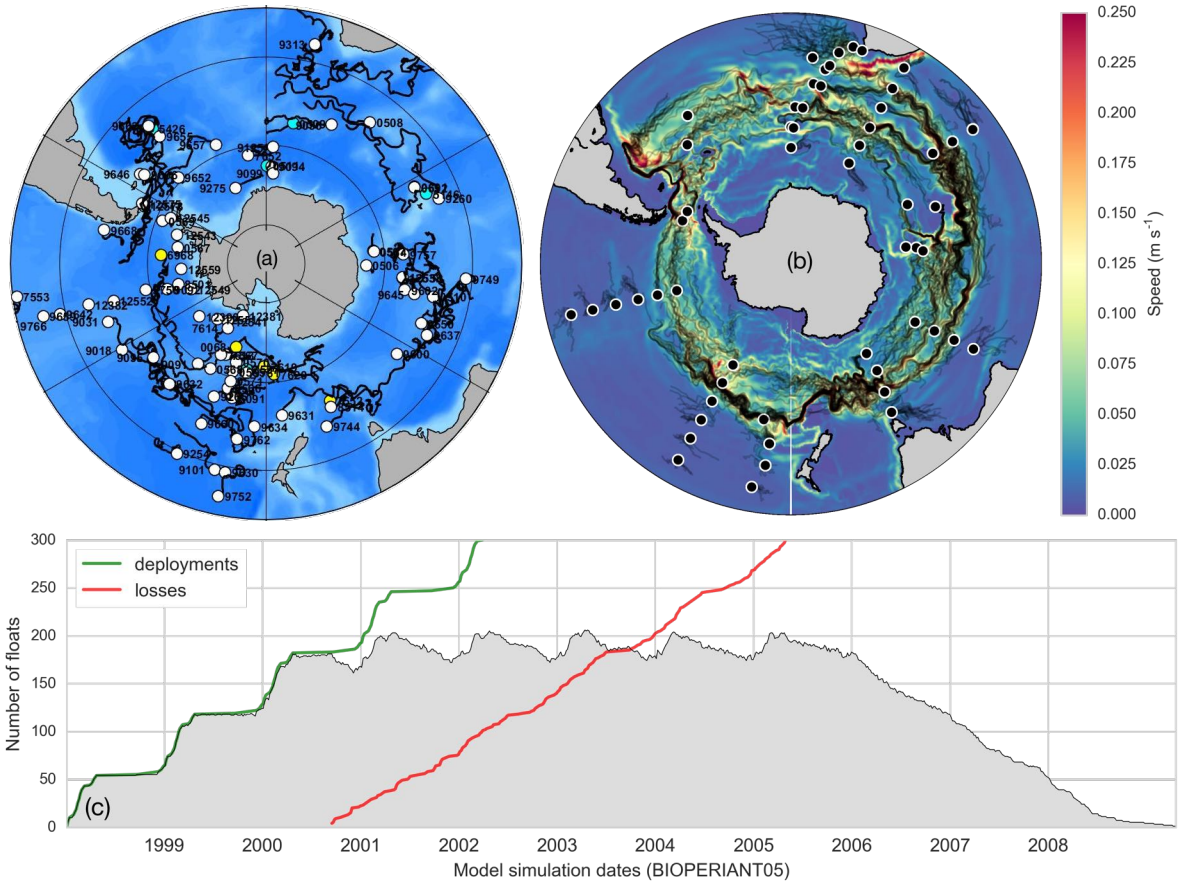

Figure 5.4: (a) Location of SOCCOM floats in the Southern Ocean in February 2017. White dots show active floats equipped with biogeochemical sensors, yellow dots show floats without these sensors and cyan dots show inactive floats. Black lines show the tracks of the floats. (`http://soccom.princeton.edu`). (b) Simulated floats in output of the BIOPERIANT05 configuration of a NEMO–PISCES model. Deployment locations (black dots, white outline) are based on GO–SHIP cruises. The float tracks are shown by the thin black lines. The underlay shows mean current speed of the model in m s^{-1}. (c) The number of sustained floats in the BIOPERIANT05 float simulation experiment (as in figure b). Deployments (green) and losses (red) of floats are shown to demonstrate the rates of each.

m. A 0.1 : 0.9 weighted average velocity of surface and 1000 m velocities were used to calculate the trajectories of the floats. In the calculation, float locations are updated every eight hours (where model data is saved as five day averages). Surface pCO_2 is sampled at a 10-day interval to mimic the sampling strategy of Argo/SOCCOM floats. Additionally it is assumed that floats have a lifespan of 3 ± 0.4 years (uniformly distributed). The outcome is that 64 floats are deployed annually for eight years maintaining roughly 200 floats in the Southern Ocean for 5 years of the time-series (Figure 5.4c). The frequency of sampling per grid cell is shown in Figure 5.5 – the profiling floats easily have the best open ocean coverage.

A SVR is then used to estimate pCO_2 using the same training procedure described in Sec-

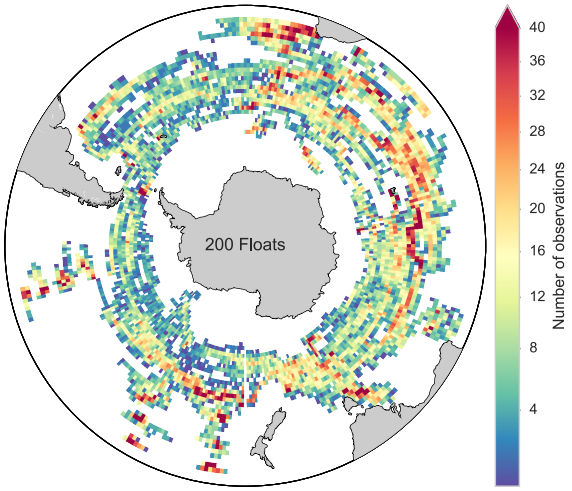

Figure 5.5: Map showing the spatial distribution of measurements made by 200 profiling floats simulated in BIOPERIANT05 output. The float trajectories were calculated based on a weighted average (0.1 : 0.9) of surface and 1000 m model velocities. The measurements shown in the figure are for a 10-day sampling interval.

tion 3.2. This is done for scenarios with and without added noise. Diagnostics for hyperparameter selection and training of the noisy training can be seen in the appendix (Figure 5.A.5). The addition of noise results in very poor r^2 scores (0.18) in the cross validation training step.

5.2.5 Multi-platform integrated sampling strategy

Lastly, two mixed sampling strategies are tested: ship + moorings and ship + floats. These multi-platform approaches may be a closer representation of reality as ship based measurements are likely to continue as opportunistic sampling on Antarctic re-supply vessels. Moreover, both moorings and floats typically require ship based deployment. Ship based measurements of pCO_2 are thus concomitant with either moorings or floats. In the simulation, the approaches are combined (*e.g.* Figure 5.2 representing ship measurements is combined with mooring measurements shown in Figure 5.3).

5.3 Results

5.3.1 Optimal number of random moorings required

Figure 5.1 shows the out-of-sample (for all estimates) root mean squared error (RMSE) of pCO_2 of randomly placed high frequency moorings (where sampling frequency matches model resolution of five days). As expected, the error decreases as the number of moorings is increased (decreasing from 8.6 μatm with 20 moorings and 6.1 μatm with 125 moorings), but the improvement is marginal and less than expected, most likely due to the fact that estimates in the marginal ice zone (MIZ) are included (moorings are not placed in this region). Root mean squared error estimates improve up until 80 moorings (6.6 μatm) – no improvement is seen when the number increases to 100 moorings (6.8 μatm), but again improves at 125 moorings. This may be an artefact of a low number of iterations, where the locations of the random moorings could have a significant impact on the outcome. Eighty randomly place moorings are used for the rest of this study, with the locations of these moorings shown in Figure 5.3. Note that 80 moorings will be compared with Majkut et al. (2014) for FCO_2 in Section 5.3.3.

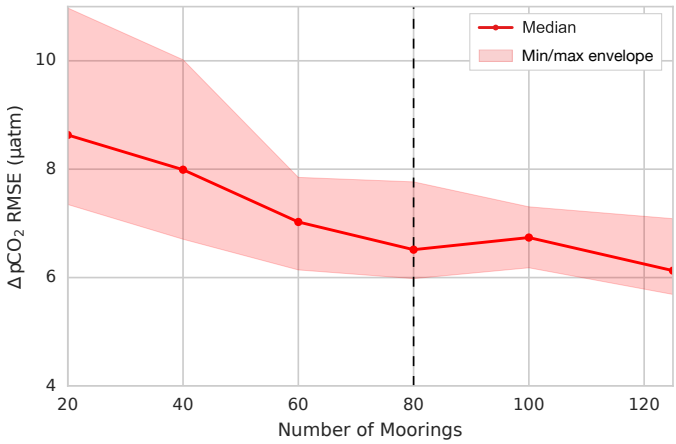

Figure 5.1: The root mean squared error (RMSE) of pCO_2 estimated using an SVR trained with a varying number of randomly located moorings. Each step was iterated 5 times. The dark red line shows the median result and the envelope shows the minimum and maximum RMSE of the iterations. The dashed line shows the number of random moorings used throughout the rest of the study.

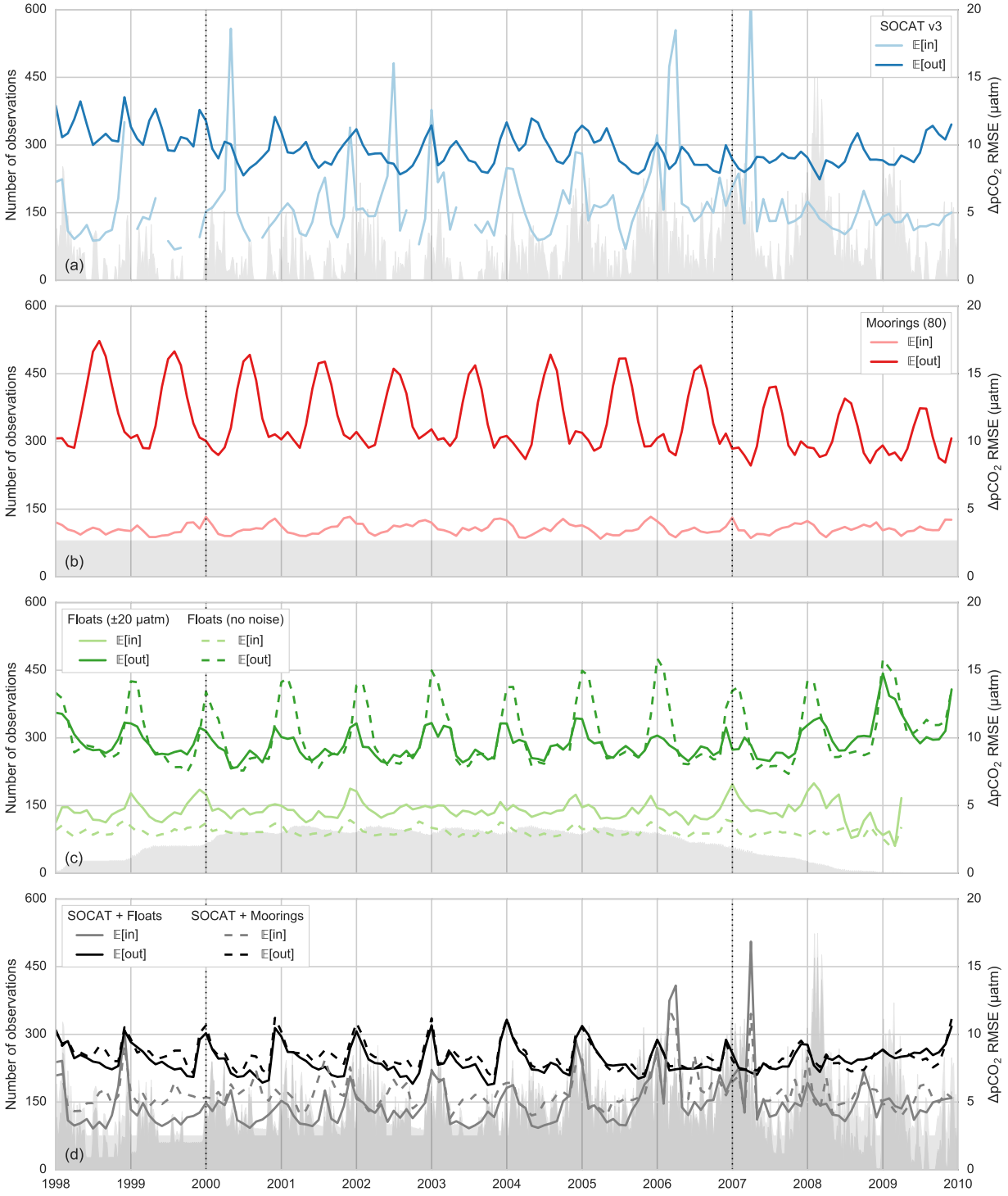

Figure 5.2: Plots showing the root mean squared error (RMSE) for each of the sampling platforms (coloured lines on the right axis) and the number of observations per month (grey fill on the left axis). The lighter shades show the in-sample error ($\mathbb{E}$[in]) and darker shades show the out-of-sample error ($\mathbb{E}$[out]). See the key on each figure for solid and dashed line definitions. The thin dotted vertical lines mark where the time-series is cut in further analyses to exclude sparse float distribution before 2000 and after 2007.

Table 5.1: The in- and out-of-sample errors for the different sampling methods tested in this study. The in-sample error is the error calculated from all the training points and the out-of-sample error is the difference between BIOPERIANT ΔpCO_2 and the SVR estimated ΔpCO_2. For more information on the different datasets see the text.

Dataset	**In-sample error** (μatm)	**Out-of-sample error** (μatm)
Ships	9.37	9.79
80 Moorings	3.57	11.75
200 Floats (no noise)	3.09	10.22
200 Floats ($\pm$20.5 μatm)	4.72	9.74
Ship + Moorings	7.53	9.33
Ship + Floats	7.53	8.34

5.3.2 SVR estimates of pCO_2

In this section the error estimates of ΔpCO_2, for both temporal and spatial, are reported (Figures 5.2 and 5.3 respectively). Figure 5.2 shows the in- and out-of-sample errors ($\mathbb{E}$[in] and $\mathbb{E}$[out] respectively). The in-sample errors are calculated from estimates corresponding only with the training data – this is the error estimate that would be used in a real problem where the true solution is not known. The out-of-sample errors are calculated from estimates of the entire domain. The time averaged in-sample and out-of-sample errors are summarised in Table 5.1. The number of samples per time step are also shown as the grey fill for each sampling approach. Figure 5.3 shows maps of the temporally averaged out-of-sample errors.

The sampling distribution of ship based sampling shows increased effort in summer (Figure 5.2a), which, counter-intuitively, occasionally leads to worse in-sample errors. This is due to increased complexity that originates from greater sampling effort in high variability regions, such as high EKE regions and MIZ (Figure 5.1b). The median of the in-sample error is much lower than the out-of-sample error, but the mean values are similar (9.37 and 9.79 μatm respectively) due to the large spikes in uncertainty during summer. The out-of-sample error is less variable than the in-sample error, though the interannual trend shows that estimates improved with the initial increase in sampling effort (1998 to 2001). The increased sampling effort from 2004 onward results in marginally improved RMSEs in summer, but the gains are not proportional to the increase in sampling effort.

In-sample RMSE of 80 moorings is the second lowest (3.57 μatm), but the out-of-sample

(11.75 μatm) error is much larger than any of the other sampling platforms (Figure 5.2b). This is due to large winter uncertainties, with average winter RMSE of 14.76 μatm where the average summer RMSE is 10.20 μatm. It is likely that these errors are contributed by the MIZ (as shown in Figure 5.3a) where moorings are not placed.

Uncertainty estimates for floats without noise and the floats with noise are shown in Figure 5.2c. Floats without noise have the lowest in-sample RMSE (3.09 μatm), but the out-of-sample error is larger than that for floats with the simulated noise (10.22 and 9.74 μatm for no-noise and $\pm$20 μatm respectively). This outcome is surprising, particularly if the low grid-search scores of the SVR with noise are considered ($r^2 = 0.18$). The "injection of noise" or jitter to target variables is a machine learning practice that is used as a computationally efficient way of regularizing estimates, in other words ovoid overfitting (Reed et al., 1992; Wright et al., 2000; Neelakantan et al., 2016; Shuryak, 2017). The result is that pCO_2 estimated from floats with the added noise have the lowest out-of-sample error of any of the single platform approaches (see Table 5.1).

The distribution of floats is not continuous throughout the period, with deployments starting in 1998 and ending in 2006. This results in a "head" and "tail" of the data where measurements are sparse. Including the head and tail results in a larger out-of-sample RMSE of 9.74 μatm (as reported in Table 5.1) and excluding these results in an RMSE of 9.35 μatm (for floats $\pm$20.5 μatm). The in-sample error continues to report low scores ($\sim$ 5 μatm) even when measurements are sparse. The poorly sampled head and tail periods are removed in further analyses of FCO_2 as shown by the dotted lines in Figure 5.2 leaving a seven year time-series from 2000 to, and including, 2006.

The integrated mixed-platform approaches have the lowest out-of-sample errors with the ship based + floats performing significantly better than ship based + moorings (8.34 and 9.33 μatm respectively with $p \ll 0.01$). Compared to the persistent sampling platforms (moorings and profiling floats), the integrated approaches have large in-sample errors due to modulation by the more complex ship based data (Table 5.1). A strong seasonality is observed in the out-of-sample errors, suggesting that even with the increased sampling effort is still not able to resolve the high variability of summer pCO_2 (Figure 5.2d). The similarity in the seasonality of the out-of-sample errors may seem surprising, given that mooring RMSE is large in winter. This shows that the ship and mooring based sampling compliment each other well, in other words the methods play to

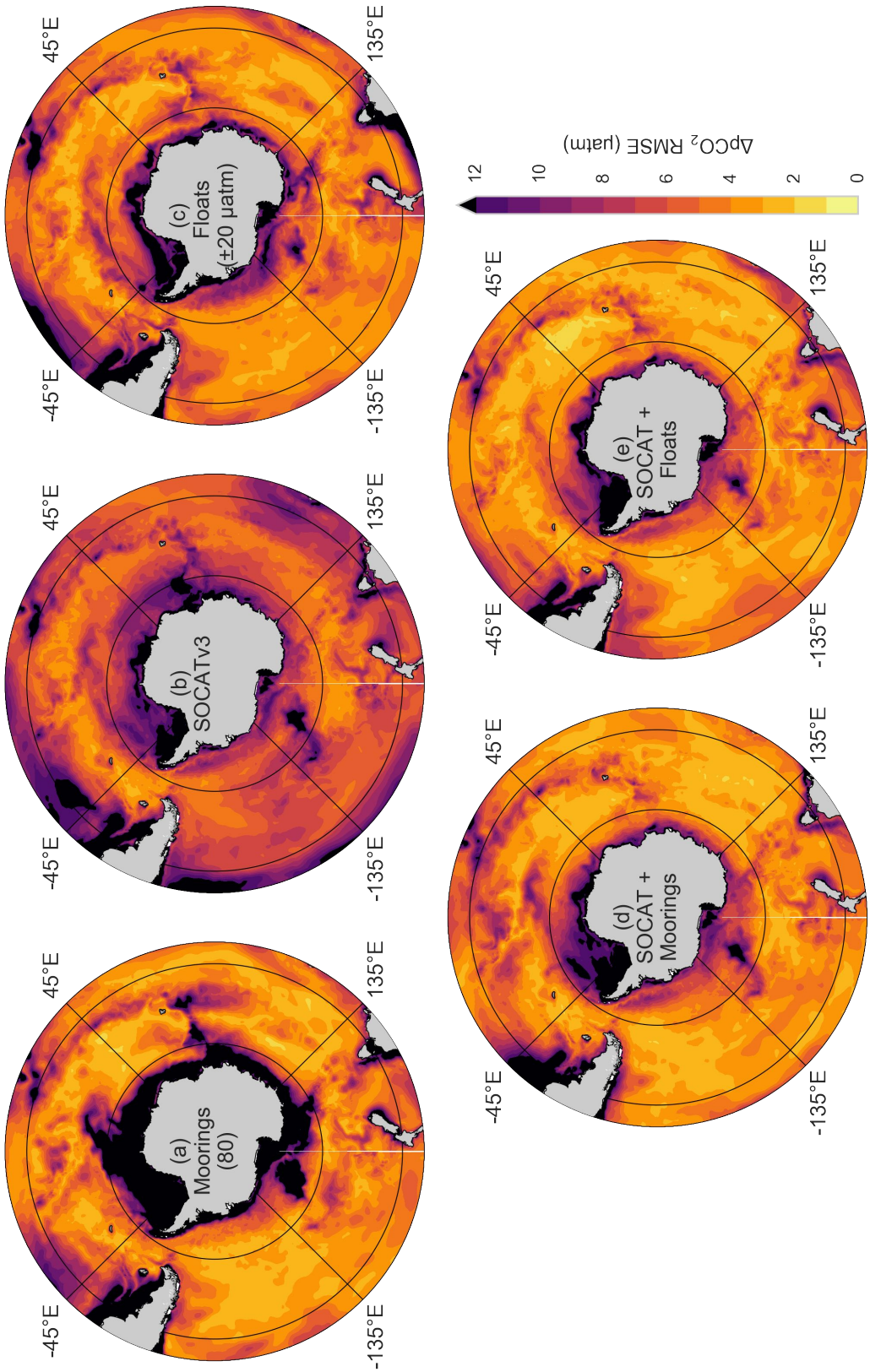

Figure 5.3: Root mean squared error of ΔpCO_2 for the various sampling approaches used in this study. The top row shows single platform approaches and the bottom row shows the mixed platform approaches.

each others' strengths.

The spatial distribution of ΔpCO_2 RMSEs ($\mathbb{E}$[out]) is shown in Figure 5.3. One of the features common to all approaches are the error "hot-spots" located in the: MIZ, Malvinas Confluence, Agulhas Retroflection, wake of the Kerguelen Plateau and the coastal waters of Australia. The magnitude of the errors in these hotspots differs for each of the approaches.

Ship based open ocean estimate errors compare poorly with other methods with the majority of errors being > 6 μatm. Though ships are better able to constrain the MIZ than other methods. Conversely, moorings have poor estimates in the MIZ, which corresponds with the high winter RMSEs in Figure 5.2b. Compared to other methods, moorings are not able to capture the variability in the wake of the Kerguelen Plateau well. Floats are better able to constrain this region as well as the MIZ (Figure 5.3c). However, the open ocean RMSEs are slightly larger for floats compared to moorings, where moorings typically score < 4 μatm for the open ocean and floats < 6 μatm. The integrated approaches nearly always improve on the individual counterparts.

5.3.3 Biases of air-sea CO_2 Fluxes

While estimating pCO_2 accurately is an important metric to assess the efficacy of a sampling approach, the final goal is to constrain air-sea CO_2 fluxes in order to resolve changes in variability and trends. However, regions with large pCO_2 errors, which could contribute significantly to the mean ΔpCO_2 RMSE, may not have the same impact on FCO_2 RMSE as winds may not be strong over these regions. And more importantly, regions that may have low ΔpCO_2 errors could contribute significantly to the FCO_2 RMSE if winds are strong over these regions.

This is demonstrated by moorings that achieve the highest RMSE for pCO_2, but scores very well for the annually integrated FCO_2 (0.063 PgC yr^{-1}) as shown in Figure 5.4b. Floats also perform well (0.068 PgC yr^{-1}), less than half the RMSE of ship based samlping, which has a FCO_2 RMSE of 0.142 PgC yr^{-1}. The errors of ship based estimates of FCO_2 are often largest during winter and spring, coinciding with periods of few measurements. Exceptions to this may be due to the increased variability of ΔpCO_2 during summer (as shown in Figure 5.1). The RMSEs of the other approaches do not have the same seasonality, despite strong seasonal cycles of ΔpCO_2 RMSE shown in Figure 5.2. There is no gain in FCO_2 uncertainties between the mooring only approach and the ships + mooring approach, both with RMSE scores of 0.063 PgC yr^{-1}. The

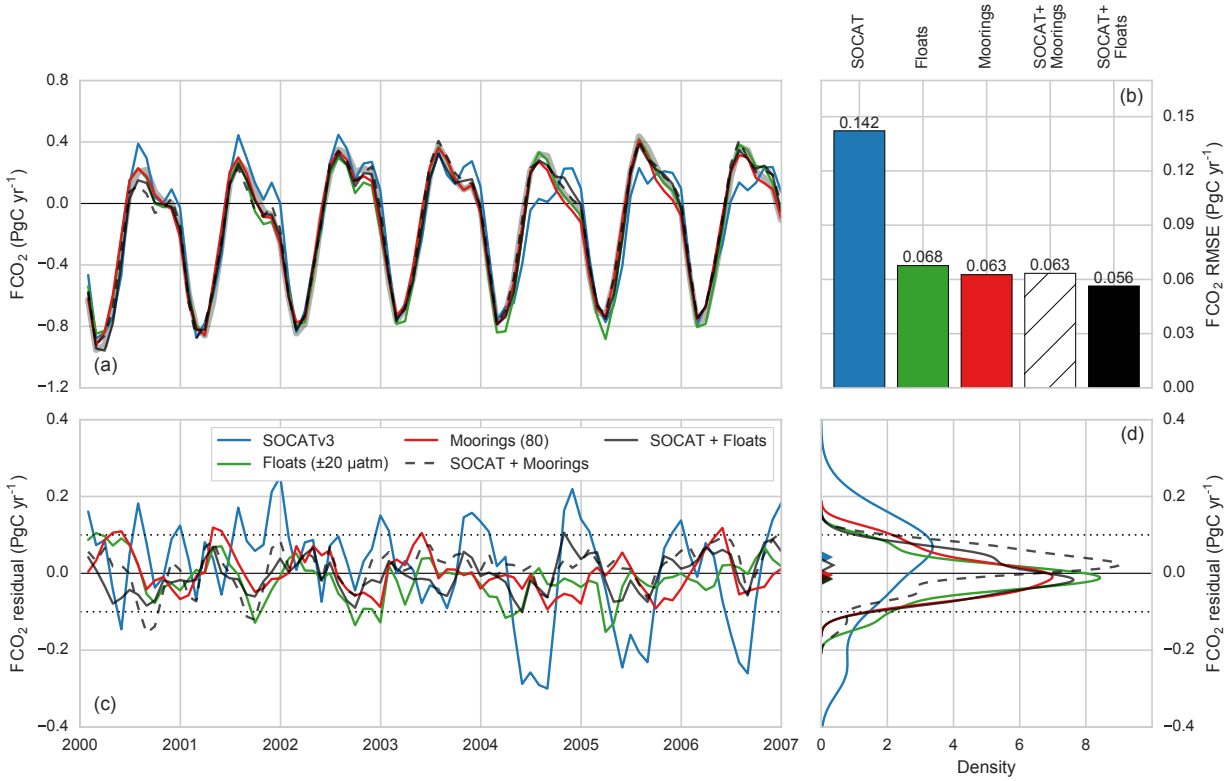

Figure 5.4: (a) Estimates of annually integrated air-sea CO_2 fluxes for the Southern Ocean. The thick underlying grey line shows the true flux. The RMSE for these estimates is shown in (b). The residual from the true flux and each of the estimates is shown in (c) and the kernel density estimate of the residual distribution is in (d). The horizontal dotted lines in (c,d) show the 0.1 PgC yr^{-1} threshold established by Sweeney et al. (2002) that is required to estimate the seasonal cycle of the Southern Ocean with 90% accuracy.

mixed platform ships + float approach performs much better than the ships or floats alone with an RMSE score of 0.056 PgC yr^{-1}.

The maps of FCO_2 RMSE (Figure 5.5) reveal that there is consistency in the distribution between each of the methods. This to be expected as the same wind speed, temperature and salinity are used to calculate FCO_2. These distributions of error are similar to the ΔpCO_2 error hot-spots with the exception of the MIZ. These errors are largest for the mooring approach (> 1.5 molC m^{-2} yr^{-1}) as the moorings may be too sparse to capture the variability in these error "hot-spots". Despite these large localised errors, moorings still have the lowest integrated FCO_2 RMSE (of the single platform approaches) due to high precision in large regions such as the Pacific. The error hot-spots are also present in other methods, but to a lesser extent than in the moorings with the integrated approaches best resolving the error hot-spots (Figure 5.5d,e).

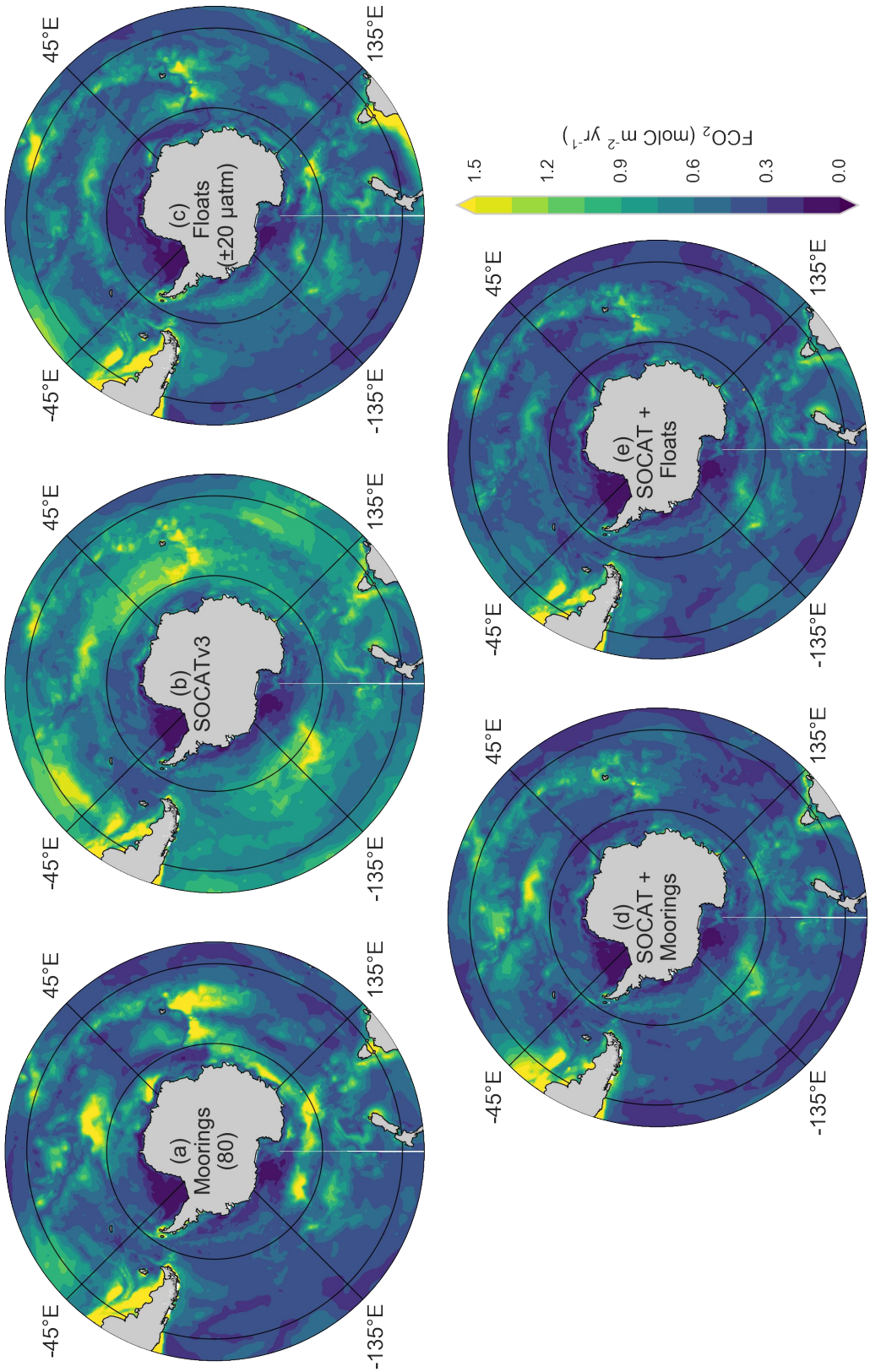

Figure 5.5: RMSE of air-sea CO_2 flux in the Southern Ocean for three different sampling methods: (a) ship based sampling, (b) 80 randomly placed moorings, and (c) ~ 200 Lagrangian profiling floats. Combinations of ship + moorings (d) and all platforms (e) are also considered as viable sampling solutions.

5.4 Discussion

5.4.1 Threshold analysis

In their study Majkut et al. (2014) found that, to capture the seasonal cycle of their OSSE, using the results from the GFDL-ESM2M model, with 99% accuracy, estimates needed to be within 1 molC m^{-2} yr^{-1} of the true fCO_2 value (see Figure 5.A.2). This was achieved with 200 floats even with the addition of uncertainties of up to 50% for fCO_2. This same threshold is applied here (Figure 5.1), though it is recognised that this threshold may be different in the BIOPERIANT05 output. In general these results compare well with the results of Majkut et al. (2014) who used objective mapping with inverse distance weighting to interpolate data.

Here I show that empirical modelling of pCO_2 using SVR is far more efficient than inverse distance weighted interpolation with only 80 moorings achieving similar results to 200 floats suggested by Majkut et al. (2014). This suggests that, in the case of moorings (Figure 5.1a), fewer platforms are required to achieve a similar result if machine learning methods are used. However, the error hot-spot in the wake of the Kerguelen Plateau, though a small region, is a large source of uncertainty for moorings, where estimates only meet the required threshold only ~ 50% of the time. This is due to the large ΔpCO_2 errors caused by high variability that is further exacerbated in the fCO_2 errors by high wind speeds over the Indian sector of the Southern Ocean (Figure 5.A.1).

Conversely, all platforms perform well in the MIZ, achieving a flux estimate within 1 molC m^{-2} yr^{-1} more than 90% of the time-series (Figure 5.1). This is due to seasonal sea ice cover and lower average wind speed over the MIZ that act to dampen outgassing of CO_2. This has the implication that lower ΔpCO_2 accuracy is required in this region of the Southern Ocean.

While performing better than moorings, floats also exceed the threshold more often (> 50% of the time) in the error hot-spots. The ship based estimates are only able to achieve the threshold < 20% of the time for the majority of the Southern Ocean, but does better to constrain large hot-spot errors.

Lastly, the benefit of integrated sampling is clear as these mixed-platform approaches are able to curtail the errors that exceed the threshold more often, particularly in the hot-spot regions (Kerguelen Plateau, south of the Campbell Plateau and Argentine Sea).

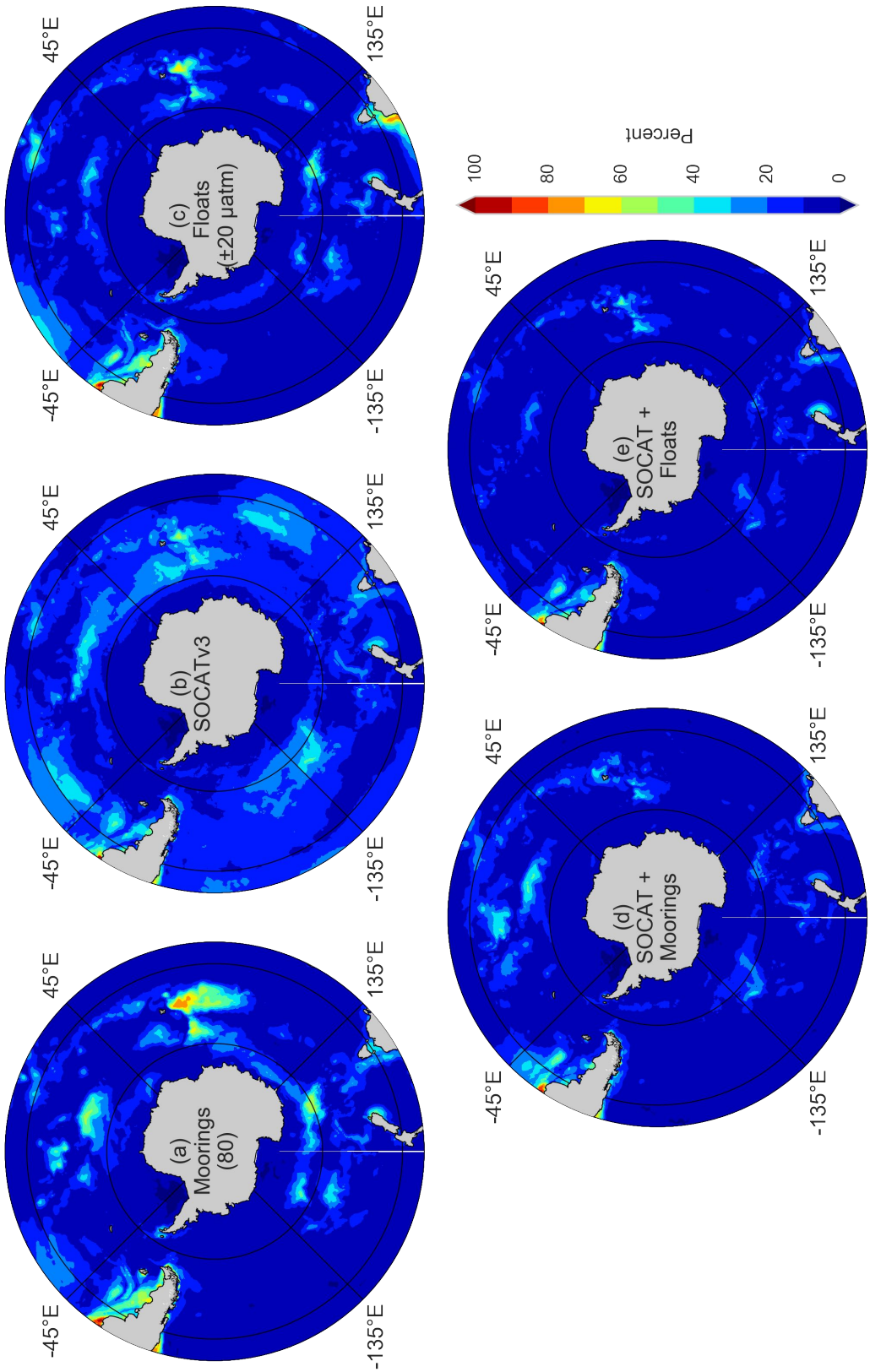

Figure 5.1: Percentage of observations with an error of greater than 1 molC m^{-2} yr^{-1}. This is a direct comparison with the figure of Majkut et al. (2014) which is shown for 200 floats in their figure Figure 5.A.2.

5.4.2 Ships: saturated efficacy

In their study, Lenton et al. (2006) found that Southern Ocean pCO_2 needs to be sampled by a 3° × 30° (latitude by longitude) grid every three months in order to resolve FCO_2 to within an uncertainty 0.1 PgC yr^{-1}. Based on the CO_2 sampling strategy of the 2000's, Lenton et al. (2006) inferred that longitudinal sampling would have to be doubled, but this still required sampling during winter – an unrealistic expectation for ships to fulfil due to the inclement winter conditions of the Southern Ocean. While sampling effort has increased in the Southern Ocean since 2006, the majority of this effort has been during summer, meaning that the winter bias still exists.

It is then not surprising that FCO_2 calculated from ship based empirically estimated ΔpCO_2 is not able to meet the 0.1 PgC yr^{-1} threshold, where the RMSE was 0.142 PgC yr^{-1} and the threshold was met only ~ 50% of the time (as shown in Figure 5.4b,c). There is thus room for improvement, particularly if we want to close the gap in our understanding between observations and process models, which may require better constraints and understanding of both seasonal and intra-seasonal variability. This improvement will not come from an increase in ship based summertime sampling effort, as shown by Lenton et al. (2006) and supported by the results. Here results show that the increased sampling effort in the late 2000's did not improve ΔpCO_2 (Figure 5.2) or FCO_2 RMSEs, with winter uncertainties exceeding the threshold 0.1 PgC yr^{-1} as frequently as when sampling effort was lower (as shown in Figure 5.4c).

This is not to say that ship based sampling efforts should be decreased, which is an unlikely scenario as many of the measurements in recent years have been made through established routes by Antarctic and Sub-Antarctic resupply vessels. Ships are also needed for the deployment (and retrieval in the case of wave gliders) of autonomous sampling platforms. Dedicated science cruises will likely also continue along GO-SHIP cruise tracks as these expeditions provide deep profiles of the ocean (> 2000 m), crucial for the understanding and monitoring of meridional overturning (Hood et al., 2010; Talley et al., 2016). Ships also aid our understanding of the role of mesoscale variability in surface pCO_2 and FCO_2. Ships are able to traverse large mesoscale features, such as eddies, in a short period, thus giving insight to spatial variability with very little temporal change. However, it needs to be recognised, as results show, that we will not be able to adequately resolve FCO_2 with ships alone.

5.4.3 Profiling floats: the problem of intra-seasonal variability

The OSSE results show that annually persistent sampling platforms (moorings and profiling floats) are better able to resolve the seasonal cycle of fCO_2 by closing the winter sampling gap left by ships (Figures 5.4 and 5.5). Of these two approaches, profiling floats are more likely to be the sampling platform that fills the gap due to the low input effort after deployment and scientific utility beyond resolving fCO_2. The water column profiles that floats measure can be assimilated into predictive climate models and aid our understanding of the current and future state of the Southern Ocean (Russell et al., 2014).

However, there is a caveat that has to be considered in the context of the OSSE approach. Process models (such as BIOPERANT05) do not yet correctly represent CO_2 in the Southern Ocean, with many of the models used in climate predictions (CMIP5 models) being inconsistent in the representation of the seasonal cycle of pCO_2 in the Southern Ocean (Lenton et al., 2013; Mongwe et al., 2016). One of the hypotheses put forward for this poor representation of pCO_2 is that coarse resolutions are not able to resolve sub-mesoscale processes (Mahadevan et al., 2010; Lévy et al., 2012, 2013; Nicholson et al., 2016). Studies have shown that meso- and sub-mesoscale processes can be regionally important in regulating the thermal – DIC controls of ΔpCO_2 (Mongwe et al., 2016).

Using a high-resolution time-series of pCO_2 in the Sub-Antarctic Zone (~43°S, 8°E) Monteiro et al. (2015) showed that intra-seasonal variability is a dominant mode in the SAZ and not resolving this may lead to severe aliasing by point measurements of pCO_2. This has important implications for profiling floats, which only sample the surface once every 10 days. In their study, Monteiro et al. (2015) used a wave glider to sample pCO_2 hourly for four months in a mooring configuration – the data is shown in Figure 5.B.1a. Figure 5.B.1b shows the 10-day rolling standard deviation of pCO_2 for this time-series for which the mean is 7.5 μatm. This uncertainty can be as high as 20 μatm in early summer when the potential for both mixing and stratification are still high (Mahadevan et al., 2012). Here we represent this variability as normally distributed noise (as described in Section 5.2). This is the same approach taken by Lenton et al. (2006) and Majkut et al. (2014), though both studies used a more conservative sub-grid variability estimate of 3 μatm, though their estimate is likely more representative of less dynamic regions as it was based on five meridional transects south of Australia. Contrary to this approach, Monteiro et al. (2015) argue

that, in regions characterized by strong sub-mesoscale responses to storms, this intra-seasonal noise/variability may play an important role in determining the error of mean annual flux.

If we consider surface pCO_2 variability purely as noise, the implications are minimal, if not advantageous, when using a proxy based interpolation approach (as done in this study). The SVR trained with "noisy" data performs better than the float simulation to which no noise is added (where RMSEs are 9.47 and 10.22 μatm respectively). In other words, the SVR without noise may be overfitting to measured data. This is an important finding as the addition of noise to the current SOCAT dataset could lead to more accurate estimates of ΔpCO_2 by "smoothing" the output of the estimates, thereby arriving closer to the true function (Wright et al., 2000). However, if intra-seasonal variability is in fact an important determinant of mean seasonal flux, then treating intra-seasonal variability as noise would induce errors to the mean seasonal flux.

In the case that intra-seasonal variability contributes significantly to mean annual FCO_2, improving estimates could be achieved by increasing sampling frequency of profiling floats, as suggested by Monteiro et al. 2015. Their concept of adaptive sampling frequency was extended to a preliminary OSSE study (shown in Section 5.C) using high resolution model output (daily $\times \frac{1}{12}°$) to estimate the required sampling rate of pCO_2 (to constrain FCO_2) in the Atlantic sector of the Southern Ocean. This work demonstrates that profiling floats need to sample pCO_2 at a two day interval in highly dynamic regions to constrain FCO_2 to within 10% of the annual flux (Figure 5.2). The regions where a high sampling rate is required coincide with regions of high eddy kinetic energy (EKE), which can be derived from remote sensing data (Hogg et al., 2015; Patara et al., 2016). This finding could pave the way for an adaptive sampling strategy for profiling floats that adjusts the sampling frequency of floats based on the satellite estimated EKE Monteiro et al. (2015). Note that this preliminary study does not consider the correlation length-scales of pCO_2. Lenton et al. (2006) approached the problem of both spatial and temporal sampling frequencies, but the regional variability of pCO_2 was not considered, meaning that effort was uniform throughout the Southern Ocean. Jones et al. (2012) found that the spatial correlation length-scales of pCO_2 varied zonally and meridionally implying that uniform sampling effort does not have to be applied in different regions to resolve pCO_2 accurately. Moreover, their findings show that regions with high EKE should be sampled at least every 50 km (Jones et al., 2012).

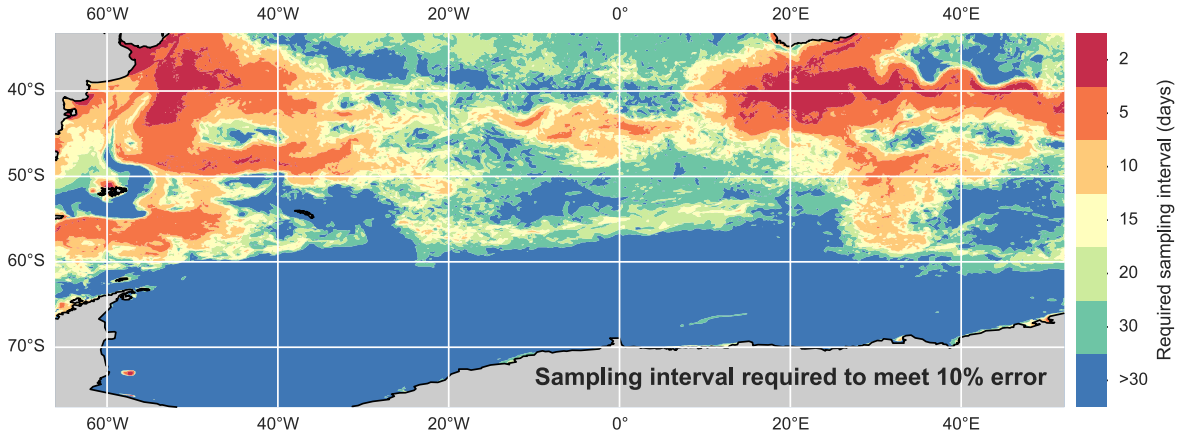

Figure 5.2: The sampling interval required to estimate FCO_2 to within 10% of the annual flux. Details of this preliminary study are shown in Section 5.C.

The implementation of the Bio-Argo float program seems inevitable, as it builds on the success of the Argo program and is already being led by the SOCCOM group (Russell et al., 2014). It may seem that this chapter is overly critical of profiling floats, but the points raised here should be considered as it is recognised that profiling floats are the most feasible solution for resolving winter FCO_2 in the Southern Ocean. Biogeochemical-Argo Planning Group (2016) proposed a global effort to maintain 1000 biogeochemical Argo (Bio-Argo) floats requiring deployment of 250 floats per year. The estimated cost of this undertaking would be $25,000,000 per year at $100,000 per float – this translates to $5, 000, 000 per year to maintain 200 floats in the Southern Ocean, as suggested by Russell et al. (2014). Given the results of this study, where 80 "stationary floats" are able to resolve pCO_2 adequately with machine learning, fewer floats may be required to achieve to same threshold set by Majkut et al. (2014). This could reduce the cost to $2, 000, 000 per year to maintain 80 floats, but this may impact model assimilation studies as there would be fewer vertical profiles of the ocean.

5.4.4 Moorings: constraining high frequency variability

The random mooring simulation showed that estimates of ΔpCO_2 had larger errors in winter than in summer (14.76 μatm and 10.20 μatm respectively). The spatial distribution of the ΔpCO_2 errors shows that the MIZ, where moorings are not placed, is the most dominant contributor to RMSE. This implies that BIOPERIANT05 winter pCO_2 in the MIZ is significantly different to the

PFZ and SAZ, where moorings are placed. Moreover, the improved summer estimates suggest that MIZ variability, at least in BIOPERANT05, can be estimated based on measurements made elsewhere in the FPZ and/or SAZ. This is an important and surprising finding as it highlights the small role that the MIZ plays in determining the mean FCO_2 of the Southern Ocean. The outcome is that FCO_2 estimates made by moorings have the lowest error of the single platform approaches.

This being said, the deployment of 80 wave gliders or pseudo-moorings in the Southern Ocean is perhaps ambitious. The cost of a wave glider is ~$200,000, but this does not include the life-time cost of data transmission, maintenance and deployment/retrieval (Monteiro, P.M.S., personal communication, Feb 15, 2017). Moreover, these platforms only provide surface measurements. However, wave gliders offer the capabilities of a mooring, that is, high frequency sampling at a fixed location (Monteiro et al., 2015).

Unfortunately, the high frequency sampling application could not be effectively tested in this study as the temporal resolution of BIOPERIANT05's output (5 days) is much lower than the potential sampling frequency of a wave glider (hourly). This is not to say that high frequency sampling is required in all regions of the Southern Ocean, as is shown in Figure 5.2. These results suggest that high frequency variability of pCO_2 occurs primarily in regions of high intra-seasonal and sub-mesoscale variability. This means that wave gliders may be more suited to measuring pCO_2 in these regions of high frequency variability thereby aiding our understanding on the role of these fine scale processes in FCO_2 (Monteiro et al., 2015).

The deployment of wave gliders in high EKE regions may be a more feasible implementation than randomly scattering these platforms throughout the Southern Ocean (as done in this experiment). Regions of extraordinarily high EKE (> 800 cm) in the Southern Ocean are associated with the Malvinas confluence in the western Atlantic and the Agulhas Retroflection in the western Indian sectors of the Southern Ocean. Understanding the role of high frequency, sub-mesoscale variability in these accessible areas may will allow us to gain insights for other high EKE regions that are less accessible (*e.g.* south of the Campbell Plateau south of New Zealand and the wake of the Kerguelen Plateau).

These accessible regions are near enough for wave gliders to navigate the distance without the need for large vessel deployment. The Southern Ocean Carbon and Climate Observatory (SOCCO)

group based in Cape Town, South Africa has recently proven that this is possible by navigating a wave glider from 43° S, (8) (°E) to Cape Town – nearly 1500 km. Wave gliders could thus be used to monitor ΔpCO_2 and FCO_2 in regions < 1500 km from a terrestrial launch base, where only a small vessel would be required to deploy and retrieve wave gliders. This high EKE/coastal application of wave gliders in the Southern Ocean has not been tested in this OSSE framework, but would require high frequency model data, with daily output, for the true utility to be realised.

5.4.5 A proposal for the way forward: An adaptive sampling strategy

Collectively, these findings point to the need for an adaptive integrated sampling plan shown in Figure 5.3 As the description suggests, the plan uses the strengths of each of the sampling platforms to arrive at an efficient and effective sampling regime.

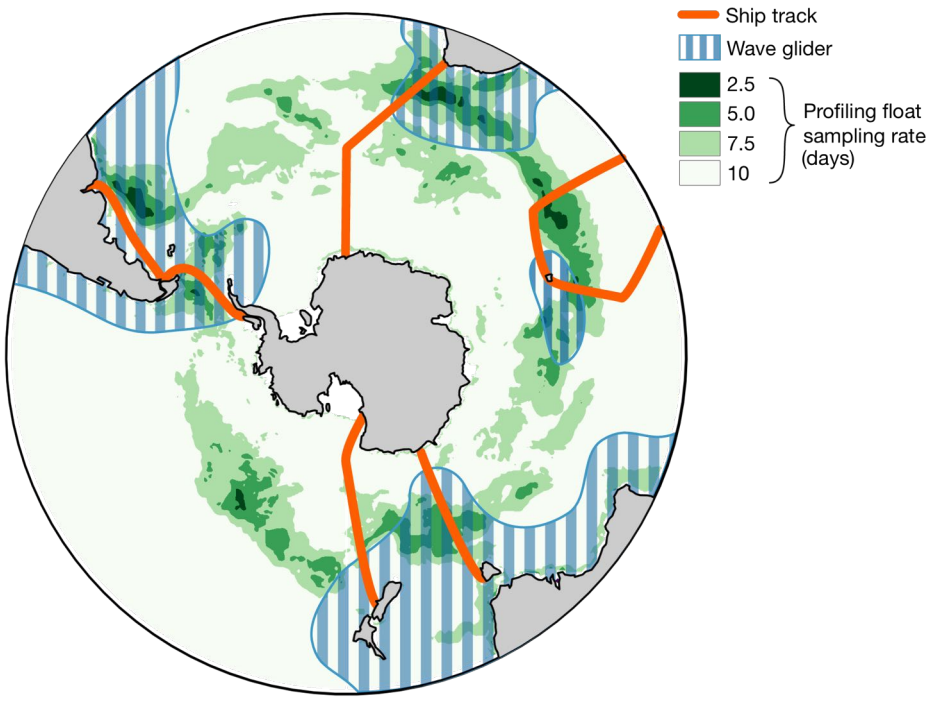

Figure 5.3: A sampling guideline for resolving air-sea CO_2 fluxes adequately. The ship based sampling is modelled from repeat cruises in the SOCAT dataset – these cruise tracks are Antarctic and Sub-Antarctic supply routes. The float sampling frequency is an example of an adaptive sampling frequency that would be able to capture the high frequency variability. The sampling frequencies based on the EKE of the BIOPERIANT05 model used in the rest of the chapter. The wave glider sampling regions are within 1500 km of continental coastlines (excluding Antarctica), with the exception of Kerguelen, where there is a research station.

Ships will continue to sample along supply lines marked by orange lines in Figure 5.3. These

lines would also serve as adequate deployment routes for profiling floats. Float sampling frequency would be prescribed by satellite EKE, where very dynamic regions would be sampled more frequently (shown as shades of green in Figure 5.3. The sampling frequencies shown in Figure 5.3 are based on the EKE of BIOPERIANT05 output where the thresholds are 20, 100, 400, 1000 cm^2 s^{-2} for 10, 7.5, 5 and 2.5 day sampling respectively. Note that these have only been selected as an example – more work will have to be done to determine the thresholds associated with observed EKE. Lastly, wave gliders would be able to sample regions of high EKE that are within navigable distance from deployment sites (Argentina, South Africa, Australia, New Zealand and Kerguelen as shown by the blue hatching).

A comprehensive study would have to be performed to assess the true performance of this integrated approach.

5.5 Synthesis

In this chapter an OSSE approach was used to test the efficacy of various sampling approaches in estimating model ΔpCO_2 (using BIOPERIANT05). Some key assumptions made in this study were that: the model was representative of reality; there was no cloud cover or measurement error in proxy variables, which were used to estimate ΔpCO_2 with an SVR; and there was no error in calculating fluxes from ΔpCO_2.

The SOCAT dataset (representing ships), used in Chapters 3 and 4, was tested. It was found that the dataset was able to estimate FCO_2 accurately enough 80% of the time (with errors less than 1 molC m^{-2} yr^{-1}). The periods when this threshold was exceeded were typically during winter, suggesting that there is a bias of FCO_2 estimates due to biased effort towards summer sampling. Because of this, ships were able to estimate pCO_2 better than floats and moorings in the MIZ, but this had little impact on FCO_2 due to the damping effect of sea ice. Increasing sampling effort in summer will not improve these estimates as the strongest biases occur during winter (Figure 5.2).

Profiling floats and wave gliders (operated as a mooring) were tested as persistent sampling platforms. It was found that 200 profiling floats were able to estimate accurately even with large sampling error (±20 μatm) to account for measurement error and sub-mesoscale variability. Despite the variability, FCO_2 was adequate and, surprisingly, more accurate than FCO_2 estimates without the added noise (Figure 5.2c and Table 5.1). It was found that 80 randomly placed wave gliders would be able to estimate pCO_2 optimally without redundancy and performed similarly to 200 profiling floats.

Two mixed platform scenarios were also simulated: ships + moorings, and ships + profiling floats. It was assumed that ships would continue to sample pCO_2 due to the necessity of supply vessels to Antarctic and Sub-Antarctic bases. Both mixed approaches estimated FCO_2 below the threshold more often than the single platform strategies (> 90% of the time for nearly the entire Southern Ocean).

It is recognised that of the two persistent sampling platforms, the profiling floats are most likely to become the platform of choice due to the success of the Argo program, added benefit of subsurface profiles and low post-deployment effort and cost. However, measurements made

by profiling floats may alias mean fluxes in areas of high sub-mesoscale and intra-seasonal variability in surface waters due to the 10-day sampling frequency (Monteiro et al., 2015). It is proposed that satellite derived EKE could be used as an indicator for where profiling floats need to increase sampling frequency in order to capture this variability. In regions of extremely high EKE, such as the Malvinas confluence and Agulhas Retroflection, FCO_2 may best be resolved with the high frequency sampling that a wave glider is able to provide.

An integrated adaptive sampling strategy was proposed and should be explored in future studies (Figure 5.3). This sampling strategy combines the strengths of each of the tested platforms: 1) where ships maintain contemporary sampling approach (based on SOCAT repeat cruises), 2) profiling floats (between 80 and 200 floats) are deployed from these ship routes to sample the open ocean regions, and 3) wave gliders sample the high EKE regions that are within navigable distance from a land based launch station. This suggested plan has not yet been tested in an OSSE framework and could be the subject of future studies.

5.A Additional figures

The additional figures contains firstly the mean wind stress (2003 to 2006) of the BIOPERIANT05 model where ERA Interim winds are used to force the model (Dee et al., 2011). The wind stress is the largest in the Indian sector of the Southern Ocean, strongest in the lee of the Kerguelen Plateau.

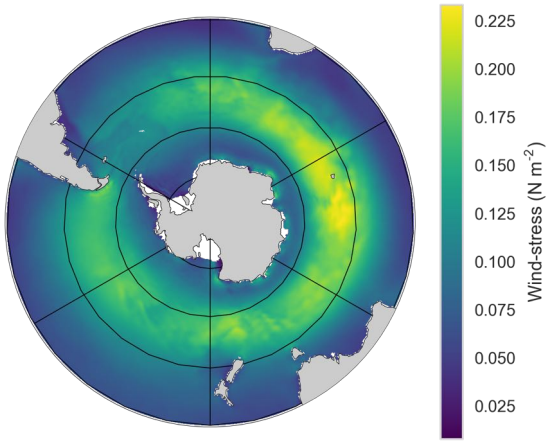

Figure 5.A.1: Time mean of wind stress for BIOPERIANT05 for the years 2003 to 2006, where ERA Interim winds are used to force the model (Dee et al., 2011).

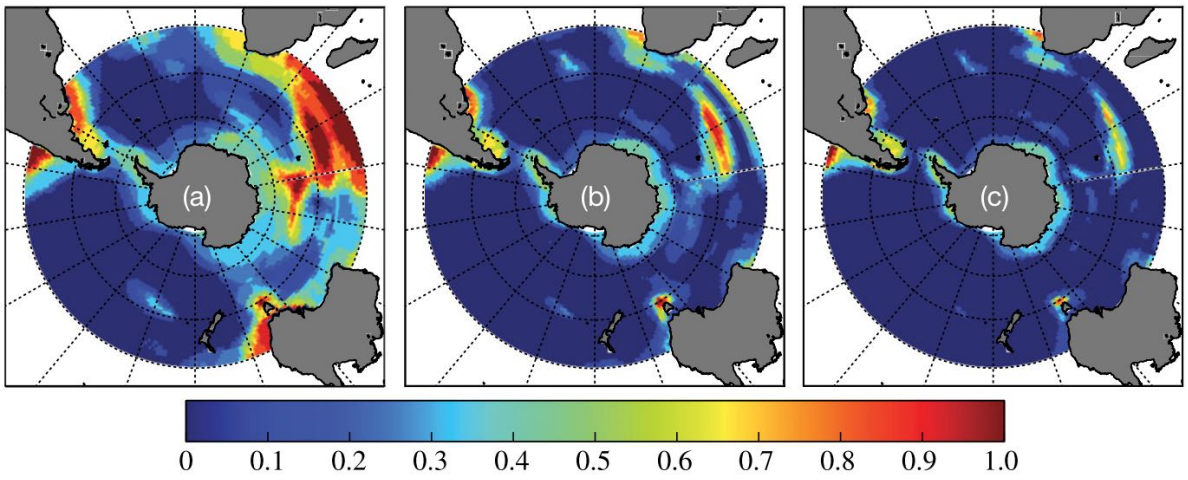

Figure 5.A.2: A figure from Majkut et al. (2014) showing the proportion of months for which the bootstrapped error estimate is larger than the threshold value of 1 molC m^{-2} yr^{-1}. The area of exceedance decreases from samplings with 75 (a), 200 (b) and 400 (c) floats. The bootstrapped errors come from the 1000-member Monte Carlo simulation for each number of float.

Diagnostic SVR Figures

The diagnostic SVR figures show in the first row the r^2 estimates during the nested K-fold grid-search (8 folds). The second row shows two 2D histograms of the estimated and target data for training and test data with a $0.75 : 0.25$ split respectively and third shows the 1D histogram of the estimated training (blue) and test (green) data. SOCAT, mooring and profiling float (with noise) training plots are shown (in that order). Note that epsilon, the SVR error margin was set to 5 μatm for both the SOCAT and the mooring training. For the profiling float with noise (20.5 μatm), epsilon was increased to 11 μatm to accommodate for the normally distributed noise. The normally distributed noise resulted in a very low r^2 result (0.18). This resulted in a far larger number of support vectors being selected. The profiling float results shown in the histograms use the true ΔpCO_2, not the noisy ΔpCO_2, for comparison. This shows that the SVR is able to accurately estimate ΔpCO_2 despite the addition of 20.5 μatm of noise. Another point worth noting is that the distribution of the SOCAT data is far broader than for moorings or floats. Mooring data is also marginally broader than float data.

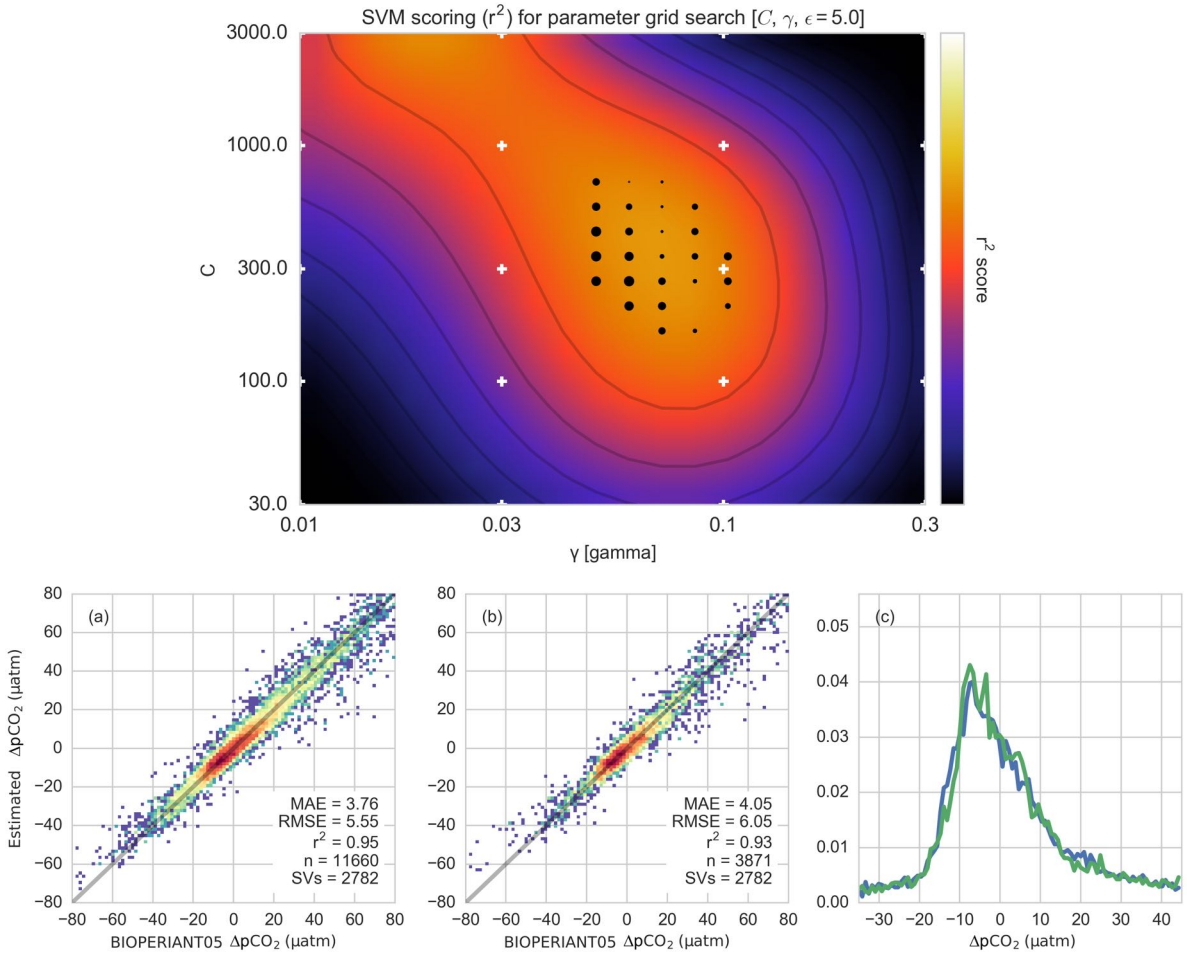

Figure 5.A.3: SOCAT SVR training. Top row: Grid search results from the hyper-parameter training for the SOCAT v3 dataset run for the BIOPERIANT05 model output. The best r^2 score was 0.83. Bottom row: Training (a) and test (b) histograms for SVR trained with SOCAT v3 in the BIOPERIANT05 model output. (c) shows the 1D histograms of training (blue) and test (green) distributions. The uncertainties achieved in this data is much lower than for observations due to lower variability of the data. This can be seen by the narrow distribution (c) of pCO_2 . The SVR does well to capture this distribution.

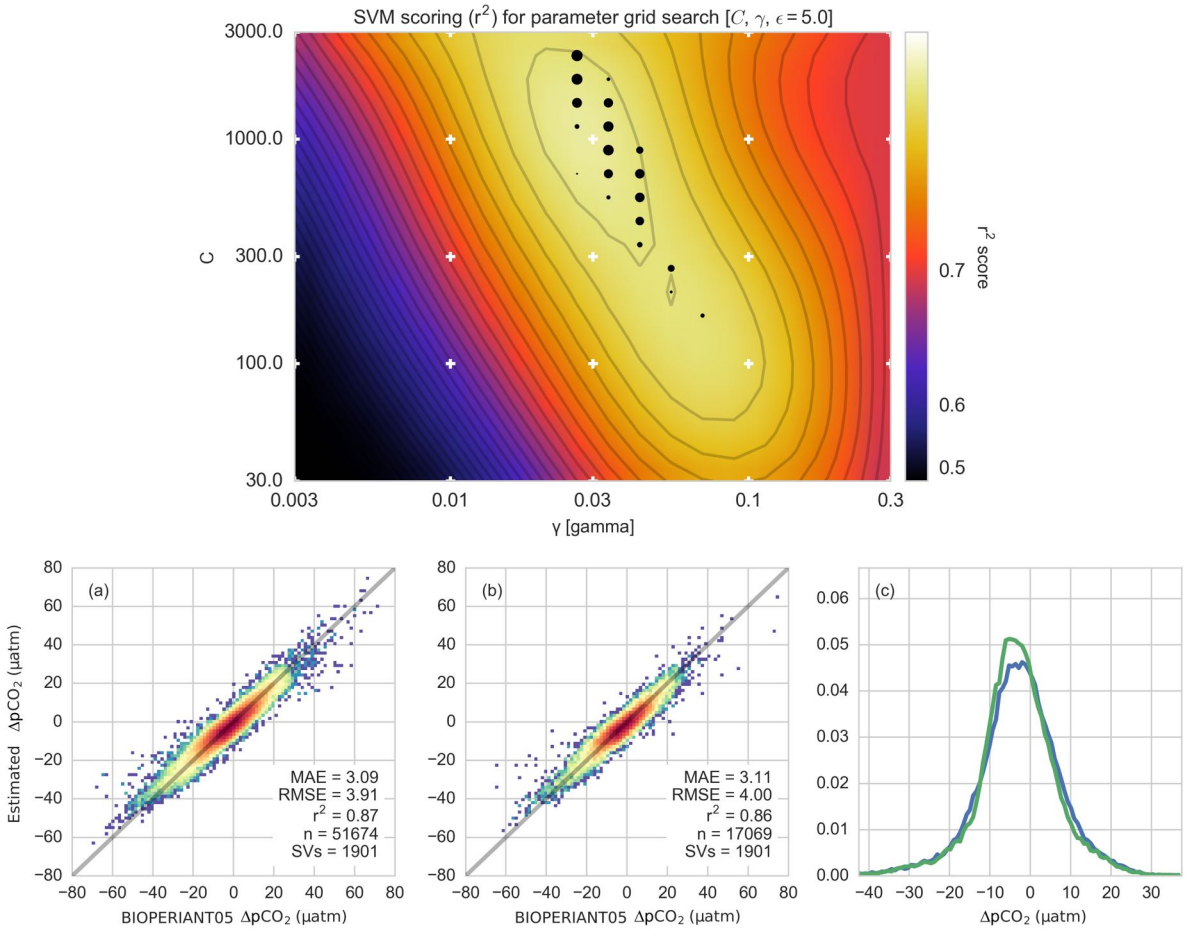

Figure 5.A.4: Mooring SVR training. Top row: Grid search results from the hyper-parameter training for the mooring gridt run for the BIOPERIANT05 model output. The best r^2 score was 0.79. Bottom row: Training (a) and test (b) histograms for SVR trained with a 4° × 5° grid of moorings in the BIOPERIANT05 model output. (c) shows the 1D histograms of training (blue) and test (green) distributions.

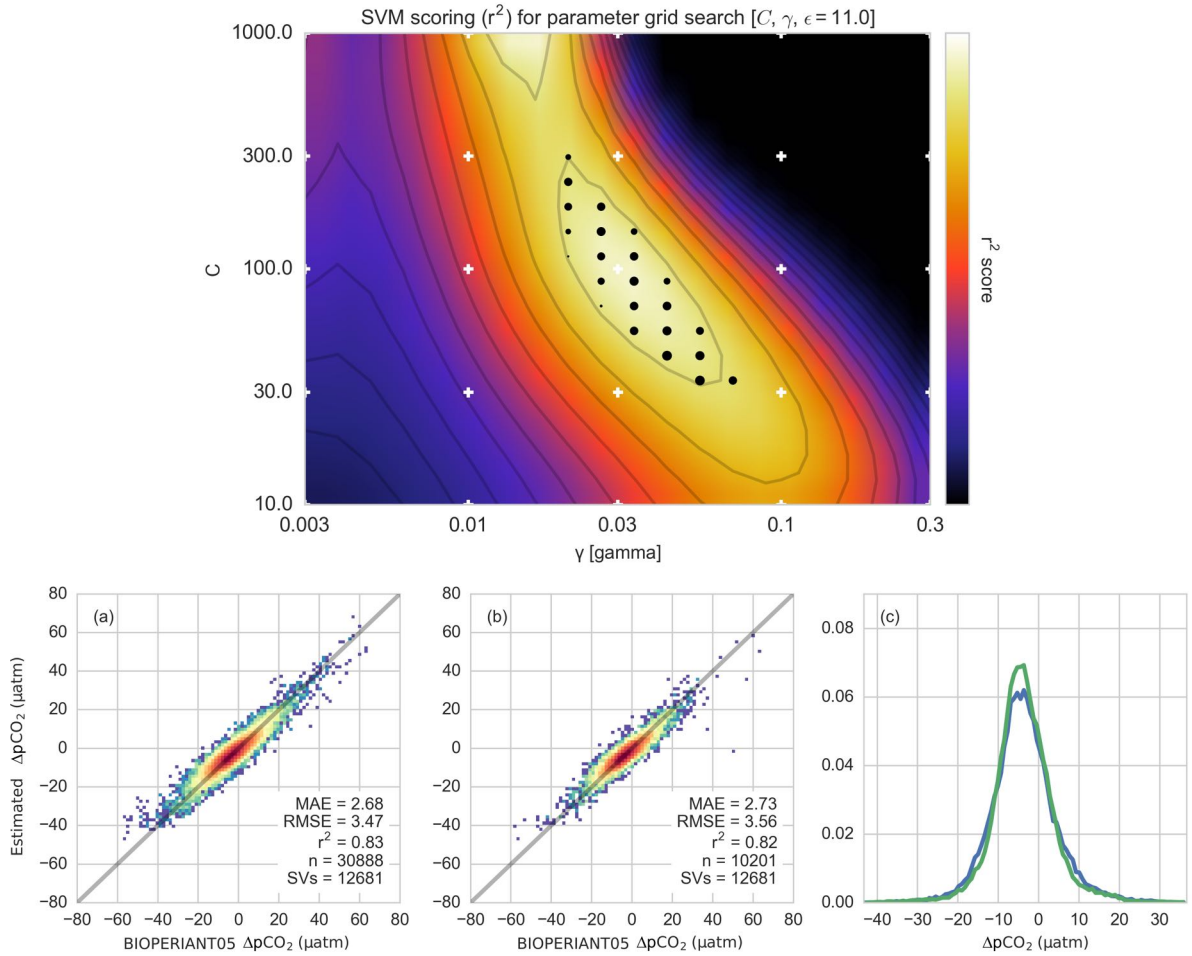

Figure 5.A.5: Profiling float SVR training. Top row: Grid search results from the hyper-parameter training for simulated profiling floats run for the BIOPERIANT05 model output. The best r^2 score was 0.18 – this low score, compared to other approaches, is due to the fact that the training data are also noisy. Bottom row: Training (a) and test (b) histograms for SVR trained with profiling floats. Note that the data are compared to ΔpCO_2 with no added noise. (c) shows the 1D histograms of training (blue) and test (green) distributions. The model does well to approximate the true estimate despite the addition of ± 13 muatm of normally distributed noise..

5.B Wave glider observations

A wave glider fitted with a pCO_2 sensor was deployed in the Sub-Antarctic Zone for nearly four months making hourly measurements shown by the time-series in Figure 5.B.1a. This data has been published in Monteiro et al. (2015). The purpose here is to show the ΔpCO_2 variability over a four month period. To then estimate the average "noise" contribution of high frequency variability a ten-day rolling standard deviation of ΔpCO_2 is taken (Figure 5.B.1b).

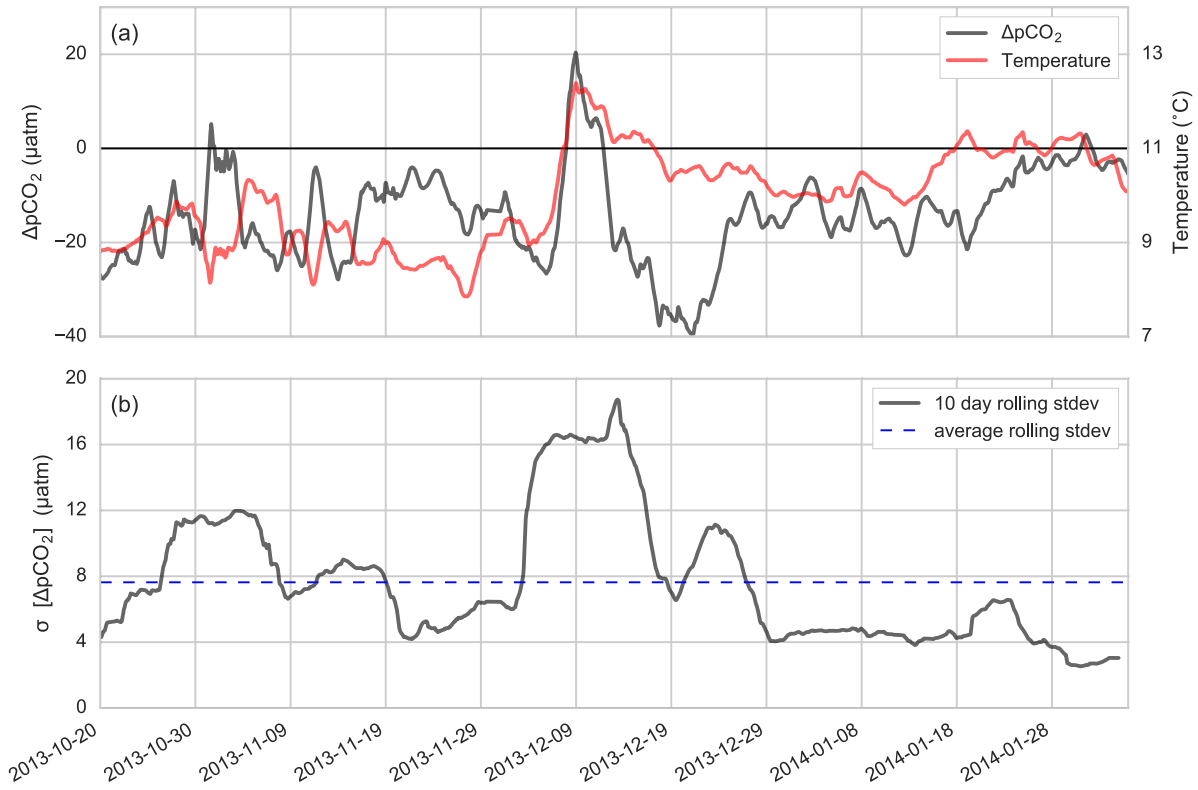

Figure 5.B.1: A three month time-series of ΔpCO_2 in the Sub-Antarctic Zone (at 43°S, 8°E) from Monteiro et al. (2015). (a) Hourly pCO_2 and temperature data resampled with a 24 hour rolling mean. (b) A 10 day rolling standard deviation of the time-series with the dashed line showing the mean of the rolling standard deviation. The average of the rolling standard deviation is 7.5 μatm.

5.C Required sampling frequency for profiling floats: A model study

An OSSE is performed using one year of daily averages of high resolution ($\frac{1}{12}$°) NEMO-PISCES model data for the Atlantic sector of the Southern Ocean (see Table 5.C.1 for configuration specifications). The data is used to calculate the sensitivity of FCO_2 to sampling various components (wind stress, pCO_2, temperature and salinity) at different frequencies. Salinity is the least influential of the four variables and both wind stress and temperature can be measured remotely (see Section 2.1). This means that sampling pCO_2 at the correct interval is critical.

Figure 5.C.1 shows the error of FCO_2 if pCO_2 is sampled every 10-days – perfect knowledge of the other variables is assumed. The 10-day sampling interval is shown as this is the standard sampling rate of profiling floats that are part of the Argo program (Roemmich et al., 2009). This sensitivity is calculated for sampling intervals from 2- to 30-day sampling intervals. These outcomes are compared to a 10% threshold (0.228 molC m^{-2} yr^{-1} is 10% of the mean flux per unit area) and a recommended sampling interval for each grid-cell is calculated. The recommended sampling frequency for floats is shown in Figure 5.2, where higher sampling intervals are required in regions of high EKE. EKE could thus be used as a proxy for where sampling frequency of profiling floats should be increased to capture the additional variability.

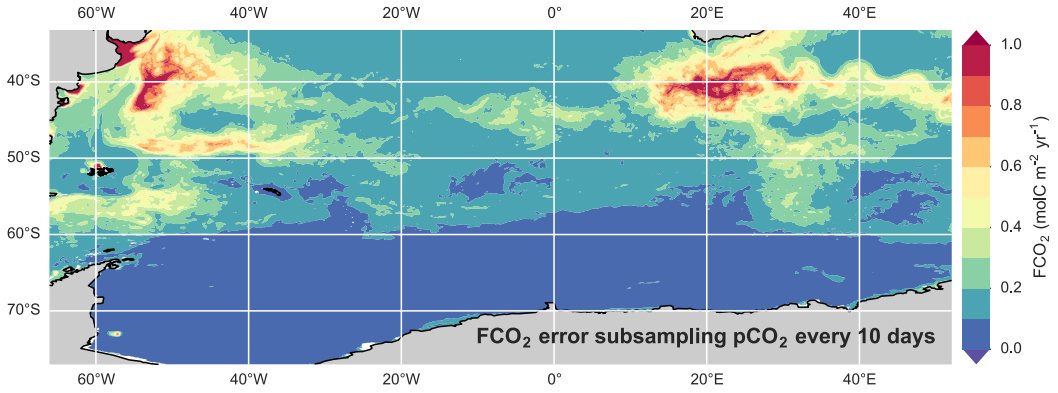

Figure 5.C.1: High resolution model data (BIOSATLANTIC12 @ $\frac{1}{12}$° resolution) was used to estimate the error of FCO_2 when sub-sampling pCO_2 at 10 day intervals.

Table 5.C.1: Specifications of the BIOSATLANTIC12-CNCRAD07A configuration.

Domain	Regional Circumpolar	70.25°E – 56.26°W 70.01°S – 29.66°S	
Horizontal Grid	Resolution $\frac{1}{12}$°	x = 1519 y = 1122	
Vertical grid	46 vertical levels z-coordinate	upper 200 m below 200 m	16 levels 19 levels
Initial conditions	Started from rest T and S from Levitus Ice from BIOPERIANT05-GAA95b		
Run duration	Spin-up (3 years) Run (20 years)	1989 – 1991 1992 – 2011	
Lateral Boundary	Only northern boundary open	5 day ocean dynamics from ORCA05-GAA95b 1 mon tracer climatologies: Alk, DIC, DOC, De, NO_3, O_2, PO_4, Si	
Surface Boundary	Atmospheric forcing	ERA Interim	
		10m u and v swrad, lwrad. tair, thumi (t2, q2) precip, snow	3 hours 24 hours 3 hours 24 hours
	Damping	T and S are damped to climatologies	
	Runoffs	S and T, are included at a frequency of 24 hours. River treatments, mixing over upper 10m	
	Sea surface restoring	Salinity only - using Levitus climatology	
	Penetration of light	2 bands, constant	
Bottom boundary	Non-linear bottom friction		
Model numerics	Advection scheme: TVD Eddy mixing parameterised (Gent and McWilliams scheme) Laplacian lateral diffusion for tracers along isoneutral surfaces Biplacian lateral diffusion of momentum along geopotential surfaces Implicit time stepping vertical diffusion is handled by TKE scheme, with tke source below the ML, langmuir paramererisation, surface mixing length scale is a function of wind stress first vertical derivative of mixing length bounded by 1		

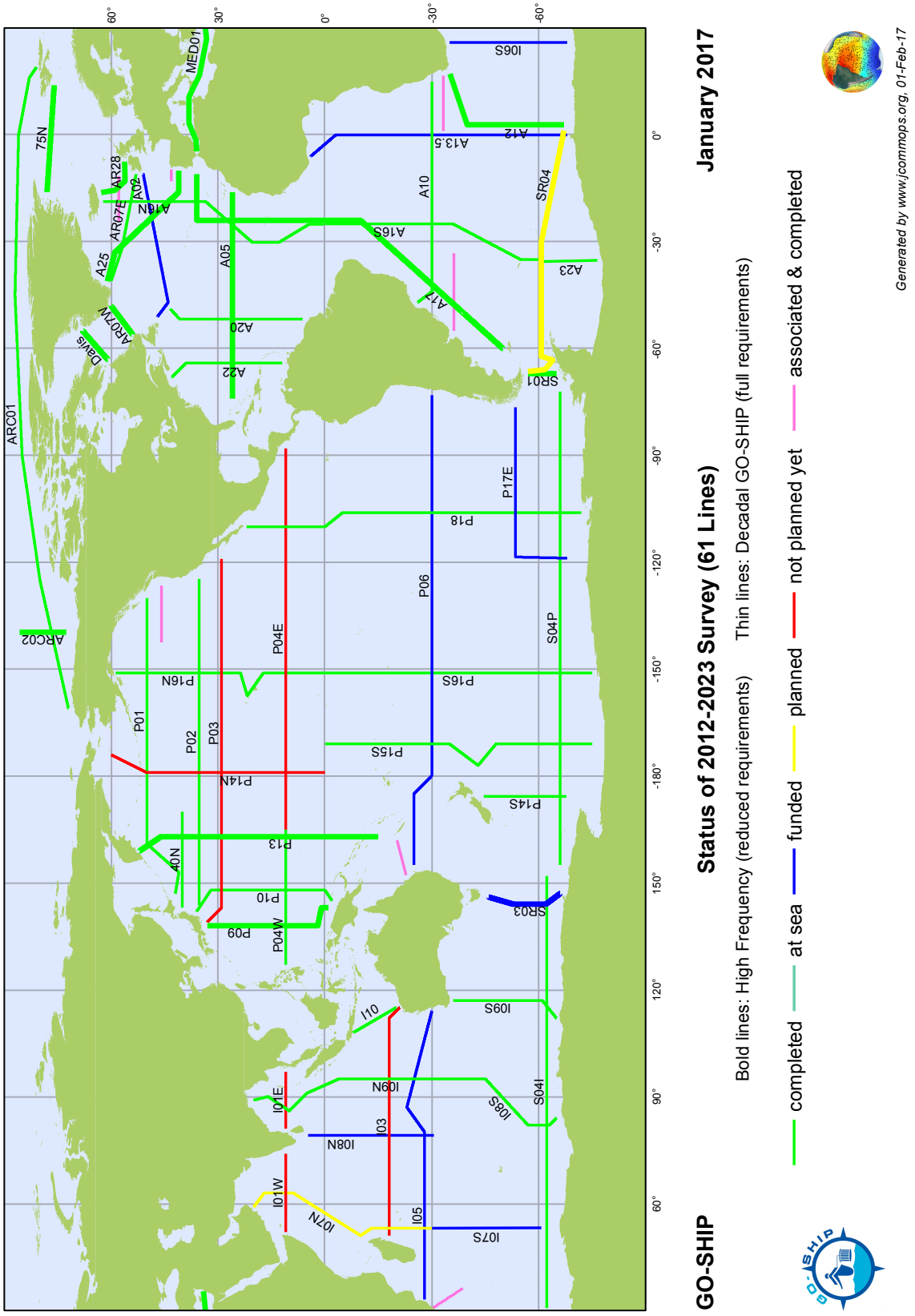

Figure 5.C.2: GO-SHIP cruise tracks for the global oceans. Several of the tracks in the Southern Ocean have already been committed to. Image downloaded from `http://www.go-ship.org/RefSecs/2017-01-GO-SHIP_Status.pdf`.

Chapter 6

Final remarks

6.1 Thesis findings

The overarching aim of this thesis is to improve the constraints and understanding of air-sea CO_2 fluxes in the Southern Ocean. This has been difficult to achieve with conventional measurements of CO_2 due to the seasonal bias and paucity of *in-situ* data.

6.1.1 Improvement of Southern Ocean CO_2 estimates

The use of empirical methods to extrapolate current CO_2 measurements with satellite data has proven successful for many regions of the ocean, but estimates of empirical methods fail to cohere in the Southern Ocean Rödenbeck et al. (2015). To improve on these empirical estimates of the fluxes of CO2 in the Southern Ocean two approaches were taken in Chapter 3: 1) implement methods appropriate to the problem of Southern Ocean CO_2; 2) improve the input data used in estimating ΔpCO_2. This was achieved by implementing two new approaches, support vector regression (SVR) and random forest regression (RFR), and by increasing the gridding resolution of the input data to improve co-location match-ups of ship based measurements and gridded proxies.

Can these methods improve on existing empirical estimates of ΔpCO_2: It was shown that RFR is able to improve marginally on the in-sample root mean squared error (RMSE) of the SOM-FFN approach by Landschützer et al. (2014), where scores were 11.48 μatm and 11.65 μatm for the

Southern Ocean respectively. The SVR was not able to improve on these scores with an RMSE of 13.41 μatm. However, both SVR and RFR were able to provide new constraints to the seasonal cycle.

Can increasing the gridding resolution of input data improve the estimates of ΔpCO_2: It was found that only RFR was able to achieve a lower in-sample RMSE with higher resolution gridded data (11.14 μatm), while the higher resolution led to poorer in-sample RMSE scores for the SVR (13.80 μatm). The proposed reason for the superior performance of the RFR over the SVR implementations is the same for both outcomes: RFR has a higher degree of non-linearity compared to SVR and even SOM-FFN, where the latter achieved higher non-linearity by first clustering data. Increasing the gridding resolution resulted in a target dataset with higher variance, which RFR was better able to represent due to the degree of non-linearity. However, it was found that RFR estimates of winter ΔpCO_2 were low relative to SVR and SOM-FFN estimates, due to its insensitivity to outliers or in this case sparse winter data. These methodological differences were small relative to the amplitude of the seasonal cycle and the dominant interannual ΔpCO_2 trends. This proved that these methods were able to estimate training dataset (SOCAT v3) relatively well, but out-of-sample testing was not possible due to the lack of data in the Southern Ocean.

6.1.2 Improving our understanding of the drivers of interannual FCO_2 variability in the Southern Ocean

The ensemble of pCO_2 estimates from Chapter 3 were used to investigate the interannual trends of ΔpCO_2 and FCO_2 in the Southern Ocean. The questions framing this research were influenced to a large extent by the work of Landschützer et al. (2015) who showed the reinvigoration of the Southern Ocean CO_2 sink.

Are mean trends driven by winter or summer? As this question suggests, a strong emphasis was placed on the different roles that winter and summer drivers play in driving interannual trends of FCO_2. This seasonal framework revealed that winter dominated the interannual variability of FCO_2, particularly in the Indian sector of the Southern Ocean, which was the primary contributor to the reinvigoration of the sink.

What are the primary driver of ΔpCO_2 for summer and winter? This question implies a more

mechanistic understanding of the drivers of the trends observed in the first question. It was shown that winter trends of ΔpCO_2 were driven primarily by weakening (strengthening) of wind stress by acting to reduce (enhance) entrainment of high DIC Circumpolar Deep Water. In summer, Chl-*a* was the dominant driver of interannual ΔpCO_2 variability. The drivers of the interannual variability of Chl-*a* were found to be a complex interaction between basin scale interannual variability of SST and wind stress with the underlying physics. Importantly, winter and summer drivers of ΔpCO_2 operate at different modes of variability, where interannual variability of winter ΔpCO_2 operates on a lower frequency than summer interannual variability. The winter variability was ascribed to the decadal mode of the SAM as was found by Landschützer et al. (2016), while the mode of summer variability was between 4–6 years, matching roughly the period of Antarctic Circumpolar Waves, which propagate eastward around Antarctica.

Do we continue to see a reinvigoration of the Southern Ocean CO_2 sink beyond 2010? Data showed that the sink continued to strengthen from 2011 to 2014. This was driven by increased uptake during summer rather than a reduction of winter outgassing, which drove the reinvigoration. A weakening sink was observed in the Atlantic sector of the Southern Ocean, but lack of coherence between ensemble members makes it uncertain if this signals the end of the reinvigoration. However, the decadal mode of variability for the Southern Ocean CO_2 sink observed by Landschützer et al. (2016) suggests that the end of the reinvigoration may be near.

6.1.3 Idealised sampling experiments

One of the conclusions in Chapter 3 was that data is too sparse in the Southern Ocean to effectively test empirical estimates of ΔpCO_2. This points to the fact that more measurements need to be made, but this is expensive due to the high costs in running ships and deploying costly sampling platforms and instruments. In the last data chapter of the thesis, the aim was to test current and potential sampling strategies in an idealised model environment. This was done to test if CO_2 would be resolved adequately with minimal redundancy to reduce cost. This Observing System Simulation Experiments (OSSE) approach was used to address the following questions:

Is there a bias in SOCAT estimates of the mean annual pCO_2 and FCO_2 given the strong bias towards summer sampling? It was found that there is only a slight bias in the SOCAT estimates of ΔpCO_2. This is due to the fact that ships sample the regions of high variability during the

periods when variability is large, in other words coastal regions and the marginal ice zone during summer. In their study, Sweeney et al. (2002) found that in order to estimate the seasonal cycle of CO_2 in the Southern Ocean with 90% accuracy an uncertainty of 0.1 PgC yr^{-1} is required. The ship based estimates of FCO_2 were not able to achieve this threshold (0.137 PgC yr^{-1}), due to poorly constrained pCO_2 in regions of high wind stress. Moreover, increased sampling effort in summer did not help to reduce the FCO_2 errors in winter.

Would 200 Lagrangian profiling floats, with large sampling error, be able to adequately estimate pCO_2? In their study, Majkut et al. (2014) showed that 200 randomly placed moorings were able to accurately resolve the seasonal cycle of FCO_2, even with considerable measurement uncertainty. Here it was found that an SVR is able to estimate FCO_2 well below the 0.1 PgC yr^{-1} threshold with an RMSE of 0.068 PgC yr^{-1}. Moreover, it was found that the addition of noise, to simulate sampling error and sub-mesoscale variability, led to improved RMSEs of ΔpCO_2 compared to when no noise was added. This technique is a known machine learning approach used to ovoid overfitting in data – this could prove useful in estimating ΔpCO_2 from the SOCAT dataset (as done in Chapter 3).

How many moorings are needed to estimate pCO_2 adequately using an SVR approach? Eighty randomly placed moorings achieved the best compromise between pCO_2 accuracy and maintaining a low number of moorings.

Do mixed platform observations achieve better FCO_2 estimates that single platform approaches? The combination of ships and profiling floats was the best performing combination (0.056 PgC yr^{-1}), with ships resolving the high variability regions in summer and floats maintaining consistent coverage in the open ocean regions where wind stress is large. The combination of ships and moorings performed no better than only moorings with an RMSE of 0.063 PgC yr^{-1}. These outcomes were combined to create a mixed platform – adaptive sampling plan that could increase the accuracy of estimates without requiring increased efforts of expensive ship based sampling.

In following section we look at the implications of the findings from Chapter 4 in the context of a changing climate.

6.2 Implications of findings for future CO_2

In their study, Landschützer et al. (2015) suggested that the reinvigoration of the Southern Ocean CO_2 sink was driven by the suppression of upwelling by warm surface waters in the Atlantic and cooling of surface waters in the Pacific (see Figure 1.5 for more details). Here, it was found that the majority of the interannual variability observed during the reinvigoration period was in fact driven by a reduction of wind stress during winter primarily over the Indian sector of the Southern Ocean. This finding is in line with previous understanding of the Southern Ocean CO_2 sink, where an increase (decrease) in wind stress south of the Polar Front (PF) would result enhanced (reduced) upwelling of Circumpolar Deep Water (CWD), thereby resulting in increased (decreased) outgassing of CO_2 (Le Quéré et al., 2007; Lenton and Matear, 2007; Lovenduski, 2007; Lenton et al., 2009b; Devries et al., 2017).

Returning to wind stress as the dominant driver of interannual CO_2 variability in the Southern Ocean significantly increases the importance in the magnitude and meridional extent of the westerlies. Observations have already shown an increase in the strength of the westerlies over the last three decades (Swart and Fyfe, 2012). And model studies have shown that the stronger westerlies in the late 20^{th} and early 21^{st} centuries are driven by an increase in atmospheric green house gas concentrations (GHG) and the depletion of stratospheric ozone as shown in Figure 6.1 (Lenton et al., 2009b). Further, models from the CMIP5 project have confirmed the strengthening of the westerlies, but Swart and Fyfe (2012) showed that the magnitude is under-represented relative to the observations and the westerly jet has an equatorward bias.

Despite these limitations, the models can still give insights into the potential future atmospheric circulation changes, and thus FCO_2, of the Southern Ocean. For instance, the predicted recovery of stratospheric ozone over Antarctica in the first half of the 21^{st} century will oppose and compensate for the continued increase in GHG (Son et al., 2010; Thompson et al., 2011; Swart and Fyfe, 2012). However, the compensation of ozone occurs primarily during summer, meaning that the other seasons will still exhibit an overall increase in the strength of the westerlies (Thompson et al., 2011). This is shown in Figure 6.2a where the depletion and subsequent recovery of stratospheric ozone results in a more positive SAM during summer. The effects of GHG (Figure 6.2b) increases steadily over time resulting in an increasingly positive SAM.

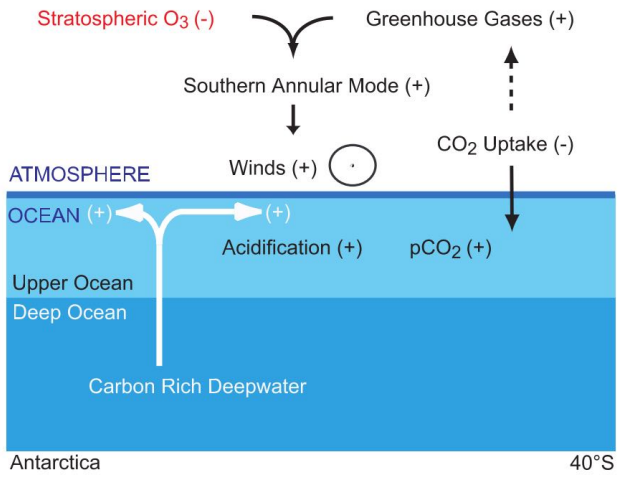

Figure 6.1: A schematic from Lenton et al. (2009b) showing that the reduction of stratospheric ozone (O_3) in the southern hemisphere leads to increased outgassing of CO_2 south of the Polar Front by an increase in the strength of the westerlies. This is over and above the intensification of the westerlies driven by greenhouse gasses (GHG).

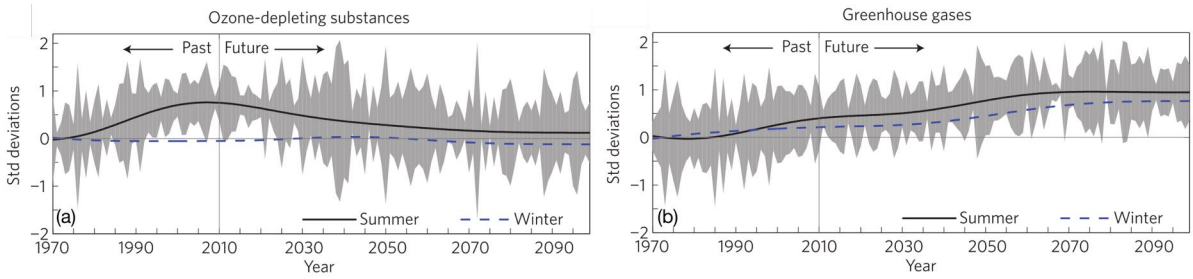

Figure 6.2: Figures showing a time-series of the SAM for two simulations with time varying forcing for (a) stratospheric ozone and (b) (a) greenhouse gasses (GHG) in a study by McLandress et al. (2011). Figures were taken from Thompson et al. (2011). Here, the SAM index is defined as the leading principal component time series of 850-hPa Z anomalies 20–90° S. Lines denote the 50-year low-pass ensemble mean response for summer (DJF; solid black) and winter (JJA; dashed blue). Grey shading denotes ± one standard deviation of the three ensemble members about the ensemble mean. The long-term means of the time series are arbitrary and are set to zero for the period 1970–1975. Past forcings are based on observational estimates.

Thompson et al. (2011) suggested that depletion of stratospheric ozone has led to a high-index polarity of the SAM, in other words, a more extreme SAM (both highs and lows). This translates to stronger westerlies during summer, which could potentially dampen the amplitude of the CO_2 seasonal cycle by enhanced upwelling of carbon-rich CDW. This is further complicated by the simultaneous increase in GHG, which would to enhanced outgassing during summer and winter.

It is predicted that stratospheric ozone will recover in the first half of the 21^{st} century (Figure 6.2a), which could lead to the reduction of summer CO_2 outgassing and thus a partial recovery of the CO_2 seasonal cycle amplitude (Thompson et al., 2011). Again, this may be opposed by continually increasing anthropogenic GHG emissions in both summer and winter (Figure 6.2b). Mayewski et al. (2015) also suggested that recovery of stratospheric ozone could lead to a more meridional pattern in atmospheric circulation. The authors explain that the southward movement of the Amundsen Sea Low in the Pacific sector of the Southern Ocean, concomitant with the southward movement of the westerlies, would create greater potential for the development of atmospheric waves.

An increase in the strength of propagating wave features could signal an increase of oceanic variability in the form of Antarctic Circumpolar Waves (ACW). With the result being an increase in zonally asymmetric anomalies of SST and wind stress and consequently CO_2 (White and Peterson, 1996; Giarolla and Matano, 2013; Landschützer et al., 2015). These effects would most likely be dominant during summer, when the effect of stratospheric ozone on the SAM is the largest and the recovery thereof is most felt (Figure 6.2). However, the continually increasing GHG would lead to enhanced outgassing south of the PF in both summer and winter. The result would be enhanced zonally asymmetric summer CO_2, while enhanced outgassing of natural CO_2 would continue to increase.

Increased outgassing will also impact the role that biology plays in the uptake of CO_2 in the Southern Ocean. Hauck et al. (2015) showed that contribution of biological uptake of CO_2 to the north and the south of the PF would change relative to the contemporary Southern Ocean. South of the PF, models showed that there is an increase in the strength of the biological sink due to enhanced upwelling of iron leading to a change in the contribution of Southern Ocean CO_2 uptake from 47% to 66%. In the SAZ (north of the PF), warming and nutrient limitation results in a reduction of the strength of this sink of equivalent magnitude to the increase to the south of the

PF. These two compensating effects are significant, but have little impact on the overall strength of the Southern Ocean CO_2 sink.

Not yet considered is the impact of CO_2 uptake on ocean acidification, which has detrimental effects on calcifying phytoplankton (McNeil and Matear, 2008; Doney et al., 2009; Boyd, 2011). Ocean pH has decreased by ~ 0.1 since pre-industrial times, which equates to a 30% increase in H^+ ions, and is said to decrease by 0.4 units by the end of the 21^{st} century (Orr et al., 2005). However, McNeil and Matear (2008) showed that aragonite[1] undersaturation will occur when atmospheric CO_2 reaches ~450 ppm – this may be as soon as 2030 during winter, when outgassing of CO_2 is strong. In a later study, McNeil and Sasse (2016) showed that by the end of the 21^{st} century surface water pCO_2 may be as high as 1000 μatm in the Southern Ocean. Such high pCO_2 levels have been shown to have behavioural impacts on marine animals that will negatively affect fisheries (McNeil and Sasse, 2016).

The overall outlook for the Southern Ocean CO_2 sink suggests a long term diminishing CO_2 sink, despite the contemporary reinvigoration (Landschützer et al., 2015). The predicted changes in atmospheric circulation may result in complex responses by the Southern Ocean CO_2 sink. Compensating forces of increasing GHG and recovery of stratospheric ozone would result in an increase in zonally asymmetric atmospheric circulation. As a result seasonal cycle amplitude of CO_2 could recover, with a decrease in summer CO_2 relative to winter, which will likely experience an increase in outgassing.

This initial increase in anthropogenic CO_2 may kick-start the Southern Ocean into a positive feedback loop (Toggweiler et al., 2006): Warming, caused by CO_2 emissions, result in stronger westerlies that enhance meridional overturning and thus outgassing of CO_2, which results in further warming. Understanding the threshold and sensitivities of this potential positive feedback system is important for us, as a community, to know if or how fast we are approaching this threshold. In the Paris climate agreement, one of the legally binding elements is to limit warming to below 2.0°C, the tipping point agreed on by the International Panel on Climate Change (IPCC). Being able to monitor, understand and predict the changes of the CO_2 in the Southern Ocean is thus critical for us to know how close we are to crossing this point. Moreover, this work will be crucial in establishing guidelines for national budgets of CO_2 emissions, which will be key in the

[1] A form of calcium carbonate

endeavour of limiting rising global temperatures.

Based on the findings of this study and the outlook on the role of the Southern Ocean in future climate scenarios, recommendations for future work can be made.

6.3 Recommendations for future work

The work addressed in this thesis has led to several additional questions that could shape future research.

How important are mesoscale and sub-mesoscale processes to understanding and predicting interannual variability at basin scale

In the development of our understanding of the summer drivers of CO_2 in Chapter 4, it was shown that Chl-*a* was affected by interannual basin scale changes in SST and wind stress, but the direct mechanism responsible for these changes could not be identified. It is understood that the changes in SST and wind stress could affect either the iron or light limitation of phytoplankton (Boyd and Ellwood, 2010; Thomalla et al., 2011). Suggested mechanisms that could effect these changes are sub-mesoscale processes that act to either shoal the mixed layer rapidly or entrain small amounts of iron that could increase primary production (Lévy et al., 2012; Mahadevan et al., 2012; Nicholson et al., 2016; Whitt et al., 2017). The conditions required for these sub-mesoscale processes to occur are quite specific, which has the implication that basin scale changes in SST or wind stress could change conditions. Such sensitivity studies, to my knowledge, have not yet been performed, but would contribute to our understanding of both Chl-*a* and pCO_2 in the Southern Ocean.

Improvements of empirical estimates of pCO_2

Improving empirical/machine learning estimates can be done by improving the method or by improving/transforming the input data.

Machine learning is a very rapidly growing and active field, meaning that more skilful empirical algorithms are constantly being developed and added to accessible toolboxes such as *Scikit-learn* in Python (Pedregosa et al., 2011). Gradient Boosted Trees is one of the methods

that has gained popularity in machine learning competitions on the on-line *Kaggle* platform[2] (Ganjisaffar et al., 2011). The theory of this method will not be discussed here.

The other alternative is to improve the input data. One of the problems encountered in the estimation of ΔpCO_2 was unreliable model estimates of mixed layer depth (MLD). The use of a more accurate MLD product or proxy variables that could account for MLD should be explored. For example heat flux, wind stress and its vector components could account for some of the variability of the MLD.

The transformation of available training data could be another way of adding improving estimates. The addition of jitter – random noise – to regularise training data was an unintentionally discovered method that could be applied to SOCAT data to improve estimates (Reed et al., 1992). However, this would have to be tested in an idealised model environment, as there would be no measurable way of identifying whether estimates have improved or not due to the lack of data (Rödenbeck et al., 2015). This ultimately points to the fact that data coverage in the Southern Ocean should be improved.

Idealised sampling of CO_2 in the Southern Ocean

The use of OSSE to estimate the bias of the SOCAT dataset proved successful in Chapter 5. Given the lack of out-of-sample data in the Southern Ocean, this approach could also be used to test the ability of methods to approximate "out-of-sample" ΔpCO_2 in model platforms. Even though models do not yet accurately represent variability of pCO_2 in the Southern Ocean, it would still be a useful measure of a methods potential bias.

The proposed sampling plan in Chapter 5 needs to be tested. This will require high resolution/frequency model output to fully understand: 1) the impact of sub-mesoscale variability in the context of point measurements such as those made by profiling floats; 2) the fewest number of profiling floats required to accurately estimate FCO_2 using an empirical approach 3) the benefit of high frequency sampling of floats in regions of high dynamic variability and the impact that this has on mean flux estimates.

Given the importance of the Southern Ocean in the non-stationary context of climate change, measuring pCO_2 adequately is crucial for us to monitor changes of the Southern Ocean CO_2

[2]Hosts machine learning competitions: `https://www.kaggle.com/competitions`

sink. Moreover, the data we collect is perhaps the most important contribution that we, the community, make. As our understanding of natural systems improves, our modelling capabilities increase and computational power increases, our contemporary models will become obsolete. However, our data will be an invaluable legacy for future generations.

This sentiment is beautifully captured in the short video documentary of billy barr: The Hermit Who Inadvertently Shaped Climate-Change Science.

Bibliography

Abernathey, R., Marshall, J. C., and Ferreira, D. (2011). The Dependence of Southern Ocean Meridional Overturning on Wind Stress. *Journal of Physical Oceanography*, 41(12):2261–2278.

Amante, C. and Eakins, B. (2009). ETOPO1 1 Arc-Minute Global Relief Model: Procedures, Data Sources and Analysis. Technical report, National Geophysical Data Center, NOAA.

Anderson, L. G. and Sarmiento, J. L. (1994). Redfield ratios of remineralization determined by nutrient data analysis.

Aoki, S., Campos, E., Chambers, D., Feely, R. A., Gulev, S., Johnson, G. C., Josey, S. A., Kostianoy, A., Mauritzen, C., Roemmich, D., and Wang, F. (2013). Climate Change 2013: The Physical Science Basis(Ch3). *Climate Change 2013: The Physical Science Basis. Contribution of Working Group I to the Fifth Assessment Report of the Intergovernmental Panel on Climate Change*, page 62.

Arblaster, J. M. and Meehl, G. A. (2006). Contributions of external forcings to southern annular mode trends. *Journal of Climate*, 19(12):2896–2905.

Arrhenius, S. (1896). On the Influence of Carbonic Acid in the Air upon the Temperature of the Ground. *Philosophical Magazine and Journal of Science*, 41(5):237–276.

Arrigo, K. R., van Dijken, G. L., and Bushinsky, S. (2008). Primary production in the Southern Ocean, 1997-2006. *Journal of Geophysical Research: Oceans*, 113(8):1997–2006.

Arrigo, K. R., Worthen, D., Schnell, A., and Lizotte, M. P. (1998). Primary production in Southern Ocean waters. *Journal of Geophysical Research: Oceans*, 103(C8):15587–15600.

Atlas, R., Hoffman, R. N., Ardizzone, J., Leidner, S. M., Jusem, J. C., Smith, D. K., and Gombos, D. (2011). A Cross-calibrated, Multiplatform Ocean Surface Wind Velocity Product for Meteorological and Oceanographic Applications. *Bulletin of the American Meteorological Society*, 92(2):157–174.

Aumont, O. and Bopp, L. (2006). Globalizing results from ocean in situ iron fertilization studies. *Global Biogeochemical Cycles*, 20(2):1–15.

Aumont, O., Ethé, C., Tagliabue, A., Bopp, L., and Gehlen, M. (2015). PISCES-v2: An ocean biogeochemical model for carbon and ecosystem studies. *Geoscientific Model Development*, 8(8):2465–2513.

Bakker, D. C. E., Hoppema, M., Schroder, M., Geibert, W., and de Baar, H. J. (2008). A rapid transition from ice covered CO2-rich waters to a biologically mediated CO2 sink in the eastern Weddell Gyre. *Biogeosciences*, 5:1373–1386.

Bakker, D. C. E., Pfeil, B., Landa, C. S., Metzl, N., O'Brian, K. M., Olsen, A., Smith, K., Cosca, C., Harasawa, S., Jones, S. D., Nakaoka, S.-i., Nojiri, Y., Schuster, U., Steinhoff, T., Sweeney, C., Takahashi, T., Tilbrook, B., Wada, C., Wanninkhof, R., Alin, S. R., Balestrini, C. F., Barbero, L., Bates, N. R., Bianchi, A. A., Bonou, F., Boutin, J., Bozec, Y., Burger, E. F., Cai, W.-J., Castle, R. D., Chen, L., Chierici, M., Currie, K., Evans, W., Featherstone, C., Feely, R. A., Fransson, A., Goyet, C., Greenwood, N., Gregor, L., Hankin, S., Hardman-Mountford, N. J., Harlay, J., Hauck, J., Hoppema, M., Humphreys, M. P., Hunt, C. W., Huss, B., Ibánhez, J. S. P., Johannessen, T., Keeling, R., Kitidis, V., Körtzinger, A., Kozyr, A., Krasakopoulou, E., Kuwata, A., Landschützer, P., Lauvset, S. K., Lefèvre, N., Lo Monaco, C., Manke, A., Mathis, J. T., Merlivat, L., Millero, F. J., Monteiro, P. M., Munro, D. R., Murata, A., Newberger, T., Omar, A. M., Ono, T., Paterson, K., Pearce, D., Pierrot, D., Robbins, L. L., Saito, S., Salisbury, J., Schlitzer, R., Schneider, B., Schweitzer, R., Sieger, R., Skjelvan, I., Sullivan, K. F., Sutherland, S. C., Sutton, A. J., Tadokoro, K., Telszewski, M., Tuma, M., Van Heuven, S. M. A. C., Vandemark, D., Ward, B., Watson, A. J., and Xu, S. (2016). A multi-decade record of high-quality fCO2 data in version 3 of the Surface Ocean CO2 Atlas (SOCAT). *Earth System Science Data Discussions*, (May):1–55.

Bakker, D. C. E., Pfeil, B., Smith, K., Hankin, S., Olsen, A., Alin, S. R., Cosca, C., Harasawa, S., Kozyr, A., Nojiri, Y., O'Brien, K. M., Schuster, U., Telszewski, M., Tilbrook, B., Wada, C., Akl, J., Barbero, L., Bates, N. R., Boutin, J., Bozec, Y., Cai, W. J., Castle, R. D., Chavez, F. P., Chen, L., Chierici, M., Currie, K., de Baar, H. J., Evans, W., Feely, R. A., Fransson, A., Gao, Z., Hales, B., Hardman-Mountford, N. J., Hoppema, M., Huang, W. J., Hunt, C. W., Huss, B., Ichikawa, T., Johannessen, T., Jones, E. M., Jones, S. D., Jutterström, S., Kitidis, V., Körtzinger, A., Landschützer, P., Lauvset, S. K., Lefèvre, N., Manke, A. B., Mathis, J. T., Merlivat, L., Metzl, N., Murata, A., Newberger, T., Omar, A. M., Ono, T., Park, G.-H., Paterson, K., Pierrot, D., Ríos, A. F., Sabine, C. L., Saito, S., Salisbury, J., S. Sarma, V. V. S., Schlitzer, R., Sieger, R., Skjelvan, I., Steinhoff, T., Sullivan, K. F., Sun, H., Sutton, A. J., Suzuki, T., Sweeney, C., Takahashi, T., Tjiputra, J., Tsurushima, N., Van Heuven, S. M. A., Vandemark, D., Vlahos, P., Wallace, D. W. R., Wanninkhof, R., and Watson, A. J. (2014). An update to the surface ocean CO2 atlas (SOCAT version 2). *Earth System Science Data*, 6(1):69–90.

Barnes, E. A. and Hartmann, D. L. (2010). Dynamical Feedbacks of the Southern Annular Mode in Winter and Summer. *Journal of the Atmospheric Sciences*, 67(2007):2320–2330.

Bates, N. R., Garley, R., Frey, K. E., Shake, K. L., and Mathis, J. T. (2014). Sea-ice melt CO2-carbonate chemistry in the western Arctic Ocean: Meltwater contributions to air-sea CO2 gas exchange, mixed-layer properties and rates of net community production under sea ice. *Biogeosciences*, 11(23):6769–6789.

Biastoch, A., Böning, C. W., Getzlaff, J., Molines, J.-M., and Madec, G. (2008). Causes of Interannual–Decadal Variability in the Meridional Overturning Circulation of the Midlatitude North Atlantic Ocean. *Journal of Climate*, 21(24):6599–6615.

Biogeochemical-Argo Planning Group (2016). The scientific rationale, design, and implementation plan for a Biogeochemical-Argo float array. pages 1–58.

Blain, S., Quéguiner, B., Armand, L. K., Belviso, S., Bombled, B., Bopp, L., Bowie, A. L., Brunet, C., Brussaard, C., Carlotti, F., Christaki, U., Corbière, A., Durand, I., Ebersbach, F., Fuda, J. L., Garcia, N., Gerringa, L., Griffiths, B., Guigue, C., Guillerm, C., Jacquet, S., Jeandel, C., Laan, P., Lefèvre, D., Lo Monaco, C., Malits, A., Mosseri, J., Obernosterer, I., Park, Y. H., Picheral, M., Pondaven, P., Remenyi, T., Sandroni, V., Sarthou, G., Savoye, N., Scouarnec, L., Souhaut, M., Thuiller, D., Timmermans, K., Trull, T., Uitz, J., van Beek, P., Veldhuis, M., Vincent, D., Viollier, E., Vong, L., and Wagener, T. (2007). Effect of natural iron fertilization on carbon sequestration in the Southern Ocean. *Nature*, 446(April):1070–1074.

Boyd, P. W. (2011). Beyond ocean acidification. *Nature Geoscience*, 4(5):273–274.

Boyd, P. W. and Ellwood, M. J. (2010). The biogeochemical cycle of iron in the ocean. *Nature Geoscience*, 3(10):675–682.

Boyd, P. W., Jickells, T., Law, C. S., Blain, S., Boyle, E. A., Buesseler, K. O., Coale, K. H., Cullen, J. J., de Baar, H. J., Follows, M. J., Harvey, M., Lancelot, C., Levasseur, M., Owens, N. P. J., Pollard, R., Rivkin, R. B., Sarmiento, J. L., Schoemann, V., Smetacek, V., Takeda, S., Tsuda, a., Turner, S., and Watson, A. J. (2007). Mesoscale iron enrichment experiments 1993-2005: synthesis and future directions. *Science (New York, N.Y.)*, 315(5812):612–617.

Breiman, L. (2001). Random forests. *Machine Learning*, 45(1):5–32.

Butterworth, B. J. and Miller, S. D. (2016). Air-sea exchange of carbon dioxide in the Southern Ocean and Antarctic marginal ice zone. *Geophysical Research Letters*, in review.

Caruana, R. and Niculescu-Mizil, A. (2006). An empirical comparison of supervised learning algorithms. *Proceedings of the 23th International Conference on Machine Learning*, pages 161–168.

CDO (2015). Climate Data Operators.

Chierici, M., Olsen, A., Johannessen, T., Trinañes, J., and Wanninkhof, R. (2009). Algorithms to estimate the carbon dioxide uptake in the northern North Atlantic using shipboard observations, satellite and ocean analysis data. *Deep-Sea Research Part II: Topical Studies in Oceanography*, 56(8-10):630–639.

Chierici, M., Signorini, S. R., Mattsdotter-Björk, M., Fransson, A., and Olsen, A. (2012). Surface water fCO2 algorithms for the high-latitude Pacific sector of the Southern Ocean. *Remote Sensing of Environment*, 119:184–196.

Cullison Gray, S. E., DeGrandpre, M. D., Moore, T. S., Martz, T. R., Friederich, G. E., and Johnson, K. S. (2011). Applications of in situ pH measurements for inorganic carbon calculations. *Marine Chemistry*, 125(1-4):82–90.

de Boyer Montégut, C., Madec, G., Fischer, A. S., Lazar, A., and Iudicone, D. (2004). Mixed layer depth over the global ocean: An examination of profile data and a profile-based climatology. *Journal of Geophysical Research*, 109:1–20.

Dee, D. P., Uppala, S. M., Simmons, A. J., Berrisford, P., Poli, P., Kobayashi, S., Andrae, U., Balmaseda, M. A., Balsamo, G., Bauer, P., Bechtold, P., Beljaars, A. C. M., van de Berg, L., Bidlot, J., Bormann, N., Delsol, C., Dragani, R., Fuentes, M., Geer, A. J., Haimberger, L., Healy, S. B., Hersbach, H., Hólm, E. V., Isaksen, L., Kållberg, P., Köhler, M., Matricardi, M., Mcnally, A. P., Monge-Sanz, B. M., Morcrette, J. J., Park, B. K., Peubey, C., de Rosnay, P., Tavolato, C., Thépaut, J. N., and Vitart, F. (2011). The ERA-Interim reanalysis: Configuration and performance of the data assimilation system. *Quarterly Journal of the Royal Meteorological Society*, 137(656):553–597.

Devries, T., Holzer, M., and Primeau, F. (2017). Recent increase in oceanic carbon uptake driven by weaker upper-ocean overturning. *Nature Publishing Group*, 542(7640):215–218.

Dickson, A. G., Sabine, C. L., and Christian, J. R. (2007). *Guide to Best Practices for Ocean CO 2 Measurements*. Number 8.

Donelan, M. A., Haus, B. K., Reul, N., Plant, W. J., Stiassnie, M., Graber, H. C., Brown, O. B., and Saltzman, E. S. (2004). On the limiting aerodynamic roughness of the ocean in very strong winds. *Geophysical Research Letters*, 31(18):1–5.

Doney, S. C., Fabry, V. J., Feely, R. A., and Kleypas, J. A. (2009). Ocean Acidification: The Other CO ₂ Problem. *Annual Review of Marine Science*, 1(1):169–192.

Dong, S., Sprintall, J., Gille, S. T., and Talley, L. D. (2008). Southern Ocean mixed-layer depth from Argo float profiles. *Journal of Geophysical Research*, 113(C6):C06013.

Dotto, T. S., Kerr, R., Mata, M. M., Azaneu, M., Wainer, I., Fahrbach, E., and Rohardt, G. (2014). Assessment of the structure and variability of weddell sea water masses in distinct ocean reanalysis products. *Ocean Science*, 10(3):523–546.

Dufour, C. O., Sommer, J. L., Gehlen, M., Orr, J. C., Molines, J. M., Simeon, J., and Barnier, B. (2013). Eddy compensation and controls of the enhanced sea-to-air CO2 flux during positive phases of the Southern Annular Mode. *Global Biogeochemical Cycles*, 27(3):950–961.

Dufour, C. O., Sommer, L. L., Zika, J. D., Gehlen, M., Orr, J. C., Mathiot, P., and Barnier, B. (2012). Standing and transient eddies in the response of the Southern Ocean meridional overturning to the Southern annular mode. *Journal of Climate*, 25(20):6958–6974.

Eppley, R. W. and Peterson, B. J. (1979). Particulate organic matter flux and planktonic new production in the deep ocean. *Nature*, 282:677–680.

Fauchereau, N., Tagliabue, A., Bopp, L., and Monteiro, P. M. (2011). The response of phytoplankton biomass to transient mixing events in the Southern Ocean. *Geophysical Research Letters*, 38(17):1–6.

Fay, A. R. and McKinley, G. A. (2014). Global open-ocean biomes : mean and temporal variability. *Earth System Science Data*, 6:273–284.

Fay, A. R., McKinley, G. A., and Lovenduski, N. S. (2014). Southern Ocean carbon trends: Sensitivity to methods. *Geophysical Research Letters*, 41(19):6833–6840.

Feder, T. (2000). Argo begins systematic global probing of the upper oceans. *Physics Today*, 53(7):50–51.

Fogt, R. L., Jones, J. M., and Renwick, J. (2012). Seasonal zonal asymmetries in the southern annular mode and their impact on regional temperature anomalies. *Journal of Climate*, 25(18):6253–6270.

Fransson, A., Chierici, M., Yager, P. L., and Smith, W. O. (2011). Antarctic sea ice carbon dioxide system and controls. *Journal of Geophysical Research*, 116(December 2008):1–18.

Frenger, I., Münnich, M., Gruber, N., and Knutti, R. (2015). Southern Ocean eddy phenomenology. *Journal of Geophysical Research: Oceans*, 120(11):7413–7449.

Friedrich, T. and Oschlies, A. (2009a). Basin-scale pCO2 maps estimated from ARGO gfloat data: A model study. *Journal of Geophysical Research: Oceans*, 114(10):1–9.

Friedrich, T. and Oschlies, A. (2009b). Neural network-based estimates of North Atlantic surface pCO2 from satellite data: A methodological study. *Journal of Geophysical Research: Oceans*, 114(3):1–12.

Frolicher, T. L., Sarmiento, J. L., Paynter, D. J., Dunne, J. P., Krasting, J. P., and Winton, M. (2015). Dominance of the Southern Ocean in anthropogenic carbon and heat uptake in CMIP5 models. *Journal of Climate*, 28(2):862–886.

Gade, K. (2010). A Non-singular Horizontal Position Representation. *Journal of Navigation*, 63(03):395–417.

Ganjisaffar, Y., Caruana, R., and Lopes, C. V. (2011). Bagging Gradient-boosted Trees for High Precision, Low Variance Ranking Models. *Proceedings of the 34th International ACM SIGIR Conference on Research and Development in Information Retrieval*, (c):85–94.

Giarolla, E. and Matano, R. P. (2013). The low-frequency variability of the southern ocean circulation. *Journal of Climate*, 26(16):6081–6091.

Graham, R. M., De Boer, A. M., Heywood, K. J., Chapman, M. R., and Stevens, D. P. (2012). Southern Ocean fronts: Controlled by wind or topography? *Journal of Geophysical Research: Oceans*, 117(8):1–14.

Graham, R. M., De Boer, A. M., van Sebille, E., Kohfeld, K. E., and Schlosser, C. (2015). Inferring source regions and supply mechanisms of iron in the Southern Ocean from satellite chlorophyll data. *Deep-Sea Research Part I: Oceanographic Research Papers*, 104:9–25.

Hastie, T., Tibshirani, R., and Friedman, J. (2008). *The Elements of Statistical Learning: Data mining, inference, and prediction*. Springer, California, second edi edition.

Hastie, T., Tibshirani, R., and Friedman, J. (2009). *The Elements of Statistical Learning: Data Mining, Inference, and Prediction*. Number 2.

Hauck, J., Völker, C., Wang, T., Hoppema, M., Losch, M., and Wolf-Gladrow, D. A. (2013). Seasonally different carbon flux changes in the Southern Ocean in response to the southern annular mode. *Global Biogeochemical Cycles*, 27(4):1236–1245.

Hauck, J., Völker, C., Wolf-Gladrow, D. A., Laufkötter, C., Vogt, M., Aumont, O., Bopp, L., Buitenhuis, E. T., Doney, S. C., Dunne, J., Gruber, N., Hashioka, T., John, J., Quéré, C. L., Lima, I. D., Nakano, H., Séférian, R., and Totterdell, I. (2015). On the Southern Ocean CO 2 uptake and the role of the biological carbon pump in the 21st century. *Global Biogeochemical Cycles*, 29(9):1451–1470.

Ho, D. T., Law, C. S., Smith, M. J., Schlosser, P., Harvey, M., and Hill, P. (2006). Measurements of air-sea gas exchange at high wind speeds in the Southern Ocean: Implications for global parameterizations. *Geophysical Research Letters*, 33(16):1–6.

Hogg, A. M., Meredith, M. P., Chambers, D. P., Abrahamsen, E. P., Hughes, C. W., and Morrison, A. K. (2015). Recent trends in the Southern Ocean eddy field. *Journal of Geophysical Research C: Oceans*, 120(1):257–267.

Hood, E. M., Sabine, C. L., and Sloyan, B. M. (2010). The GO-SHIP Repeat Hydrography Manual: A Collection of Expert Reports and Guidelines.

Hoppema, M., Fahrbach, E., Stoll, M. H., and de Baar, H. J. (1999). Annual uptake of atmospheric CO2 by the Weddell sea derived from a surface layer balance, including estimations of entrainment and new production. *Journal of Marine Systems*, 19:219–233.

Hoppema, M., Stoll, M. H., and De Baar, H. J. W. (2000). Co2 in the Weddell Gyre and Antarctic Circumpolar Current: Austral autumn and early winter. *Marine Chemistry*, 72:203–220.

Iida, Y., Kojima, A., Takatani, Y., Nakano, T., Sugimoto, H., Midorikawa, T., and Ishii, M. (2015). Trends in pCO2 and sea–air CO2 flux over the global open oceans for the last two decades. *Journal of Oceanography*, 71(6):637–661.

Ishii, M., Inoue, H. Y., Matsueda, H., and Tanoue, E. (1998). Close coupling between seasonal biological production and dynamics of dissolved inorganic carbon in the Indian Ocean sector and the western Pacific Ocean sector of the Antarctic Ocean. *Deep Sea Research Part I: Oceanographic Research Papers*, 45(7):1187–1209.

Islam, T., Srivastava, P. K., Dai, Q., Gupta, M., and Zhuo, L. (2015). Rain rate retrieval algorithm for conical-scanning microwave imagers aided by random forest, RReliefF, and multivariate adaptive regression splines (RAMARS). *IEEE Sensors Journal*, 15(4):2186–2193.

Iudicone, D., Rodgers, K. B., Stendardo, I., Aumont, O., Madec, G., Bopp, L., Mangoni, O., and Ribera d'Alcala', M. (2011). Water masses as a unifying framework for understanding the Southern Ocean Carbon Cycle. *Biogeosciences*, 8(5):1031–1052.

Iudicone, D., Speich, S., Madec, G., and Blanke, B. (2008). The global conveyor belt from a Southern Ocean perspective. *Journal of Physical Oceanography*, 38(7):1401–1425.

James, G., Witten, D., Hastie, T., and Tibshirani, R. (2013). *An Introduction to Statistical Learning*, volume 103 of *Springer Texts in Statistics*. Springer New York, New York, NY.

Jamet, C., Moulin, C., and Lefèvre, N. (2007). Estimation of the oceanic pCO₂ in the North Atlantic from VOS lines in-situ measurements: parameters needed to generate seasonally mean maps. *Annales Geophysicae*, 25:2247–2257.

Johnson, K. S., Berelson, W., Boss, E., Chase, Z., Claustre, H., Emerson, S., Gruber, N., Körtzinger, A., Perry, M. J., and Riser, S. (2009). Observing Biogeochemical Cycles at Global Scales with Profiling Floats and Gliders: Prospects for a Global Array. *Oceanography*, 22(3):216–225.

Johnson, K. S., Jannasch, H. W., Coletti, L. J., Elrod, V. A., Martz, T. R., Takeshita, Y., Carlson, R. J., and Connery, J. G. (2016). Deep-Sea DuraFET: A Pressure Tolerant pH Sensor Designed for Global Sensor Networks. *Analytical Chemistry*, 88(6):3249–3256.

Johnson, R., Strutton, P. G., Wright, S. W., McMinn, A., and Meiners, K. M. (2013). Three improved satellite chlorophyll algorithms for the Southern Ocean. *Journal of Geophysical Research: Oceans*, 118(7):3694–3703.

Jones, S. D., Le Quéré, C., and Rödenbeck, C. (2012). Autocorrelation characteristics of surface ocean pCO(2) and air-sea CO2 fluxes. *Global Biogeochemical Cycles*, 26(2):n/a–n/a.

Jones, S. D., Le Quéré, C., Rödenbeck, C., Manning, A. C., and Olsen, A. (2015). A statistical gap-filling method to interpolate global monthly surface ocean carbon dioxide data. *Journal of Advances in Modeling Earth Systems*, 7(4):1554–1575.

Kamenkovich, I., Cheng, W., Schmid, C., and Harrison, D. E. (2011). Effects of eddies on an ocean observing system with profiling floats: Idealized simulations of the Argo array. *Journal of Geophysical Research: Oceans*, 116(6):1–14.

Khatiwala, S., Primeau, F., and Hall, T. (2009). Reconstruction of the history of anthropogenic CO2 concentrations in the ocean. *Nature*, 462(7271):346–349.

Khatiwala, S., Tanhua, T., Mikaloff Fletcher, S. E., Gerber, M., Doney, S. C., Graven, H. D., Gruber, N., McKinley, G. A., Murata, A., RÍos, A. F., and Sabine, C. L. (2013). Global ocean storage of anthropogenic carbon. *Biogeosciences*, 10(4):2169–2191.

Kim, Y. H., Im, J., Ha, H. K., Choi, J. K., and Ha, S. (2014). Machine learning approaches to coastal water quality monitoring using GOCI satellite data. *Giscience and Remote Sensing*, 51(2):158–174.

Landschützer, P., Gruber, N., and Bakker, D. C. E. (2016). Decadal variations and trends of the global ocean carbon sink. *Global Biogeochemical Cycles*, 30(10):1396–1417.

Landschützer, P., Gruber, N., Bakker, D. C. E., and Schuster, U. (2014). Recent variability of the global ocean carbon sink. *Global and Planetary Change*, pages 927–949.

Landschützer, P., Gruber, N., Bakker, D. C. E., Schuster, U., Nakaoka, S.-i., Payne, M. R., Sasse, T. P., and Zeng, J. (2013). A neural network-based estimate of the seasonal to inter-annual variability of the Atlantic Ocean carbon sink. *Biogeosciences*, 10(11):7793–7815.

Landschützer, P., Gruber, N., Haumann, F. A., Rödenbeck, C., Bakker, D. C. E., van Heuven, S., Hoppema, M., Metzl, N., Sweeney, C., Takahashi, T., Tilbrook, B., and Wanninkhof, R. (2015). The reinvigoration of the Southern Ocean carbon sink. *Science*, 349(6253):1221–1224.

Langlais, C. E., Rintoul, S. R., and Zika, J. D. (2015). Sensitivity of Antarctic Circumpolar Current Transport and Eddy Activity to Wind Patterns in the Southern Ocean. *Journal of Physical Oceanography*, 45(4):1051–1067.

Large, W. G. and Pond, S. (1981). Open Ocean Momentum Flux Measurements in Moderate to Strong Winds.

Large, W. G. and Yeager, S. G. (2009). The global climatology of an interannually varying air - Sea flux data set. *Climate Dynamics*, 33(2-3):341–364.

Le Quéré, C., Andrew, R. M., Canadell, J. G., Sitch, S., Ivar Korsbakken, J., Peters, G. P., Manning, A. C., Boden, T. A., Tans, P. P., Houghton, R. A., Keeling, R. F., Alin, S., Andrews, O. D., Anthoni, P., Barbero, L., Bopp, L., Chevallier, F., Chini, L. P., Ciais, P., Currie, K., Delire, C., Doney, S. C., Friedlingstein, P., Gkritzalis, T., Harris, I., Hauck, J., Haverd, V., Hoppema, M., Klein Goldewijk, K., Jain, A. K., Kato, E., Körtzinger, A., Landschützer, P., Lefèvre, N., Lenton, A., Lienert, S., Lombardozzi, D., Melton, J. R., Metzl, N., Millero, F. J., Monteiro, P. M., Munro, D. R., Nabel, J. E. M. S., Nakaoka, S.-i., O'Brien, K., Olsen, A., Omar, A. M., Ono, T., Pierrot, D., Poulter, B., Rödenbeck, C., Salisbury, J., Schuster, U., Schwinger, J., Séférian, R., Skjelvan, I., Stocker, B. D., Sutton, A. J., Takahashi, T., Tian, H., Tilbrook, B., Van Der Laan-Luijkx, I. T., Van Der Werf, G. R., Viovy, N., Walker, A. P., Wiltshire, A. J., and Zaehle, S. (2016). Global Carbon Budget 2016. *Earth System Science Data*, 8(2):605–649.

Le Quéré, C., Rödenbeck, C., Buitenhuis, E. T., Conway, T. J., Langenfelds, R., Gomez, A., Labuschagne, C., Ramonet, M., Nakazawa, T., Metzl, N., Gillett, N. P., and Heimann, M. (2007). Saturation of the Southern Ocean C02 Sink due to recent climate change. *Science*, 316(5832):1735–1738.

Lee, K., Tong, L. T., Millero, F. J., Sabine, C. L., Dickson, A. G., Goyet, C., Park, G.-H., Wanninkhof, R., Feely, R. A., and Key, R. M. (2006). Global relationships of total alkalinity with salinity and temperature in surface waters of the world's oceans. *Geophysical Research Letters*, 33(19):L19605.

Lefèvre, N. and Taylor, A. (2002). Estimating pCO2 from sea surface temperatures in the Atlantic gyres. *Deep-Sea Research Part I: Oceanographic Research Papers*, 49:539–554.

Lefèvre, N., Watson, A. J., and Watson, A. R. (2005). A comparison of multiple regression and neural network techniques for mapping in situ pCO 2 data. *Tellus B*, 57B:375–384.

Lenton, A., Bopp, L., and Matear, R. J. (2009a). Strategies for high-latitude northern hemisphere CO2 sampling now and in the future. *Deep-Sea Research Part II: Topical Studies in Oceanography*, 56:523–532.

Lenton, A., Codron, F., Bopp, L., Metzl, N., Cadule, P., Tagliabue, A., and Le Sommer, J. (2009b). Stratospheric ozone depletion reduces ocean carbon uptake and enhances ocean acidification. *Geophysical Research Letters*, 36(12):1–5.

Lenton, A. and Matear, R. J. (2007). Role of the Southern Annular Mode (SAM) in Southern Ocean CO2 uptake. *Global Biogeochemical Cycles*, 21(2):1–17.

Lenton, A., Matear, R. J., and Tilbrook, B. (2006). Design of an observational strategy for quantifying the Southern Ocean uptake of CO2. *Global Biogeochemical Cycles*, 20(Figure 1):GB4010.

Lenton, A., Tilbrook, B., Law, R. M., Bakker, D. C. E., Doney, S. C., Gruber, N., Ishii, M., Hoppema, M., Lovenduski, N. S., Matear, R. J., McNeil, B. I., Metzl, N., Fletcher, S. E. M., Monteiro, P. M., Rödenbeck, C., Sweeney, C., and Takahashi, T. (2013). Sea-air CO2 fluxes in the Southern Ocean for the period 1990-2009. *Biogeosciences*, 10(6):4037–4054.

Lévy, M., Bopp, L., Karleskind, P., Resplandy, L., Ethé, C., and Pinsard, F. (2013). Physical pathways for carbon transfers between the surface mixed layer and the ocean interior. *Global Biogeochemical Cycles*, 27:1001–1012.

Lévy, M., Iovino, D., Resplandy, L., Klein, P., Madec, G., Tréguier, A.-M., Masson, S., and Takahashi, K. (2012). Large-scale impacts of submesoscale dynamics on phytoplankton: Local and remote effects. *Ocean Modelling*, 43-44:77–93.

Lévy, M., Klein, P., and Treguier, A.-M. (2001). Impact of sub-mesoscale physics on production and subduction of phytoplankton in an oligotrophic regime. *Journal of Marine Research*, 59(4):535–565.

Li, Z. and Cassar, N. (2016). Satellite estimates of net community production based on O 2 /Ar observations and comparison to other estimates. *Global Biogeochemical Cycles*.

Liss, P. S. and Merlivat, L. (1986). Air-Sea Gas Exchange Rates: Introduction and Synthesis. In *The Role of Air-Sea Exchange in Geochemical Cycling*, pages 113–127. Springer Netherlands, Dordrecht.

Loh, W.-Y. (2011). Classification and regression trees. *Wiley Interdisciplinary Reviews: Data Mining and Knowledge Discovery*, 1(1):14–23.

Louppe, G. (2014). *Understanding Random Forests*. Phd, University of Liege.

Lovenduski, N. S. (2007). *Impact of the Southern Annular Mode on Southern Ocean Circulation and Biogeochemistry by*. Phd, University of California.

Lovenduski, N. S., Gruber, N., and Doney, S. C. (2008). Toward a mechanistic understanding of the decadal trends in the Southern Ocean carbon sink. *Global Biogeochemical Cycles*, 22(3):9.

Lovenduski, N. S., Gruber, N., Doney, S. C., and Lima, I. D. (2007). Enhanced CO2 outgassing in the Southern Ocean from a positive phase of the Southern Annular Mode. *Global Biogeochemical Cycles*, 21(2):1–14.

Lovenduski, N. S. and Ito, T. (2009). The future evolution of the Southern Ocean CO_2 sink. *Journal of Marine Research*, 67:597–617.

Luis, A. J. and Pandey, P. C. (2004). Seasonal variability of QSCAT-derived wind stress over the Southern Ocean. *Geophysical Research Letters*, 31(13).

Madec, G. (2015). NEMO ocean engine.

Madec, G., Delecluse, P., Imbard, M., and Levy, C. (1998). OPA 8.1 Ocean General Circulation Model Reference Manual. *Notes du Pôle de Modélisation, Institut Pierre Simon Laplace*, (11):97pp.

Mahadevan, A., D'Asaro, E., Lee, C., and Perry, M. J. (2012). Eddy-Driven Stratification Initiates North Atlantic Spring Phytoplankton Blooms. *Science*, 337(6090):54–58.

Mahadevan, A., Lévy, M., and Mémery, L. (2004). Mesoscale variability of sea surface pCO2: What does it respond to? *Global Biogeochemical Cycles*, 18(GB1017):1–35.

Mahadevan, A., Tagliabue, A., Bopp, L., Lenton, A., Memery, L., and Lévy, M. (2011). Impact of episodic vertical fluxes on sea surface pCO2. *Philosophical Transactions of the Royal Society A: Mathematical, Physical and Engineering Sciences*, 369(1943):2009–2025.

Mahadevan, A., Tandon, A., and Ferrari, R. (2010). Rapid changes in mixed layer stratification driven by submesoscale instabilities and winds. *Journal of Geophysical Research: Oceans*, 115(3):1–12.

Majkut, J. D., Carter, B. R., Frölicher, T. L., Dufour, C. O., Rodgers, K. B., and Sarmiento, J. L. (2014). An observing system simulation for Southern Ocean carbon dioxide uptake. *Philosophical transactions. Series A, Mathematical, physical, and engineering sciences*, 372:20130046–.

Marshall, G. J. (2003). Trends in the Southern Annular Mode from observations and reanalyses. *Journal of Climate*, 16(24):4134–4143.

Marshall, J. C. and Speer, K. (2012). Closure of the meridional overturning circulation through Southern Ocean upwelling. *Nature Geoscience*, 5(3):171–180.

Martin, J. H. (1990). Glacial-interglacial CO 2 change: The Iron Hypothesis. *Paleoceanography*, 5(1):1–13.

Mayewski, P. A., Bracegirdle, T., Goodwin, I., Schneider, D., Bertler, N. A. N., Birkel, S., Carleton, A., England, M. H., Kang, J. H., Khan, A., Russell, J., Turner, J., and Velicogna, I. (2015). Potential for Southern Hemisphere climate surprises. *Journal of Quaternary Science*, 30(5):391–395.

McGillis, W. R., Edson, J. B., Ware, J. D., Dacey, J. W. H., Hare, J. E., Fairall, C. W., and Wanninkhof, R. (2001). Carbon dioxide flux techniques performed during GasEx-98. *Marine Chemistry*, 75(4):267–280.

McLandress, C., Shepherd, T. G., Scinocca, J. F., Plummer, D. A., Sigmond, M., Jonsson, A. I., and Reader, M. C. (2011). Separating the Dynamical Effects of Climate Change and Ozone Depletion. Part II: Southern Hemisphere Troposphere. *Journal of Climate*, 24(6):1850–1868.

McNeil, B. I. and Matear, R. J. (2008). Southern Ocean acidification: A tipping point at 450-ppm atmospheric CO2. *Proceedings of the National Academy of Sciences*, 105(48):18860–18864.

McNeil, B. I. and Matear, R. J. (2013a). The non-steady state oceanic CO2 signal: Its importance, magnitude and a novel way to detect it. *Biogeosciences*, 10(4):2219–2228.

McNeil, B. I. and Matear, R. J. (2013b). The non-steady state oceanic CO2 signal: Its importance, magnitude and a novel way to detect it. *Biogeosciences*, 10:2219–2228.

McNeil, B. I. and Sasse, T. P. (2016). Future ocean hypercapnia driven by anthropogenic amplification of the natural CO2 cycle. *Nature*, 529(7586):383–386.

Menemenlis, D., Campin, J.-m., Heimbach, P., Hill, C., Lee, T., Nguyen, A., Schodlok, M., and Zhang, H. (2008). ECCO2 : High Resolution Global Ocean and Sea Ice Data Synthesis. *Mercator Ocean Quarterly Newsletter*, 31(October):13–21.

Meredith, M. P. and Hogg, A. M. (2006). Circumpolar response of Southern Ocean eddy activity to a change in the Southern Annular Mode. *Geophysical Research Letters*, 33(16):2–5.

Meredith, M. P., Naveira Garabato, A. C., Hogg, A. M., and Farneti, R. (2012). Sensitivity of the overturning circulation in the Southern Ocean to decadal changes in wind forcing. *Journal of Climate*, 25(1):99–110.

Metzl, N., Brunet, C., Jabaud-Jan, A., Poisson, A., and Schauer, B. (2006). Summer and winter air–sea CO2 fluxes in the Southern Ocean. *Deep Sea Research Part I: Oceanographic Research Papers*, 53(9):1548–1563.

Metzl, N., Louanchi, F., and Poisson, A. (1998). Seasonal and interannual variations of sea surface carbon dioxide in the subtropical Indian Ocean. *Marine Chemistry*, 60(1-2):131–146.

Metzl, N., Tilbrook, B., and Poisson, A. (1999). The annual fCO2 cycle and the air-sea CO2 flux in the sub-Antarctic Ocean. *Tellus B*, 51B:849 – 861.

Mikaloff Fletcher, S. E., Gruber, N., Jacobson, A. R., Doney, S. C., Dutkiewicz, S., Gerber, M., Follows, M. J., Joos, F., Lindsay, K., Menemenlis, D., Mouchet, A., Müller, S. A., and Sarmiento, J. L. (2006). Inverse estimates of anthropogenic CO2 uptake, transport, and storage by the ocean. *Global Biogeochemical Cycles*, 20(2):1–16.

Mongwe, N. P. (2014). *The Seasonal Cycle of CO2 fluxes in the Southern Ocean: a model spatial scale sensitivity analysis*. PhD thesis, University of Cape Town.

Mongwe, N. P., Chang, N., and Monteiro, P. M. (2016). The seasonal cycle as a mode to diagnose biases in modelled CO 2 fluxes in the Southern Ocean. *Ocean Modelling*, 106:90–103.

Monteiro, P. M., Gregor, L., Lévy, M., Maenner, S., Sabine, C. L., and Swart, S. (2015). Intraseasonal variability linked to sampling alias in air-sea CO ₂ fluxes in the Southern Ocean. *Geophysical Research Letters*, pages n/a–n/a.

Monteiro, P. M., Schuster, U., Hood, M., Lenton, A., Metzl, N., Olsen, A., Rodgers, K. B., Sabine, C. L., Takahashi, T., Tilbrook, B., Yoder, J., Wanninkhof, R., and Watson, A. J. (2010). A Global Sea Surface Carbon Observing System: Assessment of Changing Sea Surface CO2 and Air-Sea CO2 Fluxes. *Proceedings of OceanObs'09: Sustained Ocean Observations and Information for Society*, (1):702–714.

Mountrakis, G., Im, J., and Ogole, C. (2011). Support vector machines in remote sensing: A review. *ISPRS Journal of Photogrammetry and Remote Sensing*, 66(3):247–259.

Muller, K.-R., Mika, S., Ratsch, G., Tsuda, K., and Scholkopf, B. (2001). An introduction to kernel-based learning algorithms. *IEEE Transactions on Neural Networks*, 12(2):181–201.

Mutanga, O., Adam, E., and Cho, M. A. (2012). High density biomass estimation for wetland vegetation using worldview-2 imagery and random forest regression algorithm. *International Journal of Applied Earth Observation and Geoinformation*, 18(1):399–406.

Nakaoka, S.-i., Telszewski, M., Nojiri, Y., Yasunaka, S., Miyazaki, C., Mukai, H., and Usui, N. (2013). Estimating temporal and spatial variation of ocean surface pCO2 in the North Pacific using a self-organizing map neural network technique. *Biogeosciences*, 10(9):6093–6106.

Nandan, M., Khargonekar, P. P., and Talathi, S. S. (2014). Fast SVM Training Using Approximate Extreme Points. *Journal of Machine Learning Research*, 15:59–98.

Neelakantan, A., Vilnis, L., Le, Q. V., Sutskever, I., Kaiser, L., Kurach, K., and Martens, J. (2016). Adding Gradient Noise Improves Learning for Very Deep Networks. *ICLR*, pages 1–11.

Nicholson, S. A., Lévy, M., Llort, J., Swart, S., and Monteiro, P. M. (2016). Investigation into the impact of storms on sustaining summer primary productivity in the Sub-Antarctic Ocean. *Geophysical Research Letters*, 43(17):9192–9199.

Nightingale, P. D., Malin, G., Law, C. S., Watson, A. J., Liss, P. S., Liddicoat, M. I., Boutin, J., and Upstill-Goddard, R. C. (2000). In situ evaluation of air-sea gas exchange parameterizations using novel conservative and volatile tracers.

Ono, T., Saino†, T., Kurita, N., and Sasaki, K. (2004). Basin-scale extrapolation of shipboard pCO2 data by using satellite SST and Chla. *International Journal of Remote Sensing*, 25(19):3803–3815.

Orr, J. C., Fabry, V. J., Aumont, O., Bopp, L., Feely, R. A., Doney, S. C., Gnanadesikan, A., Gruber, N., Ishida, A., Joos, F., Key, R. M., Lindsay, K., Maier-Reimer, E., Matear, R. J., Monfray, P., Mouchet, A., Najjar, R. G., Plattner, G.-K., Rodgers, K. B., Sabine, C. L., Sarmiento, J. L., Schlitzer, R., Slater, R. D., Totterdell, I. J., Weirig, M.-F., Yamanaka, Y., and Yool, A. (2005). Anthropogenic ocean acidification over the twenty-first century and its impact on calcifying organisms. *Nature*, 437(7059):681–6.

Orsi, A. H., Whitworth, T., and Nowlin, W. D. (1995). On the meridional extent and fronts of the Antarctic Circumpolar Current. *Deep Sea Research Part I: Oceanographic Research Papers*, 42(5):641–673.

Pal, M. (2005). Random forest classifier for remote sensing classification. *International Journal of Remote Sensing*, 26(1):217–222.

Park, G.-H., Wanninkhof, R., and Trinanes, J. (2010). Procedures to create real-time seasonal air-sea CO2 flux maps. Technical Report February, NOAA.

Patara, L., Böning, C. W., and Biastoch, A. (2016). Variability and trends in Southern Ocean eddy activity in 1/12° ocean model simulations. *Geophysical Research Letters*, 43(9):4517–4523.

Pedregosa, F., Varoquaux, G., Gramfort, A., Michel, C., Thirion, B., Grisel, O., Blondel, M., Prettenhoffer, P., Weiss, R., Dubourg, V., Vanderplas, J., Passos, A., and Cournapeau, D. (2011). Scikit-learn: Machine learning in Python. *Journal of Machine Learning Research*, 12:2825–2830.

Pfeil, B., Olsen, A., Bakker, D. C. E., Hankin, S., Koyuk, H., Kozyr, A., Malczyk, J., Manke, A., Metzl, N., Sabine, C. L., Akl, J., Alin, S. R., Bates, N. R., Bellerby, R. G., Borges, A. V., Boutin, J., Brown, P. J., Cai, W.-J., Chavez, F. P., Chen, A., Cosca, C., Fassbender, A. J., Feely, R. A., ., González-Dávila, M., Goyet, C., Hales, B., Hardman-Mountford, N. J., Heinze, C., Hood, M., Hoppema, M., Hunt, C. W., Hydes, D., Ishii, M., Johannessen, T., Jones, S. D., Key, R. M., Körtzinger, A., Landschützer, P., Lauvset, S. K., Lefèvre, N., Lenton, A., Lourantou, A., Merlivat, L., Midorikawa, T., Mintrop, L., Miyazaki, C., Murata, A., Nakadate, A., Nakano, Y., Nakaoka, S.-i., Nojiri, Y., Omar, A. M., Padin,

X. A., Park, G.-H., Paterson, K., Perez, F. F., Pierrot, D., Poisson, A., Rios, A. F., Santana-Casiano, J. M., Salisbury, J., Sarma, V. V. S. S., Schlitzer, R., Schneider, B., Schuster, U., Sieger, R., Skjelvan, I., Steinhoff, T., Suzuki, T., Takahashi, T., Tedesco, K., Telszewski, M., Thomas, H., Tilbrook, B., Tjiputra, J., Vandemark, D., Veness, T., Wanninkhof, R., Watson, A. J., Weiss, R., Wong, C. S., and Yoshikawa-Inoue, H. (2013). A uniform, quality controlled Surface Ocean CO2 Atlas (SOCAT). *Earth System Science Data*, 5(1):125–143.

Pierrot, D., Neill, C., Sullivan, K. F., Castle, R., Wanninkhof, R., Lüger, H., Johannessen, T., Olsen, A., Feely, R. A., and Cosca, C. E. (2009). Recommendations for autonomous underway pCO2 measuring systems and data-reduction routines. *Deep-Sea Research Part II: Topical Studies in Oceanography*, 56(8-10):512–522.

Post, A. L., Meijers, A. J. S., Fraser, A. D., Meiners, K. M., Ayers, J., Bindoff, N. L., Griffiths, H. J., Van de Putte, A. P., O'Brien, P. E., Swadling, K. M., and Raymond, B. (2014). Environmental Setting. In De Broyer, C., Koubbi, P., Griffiths, H. J., Raymond, B., D'Udekem d'Acoz, C., Van de Putte, A. P., Danis, B., David, B., Grant, S., Gutt, J., Held, C., Hosie, G., Huettmann, F., Post, A., and Ropert-Coudert, Y., editors, *Biogeographic Atlas of the Southern Ocean*, pages 46–64. Scientific Committee on Antarctic Research, Cambridge UK.

Reed, R., Oh, S., and Marks, R. (1992). Regularization using jittered training data.

Resplandy, L., Boutin, J., and Merlivat, L. (2014). Observed small spatial scale and seasonal variability of the CO2 system in the Southern Ocean. *Biogeosciences*, 11(1):75–90.

Reynolds, R. W., Smith, T. M., Liu, C., Chelton, D. B., Casey, K. S., and Schlax, M. G. (2007). Daily high-resolution-blended analyses for sea surface temperature. *Journal of Climate*, 20(22):5473–5496.

Rintoul, S. R. (2006). The Global Influence of the Southern Ocean Circulation. *Proceedings of 8 ICSHMO, Foz do Iguaçu, Brazil, April 24–28, 2006, INPE*, pages 1349–1354.

Rintoul, S. R. and England, M. H. (2002). Ekman Transport Dominates Local Air–Sea Fluxes in Driving Variability of Subantarctic Mode Water. *Journal of Physical Oceanography*, 32(5):1308–1321.

Rintoul, S. R., Hughes, C., and Olbers, D. (2001). The Antarctic Circumpolar Current System. In Siedler, G., Church, J., and Gould, J., editors, *Ocean Circulation and Climate*, pages 271–301. Academic Press, New York.

Riser, S. C., Freeland, H. J., Roemmich, D., Wijffels, S., Troisi, A., Belbéoch, M., Gilbert, D., Xu, J., Pouliquen, S., Thresher, A., Le Traon, P.-Y., Maze, G., Klein, B., Ravichandran, M., Grant, F., Poulain, P.-M., Suga, T., Lim, B., Sterl, A., Sutton, P., Mork, K.-A., Vélez-Belchí, P. J., Ansorge, I., King, B., Turton, J., Baringer, M., and Jayne, S. R. (2016). Fifteen years of ocean observations with the global Argo array. *Nature Climate Change*, 6(2):145–153.

Rödenbeck, C., Bakker, D. C. E., Gruber, N., Iida, Y., Jacobson, A. R., Jones, S. D., Landschützer, P., Metzl, N., Nakaoka, S.-i., Olsen, A., Park, G.-H., Peylin, P., Rodgers, K. B., Sasse, T. P., Schuster, U., Shutler, J. D., Valsala, V., Wanninkhof,

R., and Zeng, J. (2015). Data-based estimates of the ocean carbon sink variability – first results of the Surface Ocean pCO_2 Mapping intercomparison (SOCOM). *Biogeosciences*, 12(23):7251–7278.

Rödenbeck, C., Bakker, D. C. E., Metzl, N., Olsen, A., Sabine, C. L., Cassar, N., Reum, F., Keeling, R. F., and Heimann, M. (2014). Interannual sea-air CO2 flux variability from an observation-driven ocean mixed-layer scheme. *Biogeosciences*, 11(17):4599–4613.

Rödenbeck, C., Houweling, S., Gloor, M., and Heimann, M. (2003). CO₂ flux history 1982–2001 inferred from atmospheric data using a global inversion of atmospheric transport. *Atmospheric Chemistry and Physics*, 3(6):1919–1964.

Rödenbeck, C., Keeling, R. F., Bakker, D. C. E., Metzl, N., Olsen, A., Sabine, C. L., and Heimann, M. (2013). Global surface-ocean pCO2 and sea–air CO2 flux variability from an observation-driven ocean mixed-layer scheme. *Ocean Science*, 9(2):193–216.

Rodgers, K. B., Aumont, O., Mikaloff Fletcher, S. E., Plancherel, Y., Bopp, L., de Boyer Montégut, C., Iudicone, D., Keeling, R. F., Madec, G., and Wanninkhof, R. (2014). Strong sensitivity of Southern Ocean carbon uptake and nutrient cycling to wind stirring. *Biogeosciences*, 11(15):4077–4098.

Roemmich, D., Johnson, G., Riser, S., Davis, R., Gilson, J., Owens, W. B., Garzoli, S., Schmid, C., and Ignaszewski, M. (2009). The Argo Program: Observing the Global Oceans with Profiling Floats. *Oceanography*, 22(2):34–43.

Russell, J., Sarmiento, J. L., Cullen, H., Hotinski, R., Johnson, K. S., Riser, S. C., and Talley, L. (2014). The Southern Ocean Carbon and Climate Observations and Modeling Program (SOCCOM). *Ocean Carbon and Biogeochemistry Article*, 7(2):1–28.

Sabine, C. L., Feely, R. A., Gruber, N., Key, R. M., Lee, K., Bullister, J. L., Wanninkhof, R., Wong, C. S., Wallace, D. W. R., Tilbrook, B., Millero, F. J., Peng, T.-h., Kozyr, A., Ono, T., and Rios, A. F. (2004). The Oceanic Sink for Anthropogenic CO2. *Science*, 305(5682):367–371.

Sallée, J.-B., Matear, R. J., Rintoul, S. R., and Lenton, A. (2012). Localized subduction of anthropogenic carbon dioxide in the Southern Hemisphere oceans. *Nature Geoscience*, 5(8):579–584.

Sarmiento, J. L. and Gruber, N. (2006). *Ocean Biogeochemical Dynamics*. Princeton University Press.

Sarmiento, J. L., Gruber, N., Brzezinski, M. a., and Dunne, J. P. (2004). High-latitude controls of thermocline nutrients and low latitude biological productivity. *Nature*, 427(6969):56–60.

Sasse, T. P., McNeil, B. I., and Abramowitz, G. (2013). A novel method for diagnosing seasonal to inter-annual surface ocean carbon dynamics from bottle data using neural networks. *Biogeosciences*, 10(6):4319–4340.

Schuster, U., McKinley, G. A., Bates, N. R., Chevallier, F., Doney, S. C., Fay, A. R., González-Dávila, M., Gruber, N., Jones, S. D., Krijnen, J., Landschützer, P., Lefèvre, N., Manizza, M., Mathis, J. T., Metzl, N., Olsen, a., Rios, A. F., Rödenbeck, C., Santana-Casiano, J. M., Takahashi, T., Wanninkhof, R., and Watson, A. J. (2013). An assessment of the Atlantic and Arctic sea–air CO2 fluxes, 1990–2009. *Biogeosciences*, 10(1):607–627.

Schuster, U., Watson, A. J., Bates, N. R., Corbiere, a., González-Dávila, M., Metzl, N., Pierrot, D., and Santana-Casiano, M. (2009). Trends in North Atlantic sea-surface fCO2 from 1990 to 2006. *Deep-Sea Research Part II: Topical Studies in Oceanography*, 56(8-10):620–629.

Shetye, S., Jena, B., and Mohan, R. (2016). Dynamics of sea-ice biogeochemistry in the coastal Antarctica during transition from summer to winter. *Geoscience Frontiers*.

Shuryak, I. (2017). Advantages of Synthetic Noise and Machine Learning for Analyzing Radioecological Data Sets. *Plos One*, 12(1):e0170007.

Shutler, J. D., Land, P. E., Piolle, J.-F., Woolf, D. K., Goddijn-Murphy, L., Paul, F., Gillett, N. P., Chapron, B., and Donlon, C. J. (2015). FluxEngine: A flexible processing system for calculating atmosphere-ocean carbon dioxide gas fluxes and climatologies. *Journal of Atmospheric and Oceanic Technology*, page 151208152511003.

Smola, A. J. and Olkopf, B. (2004). A tutorial on support vector regression*. *Statistics and Computing*, 14:199–222.

Sokolov, S. and Rintoul, S. R. (2002). Structure of Southern Ocean fronts at 140°E. *Journal of Marine Systems*, 37:151–184.

Sokolov, S. and Rintoul, S. R. (2007). Multiple Jets of the Antarctic Circumpolar Current South of Australia*. *Journal of Physical Oceanography*, 37(5):1394–1412.

Son, S. W., Gerber, E. P., Perlwitz, J., Polvani, L. M., Gillett, N. P., Seo, K. H., Eyring, V., Shepherd, T. G., Waugh, D., Akiyoshi, H., Austin, J., Baumgaertner, A., Bekki, S., Braesicke, P., Brühl, C., Butchart, N., Chipperfield, M. P., Cugnet, D., Dameris, M., Dhomse, S., Frith, S., Garny, H., Garcia, R., Hardiman, S. C., Jöckel, P., Lamarque, J. F., Mancini, E., Marchand, M., Michou, M., Nakamura, T., Morgenstern, O., Pitari, G., Plummer, D. A., Pyle, J., Rozanov, E., Scinocca, J. F., Shibata, K., Smale, D., Teyssdre, H., Tian, W., and Yamashita, Y. (2010). Impact of stratospheric ozone on Southern Hemisphere circulation change: A multimodel assessment. *Journal of Geophysical Research Atmospheres*, 115(19):1–18.

Speer, K., Rintoul, S. R., and Sloyan, B. (2000). The Diabatic Deacon Cell*. *Journal of Physical Oceanography*, 30(12):3212–3222.

Stocker, T. F., Dahe, Q., Plattner, G.-K., Alexander, L. V., Allen, S. K., Bindoff, N. L., Bréon, F.-M., Church, J. A., Cubash, U., Emori, S., Forster, P., Friedlingstein, P., Talley, L. D., Vaughan, D. G., and Xie, S.-P. (2013). Technical Summary.

Climate Change 2013: The Physical Science Basis. Contribution of Working Group I to the Fifth Assessment Report of the Intergovernmental Panel on Climate Change, pages 33–115.

Sutton, A. J., Sabine, C. L., Maenner-Jones, S., Lawrence-Slavas, N., Meinig, C., Feely, R. A., Mathis, J. T., Musielewicz, S., Bott, R., McLain, P. D., Fought, H. J., and Kozyr, A. (2014). A high-frequency atmospheric and seawater pCO2 data set from 14 open-ocean sites using a moored autonomous system. *Earth System Science Data*, 6(2):353–366.

Sverdrup, H. U. (1953). On Conditions for the Vernal Blooming of Phytoplankton. *ICES Journal of Marine Science*, 18(3):287–295.

Swart, N. C. and Fyfe, J. C. (2012). Observed and simulated changes in the Southern Hemisphere surface westerly wind-stress. *Geophysical Research Letters*, 39(16):6–11.

Swart, S., Speich, S., Ansorge, I. J., and Lutjeharms, J. R. E. (2010). An altimetry-based gravest empirical mode south of Africa: 2. Dynamic nature of the Antarctic circumpolar current fronts. *Journal of Geophysical Research: Oceans*, 115:1–22.

Swart, S., Thomalla, S. J., and Monteiro, P. M. (2014). The seasonal cycle of mixed layer dynamics and phytoplankton biomass in the Sub-Antarctic Zone: A high-resolution glider experiment. *Journal of Marine Systems*, 147:103–115.

Sweeney, C., Gloor, E., Jacobson, A. R., Key, R. M., McKinley, G. A., Sarmiento, J. L., and Wanninkhof, R. (2007). Constraining global air-sea gas exchange for CO ₂ with recent bomb ¹⁴ C measurements. *Global Biogeochemical Cycles*, 21(2):n/a–n/a.

Sweeney, C., Takahashi, T., Gnanadesikan, A., Wanninkhof, R., Feely, R. A., Friederich, G. E., Chaves, F., Bates, N. R., Olafsson, J., and Sarmiento, J. L. (2002). Appendix D: Spatial and temporal variability of surface water pCO2 and sampling strategies. Technical report, NOAA, Boulder, CO.

Tagliabue, A., Bowie, A. R., Philip, W., Buck, K. N., Johnson, K. S., and Saito, M. A. (2017). The integral role of iron in ocean biogeochemistry. *Nature*, 543(7643):In Press.

Tagliabue, A., Sallée, J.-B., Bowie, A. R., Lévy, M., Swart, S., and Boyd, P. W. (2014). Surface-water iron supplies in the Southern Ocean sustained by deep winter mixing. *Nature Geoscience*, 7(March):314–320.

Takahashi, T., Feely, R. A., Weiss, R., Wanninkhof, R., Chipman, D. W., Sutherland, S. C., and Takahashi, T. T. (1997). Global air-sea flux of CO2: an estimate based on measurements of sea-air pCO2 difference. *Proceedings of the National Academy of Sciences of the United States of America*, 94(16):8292–8299.

Takahashi, T., Olafsson, J., Goddard, J. G., Chipman, D. W., and Sutherland, S. C. (1993). Seasonal variation of CO 2 and nutrients in the high-latitude surface oceans: A comparative study. *Global Biogeochemical Cycles*, 7(4):843–878.

Takahashi, T., Sutherland, S. C., Sweeney, C., Poisson, A., Metzl, N., Tilbrook, B., Bates, N. R., Wanninkhof, R., Feely, R. A., Sabine, C. L., Olafsson, J., and Nojiri, Y. (2002). Global sea-air CO2 flux based on climatological surface ocean pCO2, and seasonal biological and temperature effects. *Deep-Sea Research Part II: Topical Studies in Oceanography*, 49(9-10):1601–1622.

Takahashi, T., Sutherland, S. C., Wanninkhof, R., Sweeney, C., Feely, R. A., Chipman, D. W., Hales, B., Friederich, G. E., Chavez, F., Sabine, C. L., Watson, A. J., Bakker, D. C. E., Schuster, U., Metzl, N., Yoshikawa-Inoue, H., Ishii, M., Midorikawa, T., Nojiri, Y., Körtzinger, A., Steinhoff, T., Hoppema, M., Olafsson, J., Arnarson, T. S., Tilbrook, B., Johannessen, T., Olsen, A., Bellerby, R. G., Wong, C. S., Delille, B., Bates, N. R., and de Baar, H. J. (2009). Climatological mean and decadal change in surface ocean pCO2, and net sea–air CO2 flux over the global oceans. *Deep Sea Research Part II: Topical Studies in Oceanography*, 56(8-10):554–577.

Takahashi, T., Sweeney, C., Hales, B., Chipman, D., Newberger, T., Goddard, J. G., Iannuzzi, R., and Sutherland, S. C. (2012). The Changing Carbon Cycle in the Southern Ocean. *Oceanography*, 25:26–37.

Talley, L. D., Feely, R., Sloyan, B., Wanninkhof, R., Baringer, M., Bullister, J., Carlson, C., Doney, S. C., Fine, R., Firing, E., Gruber, N., Hansell, D., Ishii, M., Johnson, G., Katsumata, K., Key, R., Kramp, M., Langdon, C., Macdonald, A., Mathis, J. T., McDonagh, E., Mecking, S., Millero, F. J., Mordy, C., Nakano, T., Sabine, C. L., Smethie, W., Swift, J., Tanhua, T., Thurnherr, A., Warner, M., and Zhang, J.-Z. (2016). Changes in Ocean Heat, Carbon Content, and Ventilation: A Review of the First Decade of GO-SHIP Global Repeat Hydrography. *Annual Review of Marine Science*, 8(1).

Telszewski, M., Chazottes, A., Schuster, U., Watson, A. J., Moulin, C., Bakker, D. C. E., González-Dávila, M., Johannessen, T., Kortzinger, A., Luger, H., Olsen, A., Omar, A. M., Padin, X. A., Rios, A. F., Steinhoff, T., Santana-Casiano, M., Wallace, D. W. R., and Wanninkhof, R. (2009). Estimating the monthly pCO(2) distribution in the North Atlantic using a self-organizing neural network. *Biogeosciences*, 6(8):1405–1421.

Thomalla, S. J., Fauchereau, N., Swart, S., and Monteiro, P. M. (2011). Regional scale characteristics of the seasonal cycle of chlorophyll in the Southern Ocean. *Biogeosciences*, 8(10):2849–2866.

Thompson, D. W. J., Solomon, S., Kushner, P. J., England, M. H., Grise, K. M., and Karoly, D. J. (2011). Signatures of the Antarctic ozone hole in Southern Hemisphere surface climate change. *Nature Geoscience*, 4(11):741–749.

Toggweiler, J. R., Russell, J. L., and Carson, S. R. (2006). Midlatitude westerlies, atmospheric CO2, and climate change during the ice ages. *Paleoceanography*, 21(2):1–15.

Tsang, I. W., Kwok, J. T., and Cheung, P.-M. (2005). Core Vector Machines: Fast SVM Training on Very Large Data Sets. *Journal of Machine Learning Research*, 6:363–392.

Valsala, V. and Maksyutov, S. (2010). Simulation and assimilation of global ocean pCO2 and air-sea CO2 fluxes using ship observations of surface ocean pCO2 in a simplified biogeochemical offline model. *Tellus, Series B: Chemical and Physical Meteorology*, 62(5):821–840.

van der Laan, S., Manning, A. C., Resplandy, L., Bopp, L., Penelope, A., van der Laan-luijkx, I. T., and Keeling, R. F. (2016). Atmospheric measurements of O2 and CO2 suggests increasing oceanic respiratory disorder. In *ICOS Science Conference*, Helsinki, Finland.

Vancoppenolle, M., Bouillon, S., Fichefet, T., Goosse, H., Lecomte, O., Angel, M., Maqueda, M., and Madec, G. (2012). The Louvain-la-Neuve sea Ice Model. (31).

Vapnik, V. (1999). An overview of statistical learning theory. *IEEE transactions on neural networks / a publication of the IEEE Neural Networks Council*, 10(5):988–99.

Venables, H. and Moore, C. M. (2010). Phytoplankton and light limitation in the Southern Ocean: Learning from high-nutrient high-chlorophyll areas. *Journal of Geophysical Research*, 115:C02015.

Verdy, A., Marshall, J. C., and Czaja, A. (2006). Sea surface temperature variability along the path of the antarctic circumpolar current. *Journal of Physical Oceanography*, 36(7):1317–1331.

Visbeck, M. (2009). A station-based southern annular mode index from 1884 to 2005. *Journal of Climate*, 22(4):940–950.

Wang, S. and Moore, J. K. (2012). Variability of primary production and air-sea CO2 flux in the Southern Ocean. *Global Biogeochemical Cycles*, 26(1):1–12.

Wanninkhof, R. (1992). Relationship Between Wind Speed and Gas Exchange. *Journal of Geophysical Research*, 97(92):7373–7382.

Wanninkhof, R., Asher, W. E., Ho, D. T., Sweeney, C., and McGillis, W. R. (2009). Advances in Quantifying Air-Sea Gas Exchange and Environmental Forcing*. *Annual Review of Marine Science*, 1(1):213–244.

Wanninkhof, R. and McGillis, W. R. (1999). A cubic relationship between air-sea CO2 exchange and wind speed.

Wanninkhof, R., Park, G.-H., Takahashi, T., Sweeney, C., Feely, R. A., Nojiri, Y., Gruber, N., Doney, S. C., McKinley, G. A., Lenton, A., Le Quéré, C., Heinze, C., Schwinger, J., Graven, H., and Khatiwala, S. (2013). Global ocean carbon uptake: magnitude, variability and trends. *Biogeosciences*, 10(3):1983–2000.

Weiss, R. and Price, B. (1980). Nitrous oxide solubility in water and seawater. *Marine Chemistry*, 8(4):347–359.

White, W. B. and Peterson, R. G. (1996). An Antarctic circumpolar wave in surface pressure, wind, temperature and sea-ice extent. *Nature*, 380(6576):699–702.

Whitt, D. B., Lévy, M., and Taylor, J. R. (2017). Low-frequency and high-frequency oscillatory winds synergistically enhance nutrient entrainment and phytoplankton at fronts. *Journal of Geophysical Research: Oceans*, 121(2):1063–1084.

Wolf-Gladrow, D. A., Zeebe, R. E., Klaas, C., Körtzinger, A., and Dickson, A. G. (2007). Total alkalinity: The explicit conservative expression and its application to biogeochemical processes. *Marine Chemistry*, 106(1-2):287–300.

Wright, W. A., Ramage, G., Cornford, D., and Nabney, I. T. (2000). Neural Network Modelling with Input Uncertainty: Theory and Application. *Journal of VLSI Signal Processing*, 26(2):169–188.

Yeo, S.-R. and Kim, K.-Y. (2015). Decadal changes in the Southern Hemisphere sea surface temperature in association with El Niño–Southern Oscillation and Southern Annular Mode. *Climate Dynamics*, 45(11-12):3227–3242.

Zeng, J., Nojiri, Y., Landschützer, P., Telszewski, M., and Nakaoka, S.-i. (2014). A global surface ocean fCO2 climatology based on a feed-forward neural network. *Journal of Atmospheric and Oceanic Technology*, 31(8):1838–1849.

Zhang, J. and Wang, Y. (2008). A rough margin based support vector machine. *Information Sciences*, 178:2204–2214.